

**Hydrogen Bond Reorganization and Vibrational
Relaxation in Water Studied with Ultrafast
Infrared Spectroscopy**

by

Rebecca Anne Nicodemus

B.S. Chemistry, Purdue University (2004)

Submitted to the Department of Chemistry
in partial fulfillment of the requirements for the degree of

Doctor of Philosophy

at the

MASSACHUSETTS INSTITUTE OF TECHNOLOGY

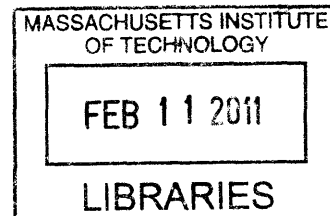
February 2011

© Massachusetts Institute of Technology 2011. All rights reserved.

Author *RA*
Department of Chemistry
December 20, 2010

Certified by *[Signature]*
Andrei Tokmakoff
Professor of Chemistry
Thesis Supervisor

Accepted by *[Signature]*
Robert W. Field
Professor of Chemistry
Chairman, Department Committee on Graduate Theses

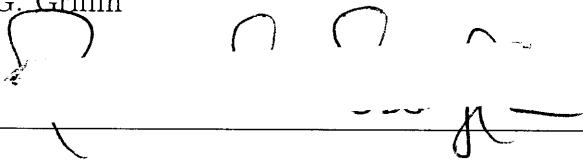


ARCHIVES

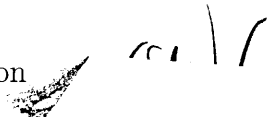
This doctoral thesis has been examined by a Committee of the Department of Chemistry that included,

Professor Robert G. Griffin

Chair

Handwritten signature of Robert G. Griffin, consisting of several loops and a long horizontal stroke.

Professor Keith A. Nelson

Handwritten signature of Keith A. Nelson, featuring a checkmark-like symbol and several vertical strokes.

Professor Andrei Tokmakoff

Thesis Supervisor

Handwritten signature of Andrei Tokmakoff, with a large 'A' and several vertical strokes, and the number '86' written below the signature line.

Hydrogen Bond Reorganization and Vibrational Relaxation in Water Studied with Ultrafast Infrared Spectroscopy

by

Rebecca Anne Nicodemus

Submitted to the Department of Chemistry
on December 20, 2010, in partial fulfillment of the
requirements for the degree of
Doctor of Philosophy

Abstract

Water consists of an extended hydrogen bond network that is constantly evolving. More than just a description of the time averaged structure is necessary to understand any process that occurs in water. In this thesis we study the dynamic regime, which involves fluctuations and rearrangements that occur on the tens of femtoseconds to picosecond time scale. The dynamic regime involves hydrogen bond breaking and forming which interlaces with translations and reorientation and ultimately large-scale reorganization. Our experimental technique is ultrafast infrared spectroscopy of the OX stretch (where X = H, D, or T) of isotopically dilute water. The OX stretch frequency is sensitive to its environment, and loss of frequency correlation provides a picture of local and collective hydrogen bond dynamics. With pump-probe experiments we are also able to measure vibrational relaxation and reorientational dynamics of water.

We present the first infrared linear absorption spectrum of the OT stretch of isotopically dilute tritiated water and compare line shape parameters to the other water isotopologues to provide further evidence that electric field fluctuations properly describe line broadening of the infrared spectrum of water. Measurement of the infrared spectrum of tritiated water is the first step towards an experiment that may be capable of directly monitoring the relative geometry between two water molecules during a hydrogen bond switch. We calculate the change in electric field and transition dipole coupling during an idealized hydrogen switch to determine the correlated frequency shifts one might observe in such an experiment.

To test the proposed vibrational relaxation pathway in isotopically dilute water, we present the first pump-probe of tritiated water and the temperature-dependent lifetime of deuterated water (or HOD in H₂O). For the OT and OH stretch, our experimental findings agree with the proposed mechanism in which the vibrational energy first relaxes to the intramolecular bend. However, evidence from the temperature-dependent measurements of the OD stretch show multiple pathways may be in competition that have different dependencies on temperature. Our results call for further experimental and theoretical studies.

We acquire temperature-dependent 2D IR and pump-probe anisotropy measurements of the OD stretch of HOD in H₂O in order to test if spectral diffusion, which reports on hydrogen bond rearrangements, and reorientation are correlated in water. We compare the temperature dependence of the picosecond decay to a number of measures of structural relaxation and find similar activation barrier heights and slightly non-Arrhenius behavior, which suggests that the reaction coordinate for hydrogen bond reorganization in water is collective.

Thesis Supervisor: Andrei Tokmakoff

Title: Professor of Chemistry

Acknowledgments

To all those who have been a part of my life - you know who you are - I thank you.

Contents

1	Introduction	23
1.1	Hypotheses of the Structure of Water	25
1.2	Infrared Spectroscopy of Hydrogen Bonded Liquids	30
1.3	Recent Experimental and Theoretical Results	33
1.3.1	Frequency Fluctuations	33
1.3.2	Vibrational Relaxation	41
1.3.3	Reorientation	42
1.4	Thesis Outline	44
2	Experimental Methods	47
2.1	Introduction	47
2.2	Generation of Ultrafast Mid-Infrared Pulses	47
2.2.1	800 nm Pulse Generation	47
2.2.2	Mid-Infrared Generation	48
2.3	Pump-probe interferometer	57
2.3.1	General Set-Up	57
2.3.2	Pulse Diagnostics	61
2.3.3	Pump-Probe Contribution from the Pump Beams	62
2.3.4	Second-Order Dispersion, or GVD	65
2.4	Data processing	67
2.4.1	Extracting Complex Correlation, Rephasing and Non-Rephasing Spectra	69
2.4.2	Cross Phase Modulation	72

2.5	Acknowledgments	76
3	Infrared Spectroscopy of Tritiated Water	77
3.1	Introduction	77
3.2	Linear Absorption of Tritiated Water	78
3.2.1	Experimental Methods	78
3.2.2	Results	79
3.2.3	Discussion	83
3.3	Model Calculations of Correlated Frequency Shifts	85
3.3.1	Diagonal Elements: Electric Field	88
3.3.2	Off-Diagonal Elements: TDC	90
3.3.3	Model Calculation of Concerted HB Switch	91
3.4	Gaussian Calculations	95
3.5	Conclusions	96
3.6	Acknowledgments	97
4	Vibrational Relaxation in Isotopically Dilute Water	99
4.1	Introduction	99
4.2	Dispersed Pump Probe of Tritiated Water	104
4.3	Temperature Dependent Lifetime of ω_{OD}	107
4.3.1	Temperature Dependent Linear Absorption	107
4.3.2	Temperature Dependent Dispersed Pump Probes	110
4.4	Thermally Shifted Ground State in Pump-Probe Measurements	116
4.5	Conclusion	118
5	Hydrogen Bond Rearrangements in Water	119
5.1	Introduction	119
5.2	Experimental Methods	121
5.3	Experimental Results	123
5.4	Spectroscopic Model	134
5.4.1	Vibrational Dephasing	135

5.4.2	Rotational Response	139
5.4.3	Thermal Effects	140
5.4.4	Modeling Results	141
5.5	Discussion	147
5.6	Molecular Dynamics Simulations	151
5.6.1	Fixed Charge SPC/E	151
5.6.2	Polarizable SPC/FQ	153
5.7	Concluding Remarks	156
5.8	Acknowledgments	157
.1	Influence of the H ₂ O Stretch and Combination Band	158
.2	Vibrational Stokes Shift	160
.3	Frequency-Dependent Reorientation	163
A	Pump-Probes and 2D IR of Pure D₂O	169
B	Linear Absorption of Isotopically Dilute Ice Ih	175
C	Urea	181
C.1	Acknowledgments	188

List of Figures

1-1	Two possibilities for the free energy surface of water	29
1-2	Geometric change during the molecular jump reorientation from [1]. Copyright 2006 American Association for the Advancement of Science.	30
1-3	Linear absorption spectrum of isotopically dilute HOD in H ₂ O (green) and HOD in D ₂ O (blue) in the mid-infrared region with the transitions indicated in blue for D ₂ O, green for H ₂ O, and black for HOD. The spectra are not offset.	31
1-4	(blue) Fit to the integrated pump-probe (PP) anisotropy for the OH stretch of HOD in D ₂ O with the decay ascribed to the librational motion indicated. (red) Best fit frequency correlation function to the 3PEPS measurement with the recurrence due to the hydrogen bond stretch indicated.	35
1-5	(Top) Model frequency correlation function, which is a single exponential with a 500 fs time constant. (Bottom) Four model 2D surfaces calculated with the model frequency correlation function at the waiting times: $\tau_1 = 0, 500, 1000,$ and 2000 fs (indicated with red circles on the frequency correlation function).	37
1-6	First moment as a function of waiting time, τ_2 of the positive signal distribution of ω_1 slices on the red and blue side of the OH stretch 2D IR line shape.	39
2-1	Schematic of the oscillator, stretcher, amplifier, compressor, and OPA lay-out (not drawn to scale). The filled black circles indicate periscopes.	48

2-2	(a) SHG FROG measured with Grenouille. (b) Spectrum of 800 nm after the oscillator (blue), amplifier (green), and measured with the Grenouille (red).	49
2-3	Transmittance of the BBO and AGS crystals	53
2-4	Layout of the OPA (not drawn to scale). The path of the 800 nm is traced in red, the dichroic beamsplitters are shown in cyan (DBS), the 800 nm beamsplitters are shown in green (BS), and the lenses are shown in orange (L).	55
2-5	Mid-IR pulses generated with the OPA by tuning the BBO and AGS crystals.	56
2-6	Spectra of the signal (blue) and idler (red) used for generating 4 μm pulses with (right) and without (left) an AR-coated piece of Si (dashed) before the monochromator.	56
2-7	Interferometer.	60
2-8	Beam layout for collecting pulse characteristics and non-linear data.	62
2-9	Pulse ordering with the chopper open and closed.	63
2-10	(a,c,d) Comparison of scanning the chopped (pump b) vs. non-chopped (pump a) beam. (b) Difference between the traces obtained by scanning each of the pumps with stage calibration (blue) and without stage calibration (green).	64
2-11	GVD of the materials in the interferometer.	66
2-12	(a) Real, (b) Imaginary, (c) Absolute Value, and (d) Phase representations of a 2D surface of HOD in H_2O at 286 K and $\tau_2 = 600$ fs.	70
2-13	(a) $\text{Re}(S_-)$, (b) $\text{Im}(S_-)$, (c) S_- , (d) $\text{Re}(S_+)$, (e) $\text{Im}(S_+)$, and (f) S_+ representations of a 2D surface of HOD in H_2O at 286 K and $\tau_2 = 600$ fs.	71
2-14	(a) Dispersed pump-probe for a pump-linearly chirped probe (left) and pump-no chirp probe (right). (b) The amplitude of the xpm at $t_p = 0$ fs. (c) Slices of the xpm in frequency at $\Omega_2 - 50 \text{ cm}^{-1}$ (red), Ω_2 (green), and $\Omega_2 + 50 \text{ cm}^{-1}$ (blue).	73

2-15	Experimental xpm (blue) compared to model calculations with linearly chirped probe (green) and unchirped probe (red).	75
2-16	2D spectra of XPM.	76
3-1	The molar absorptivity of the OT stretch of 0.3% HOT in H ₂ O	80
3-2	(A) The stretching band of each of the three isotopologues of water (ω_{OH} for HOD in D ₂ O, ω_{OD} for HOD in H ₂ O, and ω_{OT} for HOT in H ₂ O) with the frequency axis scaled by the square root of the reduced mass of each local mode. (B) The stretching band with the frequency axis scaled by the gas phase frequencies and intensities normalized to compare $\Delta\omega$. (C) Peak intensities scaled by the reduced mass of each isotope to compare ϵ	81
3-3	The OD stretch of 1% HOD in H ₂ O and the OT stretch of 0.3% HOT in H ₂ O. The maximum of the OT stretch is scaled by the ratio of the molar absorptivities. See Table 3-1.	87
3-4	The change in electric field with geometry at the proton circled in red for each atom of the adjacent water molecule. The total electric field is also shown ($E_{total}=E_{H1}+E_{H2}+E_O$). The electric field is in atomic units. 89	89
3-5	Change in TDC with geometry between the transition dipole of the proton circled in red in Figure 3-4 and each of the two transition dipoles of the adjacent water molecule. The TDC is in cm ⁻¹	91
3-6	Change in electric field and TDC during an idealized concerted HB switch. (a) The initial configuration from the top and side. The total electric field (b) and TDC (c) at the deuterium (donor) due to oxygen (red) and each hydrogen (cyan) of the first acceptor. The dashed blue indicates a broken HB with the first acceptor according to standard geometric criteria.	92

3-7	(a) Change in frequency for the OD and OT stretch during the HB switch with no TDC (solid) and with TDC and T in position 3 (dashed) and 4 (dot-dashed) [See Figure 3-6a for reference]. (b) Correlation between ω_{OD} and ω_{OT}	94
3-8	Mid-infrared spectra of dimers (b) (blue) and (d) (red); also, dimer (b) with additional H ₂ O (dashed cyan).	96
4-1	Energy level diagram of three isotopologues of water: HOD (cyan) in D ₂ O (green), HOD in H ₂ O (blue), and HOT (red) in H ₂ O.	103
4-2	The molar absorptivity of the OT stretch (blue), H ₂ O combination band, $\delta + \nu_L$ (green) [x5], and the pulse spectrum for the dispersed pump-probe measurement (dashed gray)	105
4-3	Slices in time of the transient absorption of HOT in H ₂ O (circles), the model pump-probe of ω_{OT} (blue) and the linear absorption of H ₂ O (green).	106
4-4	(a) Model pump-probe of ω_{OT} (blue) and the combination band of water (green) with the frequencies in (b) marked with lines. (b) Slices in frequency of the experimental pump-probe of HOT in H ₂ O.	107
4-5	Temperature dependent linear absorption of HOD in H ₂ O without (a) and with (b) the background H ₂ O subtracted. (Top) Linear absorption at the lowest and highest temperature of the contour plot. (Bottom) Dashed lines indicate the change in peak maxima with temperature for (a) δ_{HOD} , H ₂ O $\delta + \nu_L$, and ω_{OD} (left to right) and (b) δ_{HOD} (left) and ω_{OD} (right).	108
4-6	(a) Change in peak frequency with temperature for ω_{OD} (blue) and δ_{HOD} (green) relative to the value at 308 K (2514 and 1454 cm ⁻¹ , respectively). (b) Change in line width (FWHM) relative to the value at 308 K (166 and 83 cm ⁻¹ , respectively). Difference in wavenumbers between (c) ω_{OD} and δ_{HOD} and (d) $2\delta_{HOD}$ and ω_{OD} at the peak of each transition (cyan) and closest gap between the FWHM (red).	109

4-7	Temperature-dependent linear absorption measurements of dilute HOD in H ₂ O with (a) and without (b) the solvent H ₂ O subtracted. The spectra are offset along the absorbance axis.	111
4-8	Transient absorption measurements of HOD in H ₂ O at 278, 286, 295, 323, and 345 K and slices in frequency with maximum intensity at each of the five temperatures.	112
4-9	Experimental transient absorption at 295 K (blue) with the results from the fit (green) and $\Delta\alpha_{init}$ (red dashed) and $\Delta\alpha_{end}$ (cyan dashed) contributions shown separately at (a) $\omega = 2522 \text{ cm}^{-1}$, (b) $\omega = 2380 \text{ cm}^{-1}$, (c) $t = 1 \text{ ps}$, and (d) $t = 3.65 \text{ ps}$	113
4-10	T_1 and T^* for ω_{OD} of HOD in H ₂ O with temperature from the fit model.	115
4-11	Linear absorption coefficient, $K (=4\pi\nu k)$, of H ₂ O (1, black) and D ₂ O (2, red) from [2]. Copyright 2009 American Institute of Physics.	115
4-12	DPP of ω_{OD} without (a) and with (b) the TSGS. Slices in (c) frequency and time (d) without (solid) and with (dashed) the TSGS	117
5-1	Temperature-dependent linear absorption of dilute HOD in H ₂ O with (a) and without (b) the solvent H ₂ O subtracted. The traces are offset along the absorbance axis. The fit from our spectral model at each temperature is shown in dark gray.	124
5-2	(a) Isotropic transient absorption (offset) and (b) anisotropy (normalized at 200 fs) of dilute HOD in H ₂ O at each of the five experimental temperatures plotted as a function of delay time between the pump and probe. The best fit from our spectral model normalized at 200 fs for both (a) and (b) is shown in dark gray. (c) Phase line slope over $\omega_1 = \omega_3 = 2470 \text{ to } 2530 \text{ cm}^{-1}$ determined from the temperature and waiting time dependent 2D IR with the best fit from our model shown in gray. The experimental phase line slope and fits are offset by 0.075 per temperature as the temperature is decreased from 345 K.	125

5-3	Temperature-dependent lifetime, T_1 , (red triangles), picosecond decay of the integrated pump-probe anisotropy (green squares) and picosecond decay of the best fit frequency correlation function from the fit model (blue circles).	127
5-4	Experimental absorptive and phase 2D surfaces of dilute HOD in H ₂ O at each of the five temperatures at three waiting times: $\tau_2 = 160$ fs (top), 400 fs (middle) and 3.2 ps (bottom). The contours in the absorptive 2DIR spectra are at 12% intervals relative to the maximum. The phase spectra are plotted from $-\pi/2$ to $\pi/2$ and are windowed by 10% of the absolute value spectra.	129
5-5	Dynamic line width (DLW) for time ($\tau_2 = 40$ fs to 4 ps) and temperature-dependent (278, 295, and 345 K) 2D surfaces of the OD stretch of HOD in H ₂ O (right). 2D surfaces at 295 K and $\tau_2 = 200$ fs (top) and 2 ps (bottom) with the DLW marked in cyan (left).	130
5-6	Slope of the node (Real) for time ($\tau_2 = 40$ fs to 4 ps) and temperature-dependent (278, 295, and 345 K) absorptive 2D surfaces of the OD stretch of HOD in H ₂ O (right). 2D surfaces at 295 K and $\tau_2 = 200$ fs (top) and 2 ps (bottom) with the node marked in cyan (left).	130
5-7	Center line slope (CLS) for time ($\tau_2 = 40$ fs to 4 ps) and temperature-dependent (278, 295, and 345 K) absorptive 2D surfaces of the OD stretch of HOD in H ₂ O (right). 2D surfaces at 295 K and $\tau_2 = 200$ fs (top) and 2 ps (bottom) with the maximum of the $\nu=1\leftarrow 0$ peak marked in cyan (left).	131
5-8	Inhomogeneity index (I) for time ($\tau_2 = 40$ fs to 4 ps) and temperature-dependent (278, 295, and 345 K) 2D surfaces of the OD stretch of HOD in H ₂ O (right). Rephasing (top) and non-rephasing (bottom) surfaces at 295 K and $\tau_2 = 200$ fs normalized to the maximum of the rephasing surface.	131

5-9	Slope of the $\phi=0$ phase line, or node of the imaginary surface, for time ($\tau_2 = 40$ fs to 4 ps) and temperature-dependent (278, 295, and 345 K) 2D surfaces of the OD stretch of HOD in H ₂ O (right). 2D phase surfaces at 295 K and $\tau_2 = 200$ fs (top) and 2 ps (bottom) with the $\phi=0$ phase line marked in cyan (left).	132
5-10	Phase line slope (PLS) for time ($\tau_2 = 40$ fs to 4 ps) and temperature-dependent (278, 295, and 345 K) 2D surfaces of the OD stretch of HOD in H ₂ O (right). 2D phase surfaces at 295 K and $\tau_2 = 200$ fs (top) and 2 ps (bottom) with $\omega_1 = \omega_3 = 2470$ to 2530 cm ⁻¹ marked in magenta (left).	132
5-11	Comparison of the metrics at room temperature normalized at the initial waiting time, $\tau_2 = 40$ fs.	133
5-12	First moment of the positive amplitude for slices in ω_1 at 2454 cm ⁻¹ (red) and 2551 cm ⁻¹ (blue) at the temperatures 295 K (a) and 278 K (b). The insets show the short time behavior for each of the two temperatures.	135
5-13	Experimental linear absorption of the OD stretch of HOD in H ₂ O with the background H ₂ O subtracted (dashed gray), along with spectra calculated with the spectral model using the "full" treatment (solid blue), using $C'_\omega(t)$ with $R(t)$ and T_1 (dot dashed green), using $C_\omega(t)$ without including $R(t)$ (solid red), and using $C_\omega(t)$ without including $R(t)$ or T_1 (dot dashed cyan)	143
5-14	Absorptive and phase 2D surfaces calculated with the model at each of the five experimental temperatures at three waiting times: $\tau_2 = 160$ fs (top), 400 fs (middle) and 3.2 ps (bottom). The contours in the absorptive 2DIR spectra are at 12% intervals relative to the maximum. The phase spectra are plotted from $-\pi/2$ to $\pi/2$ and are windowed by 10% of the absolute value spectra.	144

5-15	Absorptive and phase 2D surfaces calculated with the model at $\tau_2 = 2$ ps and 278 K with (a) the "full" treatment, (b) using $C'_\omega(t)$, (c) not including the TSGS, and (d) not including the background H_2O	145
5-16	Phase line slope calculated with the spectral model for (a) 278 K and (b) 345 K with the "full" treatment (blue), using $C'_\omega(t)$ (green), not including the TSGS (red), not including the background H_2O (dot dashed cyan), and not windowing by the experimental spectrum (magenta). .	146
5-17	Arrhenius plot of the picosecond decay of the temperature-dependent best-fit frequency correlation function ($C_\omega(t)$, open circles) determined with the spectral model and anisotropy ($C_R(t)$, open squares) along with previous temperature-dependent measures of reorientational relaxation in water: optical Kerr effect [3] (OKE, filled circles), NMR [4] (crosses), terahertz time domain spectroscopy [5] (THz-TDS, asterisks), and dielectric relaxation [6] (DR, plusses). We also show the result of applying the Stokes-Einstein-Debye equation (SED, line). . .	149
5-18	Normalized temperature-dependent correlation functions for (a) the OD stretch vibrational frequency, $C_\omega(\tau)$, and (b) OD bond reorientation, $C_2(\tau)$, from MD simulations with the SPC/E water model. (c) Arrhenius plots of correlation times in femtoseconds obtained from the simulation.	152
5-19	Normalized temperature-dependent correlation functions for (a) the OD stretch vibrational frequency, $C_\omega(t)$, and (b) the bond reorientation, $C_{R,2}(t)$, from MD simulations with the SPC/FQ water model. (c) Arrhenius plot of the correlation times in femtoseconds obtained from exponential fits to the picosecond decay.	155
5-20	(a) Orientational correlation function from MD simulations for the OD bond vector (blue), out of plane vector (green), C_2 symmetry axis (red), and H-H intramolecular axis (cyan). (b) Arrhenius plot of the orientational correlation functions.	157

-21	Absorptive 2D surfaces calculated with our spectral model at 278 K at $\tau_2 = 0$ fs (first row), 600 fs (second row), and 4 ps (third row). The calculation includes only the H ₂ O combination band (first column), only the H ₂ O stretch (second column), the H ₂ O combination band and stretch and OD stretch (third column), and all three modes windowed by the experimental spectrum.	161
-22	Dispersed pump-probe calculated with the model at 278 K with (a) $C'_\omega(t)$ without including the TSGS, (b) $C_\omega(t)$ without including the TSGS, and (c) $C_\omega(t)$ including the TSGS.	162
-23	The calculated anisotropy at room temperature from our spectral model with the effect of pulse convolution (left). The frequency-dependence of the calculated anisotropy at room temperature from our spectral model including the effect of pulse convolution and cross phase modulation (right).	164
-24	Slices in frequency (left) and $t = 200$ fs (right) of the dispersed pump-probe anisotropy acquired at room temperature.	165
-25	Absolute value 2D anisotropy of dilute HOD in H ₂ O acquired at $\tau_2 = 100, 250, 300, 400, 1000$ fs.	166
-26	Slices in the 2D absolute value anisotropy with waiting time at $\omega_1 = 2475$ cm ⁻¹ (left) and $\omega_1 = 2550$ cm ⁻¹ (right)	167
A-1	Normalized linear absorption spectrum of H ₂ O (blue), D ₂ O (green), and the OD stretch of HOD in H ₂ O (red) scaled in frequency by their respective gas phase frequencies.	170
A-2	(a) DPP of pure D ₂ O in the zzzz polarization, (b) Slices in frequency of the DPP, (c) Slices in time of the DPP with the D ₂ O spectrum shown in dashed gray, and (d) Slices in time to longer delay times.	172
A-3	2D IR of pure D ₂ O at six waiting times, $T = 40, 80, 120, 160, 200,$ and 240 fs.	173
B-1	Structure of Ice Ih [206]	176

B-2	Linear absorption of H ₂ O (upper) and dilute HOD in H ₂ O (lower) in the liquid and ice phase. The peaks labeled in the upper (lower) spectra correspond to H ₂ O (HOD) transitions.	178
B-3	(a) Peak wavelength, (b) peak absorbance, (c) line width (FWHM), and (d) linear absorption of ω_{OD} of HOD in H ₂ O with the background H ₂ O subtracted.	179
C-1	(a) Linear absorption of deuterated ¹² C-urea in D ₂ O as a function of concentration normalized to the carbonyl stretch. The background D ₂ O is subtracted. (b) Difference spectrum between each concentration and the 125 mM solution and a ball and stick representation of a urea molecule [oxygen (red), carbon (black), nitrogen (blue), and deuterium (white)].	182
C-2	Shift in peak of carbonyl stretch of urea with concentration.	183
C-3	Waiting time dependent 2D IR surfaces of 1 M ¹² C-urea in D ₂ O acquired in the ZZYY polarization geometry.	184
C-4	Linear absorption of 2.5 M ¹² C-urea and ¹³ C-urea in D ₂ O (blue). Linear absorption of ¹³ C-urea and d7-NMA in D ₂ O (green). The amide I and II modes of NMA are indicated. The molecule is a ball and stick representation of NMA [oxygen (red), carbon (black), nitrogen (blue), and deuterium (white)].	185
C-5	Concentration dependent 2D IR surfaces of ¹² C-urea and ¹³ C-urea in D ₂ O acquired at $\tau_2 = 100$ fs in the ZZYY polarization geometry.	186
C-6	2D IR surfaces of 2.5 M ¹² C-urea and ¹³ C-urea in D ₂ O acquired at five waiting times in the ZZYY polarization geometry and $\tau_2 = 375$ fs in the ZZZZ polarization geometry.	187
C-7	2D IR surfaces of ¹³ C-urea and d7-NMA in D ₂ O in the ZZYY and ZZZZ polarization geometries at two waiting times.	188

List of Tables

2.1	Parameters for optical parametric amplification with a 3 mm BBO crystal	52
2.2	Parameters for difference frequency generation with a 0.5 mm AgGaS ₂	54
2.3	Second order dispersion at 4 and 6 μm (in fs ²).	66
3.1	Comparison of the absorption line shape parameters for the three isotopologues of water (ω_{OH} for HOD in D ₂ O, ω_{OD} for HOD in H ₂ O, and ω_{OT} for HOT in H ₂ O)	82
3.2	Empirical relationships using the SPC/E model relating the electric field to the frequency and transition dipole for each of the three isotopes. The relationships for OH and OD are from [7] and the relationship for OT was derived by reduced mass scaling.	88
4.1	Temperature dependencies of the line shape parameters of ω_{OD} and δ_{HOD} and the energy gap between the stretch and fundamental and overtone of the bend	110
5.1	Summary of the temperature dependent parameters contained within our spectral model for the OD stretch of HOD in H ₂ O.	147
2	Summary of the temperature-dependent parameters contained within our spectral model for the stretch (ν_S) and combination band ($\nu_L + \delta$) of H ₂ O.	159

3	Summary of the parameters contained within our spectral model for the stretch (ν_S) and combination band ($\nu_L + \delta$) of H ₂ O that do not depend on temperature.	159
---	--	-----

Chapter 1

Introduction

Set against the shimmering black background of space, the Earth appears as a bright blue marble. Indeed, it is the abundance of water on the surface that gives Earth its blue appearance. Water covers approximately 70% of the Earth's surface and the human body is made up of 55 to 78% water. Water is intrinsic to life and its unique properties are attributed to an attractive force first suggested at the beginning of last century, the hydrogen bond. The importance of the hydrogen bond has been revealed through the years, but this has not been matched with an equal understanding. Although a number of proposals of the structure of water have been made through the years, a time averaged description is not sufficient in understanding the properties of this important liquid. Dynamic properties that previously could not be explored due to experimental limitations can now be understood with ultrafast infrared spectroscopy. The dynamic regime, which is on the order of tens of femtoseconds to picoseconds, involves hydrogen bond breaking and forming which interlaces with translation and reorientation and ultimately large-scale structural rearrangement. The dynamic regime, which plays an intrinsic role in chemistry and biology, will be better understood with a motion picture of hydrogen bond rearrangement in water.

The first recorded suggestion for an attractive intermolecular force between a hydrogen and an electronegative atom was made in 1902. Alfred Werner proposed that an ammonium salt has a configuration in which a proton linked the ammonia

molecule and the ion. He symbolized the interaction $(\text{H}_3\text{N}\dots\text{H})\text{X}$ and called it Nebenvalenz, or minor valence [8]. For reference, this observation was made two years after Max Planck introduces quantum theory to explain thermal radiation and 29 years before James Chadwick discovered the neutron. Within the first half of the century of Werner's suggestion, the time-averaged radial distribution function of water was determined by x-ray diffraction [9, 10]. The first observation of the sensitivity of infrared spectroscopy to hydrogen bonding was made in 1936 [11]. To quote Pimental and McClellan, infrared spectroscopy is, "...*the* most sensitive, *the* most characteristic, and *one of the* most informative manifestations of the H bond" [12]. Time-averaged experiments have lead to convenient geometrical definitions of the hydrogen bond, for instance, "two water molecules are chosen as being hydrogen bonded only if their interoxygen distance is less than 3.5 Å, and simultaneously the O-H...O angle is less than 30°" [13]. However, to understand any process that occurs in water, more than just structure-based definition of the hydrogen bond network is required. The dynamics in water are important to a number of processes including the high mobility transport of H^+ and OH^- , dynamic solvent effects, electrochemistry, and in biology, the transport and conformational changes of macromolecules.

Dynamic information includes an understanding of how structural rearrangements occur in water. For instance, how does an initial hydrogen bond break and what becomes of the broken hydrogen bond? What is the time scale between the initial rupture of a hydrogen bond and the formation of a new hydrogen bond? Also, how many molecules are important for the description of the hydrogen bond switch? Let us consider a scenario in which (1) a water molecule that is initially hydrogen bonded has enough thermal energy to rupture a hydrogen bond, (2) with Brownian motion the water molecule undergoes diffusive motion until (3) the molecule is in a favorable geometry for hydrogen bond formation with a new partner. In this example the switching event occurs on a slower time scale than the fastest intermolecular motions in water and only one water molecule is important for the description. An experimental technique that has both the necessary temporal resolution and structural sensitivity to the motions just described is essential for a description of the structural

reorganization of water.

Ultrafast infrared spectroscopy is the tool we will use to explore the evolving structure of water. Ted Maiman invented the first operating laser in the middle of 1960 [14] and Ali Javan was credited with the first gas laser later that year [15]. In chemistry and physics, the laser has been an invaluable tool in understanding fundamental properties of molecules and macromolecules. Since the advent of the laser, the duration of the shortest pulse has been whittled down towards a single-cycle. What drives the quest for shorter pulses? Elementary chemical processes in gases and liquids take place on time scales ranging from femtoseconds to picoseconds. The fluctuations of the hydrogen bonding network of water are unusually fast compared to other simple liquids. The dynamics of the hydrogen bond network of water can only be captured with pulses shorter than the fastest events. Likewise, photographing more than just a blur when a balloon bursts or a bullet impacts an apple requires a minimum "shutter speed". Ultrafast spectroscopy, which interrogates the optical response of a system in the time-domain, is the "camera" that can capture the dynamics of water. In this thesis I present my part in unveiling the enigmatic beauty of the evolving hydrogen bond network of water.

1.1 Hypotheses of the Structure of Water

Defining the structure of any liquid is a complex problem since the instantaneous structure is disordered and the liquid is undergoing continuous reorganization. The time-averaged structure of water has been debated through the years [16], beginning even before the recognition of the hydrogen bond. In one view, the "mixture" model, a number of stable configurations exist in water. In the other, "continuum" model, the environment undergoes fluctuations about an average structure. In 1892, Roentgen proposed the first mixture model in which water consisted of a "bulky" ice-like component and a less bulky "normal liquid" component [17]. Frank and Wen suggested the "flickering cluster" mixture model, in which water consists of non-hydrogen bonded water molecules and hydrogen-bonded clusters. Hydrogen bonding is highly coopera-

tive in this model, which predicts that if one hydrogen bond breaks a cluster dissolves [18]. In 1962, Nemethy and Scheraga interpreted the radial distribution function in terms of a two component mixture model that consisted of ice-like water and water molecules with broken hydrogen bonds [19]. The interstitial model is similar in that the average structure of ice remains upon melting, but non-hydrogen bonded water molecules occupy the cavities of the lattice structure [20]. Mixture models were extended to include multiple structural components: four-, three-, and two-coordinated hydrogen bonded entities [21]. Models that can be considered "continuum" models, in that they consist of, on average, four-coordinated hydrogen bonded molecules with differing degrees of distortion, were proposed by Pople [22] and Bernal and Fowler [23]. Although the aforementioned mixture and continuum models have implications for the time-dependence of water structure (see below), they were developed to describe measures of the average structure.

Eisenberg and Kauzmann recognized that time scale must be considered when defining the structure of water [16]. In other words, the term "structure" has a different definition depending on the time interval of the measurement. They define three different structures depending on the exposure time, which are separated by the average period of a vibration, or τ_V , and the average time between two displacements, or τ_D . The first structure is the instantaneous structure, or *I-Structure*, which is the structure that will be observed if the time exposure is short compared to τ_V . To observe the vibrationally averaged structure, or *V-Structure*, the time exposure is longer than τ_V but shorter than τ_D . Finally, the last structure is the diffusionally averaged structure, or *D-Structure*, where the exposure time is longer than τ_D [16]. Time averaged experiments, such as x-ray diffraction, report on the *D-Structure* of liquid water. The ultrafast infrared experiments that will be described in this thesis report on the *V-Structure* and, therefore, provide a picture of intermolecular motion in water on a longer time scale than the vibrational period of the stretch (~ 10 and 13 fs for the OH and OD stretch, respectively). Not surprisingly, experimental techniques sensitive to different time scales have lead to debate in the literature on the structure of water. For instance, recently x-ray absorption spectroscopy (XAS) and nonresonant

x-ray Raman scatter (XRS) at the oxygen K-edge, techniques sensitive to distortions within the first coordination shell on time scales shorter than the vibrational period, or the *I-Structure*, have been measured for liquid water [24]. The authors concluded that water molecules are not on average in a tetrahedral geometry, rather each water molecule is in two hydrogen-bonded configurations with one strong donor and one strong acceptor. However, theoretical interpretations of the data have shown that the results are consistent with a unimodal density of tetrahedral liquid water [25].

Two models were developed circa 1980 that considered not only the time averaged structure, but also dynamics: the random network model [26] and the correlated-site percolation model [27]. In the percolation model, liquid water is above the percolation threshold and, therefore, consists of an extended hydrogen bond network. However, there is correlation between neighboring sites in hydrogen-bond coordination number. For instance, four coordinated water molecules, f_4 , clump together to form patches of low density. In this model, transport is dominated by the mobile fraction, which is water molecules with f_0 and f_1 coordination. However, the model does not include a description of how hydrogen bond rearrangements occur. The random network model proposed by Sceats and Rice [26] was an extension of the model proposed by Pople [22] and, therefore, predicts that on average water is four coordinated. The authors recognized that it is useful to view two different time scales for water: the inertial motion that includes librations and hindered translations and a slower time scale that includes diffusion and other relaxation processes.

Around the same time, Stillinger and Weber proposed analyzing both the thermodynamics and dynamics of water in terms of inherent structures [28]. In this treatment, the potential energy surface consists of a number of wells, or "inherent structures", and there are distortional displacements from the wells due to vibrations. Fundamental structural rearrangement can be viewed not as changes in instantaneous structures, or *I-Structures*, but rather by transitions between inherent structures with the vibrational components removed. For larger systems, inherent structures are determined by quenching along a trajectory. Within the inherent structure framework, Ohmine et al. determined the moment ratio, which reports the average displacement

of the molecules in a system, in a transition between inherent structures to determine if motion in water is collective, or delocalized [29]. For a system of 216 molecules, and upon averaging over 400 inherent structure transitions, they found ~ 20 molecules move simultaneously indicating molecular motions are quite collective in water [29]. Sciortino et al. performed another interesting study using inherent structures to understand the effect of defects on molecular mobility in liquid water [30]. They found that at low temperatures five-coordinated water molecules provide low-energy paths to transition between different tetrahedral local arrangements [30].

A simple question arises: what do the different structural models predict for the nature of a broken hydrogen bond? Figure 1-1 shows a pictorial free energy surfaces depicting two possibilities. In this figure, HB and NHB refer to water molecules in a stable and broken or highly-strained hydrogen bond, respectively. For continuum models, the average structure is a four coordinated water molecule and therefore the broken hydrogen bond is a transition state between switching hydrogen bonding partners, as shown in the lower blue curve. Defining a reaction coordinate for hydrogen bond switching would only be reasonable for the continuum model. If a water molecule is anything but, on average, four coordinated the broken hydrogen bond or a highly strained configuration would be stable, which is implied by the mixture model and shown as the green curve. In other words, a broken hydrogen bond would persist beyond the fastest intermolecular motions of water. Ultrafast infrared experiments and molecular dynamics (MD) simulations performed by the Tokmakoff group, which will be discussed below, have shown strong evidence that the nature of the broken hydrogen bond more closely follows the implications of the continuum model.

There have been recent theoretical developments in the temporal description of a broken hydrogen bond and the mechanism of hydrogen bond switching. With molecular dynamics (MD) simulations with the SPC/E model for water [31], Laage and Hynes found reorientation occurs not by small diffusive steps but rather through large amplitude angular jumps that exchange a hydrogen bond with a small contribution from the diffusive motion of the hydrogen bond frame [1, 32]. The mechanism is shown in Figure 1-2. The green lines indicate hydrogen bonds between the three

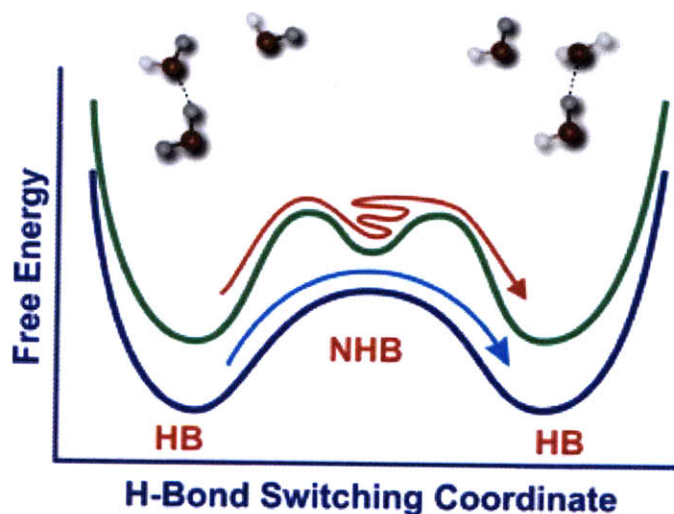


Figure 1-1: Two possibilities for the free energy surface of water

water molecules pictured and the blue lines indicate hydrogen bonds with water molecules not shown. The first and second hydrogen bond acceptors, O^a and O^b , become overcoordinated and undercoordinated, respectively, due to fluctuations in the hydrogen bond network. O^b approaches H^* from the second solvation shell as O^a moves out of the first solvation shell (Figure 1-2A) leading to the $R_{O^*O^a}=R_{O^*O^b}$ conformation (Figure 1-2B) where the H^* jump takes place. On average the jump of H^* from O^a to O^b occurs within 250 fs over an angle of 60° . The molecular jump mechanism agrees with the blue curve shown in the pictorial free energy surfaces in Figure 1-1. Interestingly, since at the bifurcation angle the water molecule that acts as the donor is five-coordinated, the mechanism also agrees with the theoretical work of Sciortino et al. [30]. Laage and Hynes also looked at the temperature dependence of reorientation and found that the large amplitude jumps and diffusive motion both contribute at every temperature, but large amplitude jumps are dominant [32]. Finally, they generated the free energy surface as a function of the change in the initial and final acceptor H-bond coordination number, the change in the distance from the rotating water and the initial and final acceptors, and the angular coordinate of the rotating water molecule. They found the translational motion of the first and second hydrogen bond acceptors had the largest contribution to the free energy barrier [32].

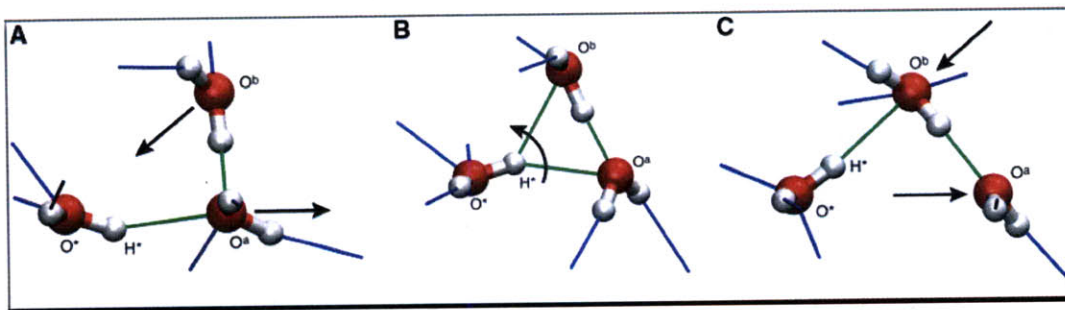


Figure 1-2: Geometric change during the molecular jump reorientation from [1]. Copyright 2006 American Association for the Advancement of Science.

The mechanism of hydrogen bond switching has also been studied with a "first principle" approach that combines *ab initio* based water potential with explicit quantum treatment of molecular motion [33]. The computational method included path-integral molecular dynamics [34] to calculate structural quantities and centroid molecular dynamics [35] to calculate dynamic and spectroscopic properties with the *ab initio* based TTM3-F water potential [36]. Paesani first shows the applicability of the model by calculating temperature-dependent linear and non-linear infrared spectra of the OD stretch of HOD in H₂O. Calculation of the molecular mechanism of hydrogen bond switching indicated that, on average, the molecules undergo a large angular jump, agreeing with the mechanism proposed by Laage and Hynes [1, 32]. However, a large number of different pathways were observed, indicating that a simple description of molecular motion was not applicable [33].

1.2 Infrared Spectroscopy of Hydrogen Bonded Liquids

Ultrafast mid-infrared spectroscopy has both the time and structural sensitivity necessary to study structural rearrangement in water. A red-shift in the fundamental and higher harmonics of the stretching mode, ν_S , upon hydrogen bond formation was first observed around 1930 for a number of molecules that contain an intramolecular hydrogen bond [37, 38]. In 1932, a shift in ν_S with concentration and temperature

was observed in solutions of alcohols [39]. In water, the OH stretch of isotopically dilute HOD in D₂O red shifts from 3707.47 cm⁻¹ in the gas phase [40] to ~3310 cm⁻¹ in hexagonal ice, a ~400 cm⁻¹ shift! In liquid water the peak of the OH stretch absorption band is ~100 cm⁻¹ blue shifted from the value for ice, indicating that the hydrogen bond strength is intermediate between ice and gas phase but more similar to ice. We show the linear absorption spectrum of isotopically dilute HOD in H₂O and HOD in D₂O from 1000 to 4000 cm⁻¹ at room temperature in Figure 1-3 with the stretch (ν_S), bend (δ), and combination bands within this spectral range indicated.

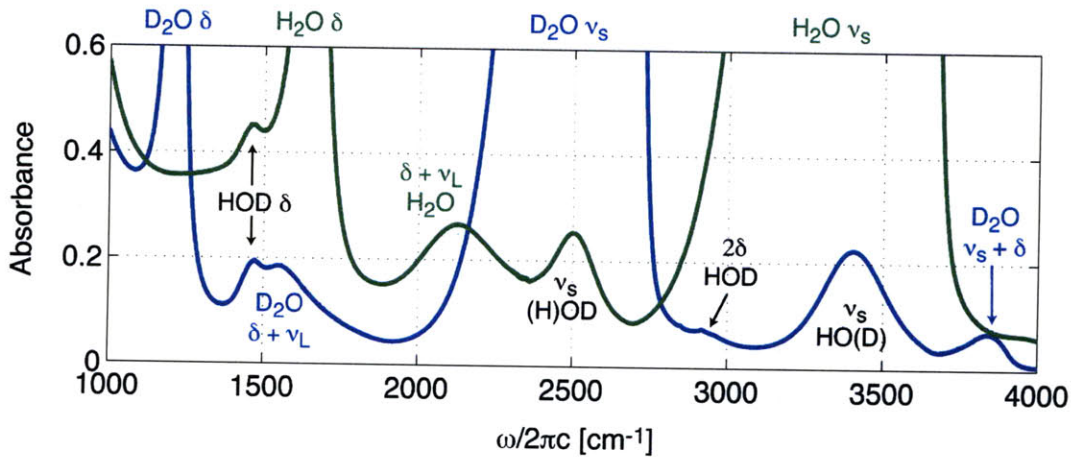


Figure 1-3: Linear absorption spectrum of isotopically dilute HOD in H₂O (green) and HOD in D₂O (blue) in the mid-infrared region with the transitions indicated in blue for D₂O, green for H₂O, and black for HOD. The spectra are not offset.

There have been many attempts to link the shift in frequency with hydrogen bonding to structure and thermodynamic properties. Only parameters that correlate with the vibrational frequency will be elucidated with infrared spectroscopy. Rundle and Parasol first noticed a relation between ν_S and R_{OO} , the O...O distance between adjacent water molecules, for hydrogen bonded solids [41]. Novak assembled a comprehensive list of ν_S and R_{OO} for strong, medium, and weak hydrogen bonded salts [42]. This correlation is based on Badger's rule, which defines a relationship between the force constant for stretching and the equilibrium intramolecular bond length [43]. Wall and Hornig used the experimentally determined relationship between ω_{OH} and R_{OO} from hydrogen bonded crystals to recast the Raman spectrum of isotopically

dilute water in terms of R_{OO} [44]. The peak corresponded to $R_{OO} = 2.85 \text{ \AA}$, which agreed within 0.04 \AA with the first peak in g_{OO} from x-ray diffraction [44].

Approximately 35 years later, the correlation between ω_{OH} and R_{OO} was tested for liquid water with mixed quantum-classical molecular dynamics (MD) simulations [45, 46, 47, 48]. The correlation on the red side was decent but dispersion was observed on the blue side (where red and blue refer to low and high frequency compared to band center, respectively). In the study by Lawrence and Skinner, the authors also decompose the frequency distribution into molecules with and without hydrogen bonds, determined by the geometric criteria given earlier. They found that although the distributions overlap, water molecules without a hydrogen bond clearly absorb on the blue side of the line width [45, 46].

Eaves et al. explored the correlation between ω_{OH} and a number of structural parameters: R_{OO} , α (the angle between the intramolecular O-H bond and R_{OO}), tetrahedrality, and the electric field and reported the correlation coefficient, ρ [46]. In this treatment, $\rho = 1$ indicates perfect correlation, $\rho = -1$ is perfectly anti-correlated, and $\rho = 0$ indicates no correlation. They found ω_{OH} and $\cos(\alpha)$ ($\rho = -0.47$) are less correlated than ω_{OH} and R_{OO} ($\rho = 0.77$), and there is even less correlation between ω_{OH} and the tetrahedrality ($\rho = -0.25$). However, the correlation between ω_{OH} and the electric field from the hydrogen bonded neighbor, E_0 , is quite good ($\rho = 0.89$) and if all the molecules in the simulation are included in the electric field calculation, E , the correlation is near unity [46]. From ab initio calculations, Hermansson first observed a relationship between ν_S and the electric field for OH^- , $\text{LiOH}\cdot\text{H}_2\text{O}$, and various water-ion/neutral clusters and crystals [49, 50, 51, 52]. In 1998, Buch and co-workers determined an empirical relationship between the shift in vibrational frequency and the electric field projected in the direction of the OH bond from experimental H_2O cluster studies [53] and in 2004 Corcelli determined a linear relationship between the electric field and frequency by performing ab initio calculations on clusters selected from MD simulations of liquid water [54]. The relationship has been refined by the Skinner group and it is found to be quadratic [55, 56]. These findings cast the system bath Hamiltonian in terms of the Stark shift Hamiltonian, which implies vibrational

dephasing is a result of electric field fluctuations [46]. However, since the electric field depends on both R_{OO} and α , ω_{OH} is related to the local structure and, therefore, the vibrational frequency is a viable tool to study local dynamics [46].

1.3 Recent Experimental and Theoretical Results

1.3.1 Frequency Fluctuations

An isotopically dilute system provides a probe of local structural dynamics, as resonant intermolecular transfer is turned off, and it imitates neat water for any process largely dominated by electrostatics. Spectral diffusion of the OH stretch of HOD in D_2O was initially reported in 1991 by Graener et al. with spectral hole burning experiments performed with relatively narrow-band mid-IR pulses [57, 58]. In a spectral hole burning experiment, a pump pulse excites a narrow spectral hole in the absorption band and a weak probe pulse monitors the spectral hole as it broadens and shifts towards band center as a result of spectral diffusion. However, there is an inherent time-bandwidth trade-off in that spectrally narrow pulses have relatively long pulse durations. The initial experiments performed with 1+ ps pulses lead the authors to conclude that the OH stretch absorption band contained several sub-bands, suggesting that the structure of water is better described with a mixture model [57, 58]. Later spectral hole burning experiments with femtosecond pulses found a ~ 1 ps correlation time and did not find evidence for sub-bands [59, 60, 61].

Stenger et al. reported the first photon-echo measurements of isotopically dilute water in 2001 [62]. Photon echo experiments are capable of discerning static, or inhomogeneous, and dynamic, or homogeneous, line broadening mechanisms and are sensitive to frequency fluctuations. Contributions to homogeneous broadening, denoted as T_2 , are population relaxation (T_1), pure dephasing (T_2^*), and reorientation (τ_{OR}). Population relaxation is an inherent property of individual molecules. Pure dephasing and reorientation are both ensemble averaged effects, in that randomization occurs through interactions with other molecules. Inhomogeneous broadening is

a consequence of the presence of distribution of frequencies, or, configurations. Conventional first order, or linear spectroscopy, is not capable of discerning between these broadening mechanisms. This quickly diminishes the hopes to extract structural information from a linear absorption spectrum and has provided fuel for the debate on the dynamic structure of water. For example, the observation of an isosbestic point in the temperature-dependent Raman spectrum lead to arguments for the "mixture" model [63]. As an aside, Smith et al. showed that an isosbestic point does not imply a multi-component mixture [64].

Stenger et al. performed a three-pulse photon echo experiment on HOD in D₂O with the second and third pulses time coincident [62]. The first pulse creates a coherence and the second pulse excites a population grating, which is instantly probed with the time coincident third pulse. The experiment is primarily sensitive to the pure dephasing time, T_2^* . The authors found $T_2^*=90$ fs, which is in between the dephasing time expected for purely homogeneous (66 fs) and purely inhomogeneous broadening (132 fs). The significant amount of homogeneous broadening suggests there are very rapid spectral fluctuations, which were estimated to be on a ~ 30 fs time scale [62]. Yeremenko et al. [65] performed a heterodyne detected two-photon echo experiment on HOD in D₂O. The goal of the measurement was to track the transition frequency fluctuation correlation function, $C_\omega(\tau)=\langle\delta\omega(\tau)\delta\omega(0)\rangle$, to understand the structural fluctuations of the hydrogen-bonded network. The two-point frequency correlation function is exact if frequency fluctuations are Gaussian. The authors modeled their results with a bi-exponential frequency correlation function with a 130 fs and 900 fs time constant attributed to hydrogen bond breaking and rearrangement of the hydrogen bond network, respectively [65].

Stenger et al. reported the first three-pulse echo peak shift (3PEPS) measurement of HOD in D₂O [66]. With 90 fs pulses the authors found the spectral diffusion contained a slow component on the order of 5-15 ps [66]. However, Yeremenko et al. found interference from the background D₂O greatly affects photon echo experiments at long time delays [67]. The Tokmakoff group measured the three-pulse photon echo peak shift of HOD in D₂O with 50-fs pulses spanning the line width of the OH

stretch [68, 69]. The temporally short pulses ensure that the fastest dynamics are captured. In three-pulse photon echo peak shift measurements, the time τ_1 , or the time between the first and second pulses, that maximizes the signal for each τ_2 is denoted as τ_1^* . The decay of τ_1^* with τ_2 indicates loss of inhomogeneity due to spectral diffusion. The signal is integrated over τ_3 so the measurement is an average over all microscopic environments. The experimental peak shift displayed a fast decay within 75 fs, a recurrence at 150 fs followed by a 1.2 ps exponential decay. With a response function formalism [70], the peak shift was self-consistently modeled with the vibrational lifetime, anisotropy decay, and linear absorption spectrum to extract the two-point frequency correlation function, $C_\omega(\tau)$. The best fit resulted in slightly different amplitudes and timescales with a fast decay in 50 fs, a recurrence at 180 fs, and 1.4 ps exponential decay [69]. We show the best fit correlation function in Figure 1-4. The difference lies within the assumptions made to relate the two-point correlation function to the peak shift measurement.

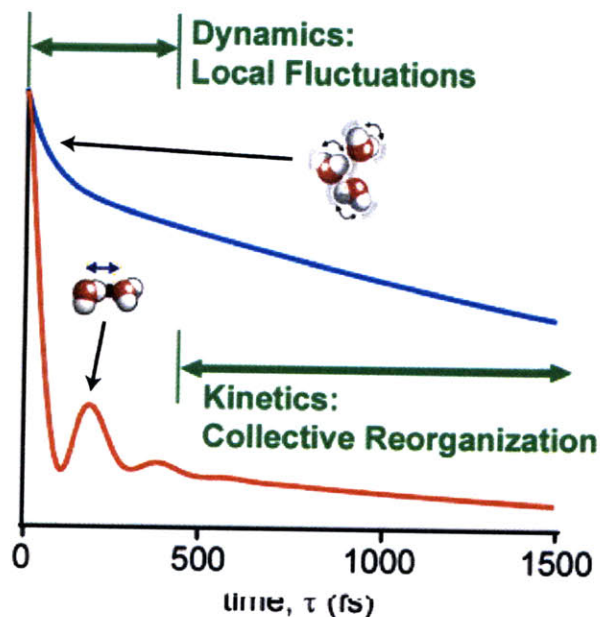


Figure 1-4: (blue) Fit to the integrated pump-probe (PP) anisotropy for the OH stretch of HOD in D₂O with the decay ascribed to the librational motion indicated. (red) Best fit frequency correlation function to the 3PEPS measurement with the recurrence due to the hydrogen bond stretch indicated.

In order to interpret the experimental results, one must first understand how structural dynamics are related to the frequency correlation function. As we discussed in Section 1.2, with MD simulations Eaves et al. found that the frequency of the stretch correlates nearly perfectly with the projection of the electric field from all the molecules in the simulation on the proton of interest (E) [46]. The electric field is dominated by the hydrogen bond partner (E_0). In order to understand the dynamics that drive vibrational dephasing, the time correlation function (TCF) of ω_{OH} and the proposed structure parameters should be compared. At early times, the TCF of ω_{OH} , E , E_0 , and R_{OO} display similar behavior, including a recurrence in a similar time period, and the TCF of E follows that of ω_{OH} nearly perfectly. The beat is not present in the TCF of the entire electric field minus that of the hydrogen bonded partner. Therefore, the local electric field fluctuation from the hydrogen bonded partner produces the beat and the molecular origin is the intermolecular hydrogen bond stretch. Interestingly, the long time decays of all the structural parameters studied show a similar behavior on a time scale greater than 200 fs, even those that were not similar to the early time behavior of $C_\omega(\tau)$ and had poor correlation with ω_{OH} . This suggests that large scale, or collective, rearrangements dominate on the longer timescales and a picture of local dynamics is lost as one moves into the kinetic regime (see Figure 1-4) [68, 46].

The broadband pulses in the aforementioned photon echo experiments ensure the fastest motions are captured. However, all microscopic environments contribute to the integrated signal. Two dimensional infrared spectroscopy (2D IR) is a technique capable of providing information on spectrally distinct environments while retaining fast temporal resolution. Put another way, the previous homodyne experiments provided a glimpse into local structural dynamics averaged over all hydrogen-bonded environments and heterodyned 2D IR measurements can report on the local structural dynamics in spectrally distinct hydrogen-bonded environments. 2D IR is a third order technique in which three pulses create a third order nonlinear polarization that radiates a signal field. For well-separated pulses, the first pulse creates a coherence and after the evolution time, τ_1 , the second pulse creates a population state. In the

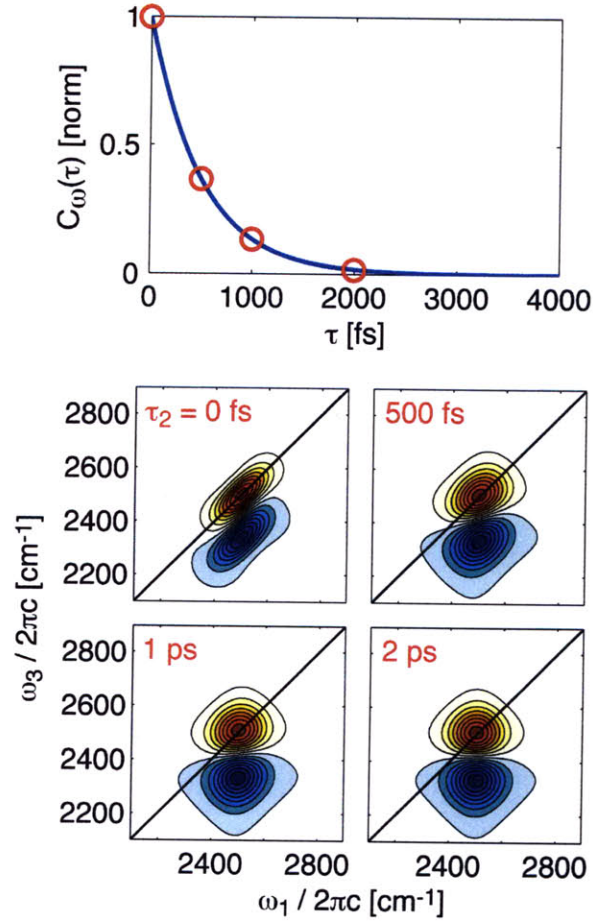


Figure 1-5: (Top) Model frequency correlation function, which is a single exponential with a 500 fs time constant. (Bottom) Four model 2D surfaces calculated with the model frequency correlation function at the waiting times: $\tau_1 = 0, 500, 1000,$ and 2000 fs (indicated with red circles on the frequency correlation function).

pump-probe geometry, which we will describe in detail in the next chapter, the third pulse, which arrives after a waiting time, τ_2 , relative to the second pulse, acts also as the local oscillator that heterodynes the signal field. τ_1 is numerically Fourier transformed to create the ω_1 axis and the signal and local oscillator are dispersed with a grating to create the ω_3 axis. Example 2D surfaces are shown in Figure 1-5 for a system with peak absorption at 2500 cm^{-1} and 160 cm^{-1} line width at full-width half maximum (FWHM). In the example the dynamics are the same across the line shape. Each 2D surface displays a positive $\nu=1 \leftarrow 0$ peak and a negative $\nu=2 \leftarrow 1$ peak

that is anharmonically shifted in ω_3 . The line shape as a function of waiting time, τ_2 , relays spectral diffusion. The 2D surfaces shown in Figure 1-5 were calculated at four waiting times: $\tau_2 = 0$ fs, 500 fs, 1 ps, and 2 ps. The time points are marked on the frequency correlation function for the model system, which is a single exponential with a 500 fs correlation time. At $\tau_2 = 0$ fs, the system retains memory of the initial excitation frequency, and therefore there is positive correlation along the diagonal. With increasing waiting time frequency memory is lost and the peaks appear uncorrelated. The homodyne photon echo peak shift can be recovered from the absolute value of the 2D IR spectra projected onto the τ_1 axis. The decrease in amplitude with τ_2 is a result of population relaxation and molecular reorientation. The projection on the ω_3 axis is equivalent to the dispersed pump probe. For waiting times longer than the lifetime, T_1 , thermalization from population relaxation needs to be accounted for in water.

The 2D IR spectrum of HOD in D₂O as a function of waiting time has been measured by the Tokmakoff group [71, 72, 73]. Even at $\tau_2 = 0$ an asymmetry between the red and blue sides is evident. For an inhomogeneous system, the anti-diagonal width ($\omega_1 + \omega_3 = 2\Omega$) is related to the homogeneous line width [33]. The broader anti-diagonal width on the blue side indicates quicker dephasing relative to the red side. The waiting time dependence was quantified with the first moment of the positive signal distribution for slices in ω_1 , which is shown in Figure 5-12. A marked difference is observed as the blue side decays monotonically and reaches an asymptotic value in 100 fs and on the red side an oscillation is observed at ~ 130 fs followed by a slower decay to band center. This observation, along with others, resulted in the conclusion that hydrogen bonds are broken only fleetingly, or, the NHB is a transient species that appears due to fluctuations about a hydrogen bond or in concerted switching of hydrogen bonded partners. The transient behavior suggests that hydrogen bond switching is concerted. The observations from the ultrafast measurements have been corroborated with molecular dynamics simulations [71, 73, 74].

The nonlinear experiments described thus far have been on the OH stretch of HOD in D₂O. In 2001, Kropman et al. performed a spectral hole burning experiment

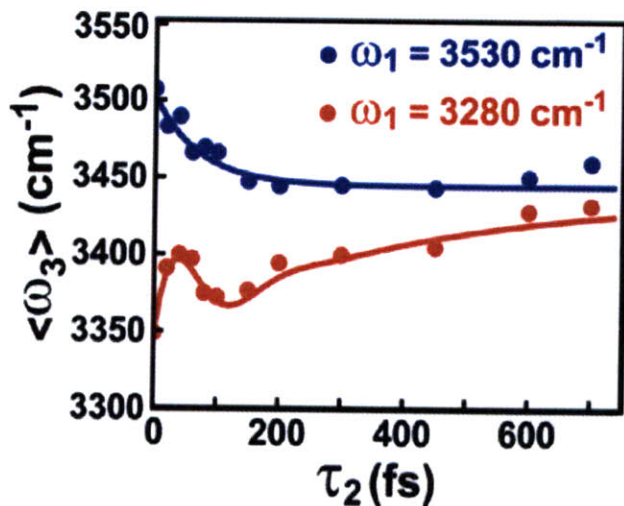


Figure 1-6: First moment as a function of waiting time, τ_2 of the positive signal distribution of ω_1 slices on the red and blue side of the OH stretch 2D IR line shape.

on the OD stretch of HOD in H_2O and found a frequency correlation time of 400 fs [75]. Laenen et al. also performed a spectral hole burning experiment and found not only multiple sub-bands but a 2 ps correlation time [76]. Asbury et al. acquired a waiting time series of 2D IR surfaces of the OD stretch of HOD in H_2O [77]. The authors characterized spectral diffusion by determining the dynamic line width, or, the full width at half maximum (FWHM) of a slice along ω_1 taken at the maximum in ω_3 , at each waiting time. Similar to the treatment by Fecko et al. [69] the 2D surfaces were modeled with a response function formalism to determine the best fit frequency correlation function, $C_\omega(\tau)$. The decay constants of the best fit triexponential correlation function were 48 fs, 400 fs, and 1.4 ps with the amplitudes 41%, 15%, and 44%, respectively [77]. The long time decay is in reasonable agreement with the best-fit correlation function determined for the OH stretch of HOD in D_2O [69], however, the recurrence in the correlation function from the hydrogen bond stretch was not experimentally observed for the OD stretch.

Theoretical modeling has been indispensable for interpreting experimental results and providing a microscopic picture of the dynamics in water. As discussed in Section 1.2, the stretch frequency is correlated to the electric field of the surrounding

environment. With the development of an empirical relationship between the frequency and electric field, frequencies can be efficiently calculated "on the fly" during molecular dynamics (MD) simulations. Skinner and coworkers have been instrumental in developing and refining an approach that combines electronic structure methods and molecular dynamics simulations (ES/MD) to study linear and nonlinear infrared spectroscopy of water [54, 7, 78, 55, 56]. Initial work by Corcelli et al. [54] based the approach to determine an empirical relationship between frequency and electric field upon similar approaches for water clusters [53, 79, 80] and N-methylacetamide (NMA) in water [81, 82, 83, 84]. Here we will present a basic outline of the approach. During a MD simulation of a water model, for instance the SPC/E model, clusters are randomly selected and the electric field at the proton of interest projected along the intramolecular bond is determined and the frequency is directly calculated by generating the one-dimensional potential energy curve and solving the relevant Schrödinger equation. Clusters are chosen from a MD simulation and not optimized in order to better estimate geometries that would be found in the liquid. Initial work found an approximately linear relationship between the *ab initio* frequency and electric field [54], which can be used with MD simulation to calculate the frequency correlation function and distribution of frequencies. This approach can also be applied to determine an empirical relationship between the electric field and transition dipole or molecular polarizability for calculations of the infrared and Raman spectra. The empirical relationship has been refined by the Skinner group and a quadratic relationship between the frequency and electric field has been found to be more accurate [55, 56].

The frequency correlation function has been calculated with MD simulations using a number of water models [46, 85, 86]. To obtain better statistics, Corcelli et al. performed a calculation with pure H₂O, rather than isotopically dilute water, such that every OH bond in the simulation could be treated as the OD vibration of interest for the purpose of comparing to experimental results on the OD stretch of HOD in H₂O. They found the frequency correlation function calculated with the fixed charge SPC/E and TIP4P [87] models displayed an oscillation due to the hydrogen bond stretch but the polarizable SPC/FQ [88] model did not. However, after fitting the

calculated frequency correlation functions with triexponentials, they found the long time decay of the SPC/FQ correlation function agreed much better with experiment: 1.45 ps for the SPC/FQ model compared to 900 fs for the SPC/E model. Schmidt et al. calculated the infrared and Raman line shape and observables from third-order experiments with MD simulations with the SPC/E, TIP4P, SPC/FQ, TIP4P/FQ [88], TIP5P/E [89], and Dang-Chang [90] water models and determined that the SPC/E model gave the best overall agreement with experiment [86].

1.3.2 Vibrational Relaxation

Pump-probe (or transient absorption) experiments are capable of measuring population relaxation and molecular reorientation. The first two interactions come from the first pulse, or pump, therefore $\tau_1 = 0$. The signal is measured as a function of τ_2 , the delay between the pump and probe pulse, and the measurement detects pump-induced transmission changes of a weak probe pulse. The signal is emitted in the direction of the probe pulse and, as in FTIR measurements, the decrease in transmission is due to the interference between the probe pulse and out of phase emitted signal. The vibrational lifetime of an excited vibration can be measured by the decay of the magic angle pump probe, or S_{iso} , which is free from molecular reorientation. Magic angle refers to the relative polarization between the linearly polarized pump and probe pulses. S_{iso} can also be constructed from the separately measured parallel and perpendicular pump-probes, as: $S_{iso}(\tau_2) = (S_{zzzz} + 2S_{zzyy})/3$. Since multiple vibrational levels are accessible, the dispersed pump probe displays a positive peak from the $\nu=1 \leftarrow 0$ ground state bleach and stimulated emission and an anharmonically shifted negative peak from the $\nu=2 \leftarrow 1$ induced absorption. The signal can be integrated (homodyne) or dispersed into frequency components.

In isotopically dilute water, the lifetime of the OH stretch of HOD in D₂O has been reported to be 0.5 to 1 ps [91, 92, 76, 93], which is shorter than the measured lifetime of the OD stretch of HOD in D₂O that has been reported to be 1.45 to 2 ps [92, 75, 76, 94, 95]. The lifetime of the bend, δ of HOD in D₂O, was found to be 380 fs [96]. Temperature-dependent measurements of the lifetime of the OH stretch

[97, 98, 99] and OD stretch [100, 101, 102] have found the lifetime generally increases with increasing temperature. Theoretical studies of vibrational relaxation of the OH stretch of HOD in D₂O have found the dominant pathway for relaxation is through the overtone of the HOD bend a lifetime of 7.7 ps [103], 2.7 ps [104], and 2.3 ps [105]. A theoretical study of vibrational relaxation of the OD stretch of HOD in H₂O performed similarly to the theoretical investigations of the OH stretch, found the primary pathway was through the fundamental of the bend (19.05 ps) or directly to the ground state (5.04 ps) depending on if the solvent was treated as rigid or flexible, respectively [106]. For both the OH and OD stretch the calculated lifetime is considerably longer than the measured lifetime. Vibrational relaxation of ν_S of pure H₂O [107, 108, 109], δ of pure H₂O [109, 110, 111], the combination band, or $\nu_L + \delta$, of pure H₂O [112], the high frequency portion of ν_L of pure H₂O, and ν_S of pure D₂O [113] have also been measured to understand energy flow in pure water.

1.3.3 Reorientation

Reorientation in water can be studied with time dependent pump-probe anisotropy determined from the parallel and perpendicular pump-probes:

$$R(\tau_2) = (S_{zzzz} - S_{zzyy}) / (S_{zzzz} + 2S_{zzyy}). \quad (1.1)$$

The anisotropy is proportional the second rank Legendre polynomial orientational correlation function: $R(\tau_2) = (2/5)C_R(\tau_2)$, where $C_R(\tau_2) = \langle P_2[\hat{\mu}(t) \cdot \hat{\mu}(0)] \rangle$, P_2 is the second order Legendre polynomial, and $\hat{\mu}$ is the transition dipole. Other measurements sensitive to reorientation include dielectric relaxation (DR) [6], THz time domain spectroscopy (THz-TDS) [5], NMR [4, 114], optical Kerr effect (OKE) spectroscopy [3], and quasi-elastic neutron scattering (QENS) [115]. With the proper assumptions, DR and THz-TDS are related the first order Legendre polynomial and NMR, OKE, and QENS are related to the second order Legendre polynomial. If reorientation occurs diffusively, the relationship between the first and second order decay time is: $\tau_{R,2} = \tau_{R,1}/3$.

The infrared pump-probe anisotropy has been measured for the OH stretch of HOD in D₂O [116, 117, 118, 93]. The pump-probe anisotropy measured by Loparo et al. with ~ 50 fs pulses, which was integrated over the $\nu=1\leftarrow 0$ peak, showed two distinct decay components. The decay was fit with a biexponential with the time constants 60 fs and 3 ps [93]. The fast, or inertial, decay was ascribed to the libration, or hindered rotation, and slow decay to diffusive reorientation. The fit to the integrated anisotropy is shown in Figure 1-4 along with the best fit frequency correlation function determined by Fecko et al. [69]. The pump-probe anisotropy of the OD stretch of HOD in H₂O shows a long time decay of ~ 2.5 ps [119, 120, 121, 95].

Frequency resolved pump probe anisotropy of isotopically dilute water has been measured to study the rotational dynamics of water molecules initially excited in different environments [119, 121]. Bakker et al. measured the pump-probe anisotropy of the OD stretch of HOD in H₂O pumping at the center and blue wing of the line width [119]. They find that when pumping at the center of the line width the anisotropy decay is independent of frequency. However, when pumping on the blue wing, the anisotropy of the molecules on the red side of the line width drops to 0.2 by the initial time point, 200 fs. This observation suggests that molecules initially excited on the blue wing must reorient to return to the red side of the line width [119]. Moilenan et al. measured the dispersed pump-probe (DPP) anisotropy of the OD stretch of HOD in H₂O [121]. Although spectral information is obscured within the first 200 fs due to non-resonant effects, the authors extrapolate to 100 fs and find there is a greater initial drop in anisotropy on the blue side of the line width (~ 0.36 at 2500 cm^{-1} compared to ~ 0.32 at 2625 cm^{-1}) and after 200 fs, the anisotropy decay is frequency independent. This observation agrees with MD simulations performed by Lawrence and Skinner, which show there is a correlation between frequency and reorientation [45]. The authors found a larger amplitude inertial reorientation in the orientational correlation function for molecules absorbing on the blue side of the line width [45], which corresponds to molecules in the NHB configuration.

1.4 Thesis Outline

Previous studies of the hydrogen bond rearrangements of water have concluded that hydrogen bonds are broken only fleetingly as hydrogen bonding partners rearrange. This observation has been made experimentally in our group with a waiting time series of two-dimensional infrared (2D IR) surfaces of the OH stretch of HOD in D₂O. 2D IR is a structural sensitive technique that offers ultrafast time resolution. The fleeting nature of broken hydrogen bonds observed experimentally agrees with the molecular jump mechanism for hydrogen bond rearrangement proposed with molecular dynamics simulations. However, this agreement is only circumstantial and further experiments are necessary to understand the relationship between reorientation and hydrogen bond rearrangements. In this thesis we present first and third-order experiments of isotopically dilute water aimed to understand vibrational population relaxation, reorientational motion, and the relationship between reorientation and hydrogen bond reorganization in water measured with the frequency correlation function. We also use temperature as an experimental handle in the measurement of all three phenomena.

In Chapter 2 we detail our method for generating ultrafast mid-infrared pulses and performing third-order experiments. Traditionally, 2D measurements have been acquired in the background free "boxcar" geometry, in which the three input fields are at three corners of a box and, to conserve momentum, the signal is emitted in the fourth corner. However, the third order experiments presented in this thesis were acquired in the pump-probe geometry, in which a collinear pump pair creates a vibrationally excited state and the third interaction is also the local oscillator. We will therefore detail the pump-probe interferometer and discuss aspects unique to the data collection geometry.

In Chapter 3 we present the first infrared linear absorption spectrum and in Chapter 4 the first non-linear measurement of radioactive isotopically dilute HOT in H₂O. Experiments with isotopically dilute water provide a local picture of hydrogen bond dynamics but information on the environment is inferred, as dephasing is controlled

by system-bath interactions. Monitoring the waiting time dependence of the cross peak, which requires the interaction of two spectrally distinct species, in 2D IR measurements of isotopically dilute HOD and HOT in H₂O is a way to directly study the relative motion between two water molecules in solution. As a step in the direction we measured the first linear absorption spectrum of tritiated water. We compare the linear absorption of the OT stretch, or ω_{OT} , with ω_{OD} and ω_{OH} of isotopically dilute water to test the reduced mass scaling relationships for frequency, line width, and extinction coefficient. Harmonic scaling relationships are found to be inadequate, and deviations are discussed in terms of electrical and mechanical anharmonicity. The inverse scaling of the line width with the square root of reduced mass provide further evidence that electric field fluctuations properly describe the line broadening in water. In the chapter we also present model calculations of the correlated frequency shifts of ω_{OT} and ω_{OD} relevant for the proposed experiment by calculating on site frequencies and off-diagonal coupling during an idealized hydrogen bond switch. Finally, we present Gaussian calculations used to determine the intermolecular coupling between ω_{OT} and ω_{OD} .

In Chapter 4 we present an investigation into the vibrational relaxation pathway in isotopically dilute water. Ideally vibrational relaxation would be studied with pulses broad enough to span the entire mid-infrared with the time-resolution to capture even the initial energy transfer. Before this experiment is realized we study the proposed relaxation pathway by comparing the vibrational lifetime between isotopes and comparing the temperature-dependent lifetime to temperature-dependent shifts in frequency of the linear absorption spectrum. We find evidence that the fundamental of the bend is the dominant accepting mode for ω_{OH} and ω_{OT} . However, for ω_{OD} the temperature dependence of the lifetime indicates that there may be additional pathways in competition that have different dependencies on temperature.

In Chapter 5 we use temperature-dependent ultrafast infrared spectroscopy of dilute HOD in H₂O to study the picosecond reorganization of the hydrogen bond network of liquid water. Temperature-dependent 2D IR, pump-probe, and linear absorption measurements are self-consistently modeled with a response function formal-

ism that includes the effects of spectral diffusion, population lifetime, reorientational motion, and non-equilibrium heating of the local environment upon vibrational relaxation. Over the range of 278 to 345 K, we find the time scales of spectral diffusion and reorientational relaxation decrease from approximately 2.4 to 0.7 ps and 4.6 to 1.2 ps, respectively, which corresponds to the barrier heights of 3.4 and 3.7 kcal/mol, respectively. We compare the temperature dependence of the time scales to a number of measures of structural relaxation and find similar effective activation barrier heights and slightly non-Arrhenius behavior, which suggests that the reaction coordinate for the hydrogen bond rearrangement in water is collective. Frequency and orientational correlation functions calculated with molecular dynamics (MD) simulations over the same temperature range support our interpretations.

In Chapter 5 we also present dispersed pump-probe and 2D IR anisotropy measurements of the OD stretch of HOD in H₂O to test proposed molecular jump mechanism of hydrogen bond switching. The proposed mechanism predicts that water molecules initially excited in a weak or broken hydrogen bond will rapidly rotate in order to form a hydrogen bond. Rotational dynamics of water molecules initially excited in different hydrogen bond configurations can be resolved by spectrally dispersing the signal. Preliminary measurements show that molecules initially excited on the blue side of the line shape display faster reorientational motion. Our predictions from previous experimental results and the implications of the proposed mechanism also suggest that the long time anisotropy decay will be uniform across the absorption band since broken hydrogen bonds do not persist, or, water molecules originally tagged on the blue side of the line shape will have statistically sampled the entire absorption band within the first couple hundred femtoseconds. Preliminary measurements show a similar long time decay across the band. Finally, in the 2D measurement we find the anisotropy along the diagonal on the blue side of the line shape and in the off-diagonal region decays faster than along the diagonal on the red-side. This observation indicates that water molecules must reorient in order to switch hydrogen bond partners.

Chapter 2

Experimental Methods

2.1 Introduction

We use ultrafast infrared spectroscopy to study the intermolecular motions and vibrational relaxation in water. In this chapter we present our method for generating and characterizing ultrafast infrared pulses. We first generate and amplify 800 nm with a Ti:sapphire oscillator and regenerative amplifier. We create near-infrared pulses with optical parametric amplification with which we create mid-infrared pulses with difference frequency generation. We describe our method for acquiring third-order measurements in the pump-probe geometry and the pulse diagnostics that are acquired prior to and concurrently with data acquisition. Finally, we present our method for data processing, which is unique to the pump-probe geometry.

2.2 Generation of Ultrafast Mid-Infrared Pulses

2.2.1 800 nm Pulse Generation

We generate sub 100 fs mid-infrared (IR) pulses in a home-built optical parametric amplifier (OPA) pumped with 800 nm at 1 kHz (1.05 mJ, 40 fs). A schematic of the set-up is shown in Figure 2-1. A home-built Ti:Sapphire oscillator pumped with a Spectra-Physics Millennia Nd:YLF laser generates a pulse at 86 MHz with ~ 40 nm of

bandwidth (FWHM) and a center wavelength of ~ 790 nm. An example spectrum of the oscillator output is shown in Figure 2-2b. After passing through a KMLabs ultrafast pulse stretcher, the pulse is amplified in a home-built Ti:Sapphire regenerative amplifier [122] pumped by a Spectra-Physics Empower Nd:YAG laser. The pulse is then compressed in a KMLabs ultrafast compressor before entering the OPA. Both the stretcher and compressor consist of a grating pair. Figure 2-2 shows a frequency and time resolved spectrum of the output pulse from the amplifier recorded by second harmonic generation (SHG) frequency resolved optical gating (FROG) with the commercial system, Grenouille [123]. The oscillator spectrum is peaked at 794 nm with a pulse width 43.8 nm at full width half maximum (FWHM). The Grenouille measures a pulse centered at 800 nm with 25.7 nm FWHM. The pulse has negligible third order dispersion. The FWHM in time is 54.44 fs, which gives a pulse length of 38.88 fs.

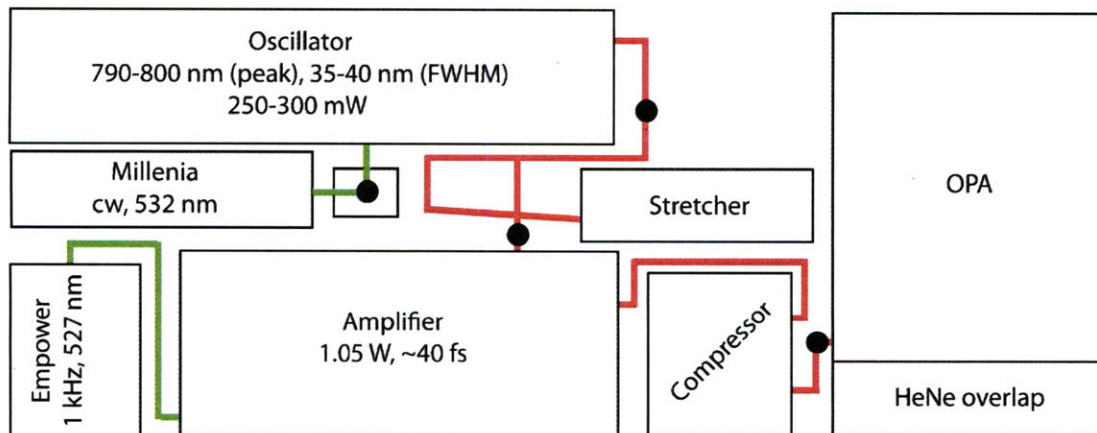


Figure 2-1: Schematic of the oscillator, stretcher, amplifier, compressor, and OPA lay-out (not drawn to scale). The filled black circles indicate periscopes.

2.2.2 Mid-Infrared Generation

From the 800 nm we generate ultrafast mid-infrared pulses with non-linear optical transformations. From Maxwell's equations and the constitutive relations for a nonmagnetic material we can derive the wave equation for nonlinear polarization

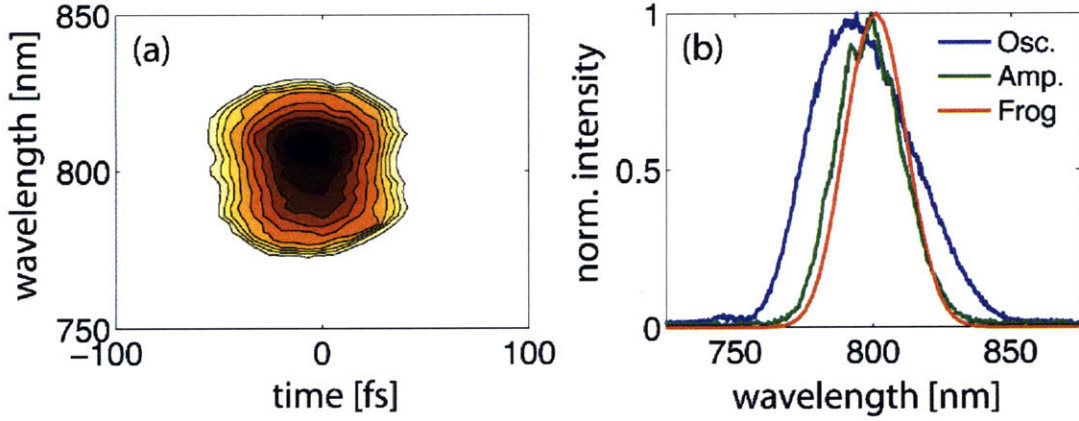


Figure 2-2: (a) SHG FROG measured with Grenouille. (b) Spectrum of 800 nm after the oscillator (blue), amplifier (green), and measured with the Grenouille (red).

(assuming $\nabla \cdot \mathbf{E} = 0$)

$$(\nabla^2 - \mu_o \sigma \frac{\partial}{\partial t} - \mu_o \epsilon \frac{\partial^2}{\partial t^2})E = \mu_o \frac{\partial^2}{\partial t^2} P^{NL}. \quad (2.1)$$

Inserting the dispersion relation $k^2 = \mu_o \epsilon \omega^2$, and applying the slowly varying envelope approximation yields

$$\frac{\partial E}{\partial z} + \alpha E + \frac{n}{c} \frac{\partial E}{\partial t} = \frac{-i \omega \mu_o c}{2n} (e \cdot p) P^{NL} e^{i(k - k_p)z}, \text{ where } \alpha = \frac{\mu_o \sigma c}{2n}. \quad (2.2)$$

In a lossless material and within the steady state approximation the second two terms on the left hand side disappear. If we consider second harmonic generation and assume the pumping field, $E(\omega_1)$, is undepleted we can directly integrate the equation from $z = 0$ to L . With the boundary condition $E(\omega_2, z=0) = 0$ this integration yields the intensity

$$I(\omega_2, L) = \frac{2\omega_2^2 d_{eff}^2}{n_2^3 c^3 \epsilon_o} L^2 I(\omega_1)^2 \left[\frac{\sin \Delta k L / 2}{\Delta k L / 2} \right]^2, \text{ where } \Delta k = k(\omega_2) - 2k(\omega_1), \quad (2.3)$$

where d_{eff} is a scalar calculated from the nonlinear coefficients, d_{il} . Notice that assuming the pump field is undepleted results in an intensity that will increase without bound with the length of the crystal. Δk is referred to as the phase mismatch and

efficient nonlinear processes require phase matching, or $\Delta k = 0$.

In optical parametric generation (OPG) the idler and signal are created from quantum noise or parametric fluorescence. Here one intense pump wave at ω_3 generates two waves at ω_1 and ω_2 (idler and signal, respectively) with the convention $\omega_3 > \omega_2 > \omega_1$. If, in addition to ω_3 , a weak seed pulse at ω_1 or ω_2 is present the process becomes optical parametric amplification. Compared to optical parametric amplification, OPG needs high pump intensities that can only be achieved with ultrashort laser pulses and/or by using a resonator for multiple amplification. The last possibility is termed optical parametric oscillation (OPO). In our application ultrafast mid-infrared pulses are created with optical parametric amplification followed by difference frequency generation (DFG), where two waves at frequencies ω_3 and ω_2 generate a field at ω_1 , or $\omega_1 = \omega_3 - \omega_2$.

The two coupled wave equations that describe OPG (assuming $E(\omega_3)$ is undepleted) are

$$\left(\frac{\partial}{\partial z} + \alpha\right)E_1 = -i\frac{\omega_1 d_{eff}}{n_1 c} E_3 E_2^* e^{-i\Delta k z} \quad (2.4)$$

$$\left(\frac{\partial}{\partial z} + \alpha\right)E_2 = -i\frac{\omega_2 d_{eff}}{n_2 c} E_3 E_1^* e^{-i\Delta k z} \quad (2.5)$$

where $\Delta k = k_3 - k_2 - k_1$ and α_1 and α_2 have been set to α . Solving the equations yields the eigenvalues

$$\begin{aligned} \gamma'_{\pm} &= -\alpha \pm \sqrt{\gamma^2 - \left(\frac{\Delta k}{2}\right)^2} \\ \gamma^2 &= \frac{\omega_1 \omega_2 d_{eff}^2}{n_1 n_2 c^2} |E_3|^2 = \frac{2\omega_1 \omega_2 d_{eff}^2}{n_1 n_2 n_3 \epsilon_0 c^3} I_3. \end{aligned} \quad (2.6)$$

γ is known as parametric gain and the equation written as $\gamma'_{\pm} = -\alpha \pm g$ introduces the variable g , defined as total gain. To have effective energy exchange between the pump and signal pulses, the group velocity mismatch (GVM) must be small to avoid temporal walk-off. This condition sets a lower limit on the duration of the pump

pulse [124],

$$\tau_3 \geq L \left| \frac{1}{\nu_2} - \frac{1}{\nu_3} \right| \quad (2.7)$$

where L is the length of the crystal. ν_2 and ν_3 are the group velocities of the signal (or idler) and pump, respectively. To obtain the shortest pulse possible the gain bandwidth must be as large as possible. An approximation of the parametric gain bandwidth for an OPG/OPA is given by [124],

$$\Delta\nu = \frac{0.53}{c|1/\nu_2 - 1/\nu_3|} \sqrt{\frac{\gamma}{L}} \quad (2.8)$$

where c is the speed of light. This expression is derived for when ω_3 is narrow band, which is not valid for femtosecond pulses. Generally a numerical treatment is necessary to take into consideration depletion, saturation effects, and GVM [125].

β -Barium Borate (BBO) is a common crystal used in the generation of near-IR pulses due to its high damage threshold, high non-linear coefficients, and commercial availability, amongst other advantages. One drawback is the transparency range, shown in Figure 2-3, as wavelengths above 2.6 μm cannot be generated with high efficiency for typical lengths of a few millimeters. An important requirement is for the crystal to have a UV band edge that prevents two photon absorption at high pump intensities of 800 nm. BBO satisfies this requirement since it is transparent at 400 nm. The angular dependence of the indices of refraction, n_o and n_e , are described by the Sellmeier equations. For BBO they are [126]

$$n_o^2 = 2.7359 + \frac{0.01878}{\lambda^2 - 0.01822} - 0.01354\lambda^2 \quad (2.9)$$

$$n_e^2 = 2.3753 + \frac{0.01224}{\lambda^2 - 0.01667} - 0.01516\lambda^2 \quad (2.10)$$

where λ is in microns. Since $n_o > n_e$, BBO is a negative uniaxial crystal. ω_3 must be extraordinary to achieve phasematching. The two possibilities for phasematching are then type-I, where both ω_1 and ω_2 are ordinary, and type-II, where ω_1 (or ω_2) is extraordinary and the other is ordinary. Type-II phasematching has the advantage

that the signal and idler can be separated after the first pass. As can be seen in equation 2.6, the parametric gain is dependent on d_{eff} . For BBO,

$$d_{eff,I} = d_{31}\sin\theta - d_{22}\cos(\theta)\sin(3\phi) \quad (2.11)$$

$$d_{eff,II} = d_{22}\cos^2(\theta)\cos(3\phi) \quad (2.12)$$

where $d_{22} = 2.2$ and $d_{31} = 0.08$ pm/V [126]. The bandwidth (fs/mm) is estimated from the group velocity mismatch between the pump and signal (idler) and calculated with the equation,

$$\frac{t_p}{L} = 2\left(\frac{1}{\nu_g(\omega_3)} - \frac{1}{\nu_g(\omega_{2(1)})}\right). \quad (2.13)$$

The group velocity is calculated by,

$$\frac{1}{\nu_g} = \frac{n}{c}\left(1 - \frac{\lambda}{n}\frac{dn}{d\lambda}\right). \quad (2.14)$$

Table 2-1 gives the signal and idler wavelengths, phasematching angle, $|d_{eff}|$, gain, and bandwidth (BW) for a 3 mm crystal estimated from the GVM for mid-infrared pulses generated at 4, 5, and 6 μm . The calculation is performed for type-II phase-matching in which the ω_1 is extraordinary and ω_2 is ordinary. The parametric gain, in cm^{-1} , can be obtained from the gain given in the table by multiplying by the square root of the pump intensity (in W/cm^2).

Target mid-IR λ :	4 μm	5 μm	6 μm
signal [μm]	1.33	1.38	1.42
idler [μm]	2.00	1.90	1.85
θ [degrees]	26.2	26.6	26.9
d_{eff} [pm/V]	1.57	1.55	1.54
γ' [$\text{W}^{-1/2}$]	7.90×10^{-5}	7.89×10^{-5}	7.87×10^{-5}
BW [cm^{-1}], ω_2	281	270	260
BW [cm^{-1}], ω_1	409	350	326

Table 2.1: Parameters for optical parametric amplification with a 3 mm BBO crystal

Similar coupled differential equations for wave propagation as those expressed for

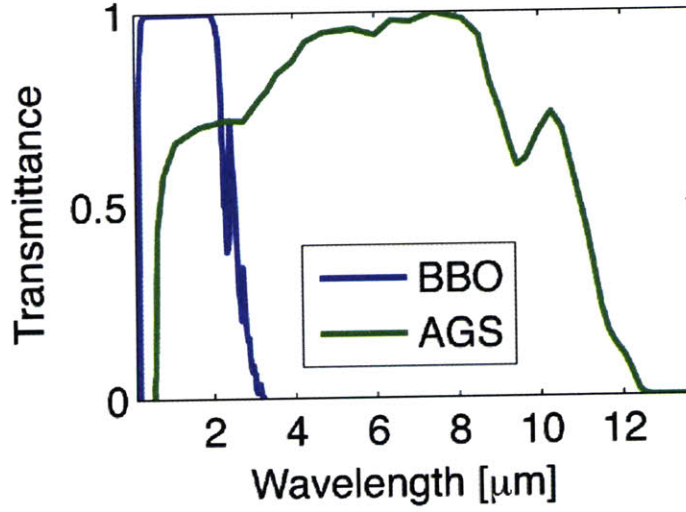


Figure 2-3: Transmittance of the BBO and AGS crystals

optical parametric amplification can be written for DFG. The phase mismatch is $\Delta k = k_3 - k_1 - k_2$ and the solution assuming ω_3 is undepleted is:

$$I_2(L) = I_2(0) \cosh^2 \gamma z \quad (2.15)$$

$$I_1(L) = \frac{\omega_1}{\omega_2} I_2(0) \sinh^2 \gamma z \quad (2.16)$$

where γ is the gain defined above.

A common crystal for the generation of mid-infrared light is AgGaS₂ (AGS) through difference frequency generation (DFG) [127, 128, 129, 130]. The transmission curve for AgGaS₂ is shown in Figure 2-3. The Sellmeier equations for AgGaS₂ are:

$$n_o^2 = 5.7975 + \frac{0.2311}{\lambda^2 - 0.0688} - 0.00257\lambda^2 \quad (2.17)$$

$$n_e^2 = 5.5436 + \frac{0.2230}{\lambda^2 - 0.0946} - 0.00261\lambda^2. \quad (2.18)$$

AgGaS₂ is also a negative uniaxial material and setting ω_1 to the mid-infrared wavelength allows for three types of phasematching. ω_3 is extraordinary in all three types. In Type-I phasematching ω_1 and ω_2 are ordinary and in Type IIa(b) ω_1 is extraordinary (ordinary) and ω_2 is ordinary (extraordinary). The effective nonlinear coefficients

are:

$$d_{eff,I} = d_{36}\sin(\theta)\sin(2\phi) \quad (2.19)$$

$$d_{eff,II} = d_{36}\sin(2\theta)\sin(2\phi). \quad (2.20)$$

where $d_{36} = 13$ pm/V [131]. The phasematching angle, d_{eff} , gain, and bandwidth at 4, 5, and 6 μm for type-II phasematching of a 0.5-mm AgGaS_2 are given in Table 2-2.

Target mid-IR λ :	4 μm	5 μm	6 μm
θ [degrees]	51.8	45.5	41.8
d_{eff} [pm/V]	14.8	15.3	15.3
γ' [$\text{W}^{-1/2}$]	2.43×10^{-4}	2.30×10^{-4}	2.13×10^{-4}
BW [cm^{-1}], ω_1	287	324	373

Table 2.2: Parameters for difference frequency generation with a 0.5 mm AgGaS_2 .

We generate mid-infrared light with white light seeded two stage optical parametric amplification followed by difference frequency generation (DFG). A schematic of the OPA is shown in Figure 2-4. A beamsplitter transmits 1% of the 800 nm to create a white light continuum in a sapphire plate, which mixes with a second portion of the 800 nm (9%) in a 3 mm Type-II BBO crystal ($\theta=26^\circ$, $\phi=0^\circ$) to create a higher frequency (signal) and lower frequency (idler) pulse. The two 800 nm beamsplitters are shown in green in Figure 2-4. After the first pass, a dichroic reflects the signal into a beam dump and transmits the idler, which passes back through the BBO with the third portion of 800 nm (90%). The dichroics, which are shown in cyan, are highly reflective at 1.2 to 1.46 μm and highly transmissive at 1.64 to 2.1 μm . The idler is the seed in the second pass to create higher power signal and idler. Finally, the mid-IR is created through difference frequency generation of the signal and idler in a 0.5 mm AgGaS_2 crystal. The OPA is tunable between $\lambda_{max} \approx 4\text{-}7$ microns (see Figure 2-5). Notice the absorption lines in the red-shifted spectrum from the absorption by water vapor and the relatively narrow CO_2 absorption at ~ 2370 cm^{-1} in the green and blue spectra. The water vapor lines and CO_2 absorption are marked at the top of the figure.

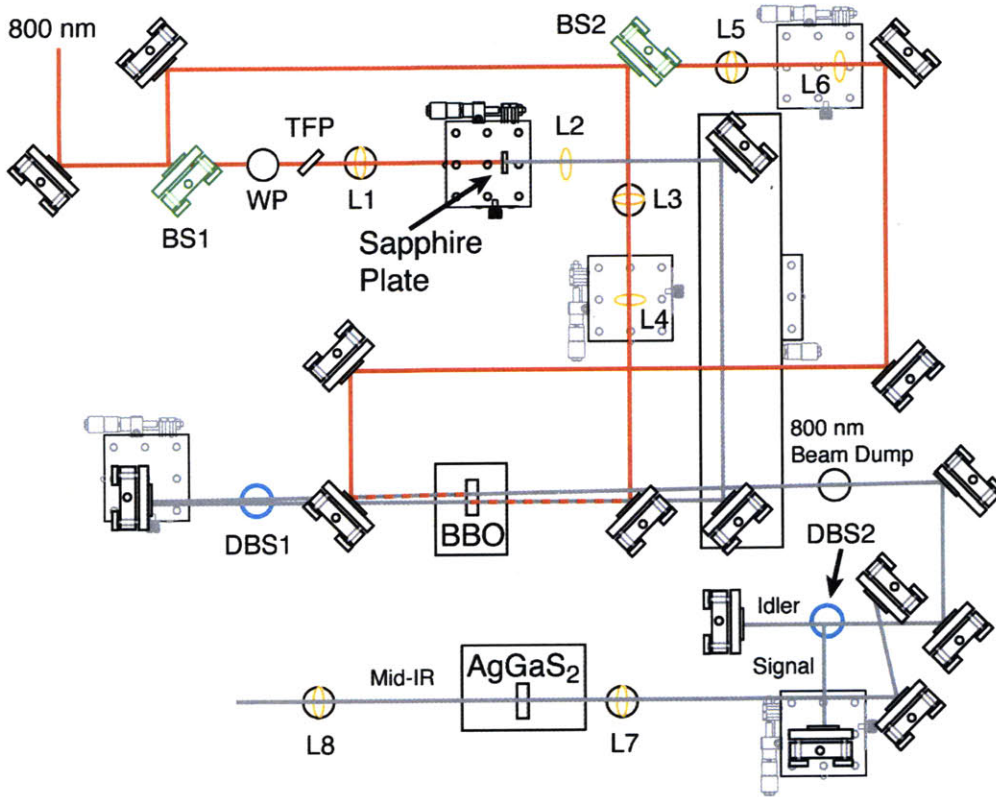


Figure 2-4: Layout of the OPA (not drawn to scale). The path of the 800 nm is traced in red, the dichroic beamsplitters are shown in cyan (DBS), the 800 nm beamsplitters are shown in green (BS), and the lenses are shown in orange (L).

The spectra of the signal and idler used for generating $4 \mu\text{m}$ pulses are shown in Figure 2-6. The spectrum is taken after the mid-IR/signal/idler pass through 1 mm of Ge rotated to Brewster's angle used for HeNe overlap. Although Ge greatly decreases the amount of signal and idler, they are still present ($\sim 7\%$ and $\sim 23\%$ of the total light, respectively). Ideally, if dispersion can be matched, one would use a thicker piece or additional piece of Ge (or Si) to further decrease the amount of signal and idler (see the section on dispersion). The wavelength axis is from 20 to $1.67 \mu\text{m}$ since the detector sensitivity is peaked at $8 \mu\text{m}$ and is therefore not sensitive at $1.33 \mu\text{m}$ (the wavelength of the signal). Although only the $2 \mu\text{m}$ idler peak is expected within this wavelength range, there is intensity at multiple wavelengths for both the signal and idler. We placed a piece of anti-reflection (AR) coated silicon before the monochromator to see if the extra peaks are real or from higher order diffraction off

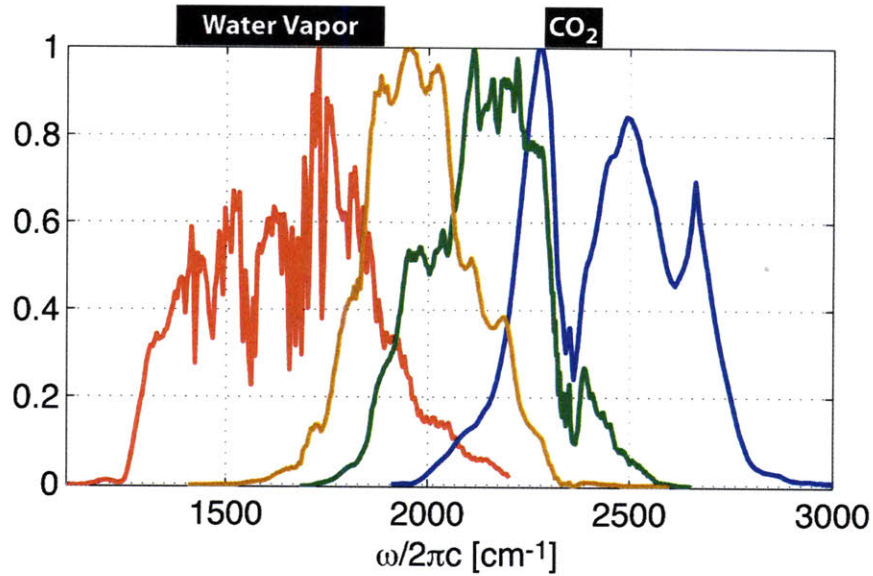


Figure 2-5: Mid-IR pulses generated with the OPA by tuning the BBO and AGS crystals.

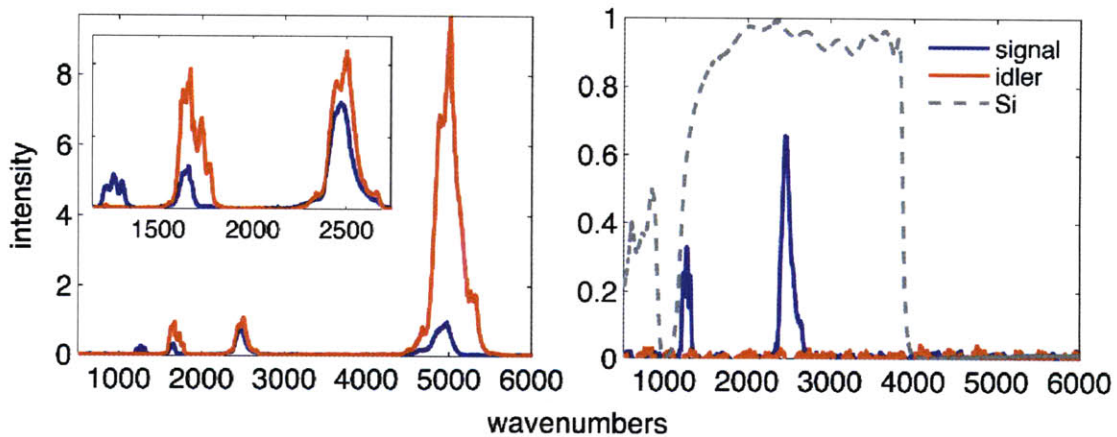


Figure 2-6: Spectra of the signal (blue) and idler (red) used for generating $4 \mu\text{m}$ pulses with (right) and without (left) an AR-coated piece of Si (dashed) before the monochromator.

the grating. The transmittance of the Si is shown as a gray dashed line on the right-hand side of the figure. The peaks in the idler spectrum at 4 and $6 \mu\text{m}$ disappear with the Si showing that the peaks are not real. The peak at $6 \mu\text{m}$ in the signal spectrum disappears with the Si but the peaks at $8 \mu\text{m}$ and $4 \mu\text{m}$ remain, showing that another non-linear process is occurring to create these wavelengths. However,

the 8 μm peak may be second order diffraction from the 4 μm peak.

2.3 Pump-probe interferometer

2.3.1 General Set-Up

The interferometer is designed to acquire non-linear measurements in the pump-probe geometry [132]. We use two beamsplitters to split the mid-infrared into three pulses. A third beamsplitter recombines the collinear pulse pair that creates the population state. The third pulse acts as the probe and local oscillator. The interferometer set-up must also allow for pulse diagnostics to be quickly and easily acquired. It is advantageous to make the interferometer as small as possible so that fluctuations from air currents, temperature gradients, etc. are minimized. Finally, second order dispersion, which will be discussed in the next section, must be matched in order for pulses to be transform limited.

The layout of the interferometer is shown in Figure 2-7. The grey dashed line outlines the plexiglas and aluminum box and the black line outlines the 2'x2' breadboard upon which the majority of the interferometer is built. We use beamsplitters to split the infrared into three parts to acquire data in the pump-probe geometry in which a collinear pulse pair creates the population state and the third pulse acts as the probe and local oscillator. The beamsplitters, which consist of a thin layer of Ge on KBr substrate, are polarization sensitive. If the infrared is p(s)-polarized, $\sim 70\%/30\%$ ($\sim 45\%/55\%$) is transmitted/reflected. We chose to split the beams $\sim 50/50$ at each beamsplitter so we use a turning periscope between the HeNe overlap and interferometer to rotate the polarization. The first beamsplitter transmits the probe beam (cyan, $\sim 45\%$) and reflects the beam that is split into the two pump beams (green and blue), which are recombined prior to the sample ($\sim 14\%$ each). Since the beamsplitters absorb an appreciable amount of the HeNe, the interferometer was designed so that each of the three beams are transmitted once through a beamsplitter. With the retroreflectors, the probe beam is lowered by 0.5" towards the table and the two pump

beams are raised by 0.5'' so that the beams are displaced vertically by 1''. In order to avoid added dispersion, we use reflective optics (parabolics) to focus the beams into the sample position and re-collimate after the sample. Given that the effective focal length of the parabolics is 3'', the crossing angle of the pump and probe at the sample is $\sim 19^\circ$. The signal is spectrally dispersed after the sample with either a 40, 75, or 100-mm/groove grating to a 64-channel N₂ cooled MCT detector. In the pump-probe geometry, a transient absorption measurement can be acquired simply by blocking the non-chopped pump beam (top trace in Figure 2-8).

Pulse delays are controlled with a pair of AR-coated ZnSe wedges mounted to mechanical stages (Newport). The stages control the pulse delay by changing the amount of material the beam transverses by translating the wedge face perpendicular to the beam path [133]. Each wedge pair is aligned antiparallel so there is negligible beam displacement. The placement of the wedge pair is shown in the upper left hand corner of Figure 2-7. The wedges are designed to have 0.1 fs delay per μm travel and a total optical path length delay of 5000 fs, which requires a 5 cm wedge. However, since the beams are not infinitely small, an extra 1 cm in length is added. The required wedge angle can be calculated from

$$\theta = \arctan(R \times c / \Delta n), \quad (2.21)$$

where R is the resolution (0.1 fs/ μm), c is the speed of light, and $\Delta n = n_{\text{ZnSe}} - n_{\text{air}}$. The refractive index of ZnSe varies from 2.4339 to 2.4201 from 3.8 to 7.4 μm . The ZnSe wedges are 2 cm in height, 6 cm in length and have a 1.2° wedge. Data can be acquired either by step scanning, which implies there is an input equilibration time for each time point, or by fast scanning the wedges at constant velocity. The velocity is determined by:

$$V = \frac{\Delta t \times f}{R \times N_s} \quad (2.22)$$

where Δt is the input time step, R is the resolution (time/length), f is the repetition rate of the laser (1/time), and N_s is the number of shots to average for each time

point. The total time for a scan is then the total distance (determined from the total time window and resolution) divided by the velocity.

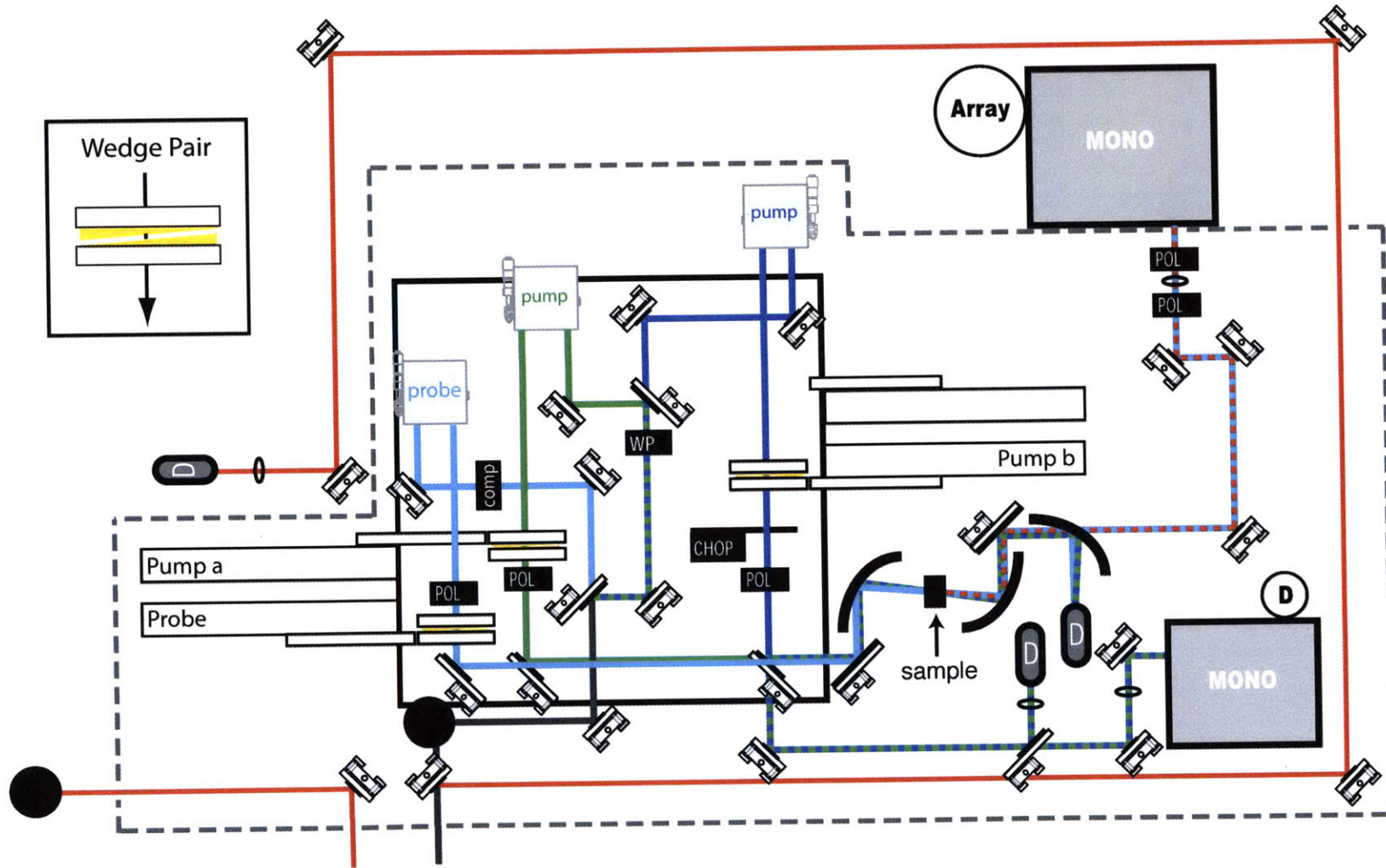


Figure 2-7: Interferometer.

2.3.2 Pulse Diagnostics

As mentioned in the previous section, the design of the beamsplitter set-up allows for pulse diagnostics to be performed relatively easily. The red line in Figure 2-7 traces the path the infrared and HeNe travel for HeNe overlap. After sending the beam into the interferometer we want to ensure the beams are tightly focused and overlapped at the sample position. We check the overlap and beam diameter with a pinhole at the sample position by focusing the beams into a room temperature MCT with a second parabolic after the sample (see Figure 2-8). In this configuration we also acquire autocorrelations either by second harmonic generation with a AgGaS₂ crystal or by collecting scatter through a small aperture pinhole [134]. The later is preferred since the interferometric measurement is not sensitive to the polarization of the pulses. Also, assuming the stages are calibrated, the array can be calibrated simply by removing the second parabolic to allow the scatter to enter the array. The replica of the pump pair created off the back side of the recombining beamsplitter is directed into the single channel monochromator. A pulse spectrum can be acquired simply by blocking one of the two pump beams and stepping the monochromator in frequency.

In the pump-probe geometry, the replica of the pump pair can be used to perform diagnostics simultaneously with data collection (in real time). We calibrate the stage scanned to create τ_1 by directing the replica of the pulse pair through a monochromator set to a frequency near the peak of the spectrum. An example of the stage calibration trace collected during data collection is shown in Figure 2-8. We assume the frequency the monochromator is correct in order to correct the τ_1 -axis by Fourier transform of the time trace. Finally, a portion of the pump pair replica can be directed into a room temperature MCT detector to collect the real-time field autocorrelation. An example time trace is shown in Figure 2-8. With real time acquisition of the zero timing between the two pump beams, collecting third order measurements in the pump-probe geometry is, in principle, free of any pulse timing ambiguity during τ_1 and τ_3 .

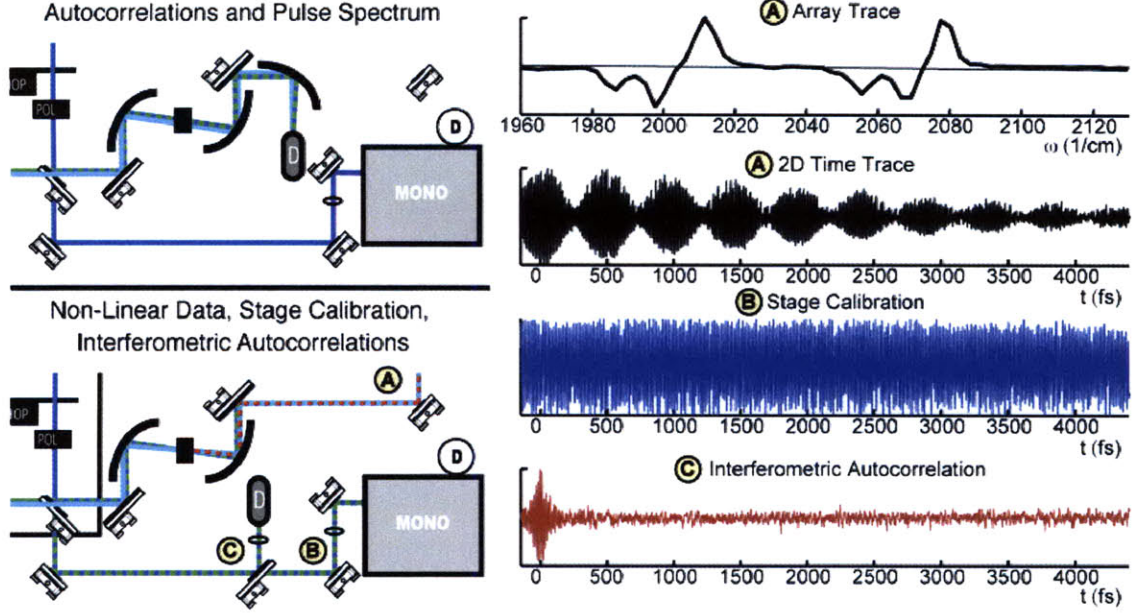


Figure 2-8: Beam layout for collecting pulse characteristics and non-linear data.

2.3.3 Pump-Probe Contribution from the Pump Beams

In the pump-probe geometry, with the signal dispersed, the total signal can be written as [135]:

$$S(\omega_3, \tau_1, \tau_2) \propto | E_3(\omega_3) + i\omega_3[P^{(1)}(\omega_3) + P^{(3)}(\omega_3, \tau_2, \tau_1) + P_{ppa}^{(3)}(\omega_3, \tau_2, \tau_1) + P_{ppb}^{(3)}(\omega_3, \tau_2, \tau_1)] |^2 \quad (2.23)$$

In this equation, E_3 is the probe field, $P^{(1)}$ is the free induction decay from the third pulse, $P^{(3)}$ is the desired third order response that requires the interaction of all three pulses, and $P_{ppa/b}^{(3)}$ are the PP signals between each pump beam and the probe. The a/b subscripts denote the pump beams a and b marked in Figure 2-7. In the current set-up pump beam b is chopped. In Figure 2-9 we show the order of the pulses impinging on the sample with and without the chopper closed when pump b is the stationary beam and pump a is scanned. The total signal with the chopper open

is:

$$S^\circ(\omega_3, \tau_1, \tau_2) \propto | E_3(\omega_3) + i\omega_3[P^{(1)}(\omega_3) + P^{(3)}(\omega_3, \tau_2, \tau_1) + P_{ppa}^{(3)}(\omega_3, \tau_2, \tau_1) + P_{ppb}^{(3)}(\omega_3, \tau_2)] |^2 \quad (2.24)$$

and with the chopper closed it is:

$$S^\bullet(\omega_3, \tau_1, \tau_2) \propto | E_3(\omega_3) + i\omega_3[P^{(1)}(\omega_3) + P_{ppa}^{(3)}(\omega_3, \tau_2, \tau_1)] |^2 . \quad (2.25)$$

If we make the safe assumption that $|E_3| \gg |P|$ we find:

$$S^\circ - S^\bullet \approx i\omega_3 E_3(\omega_3)[P^{(3)}(\omega_3, \tau_1, \tau_2) + P_{ppb}^{(3)}(\omega_3, \tau_2)] \quad (2.26)$$

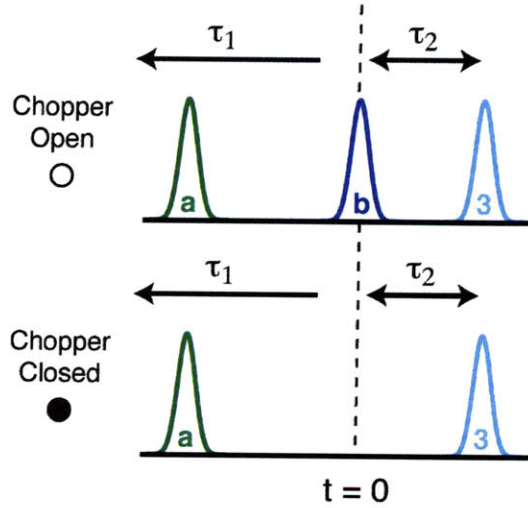


Figure 2-9: Pulse ordering with the chopper open and closed.

In Figure 2-10 we compare scanning the unchopped pump beam (stage a) and the chopped pump beam (stage b) at three wavelengths with the sample HOD in H₂O at $\tau_2=120$ fs. The PP between pump pulse b and the probe is constant with τ_1 when pump pulse a is scanned. The PP signal corresponds to a PP acquired at the waiting time: $P_{ppb}(\omega_3, \tau_2=120$ fs). However, if pump pulse b is scanned the pump-probe signal depends on τ_1 : $P_{ppa}(\omega_3, \tau_2=120$ fs + τ_1). Therefore, if only one pump pulse is chopped,

it is better to scan the non-chopped beam since the PP appears as a constant off-set and will be removed by Fourier transform to create the excitation, or ω_1 , dimension. The frequency slice in Figure 2-10a/c corresponds to a bleach/stimulated emission in the PP signal that is positive/negative at early time and decays with increased waiting time. The frequency slice in Figure 2-10d has very low PP signal and shows complicated behavior when pump b is scanned. Finally, in Figure 2-10b we compare the difference between the red and cyan trace in Figure 2-10a when stage calibration has (blue) and has not (green) been performed for each of the stages. Although both stages are off only by 1 fs over 200 fs (in the opposite manner, so 2 fs total) this can still be quite important for interferometric measurements.

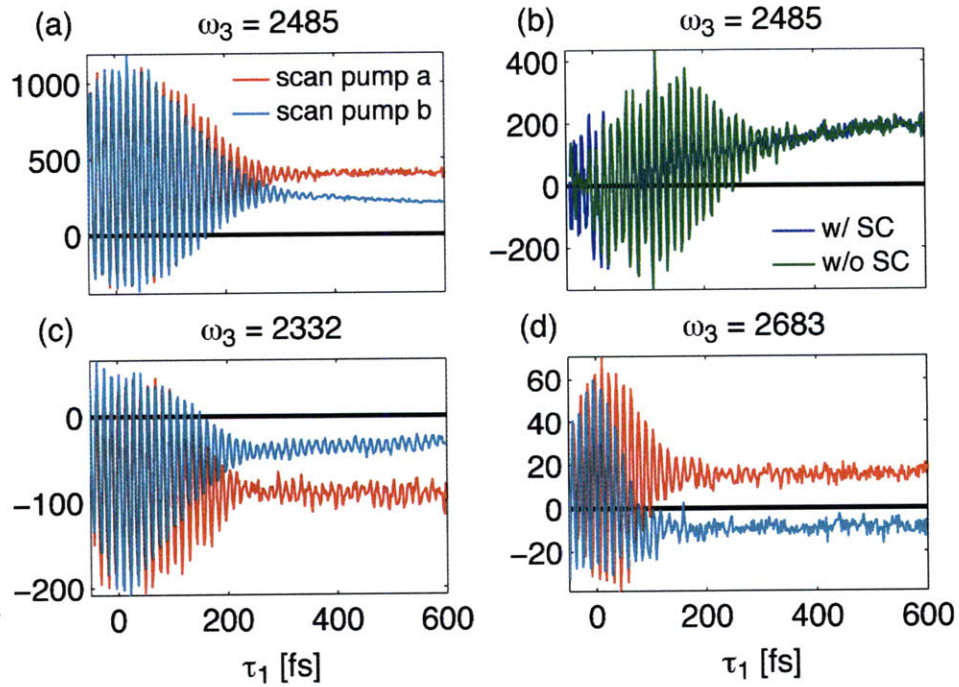


Figure 2-10: (a,c,d) Comparison of scanning the chopped (pump b) vs. non-chopped (pump a) beam. (b) Difference between the traces obtained by scanning each of the pumps with stage calibration (blue) and without stage calibration (green).

2.3.4 Second-Order Dispersion, or GVD

In H₂O, the broad libration, or hindered rotation, band is peaked at 680 cm⁻¹, which corresponds to a period of 50 fs. To follow the dynamics, we desire a probe that is sensitive to structure with a "shutter speed" faster than the fastest intermolecular motions. Ideally we will generate transform limited pulses, or, pulses without second (or higher order) dispersion. The spectral phase of the electric field can be expanded in a Taylor expansion about a center frequency [136]:

$$\phi(\omega) = \phi(\omega_o) + \phi'(\omega_o)(\omega - \omega_o) + \frac{1}{2}\phi''(\omega_o)(\omega - \omega_o)^2 + \frac{1}{6}\phi'''(\omega_o)(\omega - \omega_o)^3 + \dots \quad (2.27)$$

where ϕ' , ϕ'' , ϕ''' are derivatives of the phase with respect to the frequency and are known as the group delay, second-order dispersion (or group velocity dispersion (GVD)), and third-order dispersion (TOD), respectively. The group delay is defined as $T(\omega) = \partial\phi(\omega)/\partial\omega$, and the Taylor expansion gives:

$$T(\omega) = \phi'(\omega_o) + \phi''(\omega_o)(\omega - \omega_o) + \frac{1}{2}\phi'''(\omega_o)(\omega - \omega_o)^2 + \dots \quad (2.28)$$

Therefore when the GVD is non-zero the pulse will have a linear frequency chirp. Normal, or positive, dispersion occurs when higher frequency components travel slower than lower frequency components. The pulse is then positively chirped since frequency will increase with time. Anomalous, or negative dispersion, is the opposite situation. Demirdöven and coworkers demonstrated that the use of optical materials with GVD of opposite signs can successfully compress mid-IR pulses to 75 fs at 5 μm with 6 μJ of energy and that the approach can be used throughout the mid-infrared until third-order dispersion becomes important [130].

In Figure 2-11 we show the GVD per millimeter of material from 3.5 to 7 μm for the materials in the current interferometer. The GVD is calculated with the material dispersion equation [136] and Sellmeier equations [137]. In Table 2-3 we list the thickness of the materials and the GVD at 4 and 6 μm . Since the dispersion of all materials generally increases with decreasing wavelength, we replaced the 3 mm

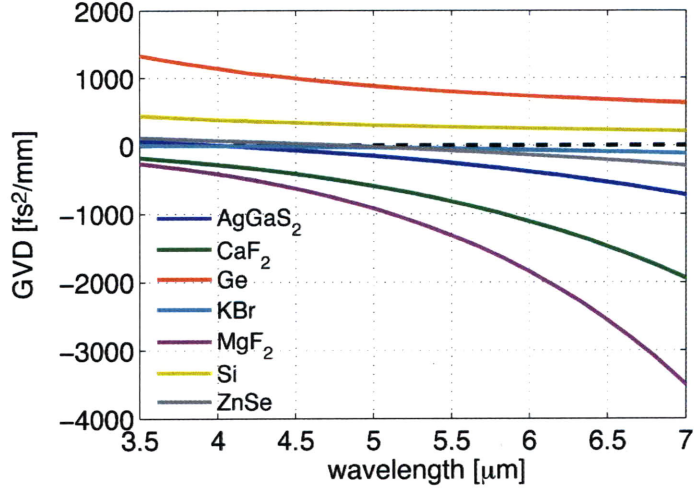


Figure 2-11: GVD of the materials in the interferometer.

	Material	T (mm)	4 μm	6 μm
DFG	AgGaS ₂	0.5	2	-19
HeNe	Ge	1 (4), 3 (6)	1140	2181
lens	KBr	2	-6	-136
bandpass	Si	1	378	
beamsplitter	KBr	3	-10	-203
wedges	ZnSe	4 to 6.4	300 to 479	-544 to -870
waveplate	MgF ₂	2.5	-1038	
polarizer	ZnSe	1	75	-136
window	CaF ₂	1	-280	-1110
Total			561 to 740	33 to -293

Table 2.3: Second order dispersion at 4 and 6 μm (in fs^2).

piece of Ge used for HeNe overlap with a 1 mm piece upon tuning from 6 μm to 4 μm . The 1 mm piece of anti-reflection coated Si (spectrum shown on the right in Figure 2-6) is used at 4 μm to absorb signal and idler in addition to the Ge. Each of the three beams are transmitted only once through a KBr beamsplitter (3 mm thick). The thickness of a single wedge varies from 2 to 3.2 mm. Therefore, the total thickness of the wedge pair can range from 4 to 6.4 mm. At 6 μm we did not use waveplates. Rather, we rotated the polarization of the probe between parallel and perpendicular relative to the pump with a turning periscope. Finally, the 1 mm CaF₂

window refers to the front window of the sample cell. At 4 μm the total dispersion at the sample from all the material in the interferometer ranges from 561 to 740 fs^2 . We found adding a 3 mm piece of CaF_2 decreased the chirp (3 mm = -840 fs^2). At 6 μm the dispersion at the sample ranges from 33 to -293 fs^2 and we found additional material was not necessary.

2.4 Data processing

The nonlinear experiments described in this thesis evaluate the interaction of matter with three infrared pulses. The third-order polarization, $\mathbf{P}^{(3)}$, is expressed as a triple convolution of the response function \mathbf{R} with the incident fields, \mathbf{E} :

$$\mathbf{P}^{(3)}(\mathbf{t}) = \int_0^\infty d\mathbf{t}_3 \int_0^\infty d\mathbf{t}_2 \int_0^\infty d\mathbf{t}_1 \mathbf{R}(\mathbf{t}_3, \mathbf{t}_2, \mathbf{t}_1) \mathbf{E}(\mathbf{t} - \mathbf{t}_3) \times \mathbf{E}(\mathbf{t} - \mathbf{t}_3 - \mathbf{t}_2) \mathbf{E}(\mathbf{t} - \mathbf{t}_3 - \mathbf{t}_2 - \mathbf{t}_1). \quad (2.29)$$

In this equation t_1 and t_2 are the time periods between the field-matter interactions and t_3 is the time between the last interaction and the detection at time t . The incident fields have a defined envelope, polarization, wave vector, frequency, and phase. The frequency is near resonant with both the $\nu=1\leftarrow 0$ peak and anharmonically shifted $\nu=2\leftarrow 1$ peak of interest. The tensorial response function is a thrice-nested commutator of the transition dipole operator, μ , evaluated at each field-matter interaction:

$$\mathbf{R}(\mathbf{t}_3, \mathbf{t}_2, \mathbf{t}_1) = (\mathbf{i}/\hbar)^3 \langle [[[\mu(\mathbf{t}_3 + \mathbf{t}_2 + \mathbf{t}_1), \mu(\mathbf{t}_2 + \mathbf{t}_1)], \mu(\mathbf{t}_1)], \mu(\mathbf{0})] \rangle. \quad (2.30)$$

The response function evolves under the material Hamiltonian and therefore it inherently contains microscopic information on the system of interest. Expanding the commutator results in eight separate terms, but only four are unique since the other four are complex conjugates. Until this point no simplifying assumptions have been applied.

The ensuing assumptions have previously proved useful in modeling third order spectroscopy. The response function is simplified by assuming the vibrational and

rotational degrees of freedom are separable and is then written as a product of the two contributions. The vibrational response function includes terms dependent on the transition dipole, eigenstate energy, and evolution under the Hamiltonian. To describe the evolution under the Hamiltonian, Sung and Silbey derived expressions for the nonlinear dephasing functions in terms of two-point energy gap correlation functions between the system eigenstates, which assumes the second cumulant approximation [138]. The cumulant approximation is exact if frequency fluctuations are Gaussian. The authors derived the theory for four wave mixing experiments of a multilevel system coupled to a harmonic bath. The energy gap correlation functions reflect the change in the system energy upon coupling to a bath mode. The orientational response function projects the polarization of the incident electric field onto the distribution of molecular coordinates and includes transition dipole unit vector and Legendre polynomials derived for a spherical rotor.

Double-sided Feynman diagrams pictorially relay the possible contributions to the signal. The pathways are termed Liouville pathways as the Liouville-von Neuman equation describes how the density matrix evolves in time under the quantum mechanical Hamiltonian. The initial pathways, which involve permutations of three time periods on the original eight Feynman diagrams, can be decreased by invoking physical arguments including, but not limited to, the rotating wave approximation and consideration of the phase matching direction. In nonlinear electronic spectroscopy four diagrams represent the possible contributions for the two level system. In nonlinear vibrational spectroscopy the multilevel structure must be taken into account. For water, a three level system, eight Feynman diagrams remain outside the regime of overlapping pulses. Four are rephasing, (S_-), in that the oscillation frequencies in the third time period are conjugate, or nearly conjugate, to those in the first time period. The ability to rephase relies on frequency correlation between the first and third time periods, and frequencies evolve during the second time period. The non-rephasing (S_+) contributions involve frequencies that are the same, or nearly the same, in the first and third time periods. 2D IR measurements are commonly acquired in the box-car geometry. In this geometry the rephasing and non-rephasing signals, emitted

in the $\mathbf{k}_{\text{sig}} = -\mathbf{k}_1 + \mathbf{k}_2 + \mathbf{k}_3$ and $\mathbf{k}_{\text{sig}} = \mathbf{k}_1 - \mathbf{k}_2 + \mathbf{k}_3$ phasematched directions, respectively, are measured separately. After Fourier transform to the frequency domain, the spectra are summed to yield the purely absorptive line shape [139].

2.4.1 Extracting Complex Correlation, Rephasing and Non-Rephasing Spectra

In the pump-probe geometry \mathbf{k}_1 and \mathbf{k}_2 are indistinguishable and, therefore, the real part of the 2D IR rephasing (S_-) and non-rephasing (S_+) pathways are collected [140]. However, utilizing the Kramers-Kronig assumption we can extract the complex correlation, rephasing and non-rephasing 2D information. The data is collected as a function of τ_1 and ω_3 , since a grating performs the Fourier transform when dispersing the signal onto a multi-channel array. The signal can be written as:

$$S = [S_-(\tau_1, \omega_3, \phi_1 = 0, \phi_3 = 0) + S_+(\tau_1, \omega_3, \phi_1 = 0, \phi_3 = 0)]. \quad (2.31)$$

where S_- and S_+ represent the rephasing and non-rephasing contributions to the nonlinear signal, respectively. A single sided, one-dimensional Fourier transform is performed in τ_1 to create the ω_1 axis and produce the 2D IR spectrum. The real (S') and imaginary (S'') components of this spectrum can be written as:

$$S' = [S_-(\omega_1, \omega_3, \phi_1 = 0, \phi_3 = 0) + S_+(\omega_1, \omega_3, \phi_1 = 0, \phi_3 = 0)] \quad (2.32)$$

$$S'' = [S_-(\omega_1, \omega_3, \phi_1 = 90, \phi_3 = 0) + S_+(\omega_1, \omega_3, \phi_1 = 90, \phi_3 = 0)]. \quad (2.33)$$

(1) S' and S'' are inverse Fourier transformed in the ω_3 dimension, (2) causality is applied by setting the time-domain signal for $\tau_3 < 0$ to zero, (3) and the signal is

Fourier transformed with respect to τ_3 to obtain complex 2D spectra:

$$\text{Re}(S') = [S_-(\omega_1, \omega_3, \phi_1 = 0, \phi_3 = 0) + S_+(\omega_1, \omega_3, \phi_1 = 0, \phi_3 = 0)] \quad (2.34)$$

$$\text{Im}(S') = [S_-(\omega_1, \omega_3, \phi_1 = 0, \phi_3 = 90) + S_+(\omega_1, \omega_3, \phi_1 = 0, \phi_3 = 90)] \quad (2.35)$$

$$\text{Re}(S'') = [S_-(\omega_1, \omega_3, \phi_1 = 90, \phi_3 = 0) + S_+(\omega_1, \omega_3, \phi_1 = 90, \phi_3 = 0)] \quad (2.36)$$

$$\text{Im}(S'') = [S_-(\omega_1, \omega_3, \phi_1 = 90, \phi_3 = 90) + S_+(\omega_1, \omega_3, \phi_1 = 90, \phi_3 = 90)] \quad (2.37)$$

$\text{Re}(S')$ and $\text{Im}(S')$ are shown in Figure 2-12a and 2-12b, respectively, for a 2D surface of the OD stretch of HOD in H_2O at $\tau_2 = 600$ fs at 286 K. At this point the complex correlation surface can be constructed from $\text{Re}(S')$ and $\text{Im}(S')$ [135]. The absolute value, $S_{Abs} = |\text{Re}(S') + i\text{Im}(S')|$, and phase representation, $S_\phi = \arctan(\text{Im}(S')/\text{Re}(S'))$, are shown in Figure 2-12c and 2-12d, respectively.

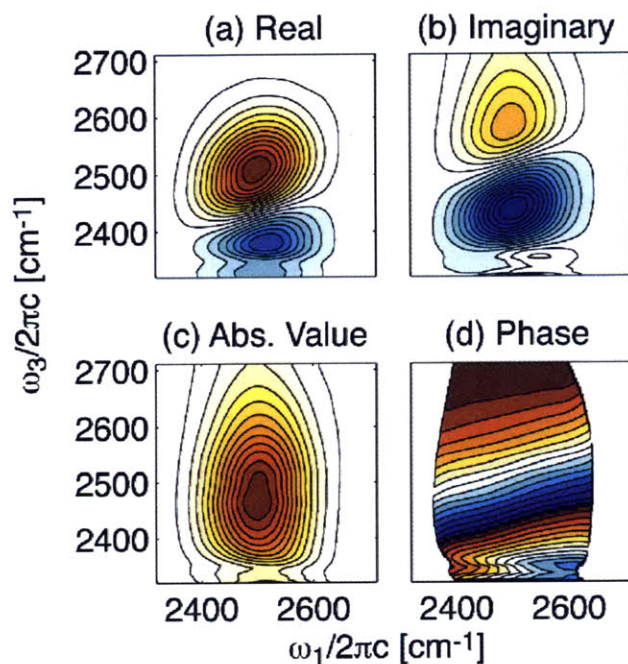


Figure 2-12: (a) Real, (b) Imaginary, (c) Absolute Value, and (d) Phase representations of a 2D surface of HOD in H_2O at 286 K and $\tau_2 = 600$ fs.

In order to separate the rephasing and non-rephasing pathways we will rewrite

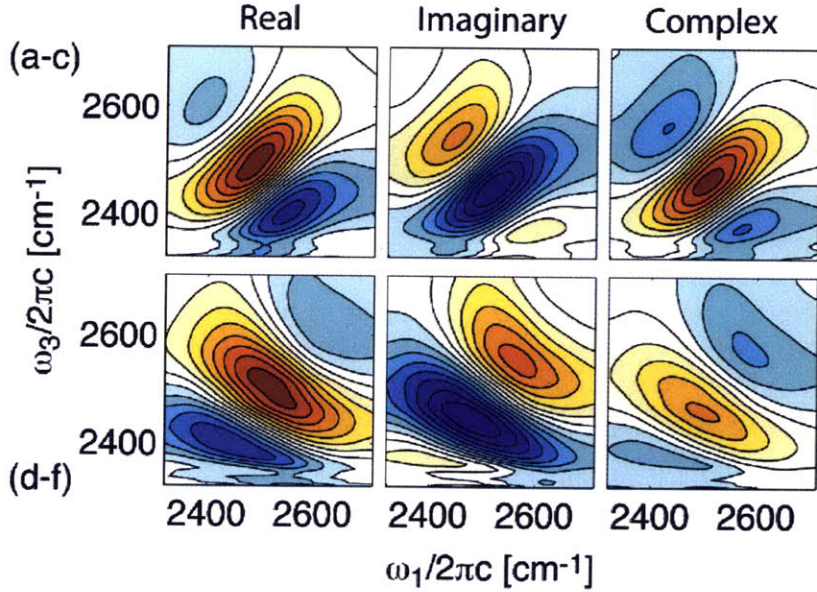


Figure 2-13: (a) $\text{Re}(S_-)$, (b) $\text{Im}(S_-)$, (c) S_- , (d) $\text{Re}(S_+)$, (e) $\text{Im}(S_+)$, and (f) S_+ representations of a 2D surface of HOD in H_2O at 286 K and $\tau_2 = 600$ fs.

the terms in the above equations as:

$$\text{Re}(S') = [S_-(\omega_1, \omega_3, \phi_1 = 0, \phi_3 = 0) + S_+(\omega_1, \omega_3, \phi_1 = 0, \phi_3 = 0)] \quad (2.38)$$

$$\text{Im}(S') = [S_-(\omega_1, \omega_3, \phi_1 = 90, \phi_3 = 0) - S_+(\omega_1, \omega_3, \phi_1 = 90, \phi_3 = 0)] \quad (2.39)$$

$$\text{Re}(S'') = [S_-(\omega_1, \omega_3, \phi_1 = 90, \phi_3 = 0) + S_+(\omega_1, \omega_3, \phi_1 = 90, \phi_3 = 0)] \quad (2.40)$$

$$\text{Im}(S'') = [-S_-(\omega_1, \omega_3, \phi_1 = 0, \phi_3 = 0) + S_+(\omega_1, \omega_3, \phi_1 = 0, \phi_3 = 0)] \quad (2.41)$$

given the following relationships:

$$S_-(\omega_1, \omega_3, \phi_1 = 0, \phi_3 = 0) = -S_-(\omega_1, \omega_3, \phi_1 = 90, \phi_3 = 90) \quad (2.42)$$

$$S_-(\omega_1, \omega_3, \phi_1 = 90, \phi_3 = 0) = S_-(\omega_1, \omega_3, \phi_1 = 0, \phi_3 = 90) \quad (2.43)$$

$$S_+(\omega_1, \omega_3, \phi_1 = 0, \phi_3 = 0) = S_+(\omega_1, \omega_3, \phi_1 = 90, \phi_3 = 90) \quad (2.44)$$

$$S_+(\omega_1, \omega_3, \phi_1 = 90, \phi_3 = 0) = -S_+(\omega_1, \omega_3, \phi_1 = 0, \phi_3 = 90) \quad (2.45)$$

Now we can separate the rephasing (S_-) and non-rephasing (S_+) pathways, for instance, by subtracting $\text{Im}(S'')$ from $\text{Re}(S')$ to obtain the real part of the rephasing

pathway. Explicitly we have:

$$\text{Re}(S') - \text{Im}(S'') = S_-(\omega_1, \omega_3, \phi_1 = 0, \phi_3 = 0) = \text{Re}(S_-) \quad (2.46)$$

$$\text{Re}(S'') + \text{Im}(S') = S_-(\omega_1, \omega_3, \phi_1 = 90, \phi_3 = 0) = \text{Im}(S_-) \quad (2.47)$$

$$\text{Re}(S') + \text{Im}(S'') = S_+(\omega_1, \omega_3, \phi_1 = 0, \phi_3 = 0) = \text{Re}(S_+) \quad (2.48)$$

$$\text{Re}(S'') - \text{Im}(S') = S_+(\omega_1, \omega_3, \phi_1 = 90, \phi_3 = 0) = \text{Im}(S_+) \quad (2.49)$$

These terms are shown in Figure 2-13a, 2-13b, 2-13d, and 2-13e, respectively. Finally in Figure 2-13c and 2-13f we show the complex rephasing and non-rephasing surfaces. We normalize both surfaces by the maximum of the rephasing surface to show that the rephasing pathway still dominates at this waiting time and temperature indicating spectral diffusion is not yet complete [141, 72].

2.4.2 Cross Phase Modulation

In pump-probe spectroscopy, an intense pump pulse can modulate the refractive index of the solvent or sample window causing a time-dependent phase modulation of the probe. This is referred to as cross phase modulation (xpm) and, since the total energy of the probe remains constant, it can only be observed if the probe is spectrally dispersed after the sample. Kovalenko et al. experimentally and theoretically explored non-resonant contributions to femtosecond visible pump-supercontinuum-probe (PSCP) spectroscopy [142]. In their treatment, they define the pump pulse as a nonchirped Gaussian

$$E_1(t) = a_1 \exp[-t^2/2\tau_1^2 + i\Omega_1 t] \quad (2.50)$$

where a_1 is the amplitude, Ω_1 is the central frequency, and τ_1 is the pulse duration. They consider a probe pulse with a linear chirp, written as:

$$E_2(t) = \exp(-t^2/2\tau_2^2 + i(\Omega_2 t + \beta t^2)), \quad (2.51)$$

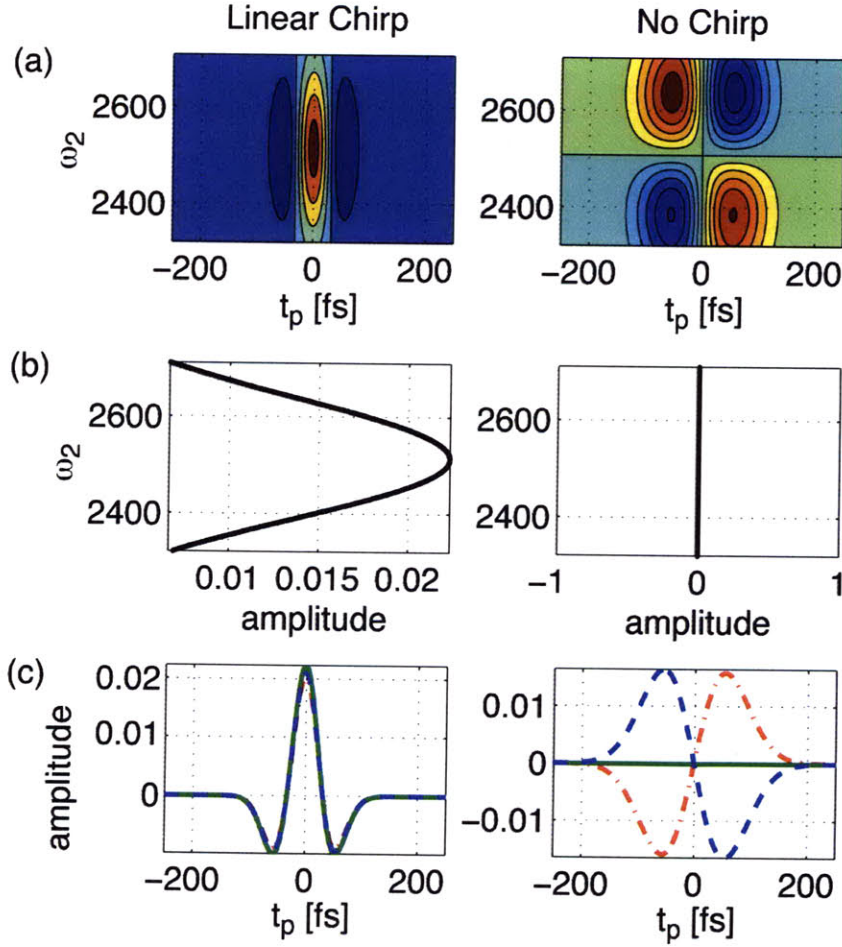


Figure 2-14: (a) Dispersed pump-probe for a pump-linearly chirped probe (left) and pump-no chirp probe (right). (b) The amplitude of the xpm at $t_p = 0$ fs. (c) Slices of the xpm in frequency at $\Omega_2 - 50 \text{ cm}^{-1}$ (red), Ω_2 (green), and $\Omega_2 + 50 \text{ cm}^{-1}$ (blue).

where β is the chirp rate. They find the differential instantaneous electronic signal can be written as:

$$\begin{aligned} \Delta D_e(\omega_2, \tau_d) = & -\frac{12\omega_2 |a_1|^2 \sigma_e}{\sqrt{|\eta|}} \text{Im}\left\{ \exp\left[-\frac{[t_d + t_o(\omega_2)]^2}{\eta\tau_1^2}\right] \right. \\ & \left. + i\frac{t_o(\omega_2)}{\beta\tau_2^2} \frac{t_d + t_o(\omega_2)}{\eta\tau_1^2} + \left(\frac{t_o(\omega_2)}{2\beta\tau_2^2}\right)^2 \frac{1}{\tau_1^2\eta} - i\phi/2 \right\} \end{aligned} \quad (2.52)$$

where σ_e is the amplitude, t_d is the delay between the pump and the probe pulse, $\eta = (1 + 2\xi^2/\alpha)$, $\alpha = 1 - i2\beta\tau_2^2$, $\xi = \tau_2/\tau_1$, $\phi = \arctan(\text{Im } \eta / \text{Re } \eta)$, and $t_o(\omega_2) \approx (\omega_2 - \Omega_2)/2\beta$.

When $2\beta\tau_2^2 \gg 1$, one has $|\eta| \approx 1$, $\phi \approx 1/\beta\tau_1^2$, and the signal becomes

$$\begin{aligned} \Delta D_e(\omega_2, \tau_d) \approx & -\frac{12\omega_2 |a_1|^2 \sigma_e}{\sqrt{|\eta|}} \exp\left[-\frac{[t_d + t_o(\omega_2)]^2}{\tau_1^2}\right] \\ & \times \sin\left[\frac{1}{2\beta\tau_1^2} - \frac{[t_d + t_o(\omega_2)]^2}{\beta\tau_1^4} - \frac{t_o(\omega_2)[t_d + t_o(\omega_2)]}{\beta\tau_2^2\tau_1^2}\right]. \end{aligned} \quad (2.53)$$

The authors did not consider the case when both the pump and probe have chirp, which, if the probe pulse has chirp, would be the case in our experiments. For a non-chirped probe pulse, $\beta = 0$, and the expression for the differential instantaneous electronic signal is:

$$\begin{aligned} \Delta D_e(\omega_2, \tau_d) = & -\frac{12\omega_2 |a_1|^2 \sigma_e}{\sqrt{|\eta|}} \exp\left[\frac{\xi^4\tau_1^2(\omega_2 - \Omega_2)}{1 + 2\xi^2} - \frac{t_d^2}{\tau_1^2(1 + 2\xi^2)}\right] \\ & \times \sin\left[\frac{2\xi^2}{1 + 2\xi^2} t_d(\omega_2 - \Omega_2)\right] \end{aligned} \quad (2.54)$$

In Figure 2-14 we show an example of cross phase modulation when the probe pulse is either linearly chirped (equation 2.53) or is not chirped (equation 2.54). In both cases $\tau_1 = \tau_2 = 45$ fs and $\Omega_2 = 2508$ cm⁻¹. When the probe pulse is not chirped the xpm is sinusoidal about $t_p = 0$ fs. Therefore the amplitude is zero at $t_p=0$ for all probe frequencies (Figure 2-14b). At the peak of the probe pulse the xpm is zero (Figure 2-14c) and flips sign on either side of Ω_2 . When the probe pulse is linearly chirped ($\beta = 1 \times 10^{-2}$ fs⁻² in this example) the xpm is not zero at Ω_2 . Rather there is positive amplitude peaked at $t_p = 0$ fs and symmetric negative side lobes. As ω_2 is tuned away from Ω_2 the side lobes become asymmetric (Figure 2-14c) and the maximum shifts from $t_p = 0$ fs (Figure 2-14b).

In Figure 2-15 we compare experimentally measured cross phase modulation with the model calculations. The experimental xpm is taken with H₂O at the sample position between two 1 mm thick CaF₂ windows with a 6 μ m spacer. Modeling the experimental data with equation 2.54 and the same input values as Figure 2-14, largely reproduces the observed xpm, although the asymmetry about t_p is not reproduced. When $\omega_2 \approx \Omega_2$ and the xpm arising from an unchirped probe pulse is ~ 0 ,

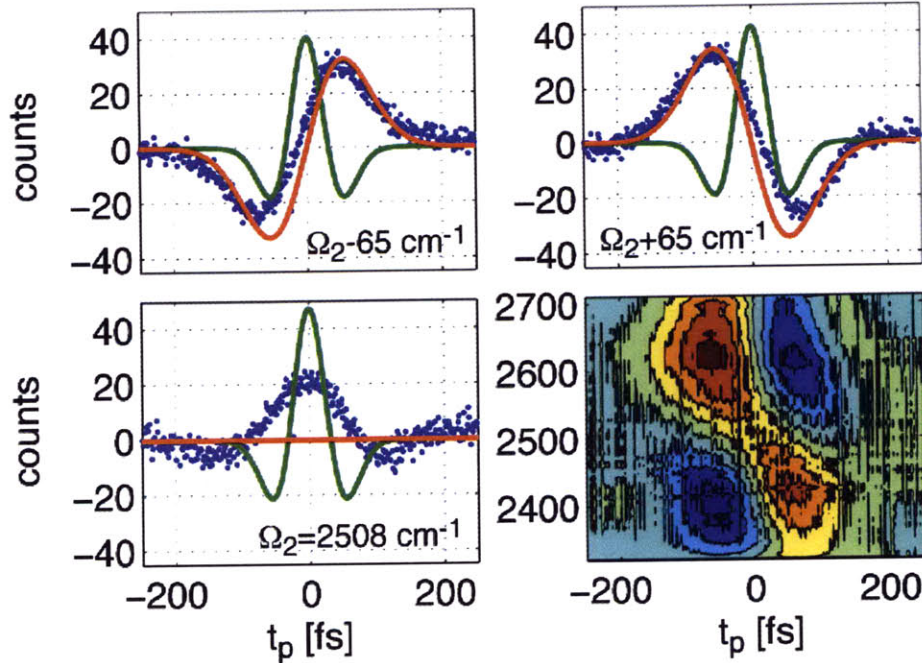


Figure 2-15: Experimental xpm (blue) compared to model calculations with linearly chirped probe (green) and unchirped probe (red).

the experimental trace resembles model xpm with a linearly chirped pulse. However, the width is not properly reproduced. τ_1 , τ_2 , and Ω_2 are set by fitting the experimental xpm with equation 2.54 and not adjusted when applying equation 2.53. Also, adjusting β only affected the number of oscillations, not the width of the envelope. The above equations assume the sample is an infinitely thin, therefore propagation effects are neglected. Ekvall et al. [143] theoretically and experimentally studied the cross phase modulation in a piece of fused silica in visible pump-supercontinuum-probe spectroscopy. They considered propagation effects by including group velocity mismatch between the pump and probe and first and second order dispersion of the white light continuum probe and numerically solved the coupled wave propagation equations. The model calculations reproduce the asymmetry about t_p we observe experimentally (Figure 4 in ref. [143]), which they attribute to propagation effects.

As far as we are aware, the effect of cross phase modulation in 2D IR measurements has not been addressed experimentally or theoretically. To get an idea of how the xpm will appear in 2D measurements we multiplied the spectra in Figure 2-14a and 2-14b

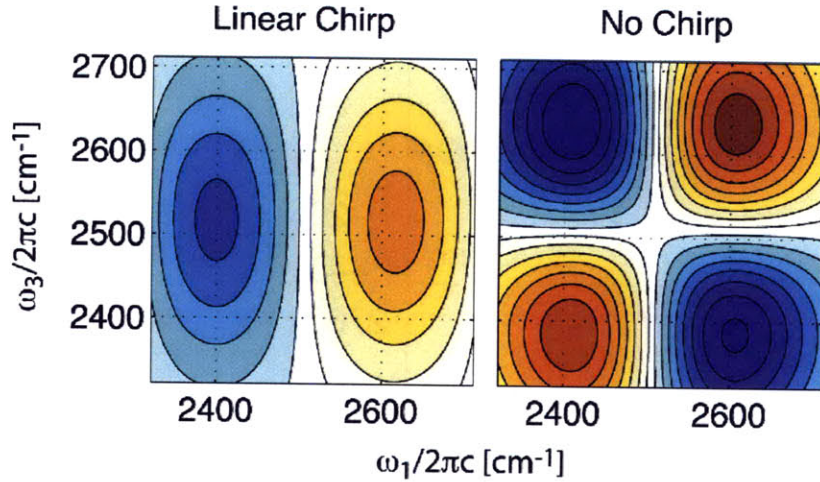


Figure 2-16: 2D spectra of XPM.

by a sine function oscillating at Ω_2 in τ_1 then Fourier transformed. The resulting 2D spectra are shown in Figure 2-16. If there is linear chirp the 2D surface shows a doublet that is negative on the red side of Ω_2 and positive on the blue side. If there is no chirp the 2D surface shows a clover shape with a node at $\omega_1 = \omega_3 = \Omega_2$. Cross-phase modulation will only be important when the pulses are overlapping.

2.5 Acknowledgments

We would like to thank Lauren DeFlores, Kevin Jones, and Matt DeCamp for their helpful insights and thoughtful discussions.

Chapter 3

Infrared Spectroscopy of Tritiated Water

3.1 Introduction

Studies of hydrogen bond dynamics of water with ultrafast non-linear infrared spectroscopy have commonly used isotopically dilute solutions such as HOD in D₂O [58, 62, 68, 67, 71] or HOD in H₂O [77, 120]. The anharmonic OH or OD stretching vibration is localized in these mixtures, and particularly sensitive to hydrogen bond configurations, as manifested by the fluctuating electric field experienced by the proton or deuteron [68, 46, 78]. However, with only one spectroscopically observable species, information on the environment is inferred indirectly. Using experiments on HOD in D₂O, we recently concluded that hydrogen bond switching involves a concerted motion of no less than three molecules: the hydrogen bond donor and the initial and final hydrogen bond acceptor molecules [73]. A more direct test of this process requires a spectroscopic probe of correlated motion between hydrogen-bonded molecules. This could potentially be observed using correlation spectroscopy between OD and OT stretches in H₂O, exploiting both the coupling between species and sensitivity of the vibrational frequency to hydrogen bond configuration. As a step in this direction, we report on the infrared absorption spectrum of ω_{OT} of HOT in H₂O. Later in the chapter we present a calculation to model what will be observed

in such an experiment. In the calculation, the diagonal frequency modulation from the intermolecular electric field and off-diagonal transition dipole coupling (TDC) are determined during an idealized, concerted hydrogen bond switch. Finally, intermolecular coupling between the OD and OT stretch is determined by performing *ab initio* frequency calculations on water isotopologue dimer combinations.

3.2 Linear Absorption of Tritiated Water

The high radioactivity of tritium has precluded previous liquid infrared studies, although a Raman spectrum of the OT stretch for 10V% T₂O in H₂O (~60 Ci) has been reported [144]. Line shape parameters for the absorption spectrum of ω_{OT} are reported, including the frequency at maximum absorbance (ω^*), integrated intensity (I), molar absorptivity (ϵ), and full width half maximum ($\Delta\omega$). Comparison of the linear infrared absorption spectra of the three isotopes, $\omega_{OT}:\omega_{OD}:\omega_{OH}$, provides information on the physical effects and interactions that influence the red-shift, broadening, and intensity gain of the OX stretch upon forming the hydrogen bond. Within the simplest harmonic approximations, the line shape parameters should remain constant for all isotopologes when scaled by reduced mass μ_R as $\omega^*\sqrt{\mu_R}$, $I\sqrt{\mu_R}$, $\epsilon\mu_R$, and $\Delta\omega\sqrt{\mu_R}$. These scaling relationships are investigated in an attempt to test the generality of electric field models for the hydride stretching line shape and predictions of the importance of mechanical and electrical anharmonicity to the line shape.

3.2.1 Experimental Methods

Dilute tritiated water, HOT in H₂O, was obtained from Sigma (W3260, CAS# 13670-17-2) and used without further purification. The extent of labeling is 5 ± 0.5 Ci g⁻¹ or 0.2 ± 0.02 M given the half-life 4500 ± 8 days for ³H [145]. FTIR spectra of tritiated water and reference deionized H₂O were obtained with a spectrometer (Mattson Infinity Gold) whose beam was routed externally to tightly focus its beam to the sample position using 10 cm parabolic mirrors. This was done to avoid contamination of the spectrometer and decrease the amount of tritiated water used. The sample

cell consisted of 120 μm thick, 9 mm ID adhesive spacers (Secure SealTM Imaging Spacers, Grace Biolabs) placed between 1 mm thick, 2" dia. CaF_2 windows. The spacer accommodated side-by-side sample and reference wells. Each well was filled by approximately 8 μL of sample (~ 40 mCi of ^3H) and translation stages provided reproducible movement between the reference and sample.

FTIR spectra of HOD in H_2O and D_2O (Cambridge Isotope Laboratories, CAS# 7789-20-0) were collected with the same spectrometer. The sample cell consisted of 3 mm thick CaF_2 windows (Pike Technologies, Inc.) and a 50 μm teflon spacer. For both ω_{OH} and ω_{OD} a dilution series of solutions were measured to separate absorption contributions from the three species present (HOD, H_2O and D_2O). The solutions were kept dilute to avoid intermolecular interactions. Spectra were obtained by iteratively solving

$$A = d(\varepsilon_{HOD}C_{HOD} + \varepsilon_{H_2O}C_{H_2O} + \varepsilon_{D_2O}C_{D_2O}), \quad (3.1)$$

using the equilibrium constant 3.82 for the reaction $\text{H}_2\text{O} + \text{D}_2\text{O} \rightleftharpoons 2\text{HOD}$ [146].

3.2.2 Results

Figure 3-1 shows the infrared absorption spectrum of the OT stretch in terms of the molar absorptivity, $\varepsilon(\omega)$ [$10^3 \text{ cm}^2 \text{ mol}^{-1}$]. The absorption line shape has a peak at $\omega^* = 2121 \text{ cm}^{-1}$, and line width of $\Delta\omega = 127 \text{ cm}^{-1}$ (FWHM), and a qualitatively similar shape to the other HOX isotopologues.

Comparison of the line shape parameters of ω_{OT} , ω_{OD} , and ω_{OH} is made in Figure 3-2 and Table 3-1. The scaling dependence of the absorption coefficient with isotopic substitution is predicted from the expression that relates it to the Fourier transform of the dipole-dipole correlation function [147]

$$\varepsilon(\omega) = \frac{2\pi}{3n\hbar c} \omega(1 - e^{-\beta\hbar\omega}) \int_{-\infty}^{\infty} dt e^{i\omega t} \langle \vec{\mu}(t) \cdot \vec{\mu}(0) \rangle. \quad (3.2)$$

As a point of reference, for a harmonic oscillator, the transition frequency ($\omega =$

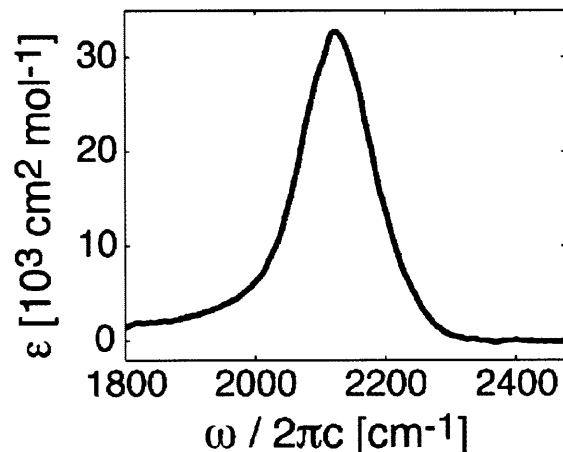


Figure 3-1: The molar absorptivity of the OT stretch of 0.3% H₂O

$\sqrt{k/\mu_R}$) and square of the transition dipole are inversely proportional to the square root of the reduced mass. Given that the transition dipole operator is linear in the system coordinate, Q , the mass weighting of the matrix element arises from $Q = \hat{x}(\hbar^2/\mu_R k)^{1/4}$. Figure 3-2a shows the molar extinction coefficient for each mode using a reduced frequency axis $\omega\sqrt{\mu_R}$ in which the reduced mass for the OX stretch is estimated from $\mu_R = m_X m_O / (m_X + m_O)$. To within 1%, this form gives the same results as modified diatomic approximations [148, 54]. The reduced mass scaling does not lead to coincident peak maxima. To account for anharmonicity of the OX stretch present before hydrogen bonding, we compare the scaling to the case where the frequency is normalized relative to the gas phase OX frequencies, ω_g . In this case (Figure 3-2b), the normalized bands align much better and showing only slight deviations in peak maxima (OH:OD:OT = 0.9184:0.9210:0.9224).

Equation 3.2 can also be used to predict the line width scaling with reduced mass for interactions of a system with a harmonic bath. Using the Condon approximation and assuming Gaussian statistics, the dipole correlation function is often expressed in terms of the fluctuating energy gap arising from a system-bath interaction

$$\langle \vec{\mu}(t) \cdot \vec{\mu}(0) \rangle = |\mu_{10}|^2 e^{-i\omega_{10}t} \exp\left(-\frac{1}{\hbar^2} \int_0^t dt'' \int_0^{t''} dt' \langle H_{SB}(t'') H_{SB}(t') \rangle\right). \quad (3.3)$$

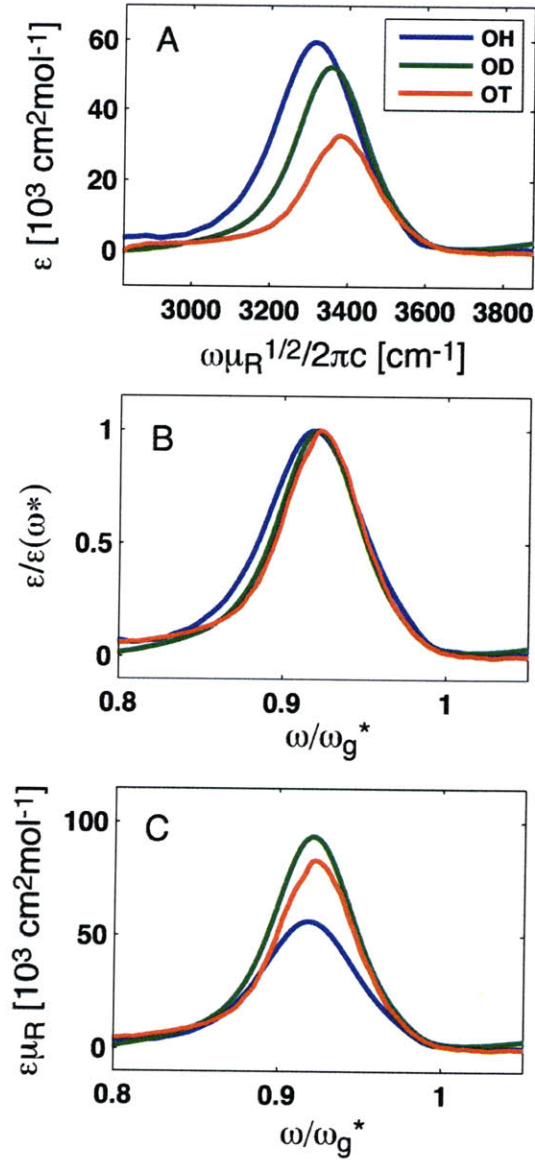


Figure 3-2: (A) The stretching band of each of the three isotopologues of water (ω_{OH} for HOD in D_2O , ω_{OD} for HOD in H_2O , and ω_{OT} for HOT in H_2O) with the frequency axis scaled by the square root of the reduced mass of each local mode. (B) The stretching band with the frequency axis scaled by the gas phase frequencies and intensities normalized to compare $\Delta\omega$. (C) Peak intensities scaled by the reduced mass of each isotope to compare ϵ .

where H_{SB} refers to the system-bath interaction Hamiltonian. The reduced mass scaling of the line width depends on the details of H_{SB} and the dynamics. In the static case, if H_{SB} is linear in the OX coordinate, an approximation that is valid for this system [46], the line width should scale inversely as $\sqrt{\mu_R}$ [69]. This observa-

tion predicts superimposed line shapes in Figure 3-2b. The correspondence is close; however, we find $\Delta\omega_{OH}$ is 17% larger than $\Delta\omega_{OD}$ on the scaled axis and 24% larger than $\Delta\omega_{OT}$. The preferential narrowing of the higher masses suggests that this may be a motional narrowing effect that results from the same spectral dynamics applied to different frequency distributions. The line shape of the OX stretch in isotopically dilute water only deviates slightly from Gaussian. The asymmetry, calculated by the variation of half-widths at half-height, $(\Delta\omega_{1/2,blue} - \Delta\omega_{1/2,red})/\Delta\omega$, is $\sim 2.5\%$ for the three isotopes.

	OH	OD	OT
μ_R	0.9481	1.7889	2.5377
ω_g (cm ⁻¹)	3707.47	2723.68	2299.77
ω^* (cm ⁻¹)	3405±2	2509±2	2121±4
I (cm ² mol ⁻¹)	4922±183	3786±97	2321±238
$\Delta\omega$ (cm ⁻¹)	254±4	160±4	127±8
ε (10 ³ cm ² mol ⁻¹)	60±2	52±1	33±3

Table 3.1: Comparison of the absorption line shape parameters for the three isotopologues of water (ω_{OH} for HOD in D₂O, ω_{OD} for HOD in H₂O, and ω_{OT} for HOT in H₂O)

The largest deviations from reduced mass scaling are observed for the molar absorptivity, $\varepsilon(\omega)$. Equation 3.2 predicts an inverse scaling of ε with μ_R , which is tested on the reduced axes in Figure 3-2c. For this parameter $\mu_{OD}\varepsilon_{OD}$ is larger than $\mu_{OH}\varepsilon_{OH}$ by $40 \pm 4\%$ and $\mu_{OT}\varepsilon_{OT}$ is larger than $\mu_{OH}\varepsilon_{OH}$ by $32 \pm 13\%$. A reduced mass scaling of $1/\sqrt{\mu_R}$ leads to somewhat better, although still unsatisfying, agreement. In Table 3-1, we also report the integrated areas calculated by

$$I = \int_{band} \frac{\varepsilon(\omega)}{\omega} d\omega. \quad (3.4)$$

The integration limits correspond to molar absorptivities at one tenth of the peak absorptivity to avoid interference of the overtone of the HOD bend centered at approximately 2950 cm⁻¹. Since I is approximately a product of ε and $\Delta\omega$, it will not be discussed further.

3.2.3 Discussion

A considerable amount of literature has been devoted to describing isotope substitution experiments for the OX stretch IR spectroscopy, and the failings of simple reduced mass scaling in the observables. Haas and Hornig found that the line width of ω_{OH} is four times greater than ω_{OH} in isotopically dilute ice and proposed proton tunneling to explain the observation [149]. Bournay and Marchal [150, 151, 152] invoked both anharmonic coupling to the hydrogen bond stretch and electrical anharmonicity to account for the anomalous intensity scaling in carboxylic acid dimers. With three isotopes, the present results provide unique opportunity to test the linearity of certain scaling relationships. Anharmonicity is seen to be clearly important, as judged by the inadequacy of harmonic reduced mass scaling relationships for ω^* and ε . The amplitude scaling offers no simple explanation; however, the ω^* scaling clearly originates in the anharmonicity of the OX stretch. This can be understood from the eigenvalues of a Morse oscillator (second order expansion), which indicate that

$$\frac{\omega_{OX}}{\omega_{OH}} = \rho(1 - 2\rho\chi_e^H)/(1 - 2\chi_e^H). \quad (3.5)$$

Here χ_e^H is the anharmonicity of the OH stretch and $\rho = \sqrt{\mu_R^{OH}/\mu_R^{OX}}$. With the gas phase anharmonicity, this expression gives close agreement to the observed ω^* .

The approximate inverse $\sqrt{\mu_R}$ scaling of line width provides more evidence for the recently proposed line broadening mechanism. A series of recent studies have used models based on molecular dynamics (MD) simulations to establish a linear correlation between OX stretching frequency and electric field projected onto the OX coordinate for ω_{OH} (HOD in D₂O) and ω_{OD} (HOD in H₂O) [46, 78, 69, 7]. In simulations of one model, which describes the spectroscopy as a linear interaction of the anharmonic OX Morse potential with the intermolecular degrees of freedom [46], we found the same $\sqrt{\mu_R}$ scaling with line width [69]. The remaining small differences in line width could arise from any of a number of sources. The most likely candidate is motional narrowing, which is seen using the Kubo model as an example

[153, 154, 155]. Given a distribution of OX frequencies $\langle\Delta^2\rangle$ and a correlation time τ_c , the linewidth is predicted to scale as $\langle\Delta^2\rangle^{1/2}$ in the inhomogeneous limit and $\langle\Delta^2\rangle\tau_c$ in the homogeneous limit. Since $\langle\Delta^2\rangle$ scales as $1/\mu_R$ and τ_c is invariant with isotope, linewidth scalings between $\sqrt{\mu_R}$ and μ_R are expected. Additionally, Fermi resonance between the OH stretch and the overtone of the HOD bend is a possible contributor to the enhanced red broadening of the OH stretch in D₂O. Anharmonic coupling between the OH stretch and hydrogen bond stretch could also play a role. It is unlikely that this difference results from differences in vibrational population lifetime or reorientational dynamics. Some of these effects are incorporated in the theoretical studies of the OH and OD line shapes by Corcelli and Skinner [54]. Using a combined electronic structure/molecular dynamics approach that correlates electric field with OX frequency, they report a linewidth ratio, $\Delta\omega_{OH}:\Delta\omega_{OD}$, of 1.36 and 1.71 for simulations with the TIP4P [87] and SPC/E [31] water model, respectively.

Electrical anharmonicity, or nonlinearity of the transition dipole moment in the OX coordinate, is a potential explanation for anomalous amplitude or line width variations. The non-Condon effect, which relates the increase of the OH transition dipole moment to an increased hydrogen bonding interaction, is another nonlinearity that has already been shown important for describing the IR-Raman non-coincidence effect [78], and for quantitative modeling of OX stretch nonlinear IR spectroscopy [7, 156]. Its importance is apparent from the 20-fold increase of infrared absorption upon going from the gas to condensed phase. It also explains [7] differences in the reported frequency time-correlation functions of HOD in D₂O [68, 69, 93] and HOD in H₂O [77, 157, 158]. The non-Condon effect will skew an otherwise symmetric line shape due to frequency dependence of the transition dipole. All three line shapes are similarly asymmetric with a deviation from a Gaussian line shape on the red side. A linear proportionality between the OH transition dipole moment and OH frequency can be used to argue that this effect should not influence the reduced mass scaling of the line shape [7]. We have argued that a nonlinear proportionality is more realistic [156], and it is unclear how this will depend on the OX reduced mass.

It is difficult to explain what leads to the relatively low transition moment for the

OH stretch relative to the OT and OD. One intriguing possibility is the increased hydrogen bond strength for the higher mass species, and the difference in solvent (H_2O vs. D_2O). Studies on H_2O - D_2O mixtures in ice [159, 160] and clusters [161], and the ion-molecule pair $\text{I}^- \cdot \text{HDO}$ [162] show the deuteron preferentially hydrogen bonds due to the difference in zero point energy. We investigated whether H_2O or D_2O forms stronger hydrogen bonds through line shape parameters of the HOD bend in both H_2O and D_2O . The peak wavelength is shifted to the red (1460 to 1457 cm^{-1}) and narrower (84 to 79 cm^{-1}) in H_2O . This corresponds to the HOD in D_2O bend parameters at a higher temperature ($\sim 40^\circ\text{C}$). Indeed it is evident that HOD forms stronger hydrogen bonds in D_2O .

3.3 Model Calculations of Correlated Frequency Shifts

Previous ultrafast infrared experiments have employed a low concentration of HOD in $\text{D}_2\text{O}/\text{H}_2\text{O}$ to study local structural changes in the hydrogen bonded environment of water. 2D IR measurements revealed heterogeneous dynamics in spectrally distinct environments and determined that hydrogen bonds are broken only fleetingly [71, 73]. The transient behavior suggests a mechanism for hydrogen bond switching that involves at least three molecules. The mechanism is an outstanding question that has recently been addressed theoretically [1, 32]. Information on the hydrogen bonded partner can be inferred in experiments on HOD in $\text{D}_2\text{O}/\text{H}_2\text{O}$ but a direct spectroscopic signature of the partner has yet to be exploited. Extending to a third isotope offers this possibility. The dynamics of the hydrogen bond environment can be studied with a two-color polarization selective two-dimensional infrared (2DIR) experiment on a low concentration of HOD and HOT in H_2O . The measured signal will not be present without the involvement of multiple distinct molecules. If coupling is dominated by electrostatics, intermolecular coupling strength will be dependent on the relative geometry of the hydrogen bonded oscillators. The experiment is there-

fore capable of directly revealing how motion of the two molecules interlaces with hydrogen bond rearrangements. A clear understanding of how correlated geometric fluctuations map onto changes in frequency is absolutely necessary to derive information from this experiment. This section presents a simple calculation to stipulate on what an experiment may show and how information can be extracted to address the mechanism of hydrogen bond switching.

The linear absorption spectra of HOT in H₂O and HOD in H₂O are shown in Figure 3-3, the peaks are separated by 380 cm⁻¹, or ~240 cm⁻¹ between the blue (red) side of the FWHM of ω_{OT} (ω_{OD}). This system extends the three levels of HOD to six levels. The six levels are the ground state, two $\nu=1\leftarrow 0$ transitions, two $\nu=2\leftarrow 1$ transitions, and the combination state. The six level systems Rh(CO)₂acac (RDC) in chloroform and hexane [163] and *N*-methylacetamide (NMA) in various solvents [164, 165] have been previously studied in the Tokmakoff group with 2D IR. In a 2D IR spectrum, spectral information is shown in the peak positions, amplitudes, and line shapes. The anharmonic vibrational potential determines the peak positions. In general, peaks along the diagonal are the $\nu=1\leftarrow 0$ and $\nu=2\leftarrow 1$ transitions of the individual modes and cross peaks involve coupling between modes. Amplitudes of the cross peaks reflect the relative magnitudes and orientations of the transition dipoles. These studies successfully determined the relative orientation of the modes and magnitude of the coupling with polarization selective 2D IR. A major difference is that these experiments studied mechanical coupling, or through bond coupling, of normal modes and the proposed experiment will study local modes coupled primarily electrostatically. However, there is some degree of charge transfer upon forming a hydrogen bond in which the lone pair orbitals of the O atom donate to the σ_{OH}^* antibonding orbital (see [166] and references within). The goal remains similar in that the cross peaks will be utilized in a time series of 2D IR spectra to observe local structure change during a hydrogen bond switching. The background free cross peaks only appear in the case that the OD and OT oscillators are within approximately one solvation shell of each other.

In the model calculation the local modes are the diagonal elements of the system

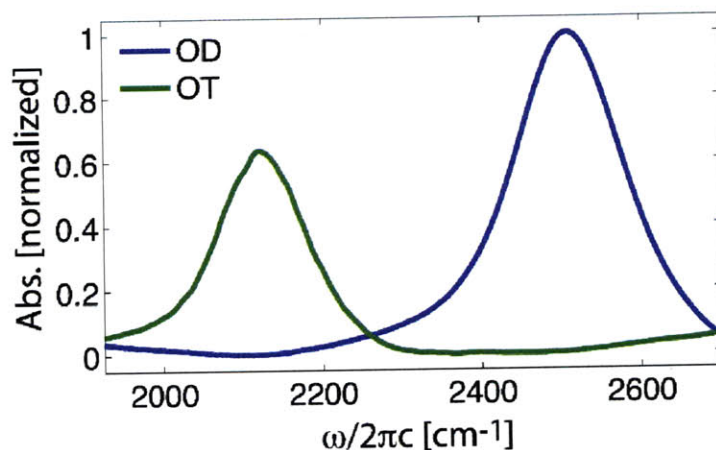


Figure 3-3: The OD stretch of 1% HOD in H₂O and the OT stretch of 0.3% HOT in H₂O. The maximum of the OT stretch is scaled by the ratio of the molar absorptivities. See Table 3-1.

Hamiltonian and the off-diagonal terms are the couplings between modes. To construct the Hamiltonian, I. Begin with the gas phase potential for the OX and OY stretch:

$$H = \begin{bmatrix} \omega_{OX}^{GAS} & \\ & \omega_{OY}^{GAS} \end{bmatrix} \quad (3.6)$$

II. Include the modulation to the diagonal terms from solvation, and:

$$H = \begin{bmatrix} \omega_{OX}^{GAS} + \Delta\omega_{OX} & \\ & \omega_{OY}^{GAS} + \Delta\omega_{OY} \end{bmatrix} \quad (3.7)$$

III. Include coupling between modes:

$$H = \begin{bmatrix} \omega_{OX}^{GAS} + \Delta\omega_{OX} & F_{OX,OY} \\ F_{OY,OX} & \omega_{OY}^{GAS} + \Delta\omega_{OY} \end{bmatrix} \quad (3.8)$$

In the calculation, the diagonal terms are modulated by the intermolecular electric field and off-diagonal coupling is computed with transition dipole coupling. First we will show the change in electric field and TDC with geometry for a hydrogen bond

dimer. Then the full Hamiltonian will be diagonalized to calculate frequencies during an idealized, concerted hydrogen bond switch

3.3.1 Diagonal Elements: Electric Field

Vibration	Empirical Relationship
OH	$\omega_{10} = 3806.1 \text{ cm}^{-1} - 10792 \text{ cm}^{-1}/\text{a.u. } E$ $x_{10} = 0.093316 \text{ \AA} - 7.3478 \times 10^{-6} \text{ \AA}/\text{cm}^{-1} \omega_{10}$
OD	$\omega_{10} = 2792.7 \text{ cm}^{-1} - 7559.5 \text{ cm}^{-1}/\text{a.u. } E$ $x_{10} = 0.081787 \text{ \AA} - 9.266 \times 10^{-6} \text{ \AA}/\text{cm}^{-1} \omega_{10}$
OT	$\omega_{10} = 2326.4 \text{ cm}^{-1} - 6596.4 \text{ cm}^{-1}/\text{a.u. } E$ $x_{10} = 0.062853 \text{ \AA} - 6.1355 \times 10^{-6} \text{ \AA}/\text{cm}^{-1} \omega_{10}$
ALL	$\mu'/\mu_g' = 1.377 + 53.03 \text{ a.u.}^{-1} E$

Table 3.2: Empirical relationships using the SPC/E model relating the electric field to the frequency and transition dipole for each of the three isotopes. The relationships for OH and OD are from [7] and the relationship for OT was derived by reduced mass scaling.

Corcelli and Skinner [78, 7] performed density functional calculations on clusters of water molecules, generated from liquid-state configurations, to empirically relate a quantity easily extracted from MD simulations to the transition frequency and transition dipole. Correlating the frequency to the electrostatic potential has been a popular technique, but the authors found that for water the electric field is superior [167]. They used linear regression to correlate the electric field from the solvent along the OH (or OD) stretch of the HOD molecule calculated at the H (or D) atom of interest with the *ab initio* frequencies. The relationships used in the model calculation, with the values for OT derived by scaling by the reduced mass, are given in Table 3-2. Auer and Skinner [55, 56] have since reported a quadratic dependence on the electric field; this would be simple to include in the calculations. The electric field at the proton of interest is calculated by:

$$E = \hat{u} \times \sum_{i=1}^{3n} \frac{q_i \hat{r}_{iX}}{r_{iX}^2} \quad (3.9)$$

where n is the total number of molecules and \hat{u} is a unit vector along the intramolecular

bond of interest. The partial charges match the SPC/E model; a three site model with a partial charge of -0.8476 at the oxygen and +0.4238 at each of the protons. As an aside, the SPC/E potential was parameterized to reproduce the experimental room-temperature density and heat of vaporization. However, the model has been shown to be a good choice for understanding dynamics experiments [86]. Each molecule is in the tetrahedral geometry (109.47°) with an intramolecular bond length of 0.97 \AA .

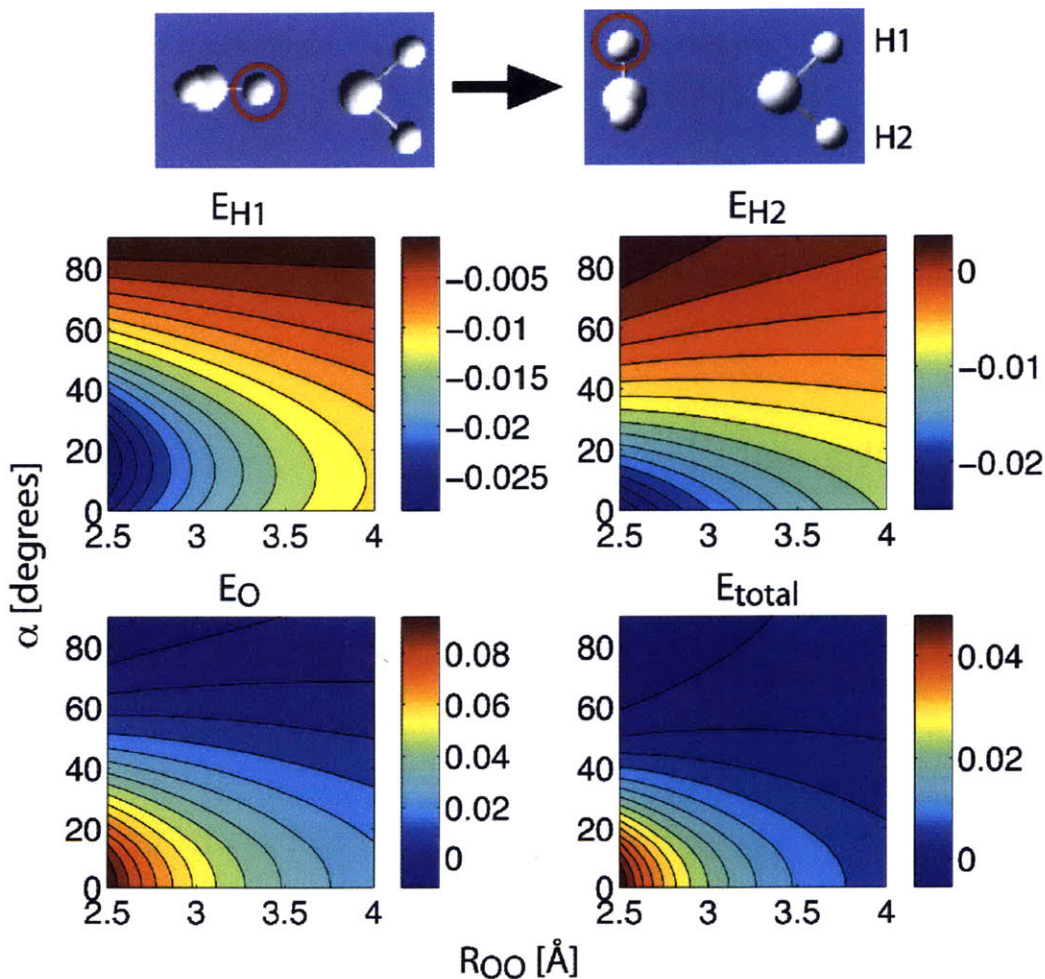


Figure 3-4: The change in electric field with geometry at the proton circled in red for each atom of the adjacent water molecule. The total electric field is also shown ($E_{total}=E_{H1}+E_{H2}+E_O$). The electric field is in atomic units.

Figure 3-4 shows the change in electric field with geometry for a pair of water molecules as R_{OO} ranges between 2.5 and 4 \AA and α , the angle between the intramolecular bond of the donating HB proton and R_{OO} , is varied from $0-90^\circ$. The

electric field from each of the three atoms of the hydrogen bond acceptor and the total electric field are shown. The oxygen has the largest contribution. Given the total electric field at $\alpha = 0^\circ$ and $R_{OO} = 2.8\text{\AA}$, the average length of a hydrogen bond in water, the frequency for an OD stretch is 2559 cm^{-1} , which is $\sim 50\text{ cm}^{-1}$ shifted to the blue from the experimental value. Decreasing R_{OO} by 0.3\AA , to 2.5\AA , red-shifts the frequency by 156 cm^{-1} . A standard geometric criteria for determining if two water molecules are hydrogen bonded is R_{OO} is less than 3.5\AA and α is less than 30° [13]. The value for R_{OO} is meant to include the range of the water molecule's first coordination shell and it is determined by the minimum in the oxygen-oxygen radial distribution function [168]. The angle component was estimated from Debye-Waller factors [169] and it is meant to represent the librational amplitude that will break a hydrogen bond. At $\alpha = 30^\circ$ and $R_{OO} = 3.5\text{\AA}$ the OD stretch frequency is 2743 cm^{-1} , $\sim 19\text{ cm}^{-1}$ greater than the experimental gas phase value.

3.3.2 Off-Diagonal Elements: TDC

The off-diagonal coupling is determined with transition dipole coupling (TDC). TDC will break down if the intramolecular bond distance is on the order of the separation of the dipoles, which are approximated as point dipoles. The TDC is calculated by:

$$F_{XY} = \frac{\partial^2 V_{OX,OY}}{\partial Q_{OX} \partial Q_{OY}} = \frac{\left(\frac{\partial \mu_{OX}}{\partial Q_{OX}}\right) \cdot \left(\frac{\partial \mu_{OY}}{\partial Q_{OY}}\right) - 3\left[\left(\frac{\partial \mu_{OX}}{\partial Q_{OX}}\right) \cdot n_{OX,OY}\right]\left[\left(\frac{\partial \mu_{OY}}{\partial Q_{OY}}\right) \cdot n_{OX,OY}\right]}{R_{OX,OY}^3} \quad (3.10)$$

Figure 3-5 shows the coupling in cm^{-1} calculated by TDC between the transition dipole of the donating proton and each transition dipole of the acceptor with the same geometric change as the electric field calculation above. The transition dipoles are placed at the protons, for convenience, and have a value of 0.5 D/\AA . Recently, Auer and Skinner found that placing the dipole along the bond 0.58\AA from the oxygen gave the best comparison between intermolecular couplings determined from *ab initio* calculations in dimers and TDC [56]. This would be simple to incorporate. Finally, the matrix element between the ground and first excited state, x_{10} , is set to 1\AA , which is exaggerated. Under these conditions the coupling with both dipoles at $\alpha =$

0° and $R_{OO} = 2.5\text{\AA}$ is -54 cm^{-1} . At $\alpha = 30^\circ$ and $R_{OO} = 3.5\text{\AA}$, the TDC is -5 and -29 cm^{-1} with the transition dipole involving H1 and H2, respectively (see Figure 3-4 for proton number assignments). For comparison, Auer and Skinner [56] calculated the TDC with SPC/E MD simulation and found the average of the largest intermolecular coupling frequencies over many chromophores to be -28 cm^{-1} .

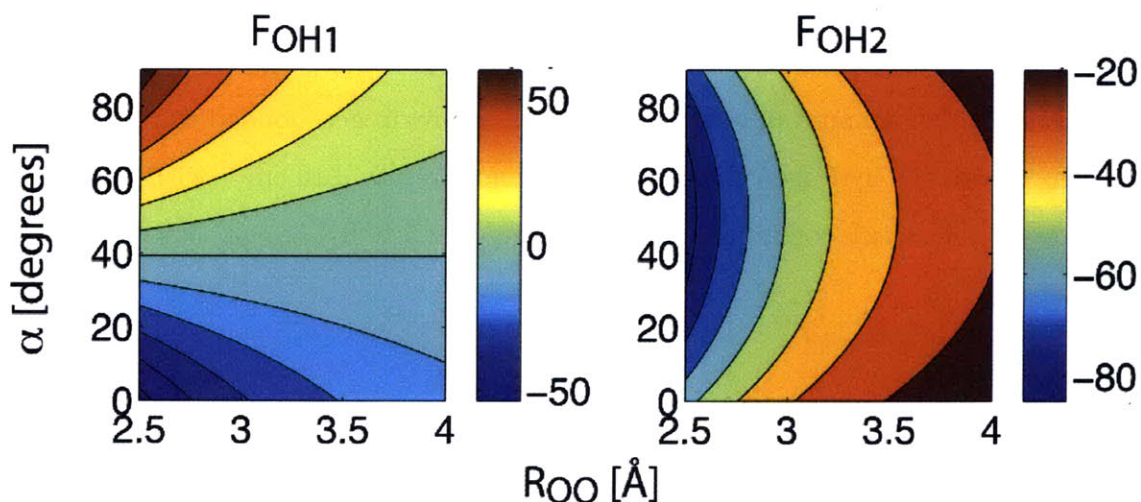


Figure 3-5: Change in TDC with geometry between the transition dipole of the proton circled in red in Figure 3-4 and each of the two transition dipoles of the adjacent water molecule. The TDC is in cm^{-1} .

3.3.3 Model Calculation of Concerted HB Switch

In the model calculation, three molecules are involved in an idealized concerted hydrogen bond switch. The geometric change is similar to that described above. An HOD molecule is undergoing a hydrogen bond switch in which the D atom is first hydrogen bonded to an H_2O molecule, then subsequently an HOT molecule. Of course, the isotopes can be interchanged. Here D, A1, and A2 refer to donor, first acceptor, and second acceptor, respectively. The switching is concerted in that $R_{O(D)O(A1)}$ increases from 2.5 to 4\AA as α increases from 0 - 90° (or α decreases from 90 - 0° with respect to $R_{O(D)O(A2)}$ and $R_{O(D)O(A2)}$ decreases from 4 to 2.5\AA). Figure 3-6a shows the initial configuration. Figure 3-6b shows the total electric field at D along with the electric field from each atom of the first acceptor. The second acceptor is the

mirror image reflected over the bifurcation angle. The total electric field is maximum when the deuterium is linearly hydrogen bonded to an acceptor and minimum at the bifurcation angle, 45° , where the distances between the deuterium and the oxygens of the first and second acceptor are equal. Notice the non-hydrogen bonded species contributes very little to the electric field. Figure 3-6c shows the TDC under the same conditions. Again, the second acceptor is the mirror image. Although the hydrogen bonded partner has stronger coupling with the donor while in a linear HB, there is still a fair amount of coupling with the non-hydrogen bonded water molecule (-54 cm^{-1} with the hydrogen bonded partner compared to $\pm 16 \text{ cm}^{-1}$ with the second acceptor at the initial configuration: $R_{O(D)O(A1)} = 2.5 \text{ \AA}$, $R_{O(D)O(A2)} = 4 \text{ \AA}$, and $\alpha = 0^\circ$).

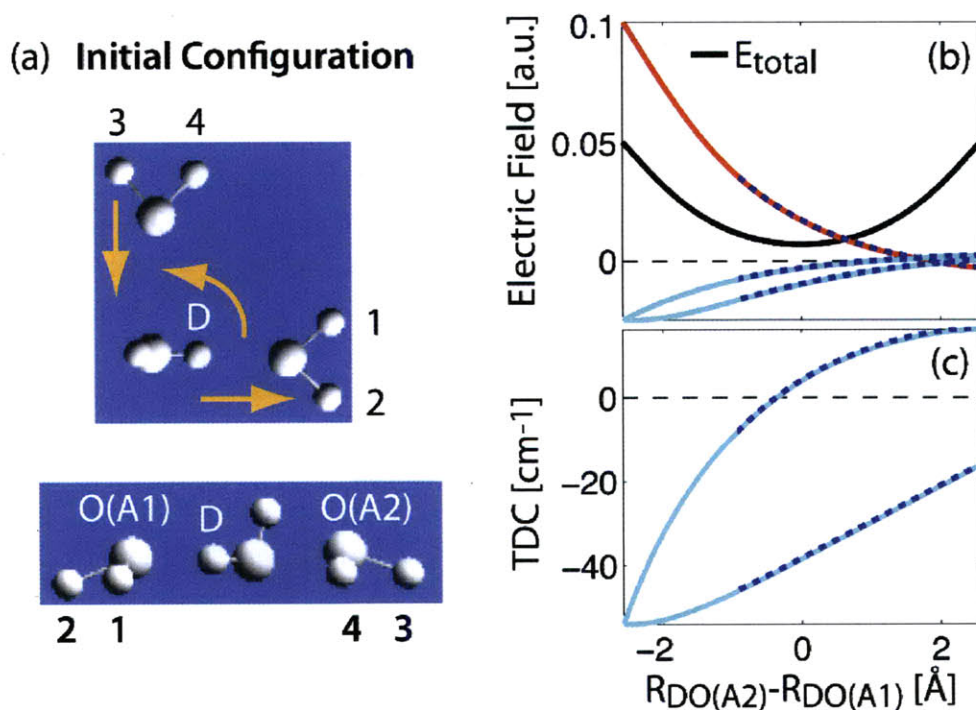


Figure 3-6: Change in electric field and TDC during an idealized concerted HB switch. (a) The initial configuration from the top and side. The total electric field (b) and TDC (c) at the deuterium (donor) due to oxygen (red) and each hydrogen (cyan) of the first acceptor. The dashed blue indicates a broken HB with the first acceptor according to standard geometric criteria.

In the calculation, each proton, beyond the proton undergoing the hydrogen bond

switch, has a dummy water molecule hydrogen bonded so that the calculated frequency better reproduces the condensed phase experimental value. The dummy molecule maintains a linear HB during the switch with $R_{OO} = 2.8\text{\AA}$. Intramolecular coupling is included for the first acceptor, H_2O , which was estimated as -50 cm^{-1} from the splitting of peaks of the isolated molecule. In the condensed phase this may not be rigorous since symmetry is broken by the fluctuating solvent. Auer and Skinner [56] determined an empirical relationship between intramolecular coupling and electric field through *ab initio* cluster calculations on H_2O and found a broad distribution with the mean coupling of -27.1 cm^{-1} . The intramolecular coupling for HOD and HOT in the calculation is set to zero.

To calculate frequencies during the switch we diagonalize the 6x6 Hamiltonian:

$$H = \begin{bmatrix} \omega_D & 0 & F_{D,H(T)} & F_{D,T} & F_{D,H(1)} & F_{D,H(2)} \\ 0 & \omega_{H(D)} & F_{H(D),H(T)} & F_{H(D),T} & F_{H(D),H(1)} & F_{H(D),H(2)} \\ F_{H(T),D} & F_{H(T),H(D)} & \omega_{H(T)} & 0 & F_{H(T),H(1)} & F_{H(T),H(2)} \\ F_{T,D} & F_{T,H(D)} & 0 & \omega_T & F_{T,H(1)} & F_{T,H(2)} \\ F_{H(1),D} & F_{H(1),H(D)} & F_{H(1),H(T)} & F_{H(1),T} & \omega_{H(1)} & \textit{intra} \\ F_{H(2),D} & F_{H(2),H(D)} & F_{H(2),H(T)} & F_{H(2),T} & \textit{intra} & \omega_{H(2)} \end{bmatrix} \quad (3.11)$$

Figure 3-7a displays the frequencies of the OD and OT stretch during the hydrogen bond switch for $\mu = 0\text{ D/\AA}$ (solid) and $\mu = 0.5\text{ D/\AA}$ (dashed and dot-dashed). The dipole moments are constant and equal for all bonds. The OD stretch frequency changes most drastically as this is the only proton switching hydrogen bond partners and, as expected, it moves from the red to the blue and back to the red during the switch. Note that with intermolecular coupling turned on, ω_{OD} is blue shifted when it is hydrogen bonded to HOD relative to H_2O . ω_{OD} is 2407 cm^{-1} and 2419 cm^{-1} when in a linear HB with H_2O ($R_{OO} = 2.5\text{\AA}$) and HOD, respectively. Although the site energy for ω_{OT} is fixed by the dummy molecule accepting a hydrogen bond from OT, ω_{OT} changes during the hydrogen bond switch due to the change in off-diagonal coupling. Figure 3-7b shows the correlation between ω_{OD} and ω_{OT} . Note that there is no correlation when the coupling is turned off. With intermolecular coupling, ω_{OD}

and ω_{OT} are positively correlated while in a hydrogen bond, which will result in a diagonally elongated cross peak parallel to the diagonal. Polarization selective 2D IR experiments can measure the average angle between the dipoles. The value is expected to be near 70.53° where the frequencies are correlated. This value can be evaluated in a time series to see how relative orientation changes as the molecule undergoes hydrogen bond breaking and reforming.

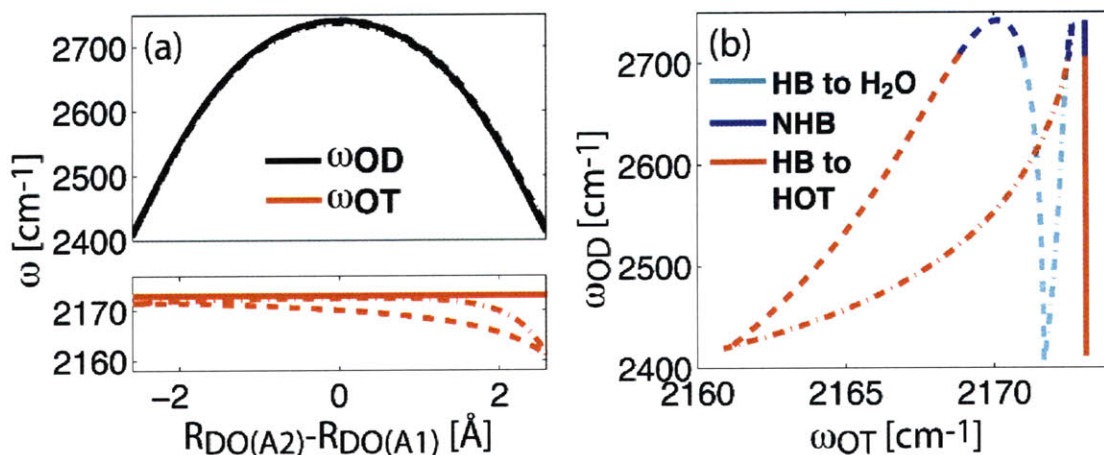


Figure 3-7: (a) Change in frequency for the OD and OT stretch during the HB switch with no TDC (solid) and with TDC and T in position 3 (dashed) and 4 (dot-dashed) [See Figure 3-6a for reference]. (b) Correlation between ω_{OD} and ω_{OT} .

This simple calculation does not take into consideration the non-Condon effect. Since the transition dipole increases with the strengthening of the hydrogen bond [156, 7] the non-Condon effect is expected to cause a larger disparity in intermolecular coupling between HB and NHB species. This can easily be included by using the relationships in Table 3-2. There are two main experimental difficulties that need to be considered. The first issue is dilution. This experiment requires an HOD and HOT molecule to be within two solvation shells of one another. If instead two HOD(T) water molecules are near each other resonant energy transfer will dominate. The second related issue is strength of coupling. The coupling must be strong enough such that the inverse time would be faster than the dynamics of interest. Otherwise, the experiment will only be able to report on the kinetics of energy transfer, however difficulties concerning the vibrational lifetime and hot ground state need to be kept

under consideration.

3.4 Gaussian Calculations

We performed B3LYP/6-311++G** density functional calculations with Gaussian98 on water isotopologue dimer combinations to determine the intermolecular coupling between ω_{OD} and ω_{OT} . The calculations were performed with water as the solvent, which applies a constant dielectric field, and the dimer geometry was optimized. The intramolecular bond lengths of the hydrogen bond accepting water molecule are 0.9629 Å. However, the intramolecular bond lengths of the hydrogen bond donating water molecule are unequal; the donating OX bond length is relatively lengthened to 0.971 Å and the free OX bond length is shortened to 0.9615 Å. Also, the angle between the protons of the accepting water molecules is 105.8098° compared to 103.983° for the donating water molecule. R_{OO} is 2.9004 Å and the intramolecular OX bond is tilted off the line that connects the two oxygens by 5.6985°. In other words, the calculation does not predict a perfectly linear hydrogen bond.

Vibrational frequencies were calculated for four dimer pairs: (a) HOD-H₂O, (b) HOD-HOT, (c) HOT-H₂O, and (d) HOT-HOD, where the atom in bold is the hydrogen bond donor. The spectra for dimers (b) and (d) are shown in Figure 3-8. In agreement with the trend observed between gas and condensed phase vibrational frequencies, the OX stretch red-shifts and the HOX bend blue-shifts upon forming a hydrogen bond. For example, the OT stretch and HOT bend shifts from 2356.1099 and 1334.0667 cm⁻¹ to 2263.3100 and 1358.2596 cm⁻¹, respectively, between dimer (b) and (d). Likewise the OD stretch and HOD bend shifts from 2808.4353 and 1417.9195 cm⁻¹ to 2697.5080 and 1430.0400 cm⁻¹, respectively, between dimer (b) and (d). Although the shift in OX stretch frequency is similar between the two isotopes, the HOT bend blue-shifts by more than 2x relative to the HOD bend upon forming a hydrogen bond. Also, the intensity of ω_{OD} increases by a factor of 6.1988 upon forming a hydrogen bond compared to 5.6528 for ω_{OT} . Furthermore, if an H₂O is added to dimer (b) hydrogen bonded to the free OH stretch of HOD, the OD

stretch blue-shifts to $2721.6995 \text{ cm}^{-1}$ (0.9689 \AA) relative to dimer (b) but the HOD bend further blue-shifts to $1470.3225 \text{ cm}^{-1}$ (104.1452°). Also, the HOD hydrogen bond becomes more linear in the trimer with the angle decreasing from 5.6985 to 3.6420° .

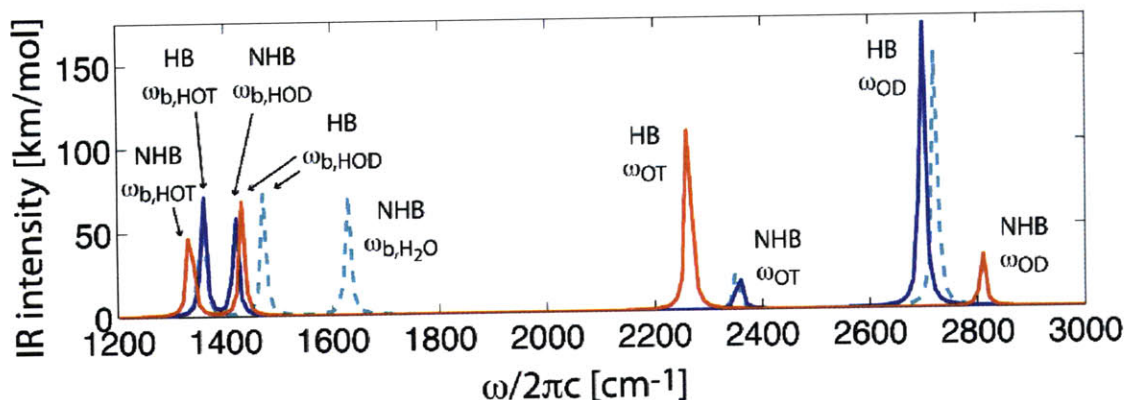


Figure 3-8: Mid-infrared spectra of dimers (b) (blue) and (d) (red); also, dimer (b) with additional H_2O (dashed cyan).

With the four dimer combinations we can estimate the intermolecular coupling between ω_{OD} and ω_{OT} . The diagonal elements are ω_{OD} and ω_{OT} when hydrogen bonded to H_2O and the off-diagonal element is the coupling between modes. Diagonalizing the matrix gives ω_{OD} and ω_{OT} when hydrogen bonded to HOD and HOD, respectively. From the calculation, the OD(T) stretch blue(red)-shifts from 2697.5743 to $2697.5080 \text{ cm}^{-1}$ (2663.4638 to $2263.3100 \text{ cm}^{-1}$) when the H_2O hydrogen bond acceptor is replaced by HOD(D). Given these frequencies, the coupling is -8.1778 cm^{-1} .

3.5 Conclusions

The infrared absorption spectrum of the OT stretch in tritiated water has been reported, making comparison of this line shape to ω_{OD} and ω_{OH} spectra. The inadequacy of harmonic scaling relationships in predicting resonance frequencies, amplitudes and line widths is an indication that these approximations, commonly used in the recent simulations of water vibrational spectroscopy, need to be re-visited. The

results suggest that a more nuanced description of electrical and mechanical anharmonicity in the interactions of the OX stretch with the electromagnetic field and intermolecular motions will be necessary to obtain a quantitative understanding of the spectroscopy. Comparison of ultrafast IR spectroscopy on these isotopologues can be used to obtain this insight.

Studies of the HOD in D₂O system with broadband infrared non-linear techniques have provided insight into the fastest timescales of motion in water. 2D IR measurements revealed frequency dependent spectral diffusion. The results imply that the non-hydrogen bond species are transient, which leads to the hypothesis that hydrogen bond switching is a many body problem. This mechanism, however, cannot be determined with the aforementioned system. Extending 2D IR measurements to directly probe two spectrally distinct species provides a route to elucidate the mechanism. Model calculations reveal that ω_{OD} and ω_{OT} are correlated when they are hydrogen bonded. Polarization selective waiting time dependent 2D IR measurements on this system may reveal the relative structural change during a hydrogen bond switch. An important quantity to consider in the feasibility of the experiment is the intermolecular coupling. With *ab initio* calculations, we found the coupling to be ~ 8 cm⁻¹.

3.6 Acknowledgments

We would like to thank Lauren DeFlores for her help in acquiring the transient absorption measurement of tritiated water. We would like to thank Ziad Ganim for his help with the Gaussian calculations of the water isotopologues.

Chapter 4

Vibrational Relaxation in Isotopically Dilute Water

4.1 Introduction

Understanding vibrational energy redistribution in solution is important for a number of reasons. First, reaction rates and product distributions can be quite different for reactions occurring in the gas and condensed phases. For instance, if vibrational energy redistribution is important in a reaction, the solvent may alter the rate by providing an efficient pathway for energy transfer. This may be an important factor in photoisomerization, proton and electron transfer, and some photodissociation reactions [170, 171]. An understanding of vibrational relaxation processes in solution is an essential piece in the development of a predictive theory of reaction dynamics. Second, comparing the experimental lifetime to the calculated lifetime provides a sensitive test of the adequacy of potential energy surfaces. Finally, we will show that vibrational relaxation and spectral diffusion occur on a similar time scale in water. A clear picture of the vibrational lifetime and pathway for vibrational relaxation will be important since energy dissipation to the low frequency modes has a non-negligible affect on our spectral measurements.

In order to characterize the vibrational relaxation pathway(s) in isotopically dilute water we will compare previous measurements of the temperature dependence of the

lifetime of the OH stretch of HOD in D₂O, or $T_{1,OH}$, with the temperature dependence of the lifetime of the OD stretch of HOD in H₂O, or $T_{1,OD}$, and the room temperature lifetime of the OT stretch of HOT in H₂O, or $T_{1,OT}$. The intramolecular vibrational modes of water are anharmonically coupled. Vibrational relaxation may include a number of downhill or uphill intramolecular pathways with the solvent taking up or contributing excess energy, respectively. What would we expect to see if instead the intramolecular modes were orthogonal? The transition frequencies of ω_{OH} , ω_{OD} , and ω_{OT} scale largely by reduced mass (see chapter 3). If the dominant relaxation pathway is to the ground vibrational level, one would expect $T_{1,OH} > T_{1,OD} > T_{1,OT}$ since $\omega_{OH} > \omega_{OD} > \omega_{OT}$. Also, one may expect the lifetime to decrease with increased temperature since there will be increased occupancy of the lower energy-accepting bath modes. Neither of these trends have been observed experimentally, however.

An early theoretical investigation of the vibrational relaxation of the OH stretch of HOD in D₂O suggested that the intermolecular hydrogen bond stretch may be the dominant accepting mode ($\sim 180 \text{ cm}^{-1}$) [172]. In other words, an initially intact hydrogen bond ruptures upon vibrational relaxation. The vibrational lifetime was calculated via a Fermi Golden Rule approach and found to be related to the shift from the gas phase absorption frequency by a power law dependence: $T_{1,OH} = a / (\delta\omega_{OH})^{1.8}$, where a is a constant. The relationship predicts the lifetime will decrease as the frequency red-shifts. Increased hydrogen bond strength softens the OH intramolecular potential, which results in a red-shift of ω_{OH} . With increased temperature there are increased fluctuations in the hydrogen bond network, which results in a blue-shift in the absorption band. The proposed mechanism, then, predicts the lifetime will increase with increased temperature.

Woutersen and coworkers measured the the vibrational lifetime of a 500 μm layer of a 1:500 solution of HOD in D₂O within the range of 30-363 K [97]. In the entire temperature range for ice there is no significant change in $T_{1,OH}$, which is approximately 380 fs. At the melting point, $T_{1,OH}$ suddenly increases from ~ 380 to ~ 750 fs and increases by an additional $\sim 20\%$ at 363 K. The observed trend could be reasonably described by the proposed vibrational predissociation mechanism. However,

the possibility that the increase in lifetime with temperature may be the result of an increasing energy gap between the OH stretch and different inter- or intramolecular accepting modes could not be ruled out.

More recent theoretical work by Rey and Hynes [103] and Lawrence and Skinner [104, 105] found that the overtone of the HOD bend was the dominant relaxation pathway for the OH stretch, which also agrees with the experimentally observed temperature dependence of the lifetime. As the temperature is increased, hydrogen bond fluctuations increase and the stretch red-shifts while the bend blue-shifts toward their respective gas phase values. If the bend anharmonicity is constant with temperature the overtone will shift in the same manner as the bend. This will decrease the overlap integral between the overtone of the HOD bend and OH stretch, which results in a decrease in coupling and a longer lifetime.

Clott and co-workers performed the only experiments on isotopically dilute water that directly probed vibrations beyond the stretch after excitation of the stretch using a mixed IR/Raman technique with ~ 1.5 ps time resolution [92]. They conclude that the primary route of energy relaxation is through a pair of HOD bend vibrations facilitated by intermolecular energy transfer to D_2O . However, it is possible the overtone of the bend was not observed given that the lifetime of the fundamental of the HOD bend in D_2O is 390 fs [96]. Lindner et al. performed two-color IR-pump probe (PP) experiments on the bend and stretch vibrations of pure H_2O with ~ 200 fs time resolution [109]. Albeit a very different species as far as vibrational relaxation is concerned, they too found the vibrational energy of the photo-excited H_2O stretch is deposited to a pair of bending vibrations.

A theoretical study on the OD stretch of HOD in H_2O , performed with a similar method as the calculations on the OH stretch [103, 104, 105], found the dominant pathway was either through the fundamental of the HOD bend or directly to the ground state depending on if the bath was treated as rigid or flexible, respectively [106]. The room temperature [95, 94] and temperature dependent [100] lifetime of the OD stretch in HOD in H_2O has been measured. Steinel et al. originally reported $T_{1,OD} = 1.45$ ps for the lifetime at the room temperature [94]. More recently, Fayer

and co-workers used a different method to analyze the dispersed pump probes (DPPs) and reported a lifetime of 1.7 ps [95]. The longer lifetime of the OD stretch compared to the OH stretch agrees with the proposed mechanism for vibrational relaxation given that the frequency difference between the OH stretch and the HOD bend overtone is $\sim 500 \text{ cm}^{-1}$ and the difference between the OD stretch and the HOD bend fundamental, the closest intramolecular mode that is lower in energy, is $\sim 1050 \text{ cm}^{-1}$. Tielrooij and Bakker [100] measured the temperature-dependence and found the lifetime increased from approximately 1.7 to 2.2 ps from 274 to 343 K. However from 274 K to room temperature the lifetime is constant within error.

The most direct method to elucidate the vibrational relaxation pathway in water is narrowband (or broadband) pump-broadband probe experiments. In this context, narrowband refers to a pulse that spans the entire spectral region of the vibration of interest ($\nu=1\leftarrow 0$ and the anharmonically shifted $\nu=2\leftarrow 1$) and the broadband probe spans the entire mid-infrared. Also, in this idealized experiment, the time resolution would be fast enough to detect even the initial energy transfer. This experiment has yet to be realized in practice, however there has been progress in this direction [173].

One way to test the proposed vibrational relaxation pathway is to compare the lifetime of different water OX stretches (where X = H, D, and T). In this chapter we report the lifetime of the OT stretch of dilute HOT in H_2O and compare the relaxation rate to the other isotopes. In Figure 4-1 we show a diagram of the peak positions of the intramolecular and intermolecular modes of HOD in D_2O (left), HOD in H_2O (middle), and HOT in H_2O (right). For ω_{OT} (2120 cm^{-1} [174]), the nearest intramolecular vibration that is lower in energy is the HOT bend. From the Gaussian calculations described in chapter 3 we can estimate the frequency of the HOT bend. The frequency of the HOD bend in a trimer in which the central HOD molecule is hydrogen bonded to two H_2O molecules is 1470 cm^{-1} and the experimental value in the condensed phase is 1450 cm^{-1} . If we replace the HOD with a HOT the frequency of the HOT bend from the calculation is 1400 cm^{-1} . If we scale this by comparing the calculated HOD bend frequency with the experimental value the HOT bend frequency is $\sim 1380 \text{ cm}^{-1}$. The frequency difference between ω_{OT} and δ_{HOT} is then $\sim 740 \text{ cm}^{-1}$.

Since the energy difference is in between the energy difference between $\omega_{OH} - 2\delta_{HOD} \approx 500 \text{ cm}^{-1}$ and $\omega_{OD} - \delta_{HOD} \approx 1050 \text{ cm}^{-1}$, one would expect $T_{1,OT}$ to also be in between 700 - 740 fs [93, 98] and 1.45 - 1.7 ps [95, 94, 100].

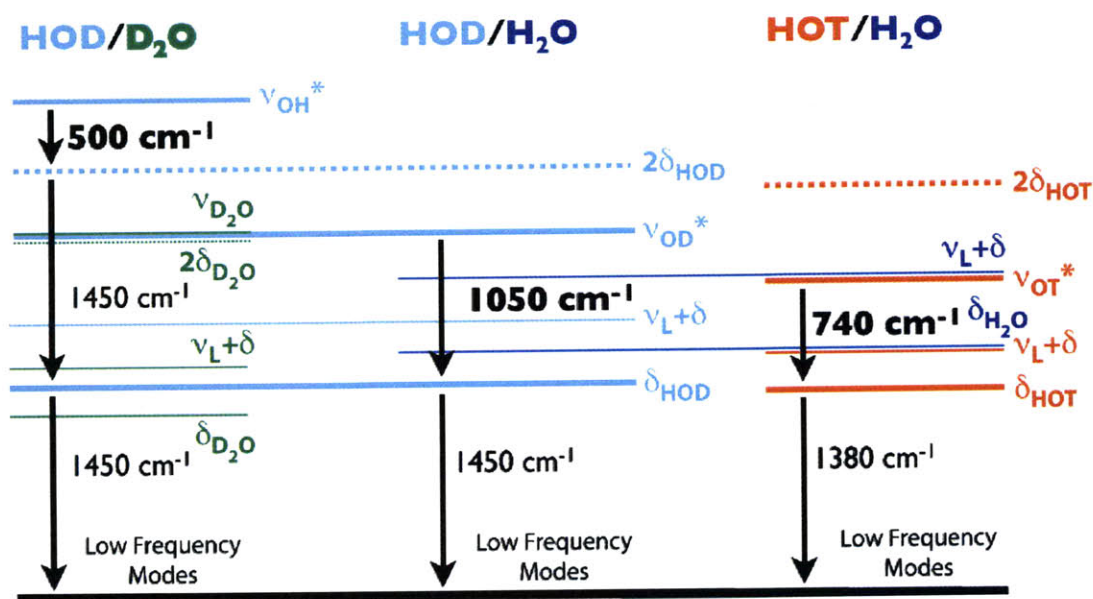


Figure 4-1: Energy level diagram of three isotopologues of water: HOD (cyan) in D_2O (green), HOD in H_2O (blue), and HOT (red) in H_2O .

Another handle we have to test the proposed vibrational relaxation mechanism is temperature. Since changing the temperature alters the fluctuations in the hydrogen bond network in water and the vibrational frequencies are sensitive to hydrogen bonding, vibrational bands shift with changing temperature. Vibrational modes are uniquely dependent on the degree of hydrogen bonding and, therefore, have unique dependencies on temperature. By changing the temperature we can tune the energy gap between modes and compare the experimentally measured change in lifetime with the predicted change. In this chapter we will present the temperature dependent lifetime of ω_{OD} of HOD in H_2O measured with dispersed pump probes and compare to changes in vibrational frequencies with temperature.

4.2 Dispersed Pump Probe of Tritiated Water

The sample conditions for transient absorption measurement of ω_{OT} of HOT in H₂O are the same as described in Chapter 3 for acquiring the absorption spectrum. The concentrations of HOT and the solvent H₂O are approximately 0.2 M and 55 M, respectively. Given the molar absorptivities [112, 174] the ratio of the optical density of the combination band to ω_{OT} is ~ 30 . Therefore, absorption from the background H₂O is a complication in the transient absorption measurement. Also, although heterodyned detected third order measurements and linear absorption measurements are proportional to the fourth and second power of the transition dipole, respectively, third order signal from the combination band may contribute to the third order signal at this concentration of HOT [112]. The pump-probe was measured with the interferometer described in Chapter 2 and the pulse spectrum is shown in Figure 4-2. It is peaked at ~ 2045 cm⁻¹ with a pulse width of ~ 220 cm⁻¹ at full width half maximum (FWHM) and pulse length of ~ 85 fs. In Figure 4-2 we show the linear absorption spectrum of the OT stretch of HOT in H₂O with the background H₂O subtracted and the absorption of the H₂O combination band plotted against the molar absorptivity. The combination band is the combination of the bend (1650 cm⁻¹) and libration (peak at ~ 680 cm⁻¹ and FWHM from ~ 420 to 860 cm⁻¹). The peak of the combination band is ~ 2130 cm⁻¹ and the linewidth is approximately 300 cm⁻¹ (FWHM) [112].

In Figure 4-3 we show slices in time of the experimental transient absorption measurement, a model pump-probe of ω_{OT} , and the absorption spectrum of the combination band of H₂O. The model pump-probe is a difference of two Gaussians with one shifted by the anharmonicity ($\omega_{10}-\omega_{21}=\Delta$):

$$S(\omega) = \exp[-(\omega - \Omega)^2/\sigma^2] - \exp[-(\omega - (\Omega - \Delta))^2/\sigma^2]. \quad (4.1)$$

In this equation, Ω is the central frequency and σ is related to the line width. In this model the line width of the $\nu=2\leftarrow 1$ is the same as the $\nu=1\leftarrow 0$, however, it has been suggested that the width of the $\nu=2\leftarrow 1$ is considerably larger than the fundamental

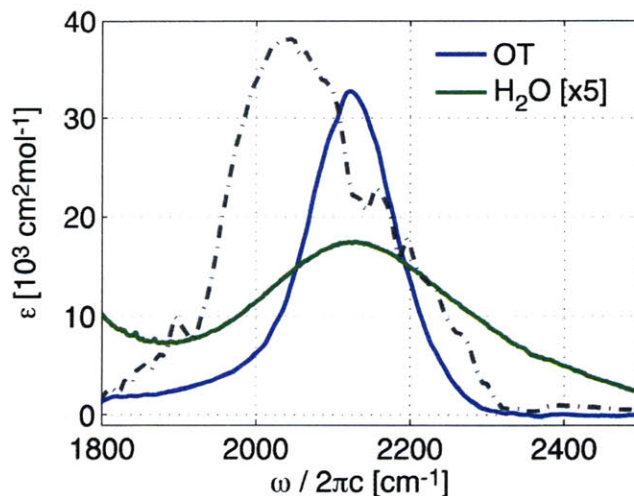


Figure 4-2: The molar absorptivity of the OT stretch (blue), H₂O combination band, $\delta + \nu_L$ (green) [x5], and the pulse spectrum for the dispersed pump-probe measurement (dashed gray)

[61]. The anharmonicity of the ω_{OT} , $\Delta = 130 \text{ cm}^{-1}$, was estimated by reduced mass scaling from the anharmonicity of ω_{OD} (160 cm^{-1} [77]) and ω_{OH} (250 cm^{-1} [60]). In the $\nu=2\leftarrow 1$ region the experimentally measured transient absorption appears quite similar to the model. The induced absorption decays towards zero as the waiting time is increased. In the $\nu=1\leftarrow 0$ region, however, the transient absorption remains largely flat with positive amplitude near the zero crossing shifting slightly towards lower frequency with increased waiting time, reminiscent of the shift observed due to the thermally shifted ground state (TSGS, discussed in the last section of this chapter). Also, there is a slight dip in the positive amplitude near the peak of the combination band. It appears as though absorption by the background H₂O is non-negligible. Also, the experiment was performed in the *zzzz* polarization geometry for maximum signal. The decay is, therefore, sensitive to vibrational relaxation and reorientation. Nonetheless we can get an idea of the vibrational lifetime by fitting the decay of the signal in the $\nu=2\leftarrow 1$ region. Fitting a mono-exponential past the cross-phase modulation (discussed in Chapter 2) results in a decay of $\sim 850 \text{ fs}$, which will be faster than $T_{1,OT}$ due to the contribution from reorientation. Indeed the decay time is in between $T_{1,OH}$ and $T_{1,OD}$, and therefore agrees with the proposed

relaxation mechanism in which the dominant relaxation pathway is through the closest intramolecular mode that is lower in energy.

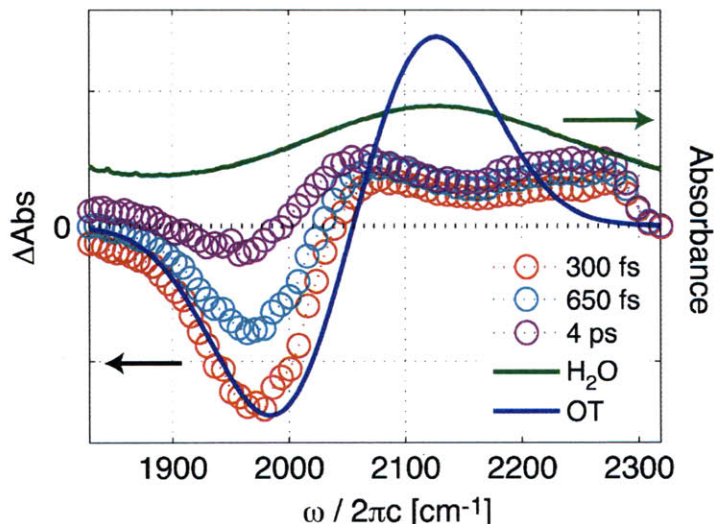


Figure 4-3: Slices in time of the transient absorption of HOT in H₂O (circles), the model pump-probe of ω_{OT} (blue) and the linear absorption of H₂O (green).

In Figure 4-4a we show a model dispersed pump-probe of ω_{OT} and combination band of H₂O. The anharmonicity of the combination band is 300 cm⁻¹ [112]. It is interesting to note that the anharmonicity is roughly equal to the line width at FWHM for all the transitions. In Figure 4-4a the frequencies marked at 1993 (blue), 2008 (green), 2023 (red), and 2038 cm⁻¹ (cyan) correspond to induced absorption for ω_{OT} and bleach/stimulated emission for the combination band of H₂O. The zero-crossing of the ω_{OT} PP is near 2054 cm⁻¹ (magenta) and at 2070 cm⁻¹ (gold) both the PP of ω_{OT} and the combination band show a bleach/stimulated emission. Slices in frequency of the PP measurement (S_{zzzz}) of HOT in H₂O is shown in Figure 4-4b for the frequencies marked in Figure 4-4a. The slices at 1993-2038 cm⁻¹ begin negative and eventually cross to positive values at longer waiting times, which is most likely due to the TSGS (which will be discussed in the last section of this chapter). At 2054 and 2070 cm⁻¹ the transient absorption is positive and remains largely flat over the time frame of the experiment. From the experimental slices in frequency we can be confident we are mainly sensitive to the transient absorption of ω_{OT} , not the

combination band of H_2O .

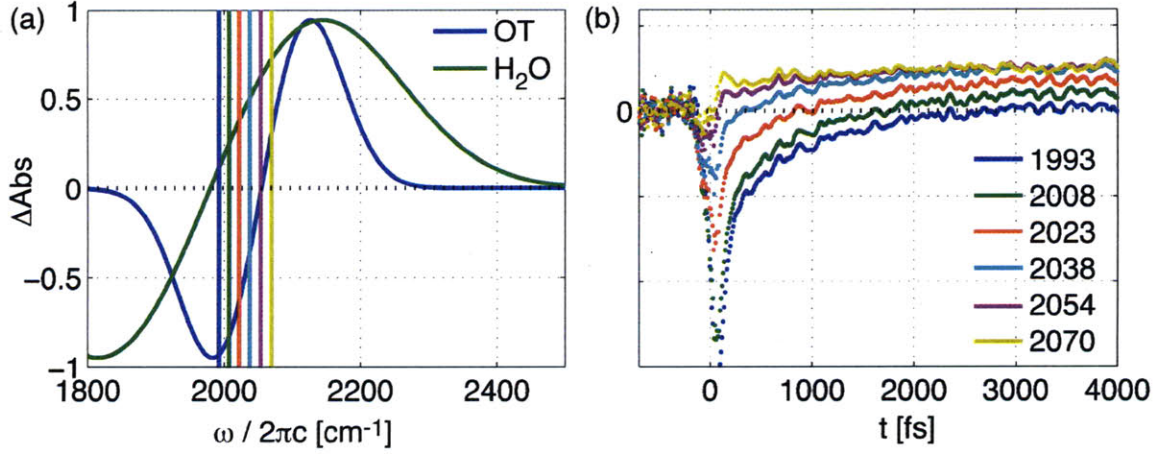


Figure 4-4: (a) Model pump-probe of ω_{OT} (blue) and the combination band of water (green) with the frequencies in (b) marked with lines. (b) Slices in frequency of the experimental pump-probe of HOT in H_2O .

4.3 Temperature Dependent Lifetime of ω_{OD}

4.3.1 Temperature Dependent Linear Absorption

We report the temperature dependence of the linear absorption of HOD in H_2O to predict the temperature dependence of $T_{1,OD}$ given the proposed mechanism in which relaxation occurs primarily through the fundamental of the HOD bend. In Figure 4-5 we show the change in linear absorption with temperature for HOD in H_2O without (a) and with (b) the background H_2O subtracted. The maximum of ω_{OD} , the HOD bend, and the H_2O combination band is shown as black dashed lines and the spectra at the two temperature extrema are shown in the top row of the figure. The HOD bend red-shifts and narrows and ω_{OD} blue-shifts and broadens with increasing temperature. In this temperature range the maximum of the H_2O combination band ($\nu_L + \delta$) red shifts by 70 cm^{-1} from 2156 cm^{-1} at 277 K to 2086 cm^{-1} at 348 K. The intense peak at $\sim 1650 \text{ cm}^{-1}$ in Figure 4-5a is the H_2O bend and the broad featureless absorption that extends from the low frequency side of the spectrum is the librational band.

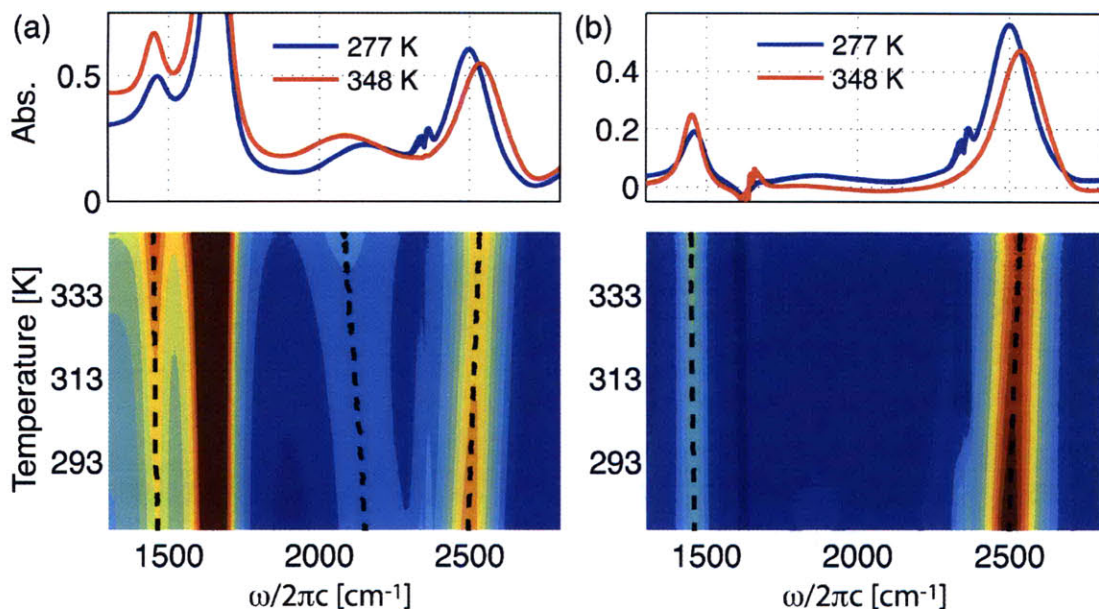


Figure 4-5: Temperature dependent linear absorption of HOD in H₂O without (a) and with (b) the background H₂O subtracted. (Top) Linear absorption at the lowest and highest temperature of the contour plot. (Bottom) Dashed lines indicate the change in peak maxima with temperature for (a) δ_{HOD} , H₂O $\delta + \nu_L$, and ω_{OD} (left to right) and (b) δ_{HOD} (left) and ω_{OD} (right).

Finally, the low intensity but relatively broad peak at $\sim 1850 \text{ cm}^{-1}$ in Figure 4-5b is the combination band ($\nu_L + \delta$) of HOD.

In Figure 4-6 we show the change in peak position (a) and line width (FWHM) (b) for ω_{OD} (blue) and δ_{HOD} (green). The change in frequency is relative to the value at 308 K, which is 2514 cm^{-1} (1454 cm^{-1}) and 166 cm^{-1} (83 cm^{-1}) for the peak and FWHM of ω_{OD} (δ_{HOD}), respectively. ω_{OD} and δ_{HOD} have the opposite trend in both frequency and FWHM with temperature and although the peak frequency of ω_{OD} is more sensitive to temperature the FWHM of δ_{HOD} changes more drastically with temperature. Equations describing the temperature dependencies are given in Table 4-1. In Figure 4-6c we show the energy gap between ω_{OD} and δ_{HOD} with temperature at the peak of each transition (cyan) and at the FWHM (red; red side of ω_{OD} minus the blue side of δ_{HOD}). The energy gap broadens from 1038 cm^{-1} (919 cm^{-1}) to 1086 cm^{-1} (963 cm^{-1}) at the peak (FWHM) between 277 to 348 K. In both cases the change with temperature is linear and the overall change is $\sim 5\%$. In Figure 4-6d

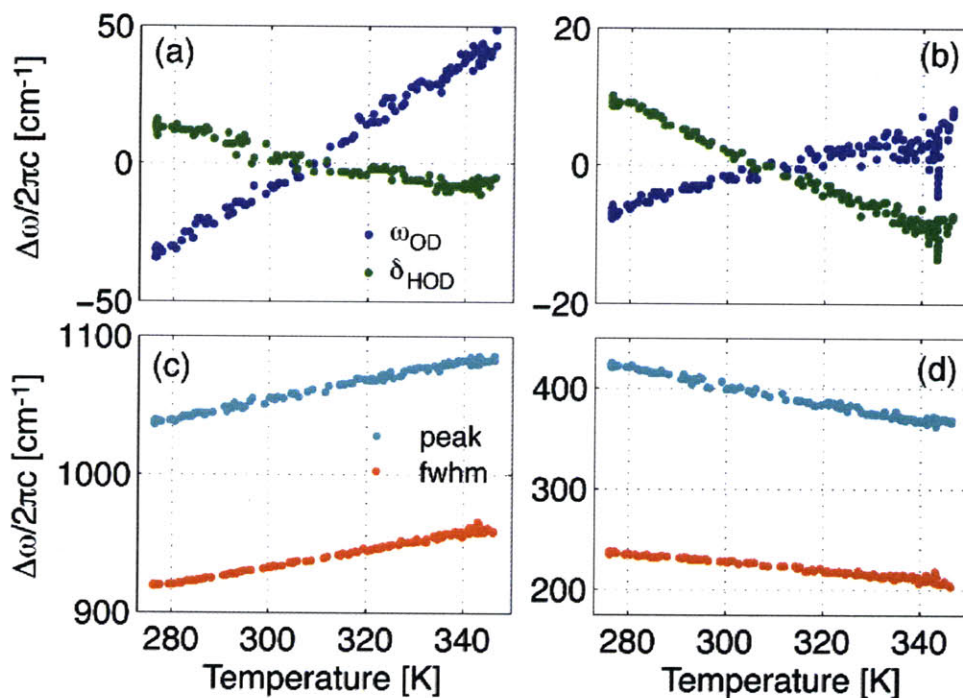


Figure 4-6: (a) Change in peak frequency with temperature for ω_{OD} (blue) and δ_{HOD} (green) relative to the value at 308 K (2514 and 1454 cm^{-1} , respectively). (b) Change in line width (FWHM) relative to the value at 308 K (166 and 83 cm^{-1} , respectively). Difference in wavenumbers between (c) ω_{OD} and δ_{HOD} and (d) $2\delta_{HOD}$ and ω_{OD} at the peak of each transition (cyan) and closest gap between the FWHM (red).

we show the energy gap between ω_{OD} and the overtone of δ_{HOD} ($2\delta_{HOD}$) at the peak (cyan) and FWHM (red; red side of $2\delta_{HOD}$ minus the blue side of ω_{OD}) assuming the anharmonicity is zero and the line width is the same for the fundamental and overtone of the bend, which are most likely not valid assumptions. Nonetheless, the energy gap narrows from 422 cm^{-1} (236 cm^{-1}) to 363 cm^{-1} (209 cm^{-1}) between 277 to 348 K at the peak (FWHM) of the two transitions. Note that 209 cm^{-1} is less than kT at 348 K. The change with temperature at the peak is quite linear although the change at FWHM is slightly quadratic and the overall change is $\sim 14\%$ and $\sim 11\%$ at the peak and FWHM, respectively.

If the OD stretch decays to the closest intramolecular mode that is lower in energy one may expect a linear increase in $T_{1,OD}$ with increased temperature since the energy gap between ω_{OD} and δ_{HOD} linearly increases with temperature. However, although

Temperature Dependence	
Peak, ω_{OD}	$0.5199 \text{ cm}^{-1}/\text{K} \times \text{T}[\text{K}] + 2354 \text{ cm}^{-1}$
FWHM, ω_{OD}	$1.601 \times 10^{-3} \text{ cm}^{-1}/\text{K}^2 \times \text{T}^2[\text{K}^2] + 1.142 \text{ cm}^{-1}/\text{K} \times \text{T}[\text{K}] - 33.69 \text{ cm}^{-1}$
Peak, δ_{HOD}	$-0.1497 \text{ cm}^{-1}/\text{K} \times \text{T}[\text{K}] + 1502 \text{ cm}^{-1}$
FWHM, δ_{HOD}	$-0.2882 \text{ cm}^{-1}/\text{K} \times \text{T}[\text{K}] + 171.9 \text{ cm}^{-1}$
Peak, $\omega-\delta$	$0.6696 \text{ cm}^{-1}/\text{K} \times \text{T}[\text{K}] + 852.9 \text{ cm}^{-1}$
FWHM, $\omega-\delta$	$0.6256 \text{ cm}^{-1}/\text{K} \times \text{T}[\text{K}] + 745.7 \text{ cm}^{-1}$
Peak, $2\delta-\omega$	$-0.8193 \text{ cm}^{-1}/\text{K} \times \text{T}[\text{K}] + 648.6 \text{ cm}^{-1}$
FWHM, $2\delta-\omega$	$-0.3879 \text{ cm}^{-1}/\text{K} \times \text{T}[\text{K}] + 343.8 \text{ cm}^{-1}$

Table 4.1: Temperature dependencies of the line shape parameters of ω_{OD} and δ_{HOD} and the energy gap between the stretch and fundamental and overtone of the bend

the energy gap between ω_{OD} and δ_{HOD} increases with increasing temperature, the energy gap between the ω_{OD} and the $2\delta_{HOD}$ decreases. Also, the energy gap between ω_{OD} and $2\delta_{HOD}$ is $\sim 2kT$ or less over the entire temperature range. Therefore, the lifetime may show a non-trivial dependence with temperature or even decrease with increased temperature if relaxation to the overtone of the bend is the dominant pathway.

4.3.2 Temperature Dependent Dispersed Pump Probes

In Figure 5-1 we show the linear absorption of HOD in H₂O at five temperatures with (a) and without (b) the background H₂O subtracted. A 5% solution of D₂O in H₂O was held in a home-built brass sample cell between 1 mm CaF₂ windows with a 6 μm teflon spacer. The temperature of the sample cell was controlled with a water-cooled chiller. The condensed phase spectra red shifts by $\sim 200 \text{ cm}^{-1}$ from the gas phase (2723.68 cm^{-1} [159]) due to hydrogen bonding. The $\sim 160 \text{ cm}^{-1}$ line width (FWHM) primarily reflects a distribution of hydrogen bond strengths [155]. From 278 to 345 K the peak blue shifts from 2499 to 2534 cm^{-1} ($0.53 \text{ cm}^{-1}/\text{K}$), indicating an increase in hydrogen bond fluctuations, and the FWHM broadens from 159 to 180 cm^{-1} . However, the total area decreases with increasing temperature due to the non-Condon effect [156, 7]. In the same temperature range the HOD bend, which can be seen in Figure 5-1b, narrows and red-shifts from 1460 to 1450 cm^{-1} .

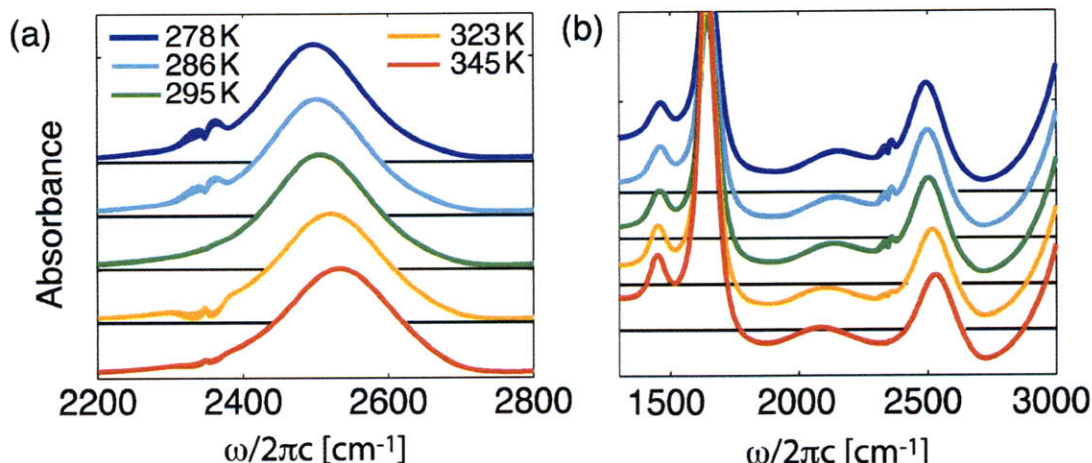


Figure 4-7: Temperature-dependent linear absorption measurements of dilute HOD in H₂O with (a) and without (b) the solvent H₂O subtracted. The spectra are offset along the absorbance axis.

Transient absorption measurements at the five temperatures shown in Figure 5-1 are shown in Figure 4-8. Experimental conditions will be described in detail in the next chapter. Briefly, the mid-infrared pulses were centered at $\sim 2520 \text{ cm}^{-1}$, the pulse width was $\sim 230 \text{ cm}^{-1}$ (FWHM), and the pulse duration was $\sim 80 \text{ fs}$. The transient absorption measurements are collected in the S_{zzzz} and S_{zzyy} polarization geometries and the magic angle signal is constructed as: $S_{iso} = (S_{zzzz} + 2S_{zzyy})/3$. Effects from the TSGS (discussed in the next section) are apparent within experimental time window ($\sim 3.65 \text{ ps}$). As the delay between the pump and probe increases, the bleach shifts towards lower frequency and a negative feature grows in above the bleach. The absorption from atmospheric CO₂ at ~ 2320 to 2360 cm^{-1} significantly decreases the signal from the $\nu=2 \leftarrow 1$ transition. The DPPs at the five temperature appear quite similar beyond the expected shift to higher frequency with increased temperature. Slices at the frequency with maximum intensity, normalized to the value at $t = 200 \text{ fs}$, are shown in the last subplot in Figure 4-8. The transient absorption appears quite similar between the five temperatures, with a possible slight increase in $T_{1,OD}$ with increasing temperature. The thermally shifted ground state (TSGS) must be accounted for, however, before $T_{1,OD}$ can be determined.

Bakker and co-workers have reported the temperature dependent transient ab-

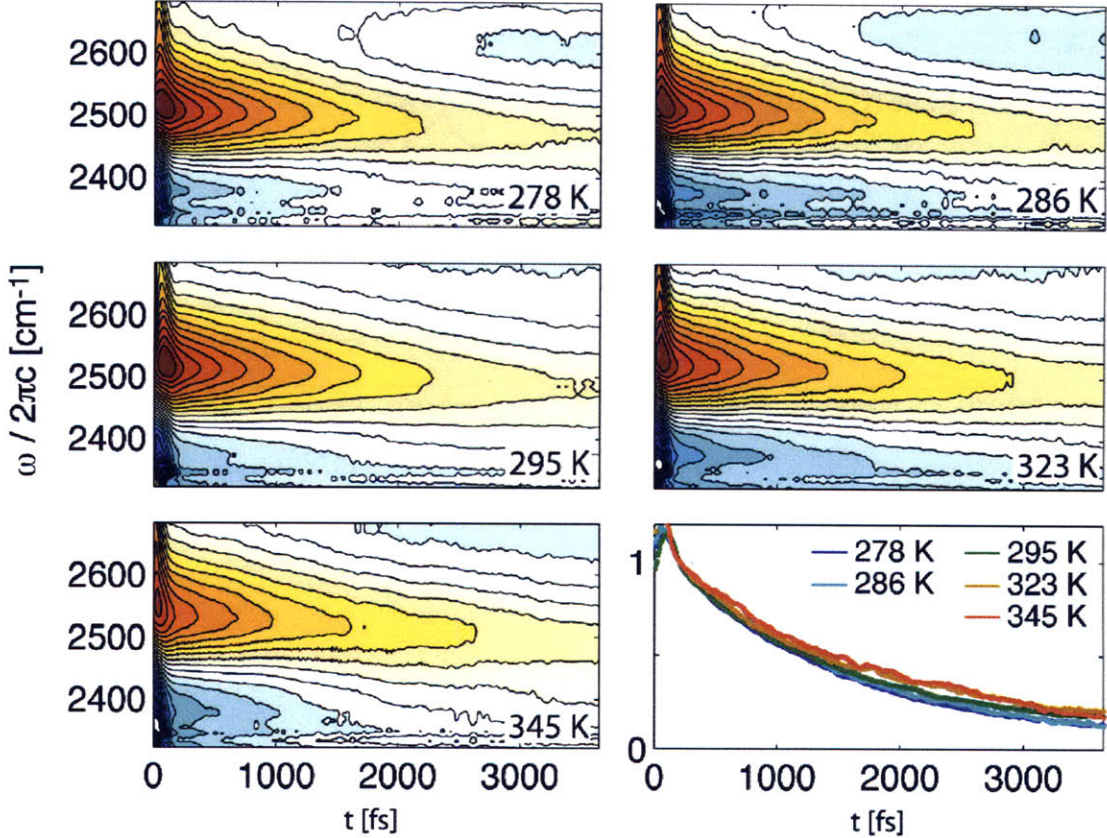


Figure 4-8: Transient absorption measurements of HOD in H₂O at 278, 286, 295, 323, and 345 K and slices in frequency with maximum intensity at each of the five temperatures.

sorption of ω_{OD} in isotopically dilute water [100]. To determine $T_{1,OD}$ they used a fit model that includes decay from $\nu=1$ to an intermediate level, which they suggest is the fundamental of the HOD bend, before relaxation to the low frequency modes [120]. The transient absorption is written as:

$$\Delta\alpha(\omega, t) = \Delta\alpha_{end}(\omega) \left[\frac{T^*}{T_1 - T^*} e^{-t/T^*} - \frac{T_1}{T_1 - T^*} e^{-t/T_1} + 1 \right] + N_1(0) \Delta\alpha_{init}(\omega) e^{-t/T_1} \quad (4.2)$$

where $\Delta\alpha_{init}(\omega)$ and $\Delta\alpha_{end}(\omega)$ denote the spectral contribution from the initial excitation, which includes $\nu=1 \leftarrow 0$ and $\nu=2 \leftarrow 1$, and TSGS, respectively. The shape of the two spectral components are independent of time delay. T_1 is the vibrational

lifetime of ω_{OD} , T^* is the lifetime of the intermediate state, and $N_1(0)$ denotes the initial population in the $\nu=1$ level. In Figure 4-9 we show the result of applying the fit model at 295 K starting at $t = 200$ fs. The model (green) fits the data (blue) very well. In Figure 4-9a we show a frequency slice at $\omega = 2522$ cm^{-1} , which is in the $\nu=1 \leftarrow 0$ region. At early delays, $\Delta\alpha_{init}$ is the dominant contribution to $\Delta\alpha$. As the delay is increased, $\Delta\alpha_{end}$ grows in causing the trace to decay to a positive offset at this frequency. In Figure 4-9c we show a frequency slice at $\omega = 2380$ cm^{-1} , which is in the $\nu=2 \leftarrow 1$ region. Although the trace begins negative, it crosses to positive value at ~ 2 ps due to the growth of the TSGS. In Figure 4-9b and d we show slices in time at $t = 1$ ps and 3.65 ps, respectively. At 1 ps, $\Delta\alpha_{init}$ is dominant but at 3.65 ps, $\Delta\alpha_{end}$ is the dominant contribution. Again, in this fit model the spectral shape of $\Delta\alpha_{init}$ and $\Delta\alpha_{end}$ are independent of delay; only the relative contribution of the two spectral components is time dependent.

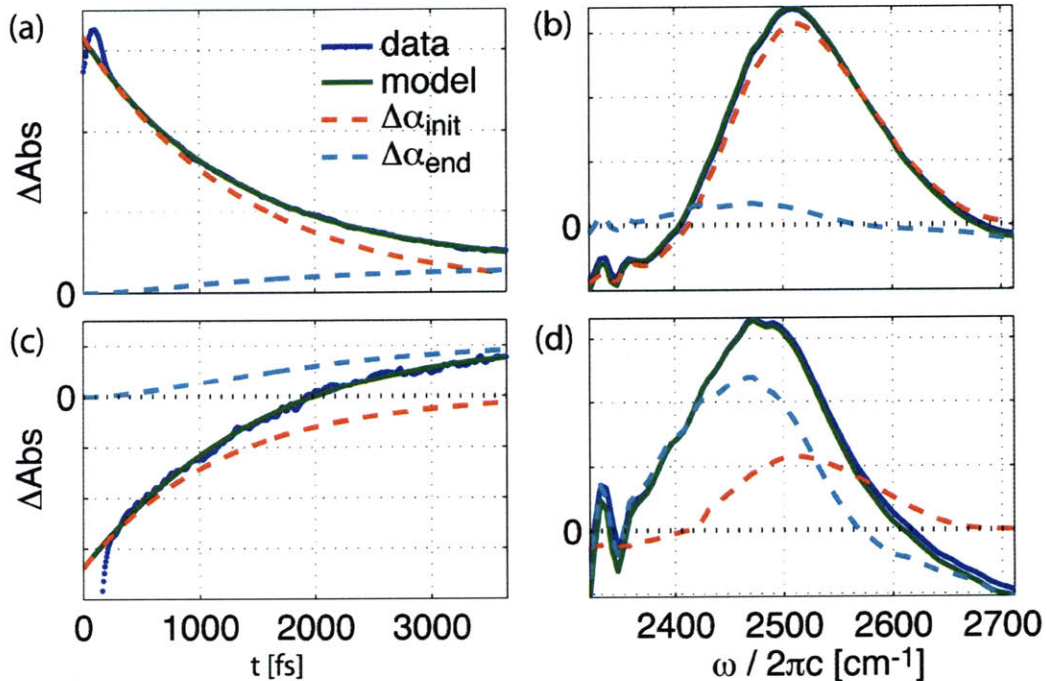


Figure 4-9: Experimental transient absorption at 295 K (blue) with the results from the fit (green) and $\Delta\alpha_{init}$ (red dashed) and $\Delta\alpha_{end}$ (cyan dashed) contributions shown separately at (a) $\omega = 2522$ cm^{-1} , (b) $\omega = 2380$ cm^{-1} , (c) $t = 1$ ps, and (d) $t = 3.65$ ps.

In Figure 4-10 we show both T_1 and T^* from the fit model for the five temperatures in this study. The uncertainty is ± 75 fs. Tielrooij and Bakker [100] measured the temperature-dependent vibrational lifetime and found it increased from approximately 1.7 to 2.2 ps from 274 to 343 K. In the current study we find the vibrational lifetime increases from 1.4 to 2.0 ps from 278 to 345 K. These lifetimes are somewhat faster than those of Tielrooij but agree with the lifetime first reported by Fayer and co-workers [94]. Also, the intermediate lifetimes in the current study increase relatively slightly from 450 to 590 fs across the temperature range compared to the decrease from ~ 900 to 350 fs from 274 to 343 K in the study performed by Tielrooij and Bakker [100]. In both studies the isotropic pump-probe is constructed from the S_{zzzz} and S_{zzyy} transient absorption measurements acquired with the pump 45° relative to the probe. An important difference is that the measurements in the former study are taken to $t = 10+$ ps but only to $t = 3.65$ ps in the current study. Measuring to longer delay times is ideal. An interesting similarity between the two measurements, however, is that the vibrational lifetime of the OD stretch is largely unchanged from the lowest temperature to room temperature. We found that fitting the integrated isotropic transient absorption assuming that the TSGS grows in at the same rate as the decay of the excited state resulted in similarly decent fits within our experimental time window. The resulting lifetimes were slightly shorter but followed the same trend. This observation does not rule out that vibrational energy decays through an intermediate state, it only implies that decay from the intermediate is very fast. Given this, we will not discuss T^* further.

Although the energy gap between ω_{OD} and the fundamental and overtone of the bend show, to first approximation, a linear dependence with temperature, the lifetime has a non-trivial temperature dependence. $T_{1,OD}$ remains largely the same from 278 K to 295 K, then increases by $\sim 40\%$ by 345 K. The overall increase in lifetime above room temperature shows that relaxation to the fundamental of the bend is an important pathway. However, the similar lifetimes at room temperature and below suggests that multiple relaxation pathways with different temperature dependencies may be in competition. The theoretical study, which was performed at room temper-

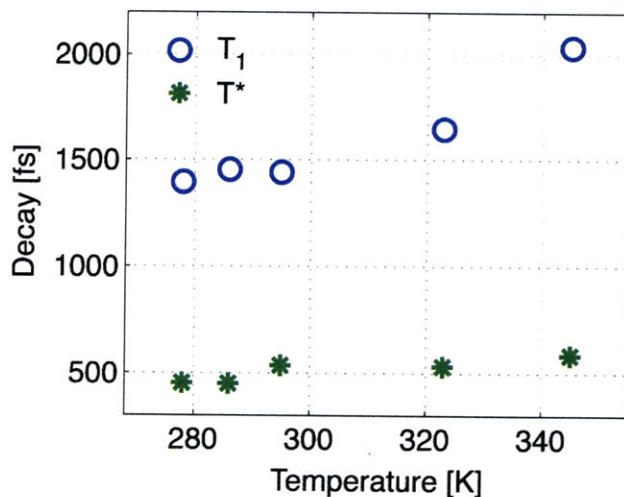


Figure 4-10: T_1 and T^* for ω_{OD} of HOD in H_2O with temperature from the fit model.

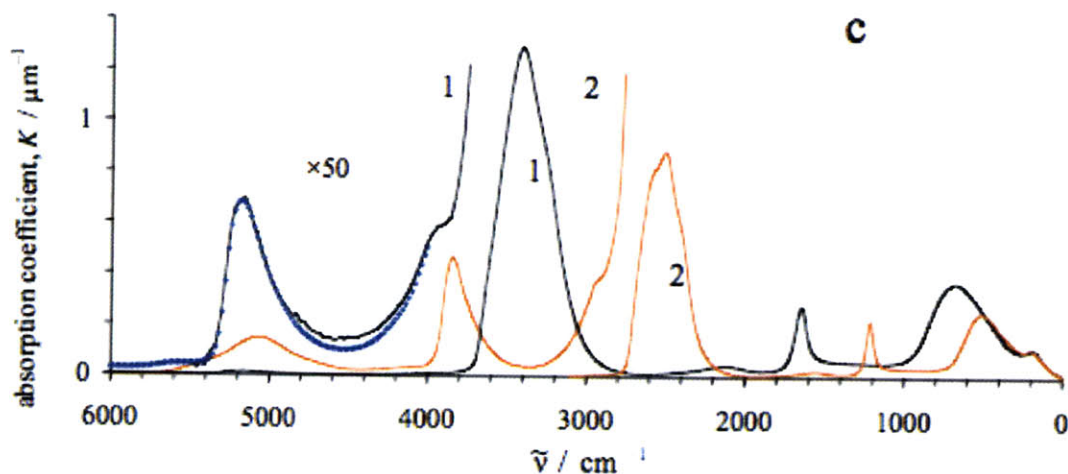


Figure 4-11: Linear absorption coefficient, K ($=4\pi\nu k$), of H_2O (1, black) and D_2O (2, red) from [2]. Copyright 2009 American Institute of Physics.

ature, considered the rate constants for energy transfer from ω_{OD} to δ_{HOD} , δ_{H_2O} , and ω_{H_2O} with excess energy taken up or contributed by the rotations and translations [106]; but it did not consider a pathway through $2\delta_{HOD}$. The energy gap between ω_{OD} and δ_{HOD} is more than 2x greater than ω_{OD} and $2\delta_{HOD}$ at all temperatures and although the energy gap between ω_{OD} and δ_{HOD} increases by $\sim 5\%$, it decreases by $\sim 14\%$ (or $\sim 11\%$ at FWHM) between ω_{OD} and $2\delta_{HOD}$. The broad librational band of H_2O , which is peaked at $\sim 680\text{ cm}^{-1}$, or a combination of low frequency modes are

capable of contributing the excess energy. In Figure 4-11 we show the linear absorption spectrum of H₂O showing the continuous absorption from 0 to 2000+ cm⁻¹. The overtone of the bend is just one suggestion for a competitive pathway that may cause the non-trivial temperature dependence. An experimental study monitoring the deposition of energy into the HOD bend upon excitation of the OD stretch at multiple temperatures and a temperature dependent theoretical study of the vibrational lifetime would be helpful in determining if there is a change in dominant mechanism with temperature.

4.4 Thermally Shifted Ground State in Pump-Probe Measurements

Non-equilibrium heating upon vibrational relaxation in water was first observed as a blue-shift in frequency and decrease in absorption cross section of the OH stretch in pump-probe (PP) experiments of HOD in D₂O [175]. Energy deposited in the stretch decays and eventually populates the low frequency modes of the originally excited molecule and surrounding solvent. The excitation of these modes appears as heating since the fluctuations of the hydrogen bond network increase, which decreases the degree of hydrogen bonding. The "thermally shifted ground state" (TSGS) prevents the equilibrium ground state hole from refilling, which gives rise to a bleach that persists until thermal diffusion out of the spectral window. Since the signal arising from the TSGS and equilibrium ground state are out of phase, at waiting times well past the vibrational lifetime the dispersed pump-probe resembles a difference spectrum between linear spectra separated by ~ 1 K [72].

In Figure 4-12 we explore the effect of the TSGS on transient absorption measurements. The dispersed pump probes are calculated for the OD stretch of HOD in H₂O with a response function formalism we will describe in detail in the next chapter. In the current calculation the frequency correlation function is real, which excludes any effect due to the vibrational Stokes shift. In the calculation, the peak of the funda-

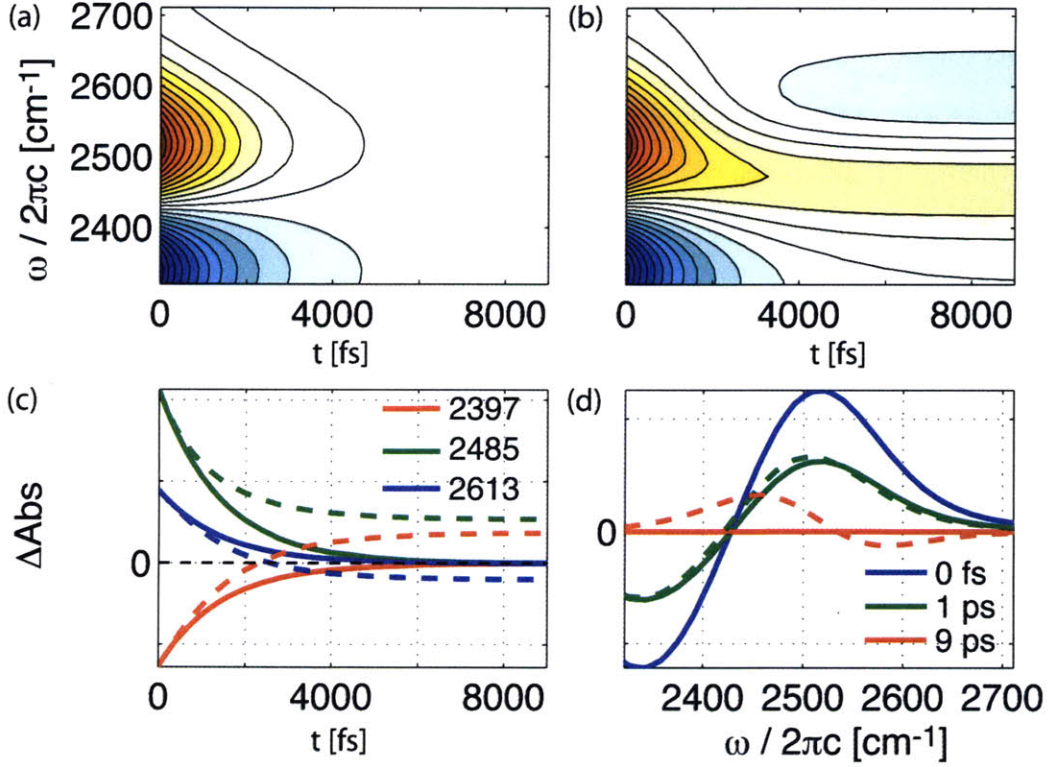


Figure 4-12: DPP of ω_{OD} without (a) and with (b) the TSGS. Slices in (c) frequency and time (d) without (solid) and with (dashed) the TSGS

mental is 2508 cm⁻¹, the line width is 166 cm⁻¹ (FWHM), and the anharmonicity, $\omega_{10}-\omega_{21}=\Delta$, is 162 cm⁻¹ [77]. The lifetime of the initially excited state is $T_1 \approx 1.45$ ps and the TSGS contribution grows in as a bi-exponential with the time scales T_1 and $T^* \approx 540$ fs, where T^* is the lifetime of an intermediate state (see Equation 4.2). In Figure 4-12a we show the dispersed pump-probe without including the TSGS. The positive amplitude is from the ground state bleach and stimulated emission of the $\nu=1 \leftarrow 0$ transition. The anharmonically shifted negative amplitude is due to the induced absorption of the $\nu=2 \leftarrow 1$ transition. We include the TSGS for the DPP calculation shown in Figure 4-12b. The bleach persists past the vibrational lifetime and negative amplitude appears above the bleach. In Figure 4-12c and Figure 4-12d we compare slices in frequency and time, respectively, between the calculated DPPs without (solid) and with (dashed) the TSGS. Figure 4-12c shows that if the TSGS is not included all three frequency slices decay to zero. However, when the TSGS is

included the frequency slices that begin negative can decay to a positive offset (red) and vice versa (blue). Figure 4-12d shows that if the TSGS is not included the zero crossing between the $\nu=1\leftarrow 0$ and $\nu=2\leftarrow 1$ peaks does not shift with waiting time. At $t=0$ fs there is no difference when the TSGS is included in the calculation (the dashed blue lies on top of solid blue). However, at longer waiting times the signal persists past the vibrational lifetime, positive amplitude shifts towards lower frequency, and the DPP dips to negative values on the high-frequency side of the line width.

4.5 Conclusion

In this chapter we studied the vibrational relaxation of isotopically dilute water. At room temperature, the lifetime of ω_{OH} is 700-740 fs [93, 98] and the lifetime of ω_{OD} is 1.45 to 1.7 ps [98, 95, 100]. We measured the dispersed pump probe of ω_{OT} in the zzzz polarization geometry and found a decay time of ~ 850 fs. Therefore we find $T_{1,OD} > T_{1,OT} > T_{1,OH}$ which agrees with the proposed mechanism for vibrational relaxation, in which the stretch decays through the closest intramolecular mode that is lower in energy, since $\omega_{OD}-\delta_{HOD}$ (~ 1050 cm^{-1}) $>$ $\omega_{OT}-\delta_{HOT}$ (~ 740 cm^{-1}) $>$ $\omega_{OH}-2\delta_{HOD}$ (~ 500 cm^{-1}). We also presented the temperature dependence of the linear absorption of HOD in H_2O and $T_{1,OD}$ as a step in testing the temperature dependence of the proposed mechanism. We found that although the linear absorption changes monotonically with temperature, $T_{1,OD}$ shows a non-trivial behavior. At room temperature and below, the lifetime is the same within error and then it increases above room temperature. Since the energy gap between ω_{OD} and δ_{HOD} increases with increasing temperature the behavior above room temperature suggests that relaxation to the fundamental of the bend is an important pathway. However the behavior at room temperature and below suggests that there may be additional competing pathways that have different dependencies on temperature. Broadband experiments and further calculations are still necessary to definitely elucidate the vibrational relaxation pathway in isotopically dilute water.

Chapter 5

Hydrogen Bond Rearrangements in Water

5.1 Introduction

Despite years of extensive study and continuous improvements in experimental and theoretical methods, the femtosecond-to-picosecond dynamics that describe changes to the hydrogen bonding structure of water continue to be difficult to describe. Being a dense medium, the liquid intermolecular dynamics involve the collective motion of large numbers of molecules, for which translational and rotational degrees of freedom are strongly intertwined. This complexity is heightened in the case of the water due to its locally structured hydrogen bond network. The details of structural relaxation in water have been studied by molecular dynamics (MD) simulations beginning with the original work of Rahman and Stillinger [176]. Intermolecular motions and the interconversion between structures have been analyzed in a number of ways including through groups, chains, polyhedra, clathrate structures, inherent structures, and instantaneous normal modes [177, 28]. No correlations between local structural variables, such as hydrogen bond participation, exist between configurational states separated by more than a few picoseconds [13]. Therefore, the dynamics of structural relaxation processes are not readily described in terms of structure on molecular length scales.

Recent experimental and theoretical studies of water have provided new perspectives on the local dynamics of hydrogen bonding, describing in detail how the hydrogen bond distances and angular motions change during the course of collective structural reorganizations [71, 1, 178]. With ultrafast infrared spectroscopy and MD simulations Eaves et al. observed that water molecules in broken or strained hydrogen bond configurations return to a stable hydrogen bond within the fastest intermolecular motions suggesting that hydrogen bond switching is a concerted process [71]. Laage and Hynes performed MD simulations and found the dominant mechanism of reorientation is through large amplitude angular jumps with a contribution from diffusive reorientation of the intermolecular O...O framework [1]. In these studies, molecular motions that have been identified as important for reorganization include concerted hydrogen bond switching, large angle jumps, translation within the first and second solvation shells, and diffusive reorientation of a hydrogen bonded pair of water molecules.

It is important to recognize that local geometric variables are just different parameters that capture the motion along a collective reaction coordinate. Different motions may be projected from the collective dynamics and certain coordinates may project more favorably than others. However, long time relaxation phenomena of internal variables should all decay in a correlated fashion [68]. Absolute time scales from different experiments are difficult to compare since the observables are uniquely sensitive to relaxation, yet the temperature dependence should be identical if rearrangements occur along a collective reaction coordinate.

In this chapter we report on the temperature dependence of spectral diffusion and reorientation of the OD stretch of dilute HOD in H₂O to determine if the relaxation of these different measures of water structural change are correlated. In order to quantify the temperature-dependent time scales we self-consistently model the pump-probe anisotropy, vibrational relaxation, and spectral diffusion with a response function formalism that includes the solvent H₂O stretch and combination band and the thermally shifted ground state (TSGS) of all three modes. We find a similar barrier height for both spectral diffusion and reorientation along with a number of

other measurements that are sensitive to collective and single molecule relaxation of water. We also observe a similar behavior for spectral diffusion and reorientation calculated with MD simulations with the SPC/E [31] and SPC/FQ [88] model of water. Finally, we find the frequency dependence of the pump-probe and 2D anisotropy suggests that water molecules in broken or strained hydrogen bond configurations reorient more quickly than band center to form a stable hydrogen bond.

5.2 Experimental Methods

Temperature-dependent Fourier transform infrared (FTIR) absorption spectra of dilute HOD in H₂O were collected at 1 cm⁻¹ resolution with a Nicolet 380 FTIR spectrometer from Thermo-Electron Corporation. The sample was contained between 1 mm thick CaF₂ windows with a path length of 6 μm set by a Teflon spacer for both linear and nonlinear measurements. The temperature of the home built brass sample cell was controlled with a water-cooled chiller, Neslab RTE-7.

Sub-100 fs infrared pulses were generated with a home-built system consisting of an amplified Ti:sapphire pulse (800 nm, 1 kHz, 1 W) pumping an optical parametric amplifier (OPA). The system was described in detail in Chapter 2. Here we will briefly mention the salient features. A small portion of 800 nm (~1%) creates white light in a sapphire plate. After the white light seed and a portion of the 800 nm (~9%) pass through a 3 mm β-Barium Borate (BBO) crystal, the idler (2 μm) seeds a second pass through the BBO with the remaining 800 nm. Mid-infrared light is created by difference frequency generation of the signal (1.33 μm) and idler in a 0.5 mm AgGaS₂ crystal. The spectrum was centered at 2500 cm⁻¹ with a FWHM of ~230 cm⁻¹. Although the infrared pulse was contained in a purged box there was still residual CO₂ creating a dip in the spectrum. The pulses were compressed to ~70 fs for the 2D measurements and ~80 fs for the pump-probe (PP) measurements. Cross phase modulation (XPM) (described in Chapter 2) obscures spectral information within approximately two times the pulse width. Pulse delays were controlled with a pair of anti-reflection (AR) coated ZnSe wedges mounted to stages that translate the wedge

face perpendicular to the beam path. The ZnSe wedges are 6 cm in length and have a 1.2° wedge.

We measured temperature-dependent two-dimensional infrared (2D IR) surfaces in the zzzz polarization geometry to characterize spectral diffusion. We used KBr beam splitters to split the mid-infrared pulse into three parts to acquire surfaces in the pump-probe geometry in which a collinear pulse pair creates a vibrational excitation, and the third pulse acts as the probe and local oscillator [132]. The measured signal is the real part of the rephasing plus non-rephasing pathways [140]. The τ_1 -axis was created by step-scanning the non-chopped pump beam in 2 fs steps to 600 fs. Scanning the non-chopped pump beam removes the contribution to the total signal of the τ_1 -dependent PP between the probe and one of the pump beams. The PP between the probe and the other pump beam is independent of τ_1 and is, therefore, removed by numerical Fourier transform to create the excitation, or ω_1 , dimension. The probe beam is spectrally dispersed after the sample with a 75-grooves/mm grating onto a 64-channel liquid nitrogen cooled MCT array. The $\sim 6 \text{ cm}^{-1}$ resolution in ω_3 gives a detection axis with 400 cm^{-1} bandwidth. In addition to the acquisition of the 2D signal, the interferometric autocorrelation and interference fringes for stage calibration are simultaneously measured from the replica of the collinear pump pair from the backside of the recombining beam splitter [132]. A small reflection is directed into a room temperature MCT to measure the interference between the pulses that constrains the relative pulse timing to the step size. The remainder is passed through a monochromator set to 2500 cm^{-1} with a resolution of 1 cm^{-1} , and the interference is collected with a single channel MCT detector and Fourier transformed to determine the correction to the τ_1 -axis [132].

We used polarization-selective transient absorption to study temperature-dependent reorientational dynamics and vibrational relaxation. In the pump-probe geometry a pump-probe can be measured simply by blocking the non-chopped pump beam. A MgF_2 $\lambda/2$ -waveplate (Alphas) is placed in the pump path to rotate the polarization 45° relative to the probe. The polarization of the pump and probe were selected with ZnSe wire-grid polarizers (Molelectron). There are two polarizers after the sample.

The analyzing polarizer is rotated between parallel (zzzz) and perpendicular (zzyy) relative to the pump. The second polarizer is set parallel to the probe such that the polarization-sensitive monochromator grating sees the same polarization for zzzz and zzyy measurements. The pump-probe measurements were acquired by fast scanning the delay between the pump and probe and averaging the scans. The isotropic signal, which is free of rotations and therefore measures vibrational relaxation, is constructed from the zzzz and zzyy measurements as:

$$S_{iso}(\tau_2) = \frac{S_{zzzz}(\tau_2) + 2S_{zzyy}(\tau_2)}{3}. \quad (5.1)$$

The anisotropy, which measures reorientational dynamics, is constructed as:

$$C_R(\tau_2) = \frac{S_{zzzz}(\tau_2) - S_{zzyy}(\tau_2)}{S_{zzzz}(\tau_2) + 2S_{zzyy}(\tau_2)}. \quad (5.2)$$

5.3 Experimental Results

Temperature-dependent linear absorption of the OD stretch of HOD in H₂O at the five temperatures in this study (278, 286, 295, 323, and 345 K) with the background H₂O subtracted are shown in Figure 5-1a and without subtraction in Figure 5-1b. The condensed phase spectra red shifts by ~ 215 cm⁻¹ from the gas phase (2723.68 cm⁻¹ [159]) due to hydrogen bonding. The ~ 160 cm⁻¹ full-width half maximum (FWHM) primarily reflects a distribution of hydrogen bond strengths [155]. From 278 to 345 K the peak blue shifts from 2499 to 2534 cm⁻¹ (0.53 cm⁻¹/K), indicating an increase in hydrogen bond fluctuations, and the FWHM broadens from 159 to 180 cm⁻¹. However, the total area decreases with increasing temperature due to the non-Condon effect [156, 7]. In the same temperature range the HOD bend, which can be seen in Figure 5-1b, narrows and red shifts from 1460 to 1450 cm⁻¹. The model calculations, which will be described below, include the combination band ($\nu_L + \delta$) and stretch of the H₂O bath. From 278 to 345 K the H₂O stretch red shifts from 3389 to 3433 cm⁻¹ (0.66 cm⁻¹/K) and the combination band blue shifts from 2134 to 2075 cm⁻¹ with a weak quadratic dependence.

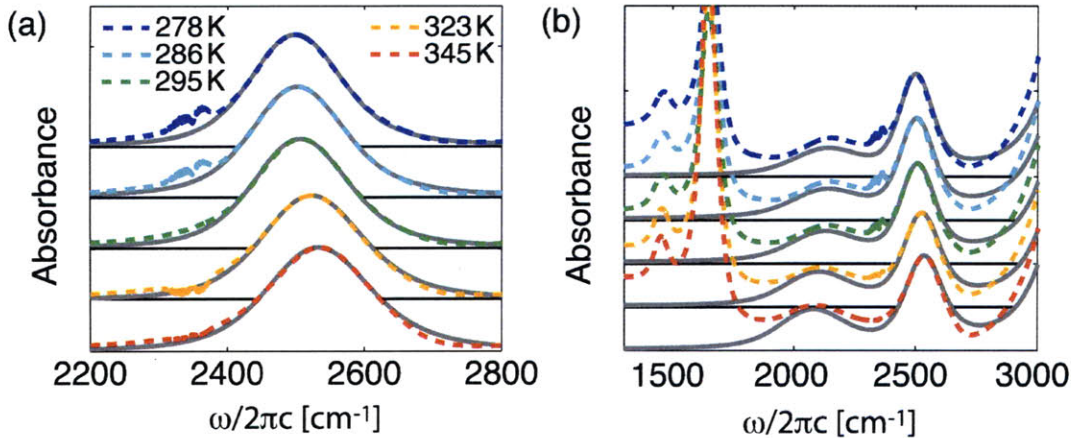


Figure 5-1: Temperature-dependent linear absorption of dilute HOD in H₂O with (a) and without (b) the solvent H₂O subtracted. The traces are offset along the absorbance axis. The fit from our spectral model at each temperature is shown in dark gray.

Isotropic transient absorption at each of the five temperatures is shown in Figure 5-2a. The temperature dependence of the lifetime is discussed in detail in Chapter 4. However, the important details will be mentioned here. The isotropic PP is calculated from the *zzzz* and *zzyy* transient absorption measurements with Equation 5.1. The dispersed PP is integrated over 75% of the maximum in frequency (of a slice taken at $\tau_2 = 200$ fs to avoid XPM) to take into account the change in center frequency with temperature. Thermalization of the low frequency modes occurs upon vibrational relaxation of the OD stretch. This causes a blue shift in the frequency of the stretch that prevents refilling of the ground state bleach. At long waiting times the thermally shifted ground state (TSGS) appears as a difference spectrum between linear spectra separated by ~ 1 K [72]. The TSGS has been included in a fit model by Rezus and Bakker [120] that also includes relaxation through an intermediate state. The fit model does not consider effects from the vibrational Stokes shift. The experimental vibrational lifetimes found by applying the fit model starting at $\tau_2 = 400$ fs for each of the five temperatures are shown in Figure 5-3.

Normalized temperature-dependent pump-probe anisotropies are shown in Figure 5-2b. Before calculating the pump-probe anisotropy, the bi-exponential growth

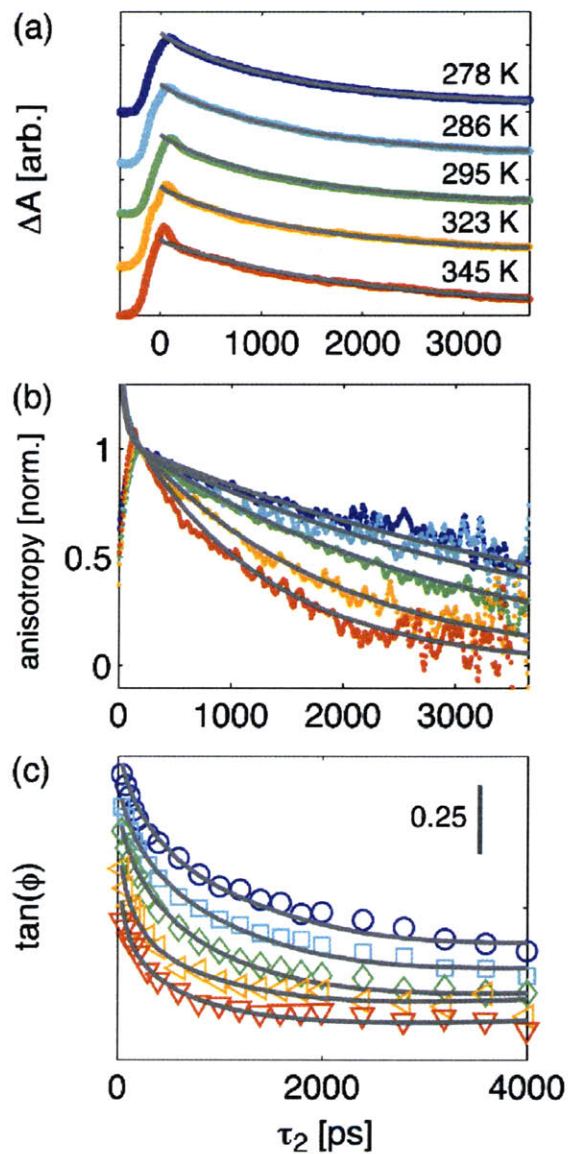


Figure 5-2: (a) Isotropic transient absorption (offset) and (b) anisotropy (normalized at 200 fs) of dilute HOD in H₂O at each of the five experimental temperatures plotted as a function of delay time between the pump and probe. The best fit from our spectral model normalized at 200 fs for both (a) and (b) is shown in dark gray. (c) Phase line slope over $\omega_1 = \omega_3 = 2470$ to 2530 cm^{-1} determined from the temperature and waiting time dependent 2D IR with the best fit from our model shown in gray. The experimental phase line slope and fits are offset by 0.075 per temperature as the temperature is decreased from 345 K.

of the TSGS, determined by fitting the isotropic PP, is subtracted from the zzzz and zzyy transient absorption measurements. This approach assumes the TSGS does not depend on the polarization, which has been shown to be a reasonable assumption for the OD stretch [119]. The dispersed anisotropies are integrated over a frequency range set by the maximum in frequency of a slice in the isotropic signal at $\tau_2 = 200$ fs. Although XPM obscures spectral information within the first ~ 150 fs, we fit the anisotropies with a bi-exponential beginning at 200 fs. A bi-exponential decay has previously been observed for the anisotropy decay of the OH stretch of HOD in D₂O measured with shorter pulses [93]. The inertial decay is set to 50 fs for all temperatures, the inertial time scale measured for the OH stretch of HOD in D₂O at room temperature [93], and the initial value is set to 0.4. We do not observe a clear trend between the inertial amplitude and temperature in the bi-exponential fits. MD simulations predict the inertial amplitude will increase with increasing temperature but experiments have reported that there is a change in frequency dependence of the inertial component with temperature, which complicates a straightforward relationship [179, 121]. The long time decay of the anisotropy, shown in Figure 5-3, becomes faster with increasing temperature. We found very similar values for the long-time decay when fitting a single exponential beginning at 200 fs without constraining the initial value.

2D IR surfaces at each of the five temperatures at three waiting times are shown in Figure 5-4. Since multiple vibrational levels are accessible within the bandwidth of our pulse, the 2D surface displays a positive peak from ground state bleach ($\nu=1\leftarrow 0$) and an anharmonically shifted negative peak from excited state absorption ($\nu=2\leftarrow 1$). At early waiting times ($\tau_2 < \tau_C$, where τ_C represents the correlation time), the peaks are diagonally elongated indicating frequency correlation between the first and third time periods. In the top row of Figure 5-4 we show 2D surfaces at $\tau_2 = 160$ fs for each of the five temperatures. Notice at 278 K the pear shape of the positive peak where the anti-diagonal line width is narrow on the red side and relatively broad on the blue side (where red and blue refer to low and high frequencies relative to band center, respectively). The asymmetry across the line width forms the basis of a previous

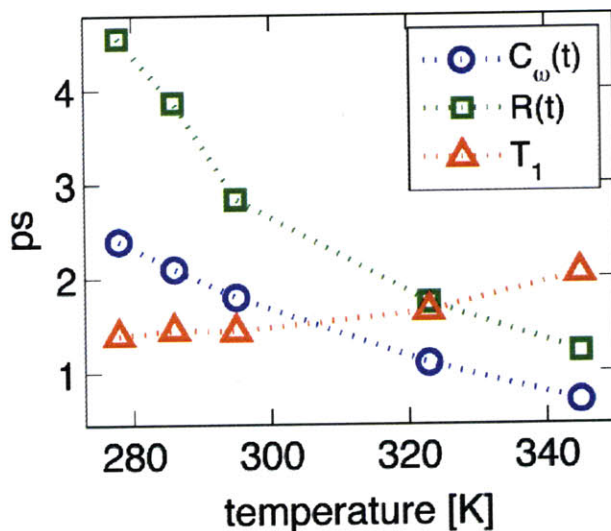


Figure 5-3: Temperature-dependent lifetime, T_1 , (red triangles), picosecond decay of the integrated pump-probe anisotropy (green squares) and picosecond decay of the best fit frequency correlation function from the fit model (blue circles).

publication in which we analyzed the waiting time dependence of the line shape for the OH stretch of dilute HOD in D_2O and found that strained or broken hydrogen bonds exist only fleetingly [71, 73]. Note that as the temperature is increased, but as the waiting time is kept constant, the asymmetry across the line shape decreases and the anti-diagonal line width becomes generally broader.

We also plot the phase representation of the surfaces. We detail how we extract the complex surface from the measured real surface in Chapter 2. At early waiting times the phase lines are tilted toward the diagonal. At $\tau_2 = 400$ fs (second row of Figure 5-4) the frequencies initially excited have more time to diffuse through the line shape. As a result the peaks are more symmetric, or appear more homogeneous, and the phase lines have tilted toward ω_1 at all temperatures. Notice, however, at low temperature the line shape is more inhomogeneous relative to high temperature. At long waiting times ($\tau_2 > \tau_C$), sufficient spectral diffusion occurs during the waiting time such that peaks appear round due to loss of correlation. Also, an additional negative feature appears above the diagonal upon sufficient vibrational relaxation due to the TSGS. In the third row of Figure 5-4 we show the temperature-dependent 2D surfaces at

3.2 ps. Note the surfaces are generally round and there is additional negative feature above the diagonal, particularly visible for the three lowest temperatures, that acts to narrow the positive amplitude along ω_3 . Finally, note that there appears to be a residual inhomogeneity, especially apparent at higher temperatures in the phase representation, on the red side of the spectrum.

We used a number of metrics to characterize the waiting time dependence of spectral diffusion [141], including the dynamic line width [77], slope of the node [180, 72], and the center line slope [181]. The dynamic line width (DLW) is the line width (FWHM) of a slice along ω_1 at the maximum in ω_3 . The DLW is shown at 278, 295, and 345 K for one data set in Figure 5-5. Due to inhomogeneous broadening the FWHM is narrowed when $\tau_2 < \tau_C$ and broadens towards the asymptotic value, set either by the line width of the absorption band or the bandwidth of the pulse, as the waiting time is increased.

The slope of the node between the $\nu=1\leftarrow 0$ and $\nu=2\leftarrow 1$ peaks of the absorptive 2D spectrum is shown in Figure 5-6 at the three temperatures for the same data set. The slope decreases as the waiting time is increased, however, the slope of the node will only be well defined if the $\nu=2\leftarrow 1$ has sufficient amplitude. If the node is ill-defined the slope will be ill-defined, which can be seen in the trace for the highest temperature (345 K).

The center line slope (CLS) for the three temperatures is shown in Figure 5-7. The CLS is similar to the slope of the node except it is the slope of a line connecting the maxima along ω_1 of the $\nu=1\leftarrow 0$ peak. It is an attractive metric in that it can still be used after the $\nu=2\leftarrow 1$ peak has decayed, however, the maximum of the peak is not as well defined as the node, in that it is gradually sloping.

After retrieving the complex correlation spectrum and the rephasing and non-rephasing surfaces on the basis of the Kramers-Kronig assumption (see Chapter 2) we also considered the normalized difference of the amplitude of the rephasing to non-rephasing surfaces, or inhomogeneity index [141, 72], the slope of the imaginary node, and the phase line slope [182]. In Figure 5-8 we show the inhomogeneity index, I , defined as $I = (A_- - A_+) / (A_- + A_+)$, where A_{\pm} is the integral over the non-

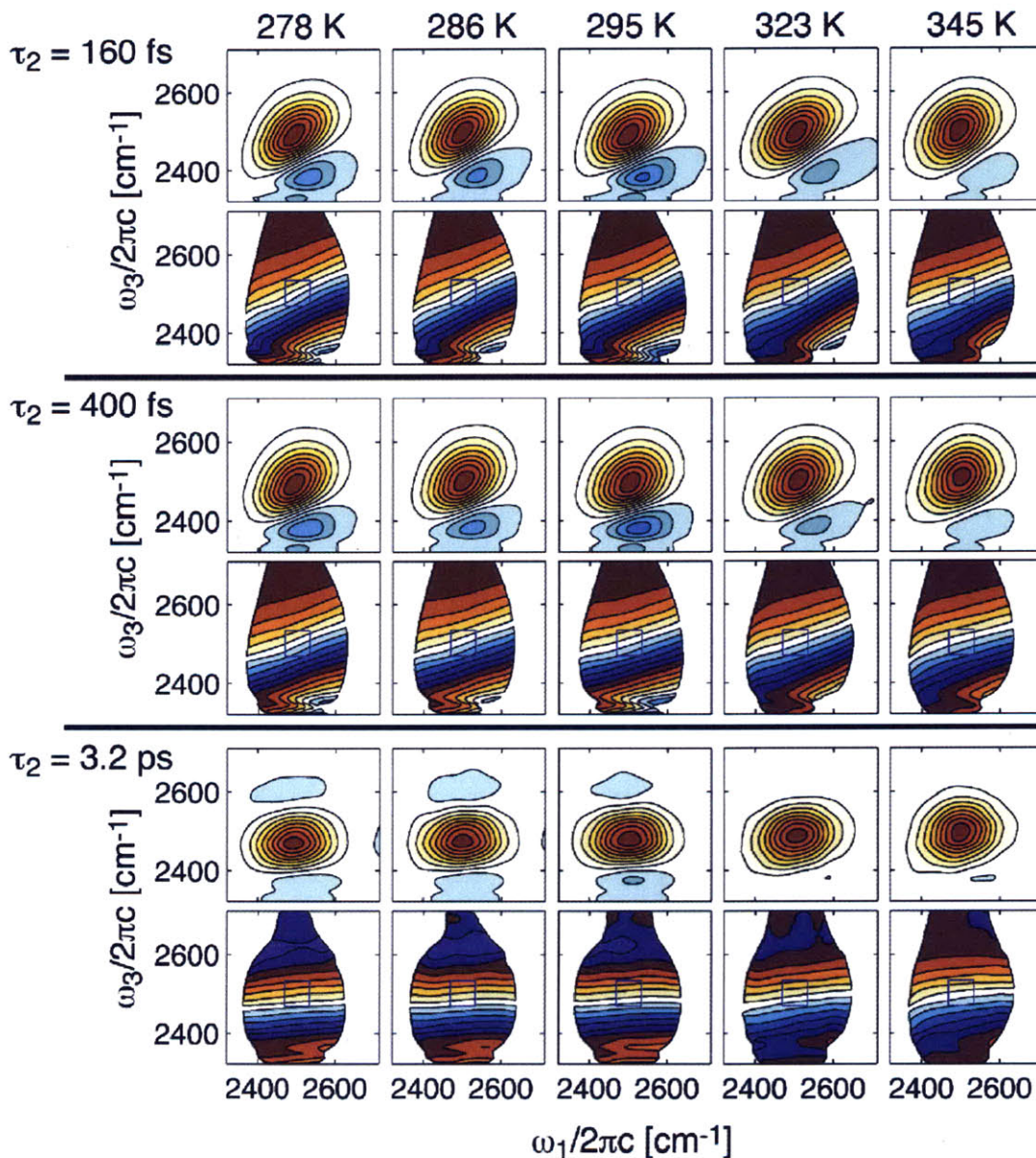


Figure 5-4: Experimental absorptive and phase 2D surfaces of dilute HOD in H₂O at each of the five temperatures at three waiting times: $\tau_2 = 160$ fs (top), 400 fs (middle) and 3.2 ps (bottom). The contours in the absorptive 2DIR spectra are at 12% intervals relative to the maximum. The phase spectra are plotted from $-\pi/2$ to $\pi/2$ and are windowed by 10% of the absolute value spectra.

rephasing and rephasing surfaces, respectively. Frequency memory is reflected in unequal weighting between the rephasing and non-rephasing pathways, with more amplitude in the rephasing pathway. Therefore, as the waiting time is increased, and frequency memory is lost, the inhomogeneity index will decrease.

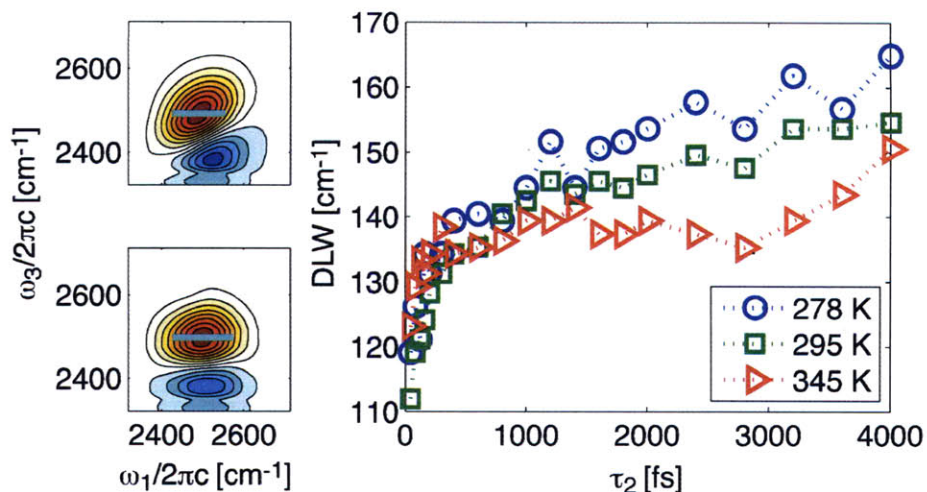


Figure 5-5: Dynamic line width (DLW) for time ($\tau_2 = 40$ fs to 4 ps) and temperature-dependent (278, 295, and 345 K) 2D surfaces of the OD stretch of HOD in H₂O (right). 2D surfaces at 295 K and $\tau_2 = 200$ fs (top) and 2 ps (bottom) with the DLW marked in cyan (left).

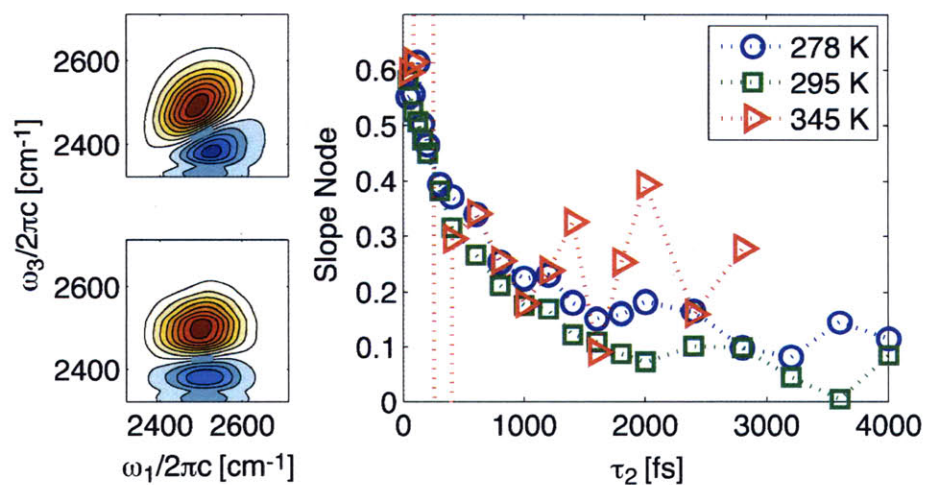


Figure 5-6: Slope of the node (Real) for time ($\tau_2 = 40$ fs to 4 ps) and temperature-dependent (278, 295, and 345 K) absorptive 2D surfaces of the OD stretch of HOD in H₂O (right). 2D surfaces at 295 K and $\tau_2 = 200$ fs (top) and 2 ps (bottom) with the node marked in cyan (left).

We show the slope of the $\phi=0$ phase line, which is equivalent to the slope of the node of the imaginary surface for the three temperatures in Figure 5-9. Again, this metric is similar to the slope of the node of the real surface and CLS, but it is

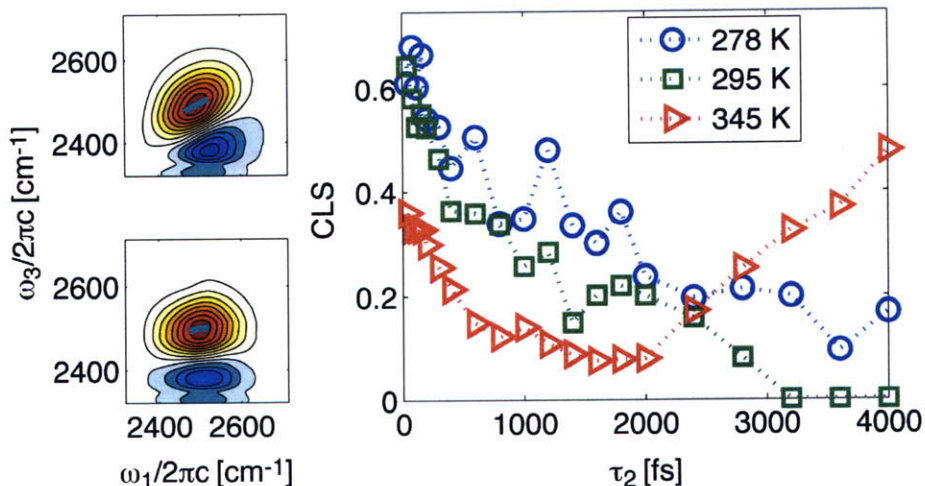


Figure 5-7: Center line slope (CLS) for time ($\tau_2 = 40$ fs to 4 ps) and temperature-dependent (278, 295, and 345 K) absorptive 2D surfaces of the OD stretch of HOD in H₂O (right). 2D surfaces at 295 K and $\tau_2 = 200$ fs (top) and 2 ps (bottom) with the maximum of the $\nu=1\leftarrow 0$ peak marked in cyan (left).

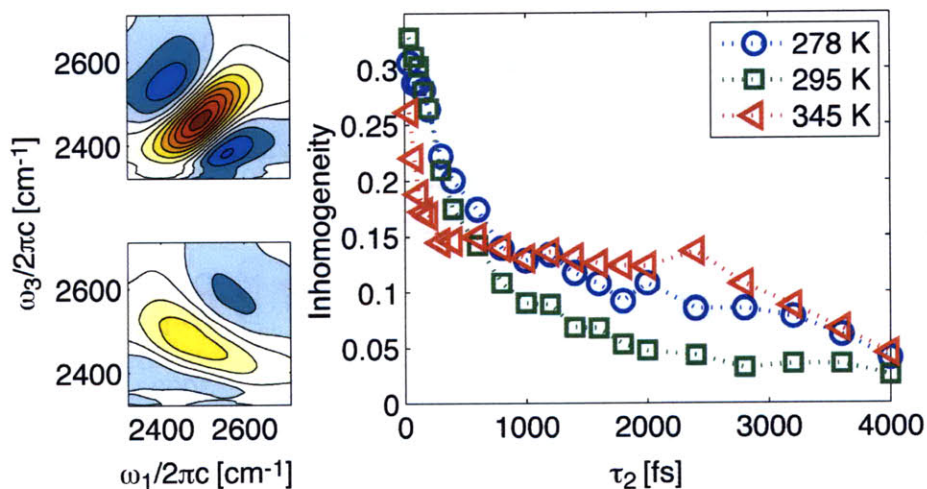


Figure 5-8: Inhomogeneity index (I) for time ($\tau_2 = 40$ fs to 4 ps) and temperature-dependent (278, 295, and 345 K) 2D surfaces of the OD stretch of HOD in H₂O (right). Rephasing (top) and non-rephasing (bottom) surfaces at 295 K and $\tau_2 = 200$ fs normalized to the maximum of the rephasing surface.

superior in that it is viable at all waiting times and the node is better defined than the maximum of the peak.

Finally, we show the phase line slope (PLS) for the three temperatures in Figure 5-10. The PLS is the average of the slopes of the phase lines contained within a box with

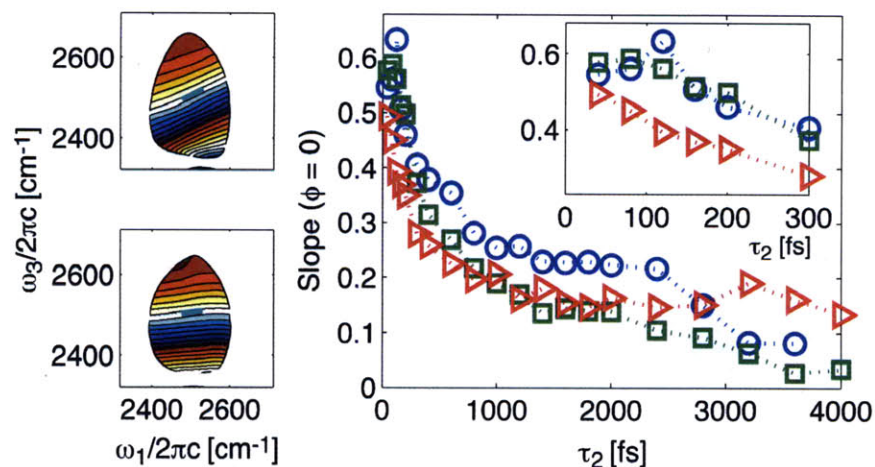


Figure 5-9: Slope of the $\phi=0$ phase line, or node of the imaginary surface, for time ($\tau_2 = 40$ fs to 4 ps) and temperature-dependent (278, 295, and 345 K) 2D surfaces of the OD stretch of HOD in H_2O (right). 2D phase surfaces at 295 K and $\tau_2 = 200$ fs (top) and 2 ps (bottom) with the $\phi=0$ phase line marked in cyan (left).

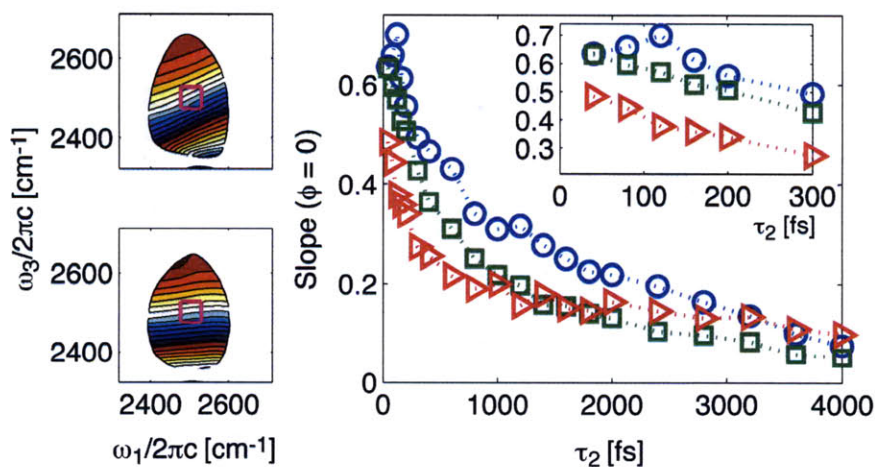


Figure 5-10: Phase line slope (PLS) for time ($\tau_2 = 40$ fs to 4 ps) and temperature-dependent (278, 295, and 345 K) 2D surfaces of the OD stretch of HOD in H_2O (right). 2D phase surfaces at 295 K and $\tau_2 = 200$ fs (top) and 2 ps (bottom) with $\omega_1 = \omega_3 = 2470$ to 2530 cm^{-1} marked in magenta (left).

the bounds set to $\omega_1 = \omega_3 = 2470$ to 2530 cm^{-1} , although the range is arbitrary. For instance, one can study the heterogeneity of spectral diffusion by selecting different frequency regions within the line shape. This is our preferred metric since it provides superior signal to noise.

All metrics generally show the same trend between temperatures in that the decay is faster with increasing temperature yet there is an offset apparent at longer waiting times that is larger with higher temperatures. We compare the normalized metrics at 295 K in Figure 5-11 (normalized at the first recorded waiting time, $\tau_2 = 40$ fs). For the DLW we subtract the last value before normalization. Ideally we would subtract that asymptotic value, so it is not surprising that this metric varies the most from the other metrics. Upon comparison, we find the CLS is the noisiest metric. In Figure 5-2c we show our preferred metric, the phase line slope, $\tan(\phi)$, over the same frequencies as Figure 5-10 for the five temperatures in this study averaged over multiple data sets. We also determined the phase line slope within a box with the bounds set to 90% of the maximum in ω_1 and ω_3 for each surface [182]. Both treatments show a very similar behavior. The phase line slope decreases with increasing temperature. However, there is an offset that appears larger with increasing temperature.

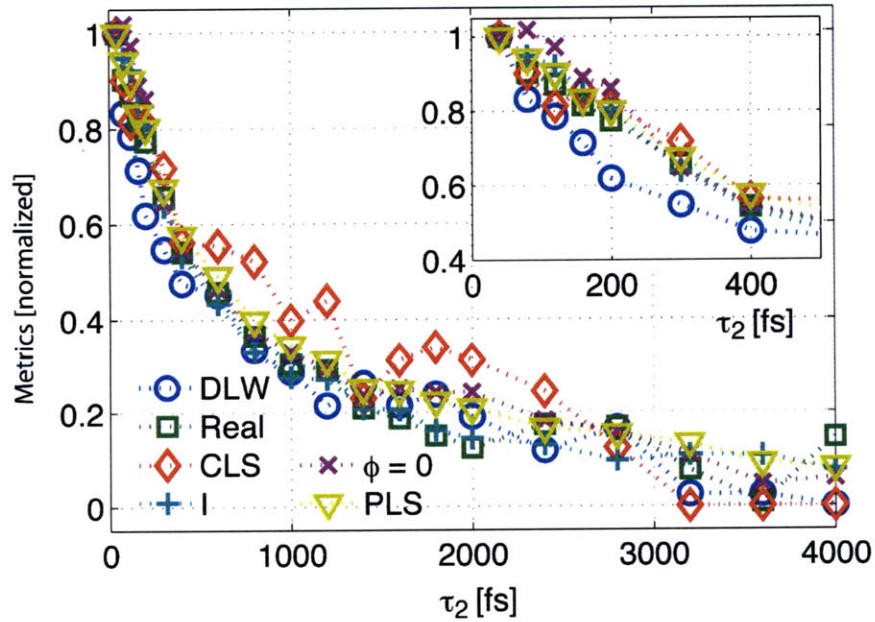


Figure 5-11: Comparison of the metrics at room temperature normalized at the initial waiting time, $\tau_2 = 40$ fs.

5.4 Spectroscopic Model

In order to quantify the temperature-dependence of spectral diffusion, reorientational dynamics, and vibrational relaxation, we employ a widely used nonlinear response function formalism to self-consistently model the FTIR, PP and 2D IR measurements [70]. The model is similar to one we used to study the OH stretch of HOD in D₂O [69]. The response function, S , describes the vibrational dynamics of OD dephasing (S_ω), vibrational population relaxation (S_{pop}), and reorientation (Y) as separable contributions to the vibronic response function, in addition to non-equilibrium heating effects that arise from vibrational relaxation of the OD stretch:

$$S = Y(S_\omega S_{pop,\omega} + S_{TSGS} S_{pop,TSGS}). \quad (5.3)$$

Dephasing is treated as fluctuations of the $\nu=0, 1$, and 2 system eigenstates that result from coupling to a harmonic bath characterized by a bath time-correlation function, $C_\omega(t)$. The remaining components are treated as phenomenological rate processes.

This model makes several approximations that assume the various dynamics can be treated as homogeneous processes. We use the Condon and second-order cumulant approximations [70, 183], which state that the transition dipole moment is independent of bath, and that the frequency fluctuations are purely Gaussian. Both approximations have been shown to be invalid for water on time scales short compared to spectral diffusion [156, 7, 73, 78, 184]. Rotation and vibrational relaxation are treated as Markovian processes that are independent of vibrational dephasing, although evidence indicates that this is a poor assumption for the same short time scales. We proceed with this analysis since the emphasis of this study is on relaxation kinetics on time-scales longer than the correlation time for spectral diffusion. On these long time-scales structural reorganization of the hydrogen bond network has effectively scrambled correlations among the different relaxation processes.

The timescale on which the assumptions become valid can be deduced from an analysis of heterogeneity within the 2D IR line shape. In Figure 5-12a we show the waiting time-dependence of the first moment of the positive signal distribution for

slices in ω_1 on the red and blue side of the line shape at 295 K [72]. The decrease in the first moment on both sides of the line width at longer waiting times is due to the growth of the TSGS. For $\tau_2 \leq 200$ fs, there is a significant difference between first moment on the red and blue side, with a fast decrease on the blue side and a slight recurrence at ~ 120 fs on the red side. A recurrence, or beat, has been observed in previous PS and 2D IR measurements of the OH stretch [68] and MD simulations of the OH and OD stretch (for certain water models) [86]. After approximately 500 fs the dynamics become more similar across the line width. At 278 K (Figure 5-12b), similar observations are made, but the difference across the line width is somewhat larger. Also, the recurrence on the red side of the line width is more pronounced at the lower temperature. These observations indicate that our model properly handles the measurement of relaxation time-scales for waiting times longer than the OD frequency correlation time.

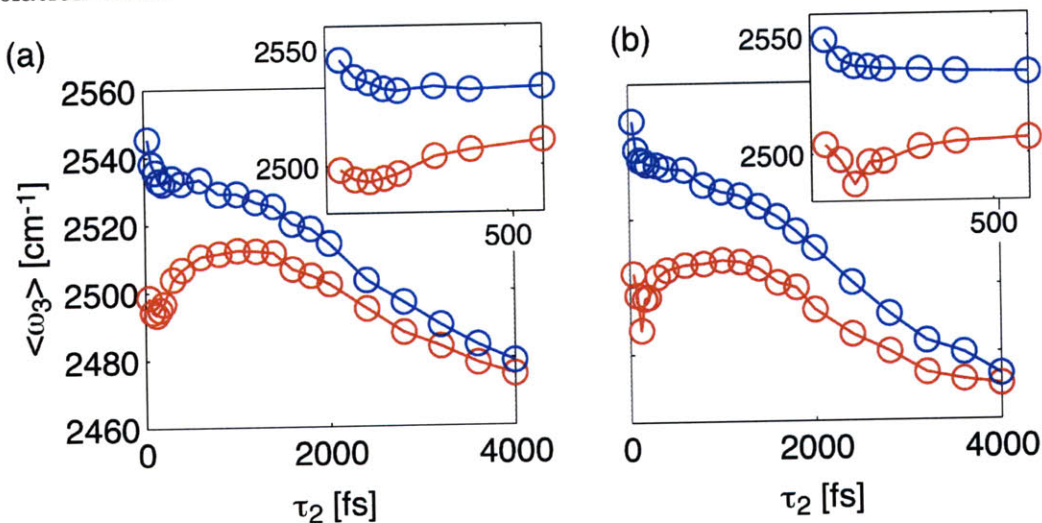


Figure 5-12: First moment of the positive amplitude for slices in ω_1 at 2454 cm^{-1} (red) and 2551 cm^{-1} (blue) at the temperatures 295 K (a) and 278 K (b). The insets show the short time behavior for each of the two temperatures.

5.4.1 Vibrational Dephasing

To model the vibrational dephasing response function S_ω , we include rephasing (-) and non-rephasing (+) pathways that contribute to third-order nonlinear experiments

for pulses separated in time. Within the Condon approximation, and combining the dephasing and vibrational population relaxation $S_\omega S_{pop}$, the response functions are

$$\begin{aligned}
S_-(\tau_3, \tau_2, \tau_1) &= |\mu_{10}|^2 \exp\left[-\frac{\tau_2}{T_1}\right] \exp\left[i\langle\omega_{10}\rangle\tau_1 - \frac{\tau_1}{2T_1}\right] \\
&\times \left\{ |\mu_{10}|^2 \exp\left[-i\langle\omega_{10}\rangle\tau_3 - \frac{\tau_3}{2T_1}\right] [F_{0101}^{(3)}(\tau_3, \tau_2, \tau_1) + F_{0101}^{(4)}(\tau_3, \tau_2, \tau_1)] \right. \\
&\left. - |\mu_{21}|^2 \exp\left[-\langle\omega_{21}\rangle\tau_3 - \frac{3\tau_3}{2T_1}\right] [F_{0121}^{(2)}(\tau_3, \tau_2, \tau_1)]^* \right\}, \tag{5.4}
\end{aligned}$$

$$\begin{aligned}
S_+(\tau_3, \tau_2, \tau_1) &= |\mu_{10}|^2 \exp\left[-\frac{\tau_2}{T_1}\right] \exp\left[-i\langle\omega_{10}\rangle\tau_1 - \frac{\tau_1}{2T_1}\right] \\
&\times \left\{ |\mu_{10}|^2 \exp\left[-i\langle\omega_{10}\rangle\tau_3 - \frac{\tau_3}{2T_1}\right] [F_{0101}^{(1)}(\tau_3, \tau_2, \tau_1) + F_{0101}^{(2)}(\tau_3, \tau_2, \tau_1)] \right. \\
&\left. - |\mu_{21}|^2 \exp\left[-\langle\omega_{21}\rangle\tau_3 - \frac{3\tau_3}{2T_1}\right] [F_{0121}^{(4)}(\tau_3, \tau_2, \tau_1)]^* \right\}. \tag{5.5}
\end{aligned}$$

In these expressions ω_{10} , ω_{21} and μ_{10} , μ_{21} denote the transition frequency and transition dipole of the $\nu=1\leftarrow 0$ and $\nu=2\leftarrow 1$ transitions, respectively. The room temperature anharmonicity is fixed at $\Delta=\omega_{10} - \omega_{21} = 162 \text{ cm}^{-1}$ for the OD stretch [77] and is taken to be independent of temperature. We assume harmonic scaling of the transition dipole, therefore $\mu_{21} = \sqrt{2}\mu_{10}$. F_{abcd} are the dephasing functions, in which the indices refer to the vibrational 0, 1 and 2 states. T_1 is the vibrational lifetime, which is determined by fitting the isotropic transient absorption. We include population relaxation during the coherence periods with the timescale determined by: $\Gamma_{ab} = (1/2)(\Gamma_{aa} + \Gamma_{aa})$, where $T_1=1/\Gamma_{11}$. We assume the population relaxation scales with quantum number, $\Gamma_{aa} = a\Gamma_{11}$, therefore T_1 is the only necessary input.

Under the second-order cumulant approximation, the dephasing functions in Equa-

tion 5.5 can be expressed in terms of line shape functions, g [138]:

$$\begin{aligned}
-\ln F_{0101}^{(1)}(\tau_3, \tau_2, \tau_1) &= g_{11}(\tau_1) + g_{11}(\tau_2) + g_{11}(\tau_3) - g_{11}(\tau_1 + \tau_2) \\
&\quad - g_{11}(\tau_2 + \tau_3) + g_{11}(\tau_1 + \tau_2 + \tau_3), \\
-\ln F_{0101}^{(2)}(\tau_3, \tau_2, \tau_1) &= g_{11}(\tau_1) + g_{11}^*(\tau_2) + g_{11}^*(\tau_3) - g_{11}(\tau_1 + \tau_2) \\
&\quad - g_{11}^*(\tau_2 + \tau_3) + g_{11}(\tau_1 + \tau_2 + \tau_3), \\
-\ln[F_{0101}^{(3)}(\tau_3, \tau_2, \tau_1)]^* &= g_{11}(\tau_1) - g_{11}(\tau_2) + g_{11}^*(\tau_3) + g_{11}(\tau_1 + \tau_2) \\
&\quad + g_{11}(\tau_2 + \tau_3) - g_{11}(\tau_1 + \tau_2 + \tau_3), \\
-\ln[F_{0101}^{(4)}(\tau_3, \tau_2, \tau_1)]^* &= g_{11}(\tau_1) - g_{11}^*(\tau_2) + g_{11}(\tau_3) + g_{11}(\tau_1 + \tau_2) \\
&\quad + g_{11}^*(\tau_2 + \tau_3) - g_{11}(\tau_1 + \tau_2 + \tau_3), \\
-\ln F_{0121}^{(2)}(\tau_3, \tau_2, \tau_1) &= g_{11}(\tau_1) + g_{11}^*(\tau_2) + g_{12}^*(\tau_2) + g_{11}^*(\tau_3) - g_{12}^*(\tau_3) \\
&\quad - g_{21}^*(\tau_3) + g_{22}^*(\tau_3) - g_{11}(\tau_1 + \tau_2) + g_{21}(\tau_1 + \tau_2) - g_{11}^*(\tau_2 + \tau_3) \\
&\quad + g_{12}^*(\tau_2 + \tau_3) + g_{11}(\tau_1 + \tau_2 + \tau_3) - g_{21}(\tau_1 + \tau_2 + \tau_3), \\
-\ln[F_{0121}^{(4)}(\tau_3, \tau_2, \tau_1)]^* &= g_{11}(\tau_1) - g_{11}^*(\tau_2) + g_{12}^*(\tau_2) + g_{11}(\tau_3) - g_{12}(\tau_3) \\
&\quad - g_{21}(\tau_3) + g_{22}(\tau_3) + g_{11}(\tau_1 + \tau_2) - g_{21}(\tau_1 + \tau_2) - g_{11}^*(\tau_2 + \tau_3) \\
&\quad - g_{12}^*(\tau_2 + \tau_3) - g_{11}(\tau_1 + \tau_2 + \tau_3) + g_{21}(\tau_1 + \tau_2 + \tau_3). \tag{5.6}
\end{aligned}$$

The line shape functions are defined in terms of two-point frequency correlation functions:

$$g_{pq}(t) = \int_0^t d\tau \int_0^\tau d\tau' C_{pq}(\tau - \tau') \tag{5.7}$$

where

$$C_{pq}(\tau - \tau') = \langle \delta\omega_{p0}(\tau) \delta\omega_{q0}(\tau') \rangle. \tag{5.8}$$

The indices p and q refer to OD vibrational energy levels. In practice, we define one correlation function $C_\omega(t) = C_{11}(t)$, and use harmonic scaling relations to relate correlation function for transitions involving $\nu = 0, 1$, and 2: $C_{22}(t) = 2C_{21}(t) =$

$$2C_{12}(t) = 4C_{11}(t).$$

Motivated by a number of observations, we use a complex frequency correlation function in the present work [70]. First, librational motion plays an important role in the short time dynamics, and it is unclear if the high-temperature limit applies to librational frequencies. Also, harmonic bath models make explicit predictions about the temperature dependence of spectroscopic observables; for instance, the absorption line width is linear in T in the high temperature limit. Also, the Stokes shift, which accounts for the response of the bath to OD excitation, has been predicted to be small but a relevant contribution to the spectroscopy. A complex exponential correlation function can be used to properly account for these effects. Computational modeling of HOD in H₂O indicated that a classical correlation function is satisfactory for linear measurements, but quantum effects may become important for nonlinear measurements, especially for strongly inhomogeneously broadened systems [185]. Overall, the analysis with a complex correlation function did not differ greatly from a real correlation function, but it does identify interesting aspects of the data that are discussed below and in the following sections.

Similar to prior studies of HOD in H₂O by Fayer and co-workers [77], a tri-exponential was chosen as the functional form of the frequency correlation function [70]:

$$C_{\omega}(t) = \sum_{j=1}^3 A_j \left[\frac{1}{\tau_{C,j}} \coth\left(\frac{\hbar}{2kT\tau_{C,j}}\right) - i\frac{1}{\tau_{C,j}} \right] \exp\left(-\frac{t}{\tau_{C,j}}\right) \quad (5.9)$$

In this equation $\tau_{C,j}$ is the correlation time for the j th exponential relaxation component and A_j is its amplitude. For this model, the reorganization energy is $\lambda = \sum_j A_j$, and 2λ is the Stokes shift. For a correlation function comprised of exponentials an approximation for the line shape function can be written as [70]:

$$g(t) = \sum_j A_j \left[\tau_{C,j} \coth\left(\frac{\hbar}{2kT\tau_{C,j}}\right) - i\tau_{C,j} \right] \left[\exp\left(-\frac{t}{\tau_{C,j}}\right) + \frac{t}{\tau_{C,j}} - 1 \right]. \quad (5.10)$$

Simulations discussed below show that the inertial decay of the frequency corre-

lation function has a weak temperature dependence. Therefore, we fixed the inertial decay time scale at $\tau_{C,1} = 50$ fs for all five temperatures, however, we found it necessary to vary the amplitude to match experiment. To add constraints, we initially attempted to keep the intermediate timescale constant at $\tau_{C,2} = 400$ fs, the intermediate timescale found by Fayer and co-workers [77], but we found the fit of the two highest temperatures, 323 and 345 K, unsatisfactory. At these temperatures the intermediate timescale was set to 200 fs. Therefore, only three parameters of the frequency correlation function are independent: the timescale of the long-time decay, $\tau_{C,3}$, and the amplitudes of the inertial and intermediate-time decays. A recurrence was not included in the correlation function since it is a relatively minor effect and we are primarily interested in the long-time behavior. In addition to the OD stretch of HOD, we also use this formalism to treat the weak background absorption from the H₂O stretch and libration-bend combination band (see Section S.1 in this chapter for details).

5.4.2 Rotational Response

For the case that vibrational and orientational response functions are separable and reorientational motion is treated as a Markovian process, the nonlinear orientational correlation functions can be written in terms of $C_{R,n} = \langle P_n[\hat{\mu}(t) \cdot \hat{\mu}(0)] \rangle$, where P_n is the n th order Legendre polynomial and $\hat{\mu}$ is the transition dipole unit vector [186]. The orientational responses are then expressed as:

$$\begin{aligned} Y_{zzzz}(\tau_3, \tau_2, \tau_1) &= \frac{1}{9}C_{R,1}(\tau_1)\left[1 + \frac{4}{5}C_{R,2}(\tau_2)\right]C_{R,1}(\tau_3), \\ Y_{zzyy}(\tau_3, \tau_2, \tau_1) &= \frac{1}{9}C_{R,1}(\tau_1)\left[1 - \frac{2}{5}C_{R,2}(\tau_2)\right]C_{R,1}(\tau_3). \end{aligned} \quad (5.11)$$

For pump-probe measurements, the isotropic response $Y_{iso} = (Y_{zzzz} + 2Y_{zzyy})/3$ is observed to be independent of orientational dynamics during τ_2 , whereas the anisotropy is proportional to the second order orientational correlation function: $C_R(\tau_2) = (2/5)C_{R,2}(\tau_2)$. Guided by observations from the MD simulations below and previous experimental results [93], we model the anisotropy and second rank rotational correlation function

as a biexponential:

$$C_R(t, T) = (1 - A_R(T)) \exp\left(\frac{-t}{\tau_{inertial}}\right) + A_R(T) \exp\left(\frac{-t}{\tau_R(T)}\right). \quad (5.12)$$

An inertial reorientational response with a time-scale of $\tau_{inertial} = 50$ fs is taken to be independent of temperature, but the amplitude A_R and reorientational correlation time τ_R are allowed to vary. For the purpose of describing 2D IR experiments, we include orientational relaxation during τ_1 and τ_3 , which requires a first rank orientational correlation function, $C_{R,1}$. We relate $C_{R,1}$ and $C_{R,2}$ by scaling their orientational correlation times, but leave the inertial time scale unchanged. Based on recent MD simulations of water [32], we use a scaling of $\tau_{R,1}/\tau_{R,2}=2.3$, although results are found to be indistinguishable within the model from results using the value of 3.0 predicted for small-angle diffusive reorientation. The linear spectrum, 2D IR and pump-probes are sensitive to the scaling; the pump-probe anisotropy, however, is not sensitive to the scaling within the model.

5.4.3 Thermal Effects

The model includes a third order response from the TSGS for all three modes. The response can be written as:

$$\begin{aligned} S_{\pm}^{TSGS} &= A^{TSGS} |\mu_{10}|^4 N^{TSGS}(\tau_2) \exp(i\langle\omega_{10}\rangle\tau_1 - i\langle\omega_{10}\rangle\tau_3) \\ &\times \exp(-g_{11}^*(\tau_1) - g_{11}(\tau_3)) [1 - |\Delta\mu_{10}|^2 \exp(-i\Delta\omega\tau_3)]. \end{aligned} \quad (5.13)$$

In this equation $\Delta\mu_{10}$ denotes the decrease in transition dipole strength, $\Delta\mu_{10}=(\mu_{10}-\mu_{10}^{TSGS})/\mu_{10}$, and $\Delta\omega$ the blue-shift in frequency, $\Delta\omega=\omega_{10}^{TSGS}-\omega_{10}$, induced upon vibrational relaxation. This formalism assumes an uncorrelated TSGS [66, 69, 187], in which frequency memory is lost upon vibrational relaxation. Temperature-dependent linear absorption spectra show that the frequency of the OD stretch changes linearly with temperature. Therefore, for all temperatures, $\Delta\omega$ is set to the frequency change for 1 K increase in temperature, 0.53 cm^{-1} . A^{TSGS} , the intensity of the thermally

induced response, and $\Delta\mu_{10}$ are determined by fitting both the integrated isotropic PP at $\tau_2 > 1.5$ ps and the 2D surface at $\tau_2 = 4$ ps projected along ω_3 .

$N^{TSGS}(\tau_2)$ represents the growth of the thermal response with waiting time determined by fitting the integrated isotropic PP measurements. The integrated isotropic PP is fit with the model developed by Bakker [120]:

$$N^{TSGS}(\tau_2) = 1 + \frac{1}{T_1 - T^*} [T^* \exp(-\tau_2/T^*) - T_1 \exp(-\tau_2/T_1)]. \quad (5.14)$$

In this equation T^* represents the lifetime of an intermediate state, which has been suggested to be the fundamental of the HOD bend [100]. Yeremenko and co-workers found an important contribution arising from the solvent D₂O in experiments on the OH stretch of HOD in D₂O [67, 187]. However, this effect is small for absorptive 2D IR and PP measurements, and is more important for measurements sensitive to dispersive changes, such as photon echo and transient grating [187]. Thermally induced shifts are also included for the background H₂O stretch and combination band, although the effect is rather small in the region of the OD stretch (see Section S.1 in this chapter).

5.4.4 Modeling Results

To apply the model to the OD stretch of HOD in H₂O, we first fit the experimental integrated isotropic PP and PP anisotropy at each temperature to determine T_1 , $N^{TSGS}(\tau_2)$, and $C_R(t)$. We make an initial guess for $C_\omega(t)$ and solve for λ by fitting the line width of the linear absorption measurement. The isotropic PP and 2D IR surfaces are calculated and compared to experiment to determine A^{TSGS} and $\Delta\mu_{10}$. The 2D surface is a two dimensional Fourier transform of $Y(S_\omega S_{pop,\omega} + S_{TSGS} S_{pop,TSGS})$. The complex surface is determined from the calculated 2D surfaces with the same method used for experimental 2D surfaces. The parameters for the frequency correlation function are adjusted at each temperature to best fit the experimental phase line slope over the same frequency range as the experiment. We allow for an arbitrary offset to the phase line slope generated from the model when comparing to the experimental

phase line slope. Although we are interested in the long time behavior we fit the entire waiting time range to obtain the most reliable information. A self-consistent fitting of all the data provides enough constraints to quantitatively extract the longest correlation times, lifetimes, and reorganization energy at any temperature.

The reorganization energy, λ , is found by fitting the FWHM of the linear spectrum. The "full" treatment of calculating the linear spectrum includes a complex frequency correlation function, reorientation, and vibrational relaxation. The absorption line width is calculated by:

$$\sigma(\omega) \propto |\mu_{10}|^2 \int_0^\infty dt \exp[i(\omega - \omega_{10})t - \frac{t}{2T_1} - g_{11}(t)] C_{R,1}(t). \quad (5.15)$$

In Figure 5-13 we show the experimental FTIR of HOD in H₂O at 295 K, with the background H₂O subtracted, along with the results of the "full" treatment using the best-fit frequency correlation function. Since we are using the cumulant approximation, the model spectrum is Gaussian. With the same input ω_{10} and $C_\omega(0)$, we calculate the linear spectrum first without including reorientation, then additionally without including vibrational relaxation. The spectrum narrows from 166 to 152 cm⁻¹ when reorientation is not included and an additional 2 cm⁻¹ when vibrational relaxation is not included. Therefore, reorientation is more important but it only accounts for ~8% of the overall width (~10% for reorientation + vibrational relaxation). We also show the result of only considering the real part of the frequency correlation function. The peak frequency is red-shifted by ~3 cm⁻¹ at this temperature when using a complex correlation function since the imaginary part introduces a Stokes shift.

The linear spectra calculated with the model for each of the five experimental temperatures are shown as solid lines in Figure 5-1. The reorganization energy, λ , and the complex initial value of the frequency correlation function, $C_\omega(0)$, for each temperature are given in Table 5-1. We find that at a given temperature the magnitude of the red-shift was most sensitive to the amplitude of the inertial decay (an increased amplitude resulted in an increased red-shift). Experimental and input fre-

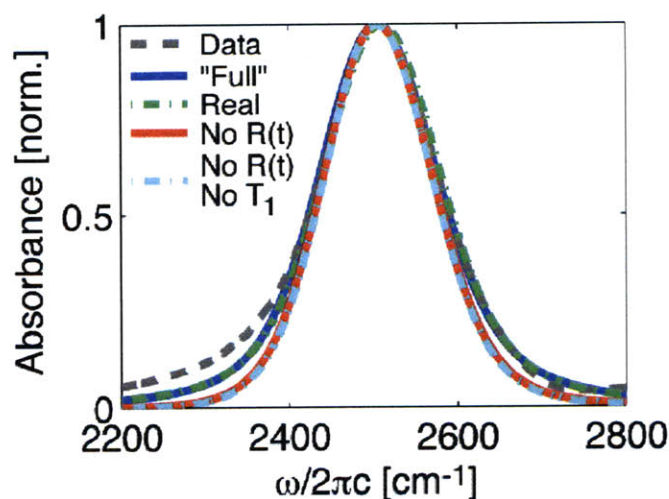


Figure 5-13: Experimental linear absorption of the OD stretch of HOD in H₂O with the background H₂O subtracted (dashed gray), along with spectra calculated with the spectral model using the "full" treatment (solid blue), using $C'_\omega(t)$ with $R(t)$ and T_1 (dot dashed green), using $C_\omega(t)$ without including $R(t)$ (solid red), and using $C_\omega(t)$ without including $R(t)$ or T_1 (dot dashed cyan)

quencies for the OD stretch, along with the amplitudes and timescales of the best fit temperature-dependent frequency correlation functions are given in Table 5-1. The temperature-dependent long time decay is also shown in Figure 5-3. The amplitude of the inertial decay increases from 41% to 71% from 278 to 345 K. The amplitude of the intermediate and long-time decays both decrease with increasing temperature. The long-time decay decreases with increasing temperature, which is in agreement with our previous study [182]. The experimental phase line slopes and best fits with the model, including the offset, are shown as solid lines in Figure 5-2c.

Temperature and waiting time-dependent 2D surfaces generated from the model with the best-fit frequency correlation functions are shown in Figure 5-14. The apparent asymmetry is in small part due to including the H₂O combination band and stretch but mainly due to windowing by the experimental pulse spectrum after the 2D surface is calculated. The 2D surfaces from the model are successful in capturing the average dynamics with waiting time and temperature. The model 2D IR surfaces agree with the experimental surfaces best at lower temperatures. As the temperature

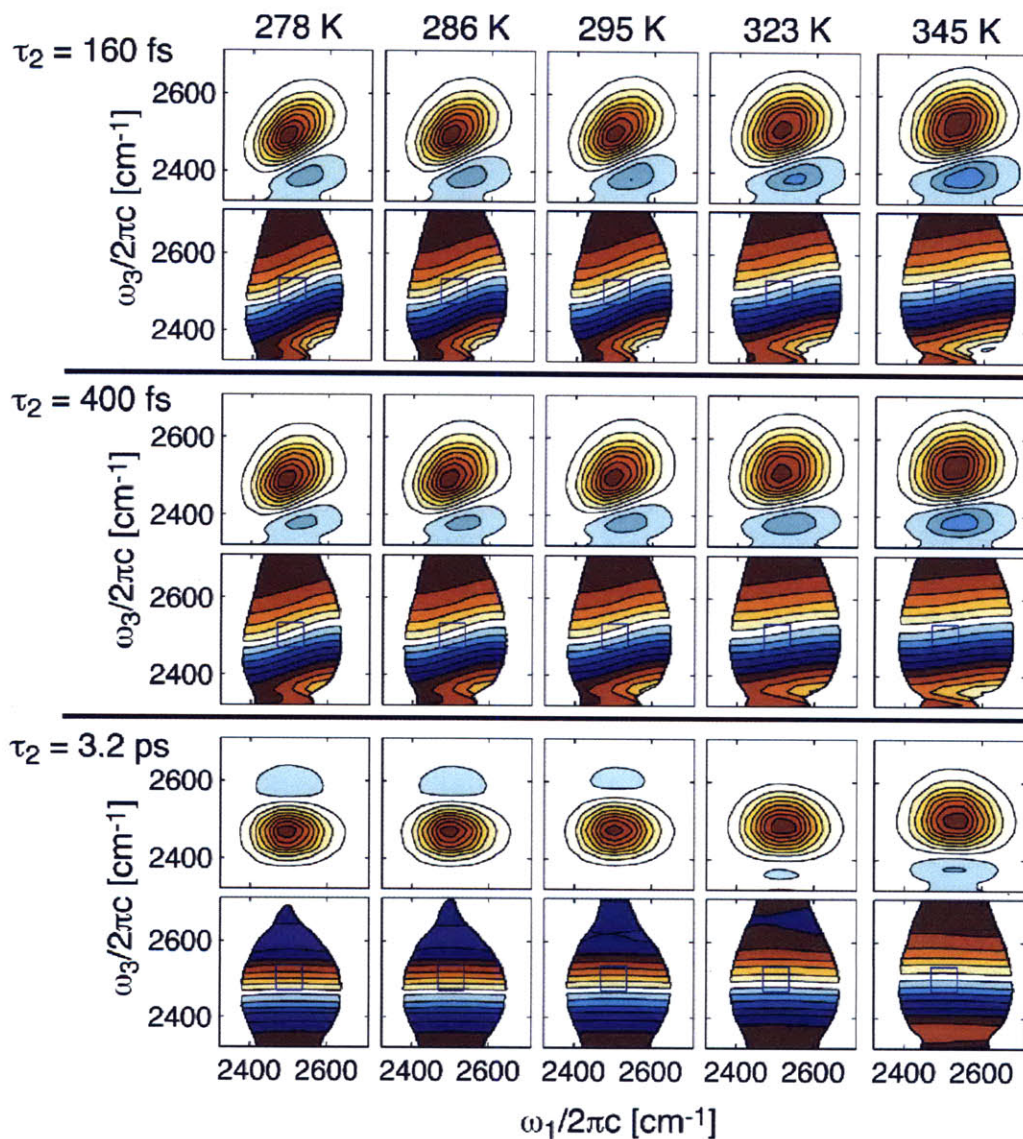


Figure 5-14: Absorptive and phase 2D surfaces calculated with the model at each of the five experimental temperatures at three waiting times: $\tau_2 = 160$ fs (top), 400 fs (middle) and 3.2 ps (bottom). The contours in the absorptive 2DIR spectra are at 12% intervals relative to the maximum. The phase spectra are plotted from $-\pi/2$ to $\pi/2$ and are windowed by 10% of the absolute value spectra.

is increased the residual inhomogeneity on the red side of the line shape, which is not captured with the model, becomes more important.

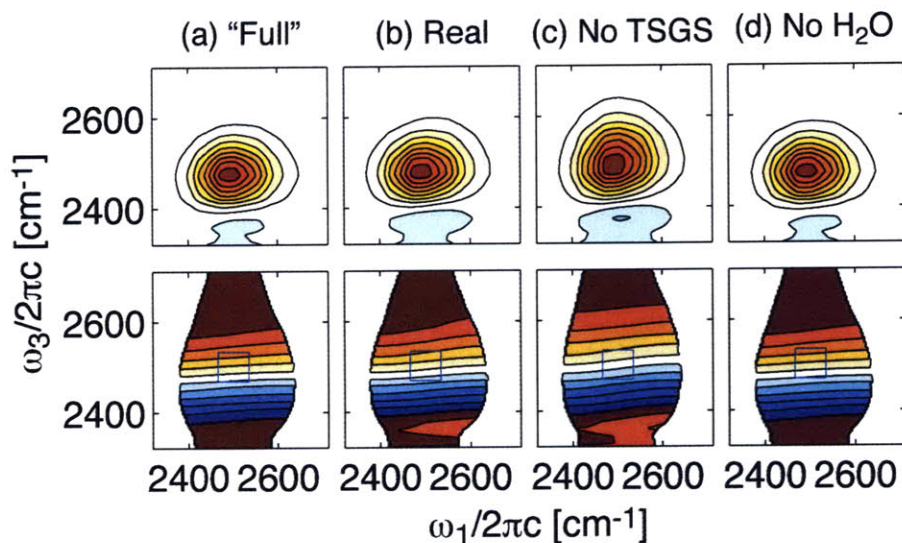


Figure 5-15: Absorptive and phase 2D surfaces calculated with the model at $\tau_2 = 2$ ps and 278 K with (a) the "full" treatment, (b) using $C'_\omega(t)$, (c) not including the TSGS, and (d) not including the background H_2O .

In order to understand the influence of a complex correlation function on the calculated time scales, we calculate the 2D surface and phase line slope with the best-fit correlation function at $\tau_2 = 2$ ps for four cases: (a) the full treatment, (b) including only the real part of the correlation function, (c) not including the TSGS, and (d) not including the response of the bath H_2O . Cases (b)-(d) are the same as (a) except for where noted (for case (b), however, the input ω_{10} was necessarily different). Figure 5-15 and Figure 5-16 show the 2D surface and phase line slope, respectively, for each of the four cases for 278 K (Figure 5-15) and 278 K and 345 K (Figure 5-16). We also show the phase line slope for the full treatment but without windowing the 2D surfaces by the pulse spectrum. As can be seen in both Figure 5-15 and 5-16 including the solvent H_2O has little to no effect on the calculated dynamics within this model. The contribution from the H_2O stretch may become more significant if the non-Condon effect were included. As can be seen in Figure 5-15b and 5-16 including the imaginary part of the correlation function makes a non-negligible difference with

a larger effect at low temperature. The effect of the TSGS, shown in Figure 5-15c and 5-16, is non-negligible and the contribution becomes more important with increased waiting time. Since the TSGS is uncorrelated, a homogeneously broadened doublet (negative above the diagonal) grows in with waiting time. Comparing Figure 5-15a and 5-15c shows the negative contribution from the TSGS above the diagonal acts to narrow the positive peak along ω_3 . The phase lines of a homogeneously broadened peak are parallel to ω_1 indicating that ω_3 is independent of ω_1 . As a result, including the TSGS acts to decrease the phase line slope, as can be seen in Figure 5-16. Finally, The effect of windowing by the experimental spectrum on the calculated dynamics is shown in Figure 5-16. The experimental spectrum makes a non-negligible difference on the dynamics, which as been observed before for the OD stretch of HOD in H_2O with similar experimental conditions [77].

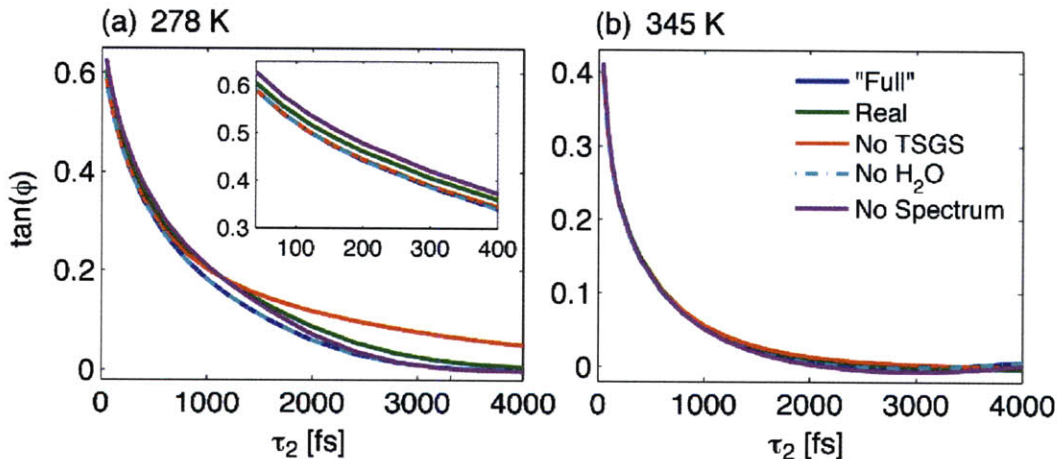


Figure 5-16: Phase line slope calculated with the spectral model for (a) 278 K and (b) 345 K with the "full" treatment (blue), using $C''_{\omega}(t)$ (green), not including the TSGS (red), not including the background H_2O (dot dashed cyan), and not windowing by the experimental spectrum (magenta).

After determination of the best-fit frequency correlation function the dispersed isotropic pump-probe is calculated using the isotropic orientational response function. The integrated isotropic signal from the model is compared to the experimental traces in Figure 5-2a. In order to compare the model and experimental anisotropy the third order response, without including the TSGS response, is calculated with the $zzzz$ and

zzyy orientational response functions. The comparison is shown in Figure 5-2b.

	278 K	286 K	295 K	323 K	345 K
ω_{OH} [cm ⁻¹] (from FTIR)	2499	2503	2508	2522	2534
ω_{OH} [cm ⁻¹] (input into model)	2503	2507	2513	2529	2544
FWHM [cm ⁻¹]	159	163	166	175	180
T_1 [ps]	1.4	1.5	1.4	1.6	2.0
T^* [fs]	450	450	540	530	590
$C_R(t)$					
$A_R \tau_R$ [ps]	(0.74) 4.5	(0.64) 3.8	(0.69) 2.9	(0.78) 1.7	(0.78) 1.3
$C_\omega(t)$					
$(A_1/\lambda) \tau_1$ [fs]	(0.41) 50	(0.44) 50	(0.45) 50	(0.57) 50	(0.71) 50
$(A_2/\lambda) \tau_2$ [fs]	(0.35) 400	(0.33) 400	(0.35) 400	(0.27) 200	(0.12) 200
$(A_3/\lambda) \tau_3$ [ps]	(0.24) 2.4	(0.23) 2.1	(0.2) 1.8	(0.16) 1.1	(0.17) 0.7
$\lambda/10^{-3}$ [fs ⁻¹]	2.6468	2.5824	2.6993	3.1906	3.3834
$C'_\omega(0)/10^{-4}$ [fs ⁻²]	1.9467	1.9542	2.1062	2.7279	3.0922
$-C''_\omega(0)/10^{-5}$ [fs ⁻²]	2.4284	2.5138	2.6956	4.1144	5.0896
Offset	8.7x10 ⁻²	8.0x10 ⁻²	6.8x10 ⁻²	1.1x10 ⁻¹	1.3x10 ⁻¹
$\Delta\mu$	0.99862	0.99865	0.99839	0.99830	0.99875
A^{TSGS}	59	70	66	61	50

Table 5.1: Summary of the temperature dependent parameters contained within our spectral model for the OD stretch of HOD in H₂O.

5.5 Discussion

Over the past decade, the combination of ultrafast infrared spectroscopy and MD simulations of isotopically dilute water have developed an increasingly detailed molecular picture of the structural dynamics of water on the femtosecond to picosecond time scale. Since the frequency at which water absorbs is sensitive to its local hydrogen bonding environment, monitoring frequency evolution provides a picture of the evolving structure. On the picosecond time scale, theoretical work has shown that a number of relaxation mechanisms, including density and polarization fluctuations on length scales longer than the molecular diameter, occur on the same time scale as spectral diffusion suggesting that the picosecond time scale can not be assigned to

local molecular motions but rather to collective rearrangements [68, 46]. Although absolute time scales cannot be compared between experiments that are sensitive to different relaxation phenomena, if the structural evolution is collective the temperature dependence of these measurements will be correlated.

The inertial decay of the pump-probe anisotropy has been attributed to librations, or hindered rotations, of the OX (where X = H or D) transition dipole, and long time decay to collective reorientation [93]. The observed temperature-dependence of the long time relaxation agrees with previous studies using methods related to (with proper assumptions) the first Legendre polynomial: dielectric relaxation [6] and THz time domain spectroscopy [5]; and the second Legendre polynomial: NMR [4, 114] and OKE [3]. Tielrooij and Bakker measured the temperature dependence of the reorientation time of the OD stretch of HOD in H₂O with ultrafast infrared spectroscopy and found it decreased from 4.8 to 0.97 ps from 274 to 343 K [100], which is in reasonable agreement with our study. Assuming the long time decay follows Arrhenius behavior, $1/\tau_c = A \exp[-E_a/RT]$, we find a barrier height of 3.7 kcal/mol compared to 4.1 kcal/mol found by Petersen and Bakker [188]. The Arrhenius plot in Figure 5-17 shows that the trend is nearly linear with a slight quadratic dependence.

Previous measurements of the spectral diffusion of isotopically dilute water have assigned the long-time decay to collective reorganization of the liquid structure [68, 69]. Using the long-time decay from the temperature-dependent frequency correlation functions determined with the model (2.4 ps for 278 K to 0.7 ps for 345 K) and assuming Arrhenius behavior we find a barrier height of 3.4 kcal/mol. As can be seen in Figure 5-17 the trend is linear, with a slight quadratic dependence in an opposite manner as the reorientation. We also determined the barrier height for the integrated real part of the correlation functions and found 2.9 kcal/mol with a trend that is quite linear. Finally, we also characterized the temperature-dependent spectral diffusion by fitting the phase slope decay with a number of functional forms and determining the correlation time either from the decay directly, integrating the normalized function, or from the 1/e period and found a barrier height of 3.4 ± 0.5 kcal/mol and a trend more similar to the reorientation [182]. The differences in barrier height and trend

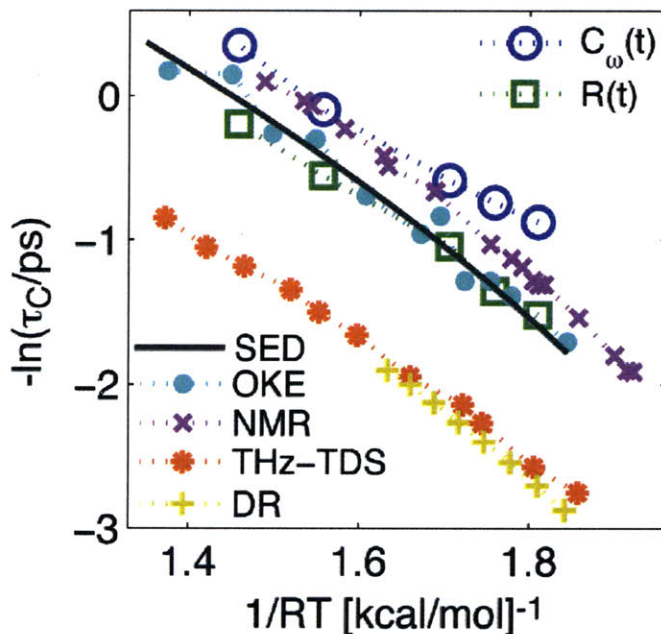


Figure 5-17: Arrhenius plot of the picosecond decay of the temperature-dependent best-fit frequency correlation function ($C_\omega(t)$, open circles) determined with the spectral model and anisotropy ($C_R(t)$, open squares) along with previous temperature-dependent measures of reorientational relaxation in water: optical Kerr effect [3] (OKE, filled circles), NMR [4] (crosses), terahertz time domain spectroscopy [5] (THz-TDS, asterisks), and dielectric relaxation [6] (DR, plusses). We also show the result of applying the Stokes-Einstein-Debye equation (SED, line).

should be taken as the uncertainty in our determination of the picosecond spectral diffusion time scale.

The similar temperature dependence for both these dynamics experiments (with activation energies of 3.4 kcal/mol for spectral diffusion and 3.7 kcal/mol for reorientation) suggests a common mechanism. Recent theoretical work by Laage and Hynes [1, 32], found that reorientation occurred through large amplitude angular jumps that exchanged a hydrogen bond with a small contribution from the diffusive motion of the hydrogen bond frame. This would suggest exactly what is observed in the current study since exchanging hydrogen bonds causes a significant change in frequency [73]. The authors also looked at the temperature dependence of reorientation and found that the large amplitude jumps and diffusive motion both contribute at every temperature but large amplitude jumps are dominant [32].

In Figure 5-17 we show an Arrhenius plot that includes previous temperature-dependent studies of the first and second order orientational correlation functions along with the results of the current study. The barrier height is similar for all the experiments included in the figure, and a similar quadratic dependence is observed. Results from quasi-elastic neutron scattering (QENS) experiments have not been included since recent theoretical work called for the reassessment of reorientation times of water determined from QENS experiments [189]. The barrier heights from the plot range from 3.9 to 4.7 kcal/mol over liquid phase temperatures where 4.7 kcal/mol is from the dielectric relaxation (DR) study, which samples the higher slope portion of the curve. The ratio between $\tau_{R,2}$, measured in the current study with pump-probe anisotropy, and $\tau_{R,1}$, measured with THz time domain spectroscopy (THz-TDS) [5] is 2.7 ± 0.1 over the temperature range in the current study and there is no clear temperature dependence. We also plot the result of calculating $\tau_{R,2}$ derived from the Stokes-Einstein-Debye (SED) equation, $\tau_{R,2} = 4\pi\eta(T)R^3/3kT$, where $\eta(T)$ is the temperature-dependent viscosity [190] and R is the hydrodynamic radius [16]. For both quantities we use the values for H₂O. The Stokes-Einstein-Debye (SED) equation assumes the reorientation is diffusive, which predicts that the ratio between $C_{R,1}(t)$ and $C_{R,2}(t)$ is 3. We do not observe this ratio experimentally and reorientation dominated by diffusive steps disagrees with the theoretical work by Laage and Hynes [1, 32]. However, the temperature dependence of τ_2 calculated with the SED equation shows a similar barrier height (4.3 kcal/mol) and quadratic behavior. Although we are comparing experiments that are each uniquely sensitive to the evolving structure of the liquid we observe a similar barrier and for the most part a similar quadratic behavior. This observation again points to the collective nature of the picosecond relaxation in water.

In previous studies, the non-Arrhenius behavior of thermodynamic and transport properties of water have been attributed to relaxation processes characteristic of supercooled liquids. Speedy and Angell found the temperature dependence of the isothermal compressibility, expansivity, isobaric heat capacity, diffusion coefficient, viscosity, dielectric relaxation, and ¹⁷O spin relaxation rate followed power law

behavior. A plot of relaxation rates against $\log(T/T_S-1)$ using a homogeneous nucleation temperature $T_S = 228$ K was linear [191, 192]. It has been suggested that water undergoes a fragile-to-strong transition at this temperature [193] and the relaxation processes subsequently assume an Arrhenius behavior until the glass formation temperature [194]. The Vogel-Fulcher-Tammann law, which has also been used to model relaxation rates in supercooled water, predicts a linear relationship between the log of the temperature dependence of the property and $1/(T-T_0)$ [114]. Although several empirical relationships have been established, the microscopic explanation for the non-Arrhenius behavior in terms of molecular behavior is unclear, and indicates that a need for further studies at this level.

5.6 Molecular Dynamics Simulations

5.6.1 Fixed Charge SPC/E

We calculate temperature-dependent OD vibrational dephasing and orientational correlation functions with MD simulations to support our conclusions on the collective nature of hydrogen bond rearrangement in water. We used the fixed point SPC/E water potential [31], which was used to illustrate concerted hydrogen bond switching and to calculate electric field induced vibrational frequency shifts [1, 46]. The method only differs from previous MD simulations performed in our group in that HOD is placed in a bath of H₂O rather than D₂O and the OD stretching frequency is calculated [68, 71]. Trajectories were calculated at four temperatures (273, 298, 310, and 330 K) with the density chosen to match experiments. The OD frequency correlation functions, $C_\omega(\tau) = \langle \delta\omega_{OD}(0)\delta\omega_{OD}(\tau) \rangle$, and OD bond reorientational correlation functions, $C_2(\tau) = \langle P_2(\hat{r}_{OD}(0) \cdot \hat{r}_{OD}(\tau)) \rangle$, are shown in Figure 5-18a and 5-18b, respectively. For $C_\omega(\tau)$, the sub-100 fs decays are indistinguishable, but the picosecond tails show relaxation times that decrease from roughly 1.4 ps at 273 K to 450 fs at 330 K. Similarly for $C_2(\tau)$, beyond the early librational time scales, the correlation functions decay faster with increased temperature, from 4.5 ps at 273 K to 1.4 ps at

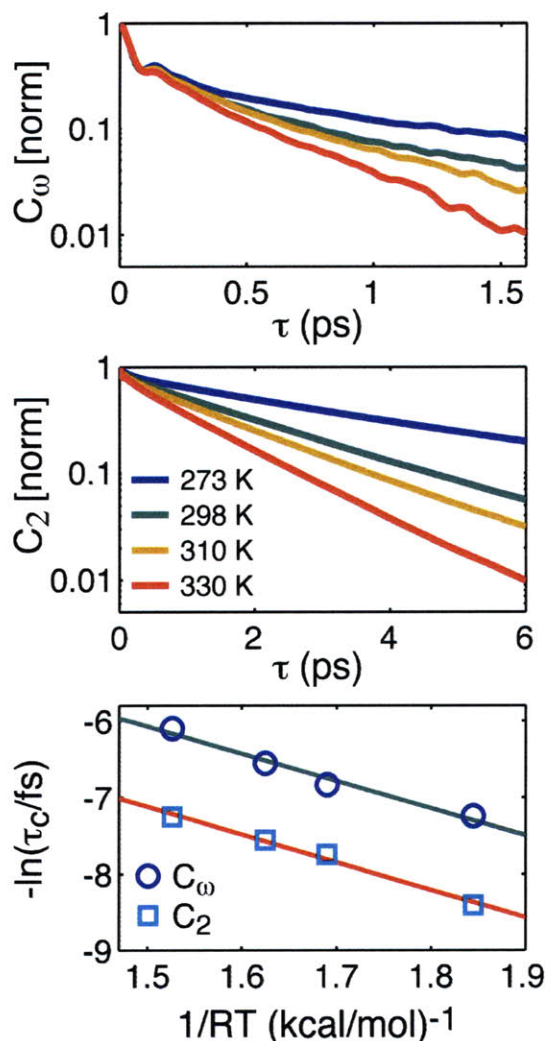


Figure 5-18: Normalized temperature-dependent correlation functions for (a) the OD stretch vibrational frequency, $C_\omega(\tau)$, and (b) OD bond reorientation, $C_2(\tau)$, from MD simulations with the SPC/E water model. (c) Arrhenius plots of correlation times in femtoseconds obtained from the simulation.

330 K. An Arrhenius plot (Figure 5-18c) for the temperature-dependent correlation times gives a barrier to frequency randomization of $E_{a,\omega} = 3.6$ kcal/mol and a barrier of $E_{a,rot} = 3.6$ kcal/mol for reorientation. The latter number is in agreement with the 3.5 kcal/mol value previously calculated by Laage and Hynes for the OH stretch [32]. These values are similar to what we observe experimentally (3.4 kcal/mol for spectral diffusion and 3.7 kcal/mol for reorientation) and the same quadratic behavior is observed for C_2 .

5.6.2 Polarizable SPC/FQ

The frequency and orientational correlation functions calculated with the SPC/FQ water model [88] were provided by Steve Corcelli (University of Notre Dame) and James Skinner (University of Wisconsin Madison). The MD simulations of neat H₂O using the electronically polarizable SPC-FQ model have been described previously. Here we will summarize the most salient details. As in the SPC/E model, in the SPC/FQ model the geometry of the individual water molecules is held rigid with an OH bond length of 1 Å and an HOH angle of 109.47°. Unlike the SPC/E model, SPC/FQ models electronic polarizability by allowing its three atomic centered point charges to fluctuate based on the instantaneous environment of the water molecule. In principle, the charges could be calculated self-consistently at each MD time step, but in practice the charges are regarded as dynamical variables in an extended Lagrangian and propagated in time [88]. This elegant approach results in a substantial computational savings. There are three reasons why the SPC/FQ model was chosen for this work on the temperature-dependent ultrafast IR spectroscopy of HOD/H₂O: (1) Previous studies at room temperature have shown that the SPC/FQ model exhibits rotational dynamics that are in better agreement with experiment than other commonly employed non polarizable water models (e.g. TIP4P [87] and SPC/E [31]) [88]. (2) At room temperature the longest time scale for the decay of the frequency fluctuation time correlation function is also in better agreement with experiment than TIP4P and SPC/E [85]. (3) The IR absorption and Raman scattering spectra computed for SPC/FQ are in excellent agreement with experiment from 10 to 90°C [78].

We calculated trajectories of 128 SPC/FQ H₂O molecules at five temperatures in cubic boxes whose sizes were chosen to mimic the experimental number density at 283, 303, 323, 343, and 363 K. The 1 ns trajectories were collected in the NVE ensemble with a 0.5 fs time step, where the charge degrees of freedom were maintained at 5 K by rescaling the charge velocities every 1000 steps. A running average of the temperature was monitored to ensure that it did not deviate outside of ± 1.5 K of

the target temperature. Other details regarding the MD simulations are contained in Reference [78].

Two quantities were computed from the trajectories: the OH bond orientational correlation function, $C_R = \langle P_2[\hat{u}_{OH}(0) \cdot \hat{u}_{OH}(t)] \rangle$, where P_2 is the 2nd Legendre polynomial and $\hat{u}_{OH}(t)$ is a unit vector that points along an OH bond, and the normalized electric field fluctuation time correlation function, $C_E(t) = \langle \delta E_{OD}(0) \delta E_{OD}(t) \rangle / \langle (\delta E_{OD})^2 \rangle$, where $E_{OD}(t)$ is the magnitude of the electric field due to the surrounding water molecules along an OH bond of interest and $\delta E_{OD}(t) = E_{OD}(t) - \langle E_{OD} \rangle$ represents the fluctuation of $E_{OD}(t)$ from its equilibrium value, $\langle E_{OD} \rangle$. $C_R(t)$ was computed for the 256 independent OH bonds in the simulations. Although the simulations were of neat H₂O, for the purposes of computing $C_E(t)$ each of the bonds in the simulation were assumed to be the OD stretch of interest, which assumes that the dynamics of a single HOD molecule in water are similar to that of an H₂O molecule. The electric fields along each OH bond were then computed using the instantaneous charges on each of the other 127 water molecules in the simulation, where the effects of long ranged electrostatics were incorporated using an approximation to the Ewald sum [195].

The rationale for computing the normalized electric field fluctuating correlation function is that, within certain approximations, $C_E(t)$ is equal to the normalized frequency fluctuation correlation function, $C_\omega(t)$, which can be extracted from the ultrafast 2D IR measurements on HOD in H₂O. The key assumption needed to connect $C_E(t)$ with $C_\omega(t)$ is that the instantaneous OD vibrational frequency of interest can be linearly related to the electric field along the bond, $\omega_{OD} = a + bE_{OD}$. Previous density functional theory calculations on 100 HOD·(H₂O)_n clusters containing between 4 and 9 water molecules extracted from a room temperature MD simulation have empirically established a linear relationship ($a = 2745.8 \text{ cm}^{-1}$ and $b = 4870.3 \text{ cm}^{-1}/\text{au}$) between the OD stretch frequency of HOD with the electric field due to the surrounding solvent along its bond. It is important to note, as a caveat, that more recent work on more and larger clusters, albeit for different water models, have found that quadratic relationships between the electric field and vibrational frequency

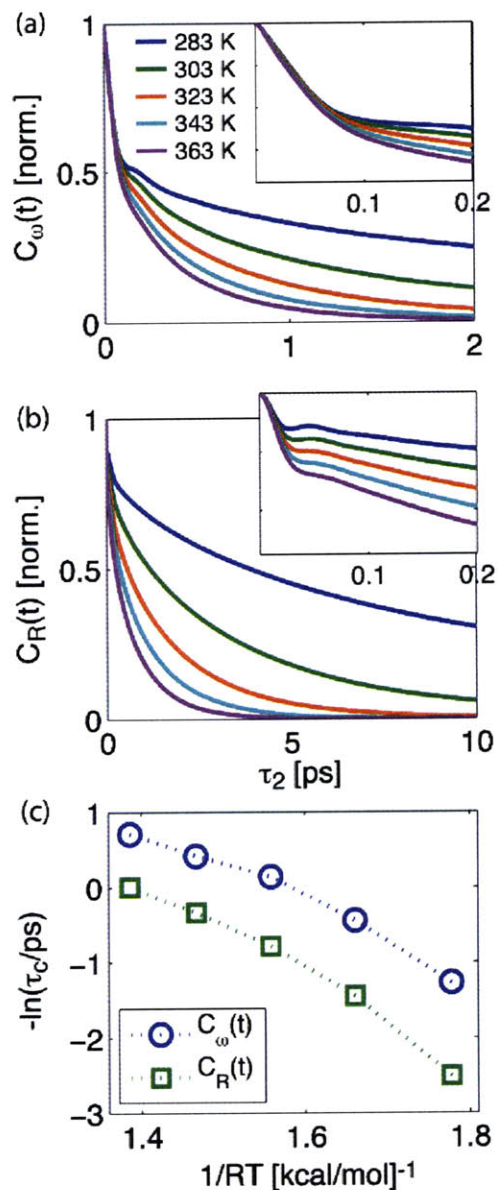


Figure 5-19: Normalized temperature-dependent correlation functions for (a) the OD stretch vibrational frequency, $C_\omega(t)$, and (b) the bond reorientation, $C_{R,2}(t)$, from MD simulations with the SPC/FQ water model. (c) Arrhenius plot of the correlation times in femtoseconds obtained from exponential fits to the picosecond decay.

are more appropriate [55, 56]. Nevertheless, for discerning trends in the long time decay of the frequency fluctuation correlation function as a function of temperature, invoking the approximately linear relationship available from the previous literature is reasonable.

The results for the frequency time correlation functions, $C_\omega(t)$, and OD bond

orientation correlation functions, $C_{R,2}(t)$ for five temperatures in the range from 283 to 363 K are shown in Figure 5-19. The functions show the same trend as observed in the experiment: the long time decay is faster with increasing temperature. Also, similar to the results using the SPC/E model, we find that the inertial dynamics are roughly independent of temperature, although the amplitude does increase with temperature for the orientational correlation functions. We fit the picosecond decay with single exponentials and the time constants are shown in an Arrhenius plot in Figure 5-19c. The behavior is clearly nonlinear, which is similar, although more pronounced, than the experimental orientational relaxation and other observables (see Figure 5-17). Interestingly, the temperature-dependent trends for the two relaxation processes are similar within a scaling factor. We find the activation energy is larger for the polarizable SPC/FQ model than the activation energy determined with the fixed-charge SPC/E model [182]: 6.4 kcal/mol for $C_{R,2}(t)$ and 5.0 kcal/mol for $C_{\omega}(t)$.

Using temperature-dependent experimental NMR measurements of specific molecule-fixed unit vectors and MD simulations, Ropp et al. showed that rotational motion in water is anisotropic [196]. We show the calculated orientational correlation function for the OD bond vector (bond), out of plane vector (perp), C_2 symmetry axis, and H-H intramolecular axis in Figure 5-20. Although the time scales differ, the non-Arrhenius behavior is the same for all the calculated orientational correlation functions.

5.7 Concluding Remarks

By using ultrafast infrared spectroscopy to measure the temperature-dependent picosecond decay of reorientation and spectral diffusion of the OD stretch of dilute HOD in H_2O , and comparing the non-Arrhenius behavior to previous measures of relaxation processes in water, we have found that hydrogen bond rearrangement in water is collective. To determine the picosecond decay we self-consistently model 2D IR, pump-probe, and linear absorption measurements with a response function formalism that includes the effects of spectral diffusion, population lifetime, and reorientation

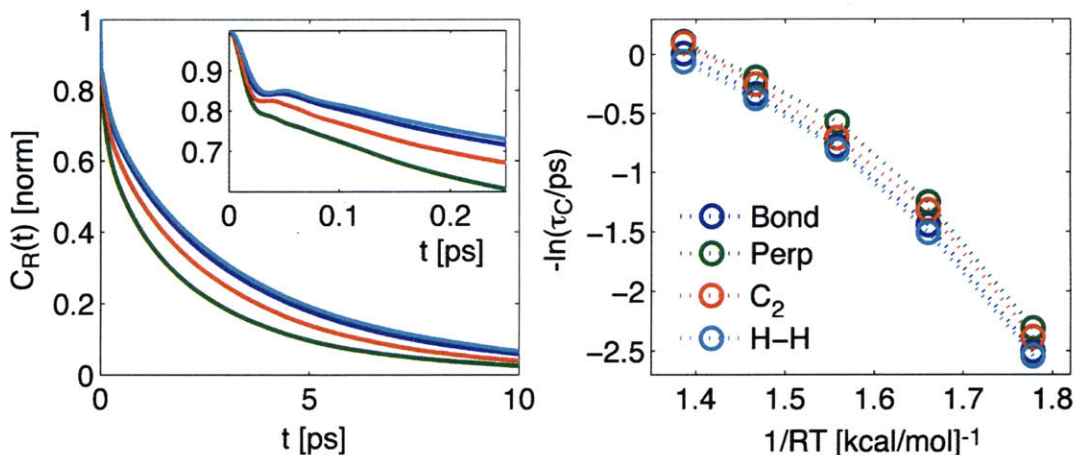


Figure 5-20: (a) Orientational correlation function from MD simulations for the OD bond vector (blue), out of plane vector (green), C_2 symmetry axis (red), and H-H intramolecular axis (cyan). (b) Arrhenius plot of the orientational correlation functions.

motion and non-equilibrium heating upon vibrational relaxation. Prior experimental and theoretical work has shown that hydrogen bond switching is concerted and involves large angle reorientation [71, 1]. This work provides evidence that translation and reorientation are intertwined with hydrogen bond rearrangement in the collective reorganization of the liquid. MD simulations of temperature-dependent OD vibrational and orientational correlation functions are used to support our conclusions. It remains a question what the correlation length for reorganization is, which collective variables may be best suited to describe or study hydrogen bond rearrangement, and the microscopic origin of the non-Arrhenius behavior from the liquid to supercooled regions of water.

5.8 Acknowledgments

We would like to thank Krupa Ramasesha, Sean Roberts, and Joel Eaves for the temperature-dependent MD simulations using the SPC/E water model. We would like to thank Krupa Ramasesha for her help acquiring the 2D IR and pump-probe anisotropy measurements.

.1 Influence of the H₂O Stretch and Combination Band

We explicitly include the background absorption of the combination band and stretch of the bath H₂O in our model to explore the origin of the long time offset observed in the phase line slope. The H₂O combination band absorbs in the OD stretch region and there is a relatively small amount of absorption from the H₂O stretch. However, linear absorption and heterodyned third order measurements scale with the transition dipole to the second and fourth power, respectively. The molar absorptivity of the H₂O combination band and stretch are ~ 3.5 and $\sim 100 \text{ M}^{-1} \text{ cm}^{-1}$ at the peak, respectively [112]. Given the sensitivity of the transition dipole on environment, with an increasing transition dipole with hydrogen bonding, it is not unreasonable for the H₂O stretch to contribute to the third order signal in the region of the OD stretch [197, 112].

Since H₂O was explicitly included in the model, all of the parameters discussed for the OD stretch had to be defined for the H₂O combination band and stretch. The transition frequencies, ω_{10} , and transition dipoles, μ_{10} , are determined by fitting the temperature-dependent linear absorption of pure H₂O. The fits are shown in Figure 5-1b. The room temperature anharmonicities used to determine ω_{21} are 300 cm^{-1} for the H₂O combination band [112] and 250 cm^{-1} for the H₂O stretch [109]. The anharmonicity is held constant for all temperatures. Room temperature vibrational lifetime, T_1 , and intermediate state lifetime, T^* , are 140 fs and 840 fs for the H₂O combination band [112] and 240 fs and 740 fs for the stretch [109], respectively, which are held constant for all temperatures. It is assumed that the H₂O background shares the same orientational and frequency correlation function as the OD stretch at each temperature. The change in transition dipole, $\Delta\mu$, and intensity of the TSGS response, A^{TSGS} , for the H₂O combination band and stretch are set to values previously found for the OH stretch of HOD in D₂O at room temperature and held constant for all temperatures [198]. The temperature-dependent parameters are given in Table 2 and the temperature-independent parameters are given in Table 3.

In Figure S-21 we show 2D surfaces calculated with the model at 278 K at $\tau_2 = 0$ fs,

H₂O $\nu_L + \delta$	278 K	286 K	295 K	323 K	345 K
ω_{10} [cm ⁻¹] (from FTIR)	2134	2128	2121	2097	2075
ω_{10} [cm ⁻¹] (input model)	2143	2138	2130	2106	2084
$\Delta\omega$ [cm ⁻¹] (with 1 K)	-0.72	-0.75	-0.80	-0.92	-1.03
H₂O ν_S					
ω_{10} [cm ⁻¹] (from FTIR)	3389	3395	3401	3419	3433
ω_{10} [cm ⁻¹] (input model)	3403	3409	3415	3432	3446
FWHM [cm ⁻¹]	393	390	392	401	409

Table 2: Summary of the temperature-dependent parameters contained within our spectral model for the stretch (ν_S) and combination band ($\nu_L + \delta$) of H₂O.

	H₂O $\nu_L + \delta$	H₂O ν_S
Δ [cm ⁻¹]	300	250
$\Delta\omega$ [cm ⁻¹]	See Table 2	0.66
FWHM [cm ⁻¹]	300	See Table 2
T_1 [fs]	140	240
T^* [fs]	840	740
$\Delta\mu$	0.9986	0.9986
A^{TSGS}	62	62

Table 3: Summary of the parameters contained within our spectral model for the stretch (ν_S) and combination band ($\nu_L + \delta$) of H₂O that do not depend on temperature.

600 fs, and 4 ps. The first and second columns show the results of the calculation with only the response of the H₂O combination band and stretch, respectively. Although the lifetimes of the H₂O stretch and combination band are relatively short ($T_1 < 300$ fs) the modes still contribute at long waiting times due to the TSGS. The H₂O stretch blue-shifts and the combination band red-shifts with increasing temperature; therefore, the signal from the TSGS is positive in the region of the OD stretch for both modes. Although the peak of the H₂O stretch is shifted from the OD stretch $\sim 2.4\times$ further than the combination band at 278 K, we find the H₂O stretch has a larger contribution to the signal, albeit still small, near the peak of the OD stretch ($\omega_1, \omega_3 \sim 2500$ cm⁻¹) at all waiting times. In the third column, we show the result when all three modes are included and the fourth column shows the result of windowing by the experimental spectrum after Fourier transform. The experimental spectrum decreases the amplitude of the $\nu=2\leftarrow 1$ signal and the TSGS; and the residual atmospheric CO₂ additionally absorbs from ~ 2320 to 2360 cm⁻¹.

.2 Vibrational Stokes Shift

The spectroscopic model used in this study assumes the OD stretch is coupled to a thermally occupied harmonic bath [70]. The complex correlation function is proportional to the coupling parameter, λ , which is determined by fitting the FWHM of the linear absorption spectrum. At room temperature $\lambda = 2.7\times 10^{-3}$ fs⁻¹, which represents a Stokes shift of 14 cm⁻¹. If the input frequency and orientational correlation functions and lifetime are kept constant, and only the temperature is changed, the FWHM calculated with the model at the four other experimental temperatures are within $\sim 1\%$ of experimental values. However, the approximation predicts a linear relationship between temperature and FWHM and a quadratic relationship is observed experimentally (see Chapter 4). If the nonlinear measurements are calculated with the same input λ , frequency and orientational correlation functions, and lifetime, but with changing temperature, there is a negligible difference in dynamics. Therefore, the correlation functions must be adjusted at each temperature to match

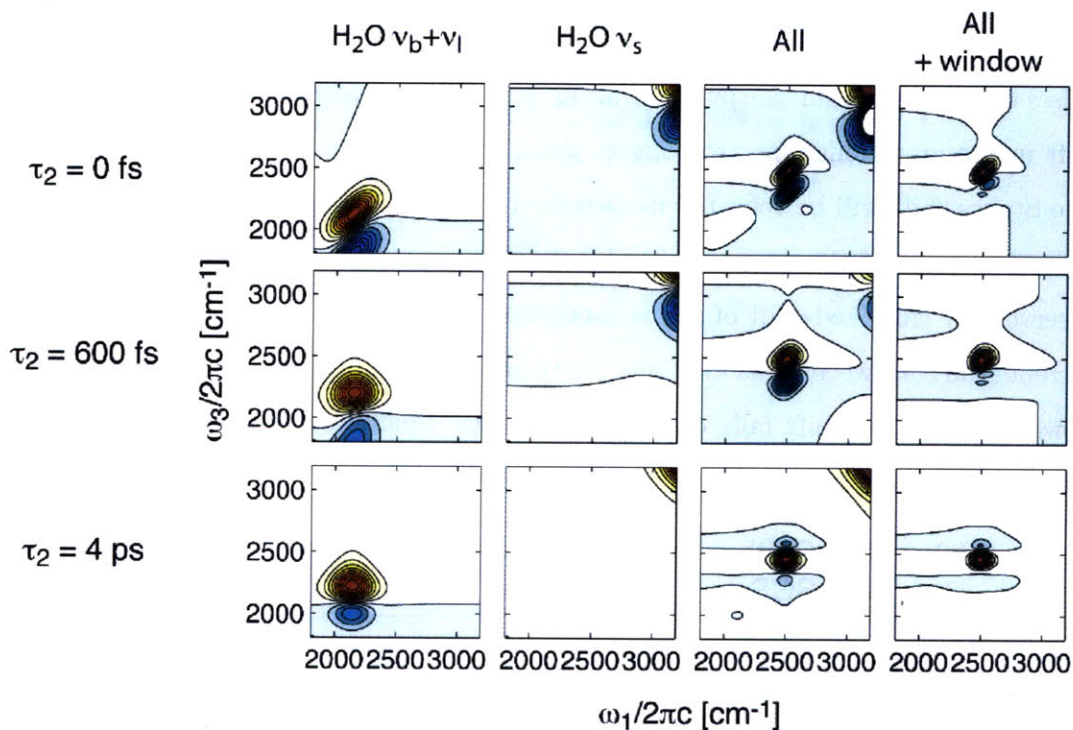


Figure -21: Absorptive 2D surfaces calculated with our spectral model at 278 K at $\tau_2 = 0$ fs (first row), 600 fs (second row), and 4 ps (third row). The calculation includes only the H₂O combination band (first column), only the H₂O stretch (second column), the H₂O combination band and stretch and OD stretch (third column), and all three modes windowed by the experimental spectrum.

the experiment, which results in a different λ for each temperature (see Table 5.1).

The model developed by Rezus and Bakker to fit vibrational transient absorption constructs the time-dependent signal from two time-independent spectral line shapes [120]. The model does not include spectral shifts that would arise from a vibrational Stokes shift. In 1999, Woutersen and Bakker reported PP experiments on the OH stretch of HOD in D₂O that probed dynamics on the red and blue side of the line shape upon pumping on the blue and red side, respectively [60]. The authors use a Brownian oscillator model to fit the experimental traces and report a Stokes shift of 74 cm⁻¹ [60]. With MD simulations, Lawrence and Skinner calculated a Stokes shift of 57 cm⁻¹ for the same system [155]. However, with a response function formalism, Yeremenko reproduced the results of Woutersen and Bakker without including a Stokes shift in the model; the observed behavior arises from the spectrally narrow pump and probe

pulses interacting within the pulse duration [187]. The existence of a dynamical Stokes shift in the vibrational spectroscopy of water has yet to be verified experimentally. The Stokes shift will be reflected in dispersed pump probe measurements as a time-dependent shift of the zero crossing between the $\nu=1\leftarrow 0$ and $\nu=2\leftarrow 1$ peaks. We observe a 27 cm^{-1} red-shift of the zero-crossing by 150 fs for all temperatures in the current study. However, this may very likely be an artifact of cross-phase modulation. However, a Stokes shift falls out of the response function formulism used to self-consistently model the linear and non-linear measurements.

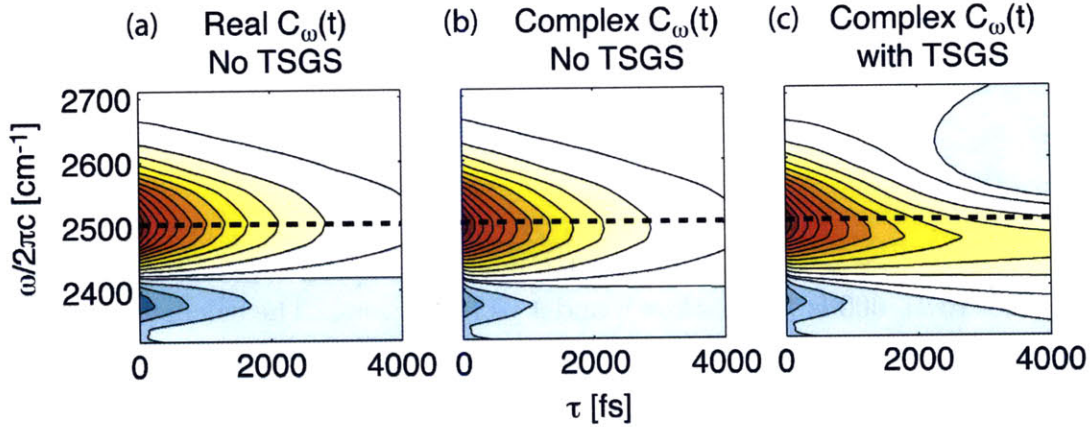


Figure S-22: Dispersed pump-probe calculated with the model at 278 K with (a) $C'_\omega(t)$ without including the TSGS, (b) $C_\omega(t)$ without including the TSGS, and (c) $C_\omega(t)$ including the TSGS.

Since the TSGS also causes a shift in the zero-crossing we calculate the dispersed pump-probe (DPP) with and without the TSGS. In Figure S-22, we show DPPs calculated from the model at 278 K for three cases: (a) only including the real part of $C_\omega(t)$, or $C'_\omega(t)$, and not including the TSGS, (b) using the complex $C_\omega(t)$ but not including the TSGS, and (c) using the complex $C_\omega(t)$ and including the TSGS. In Figure S-22a the $\nu=1\leftarrow 0$ and $\nu=2\leftarrow 1$ peaks decay at the same rate with no time-dependent shift in the zero crossing. As can be seen in Figure S-22b, there is a shift in the zero-crossing with increased delay, even when the TSGS is not included. The zero crossing red-shifts by 9.1 cm^{-1} from $\tau_2 = 0$ to 400 fs and an additional 5.9 cm^{-1} between 400 fs and 4 ps. When the TSGS is included, the zero crossing red-shifts an

additional 1.3 cm^{-1} between $\tau_2 = 0$ to 400 fs and from $\tau_2 = 400$ fs to 4 ps the zero crossing shifts a total of 62 cm^{-1} . The effect of the population relaxation induced TSGS can clearly be seen in Figure S-22c: there is a persistence of the positive peak to longer waiting times and the appearance of a negative peak at higher frequencies [175, 94].

.3 Frequency-Dependent Reorientation

With MD simulations, Laage and Hynes found the primary mechanism of reorientation in water is through a large angle jump concurrent with switching a hydrogen bond partner [1, 32]. The mechanism leads to predictions for what will be observed in a frequency-resolved anisotropy measurement since the frequency at which a molecule absorbs is sensitive to its environment. Correlation between frequency and reorientation has been observed with MD simulations of the OH stretch of HOD in D_2O , which found a larger amplitude inertial reorientation in the orientational correlation function for molecules absorbing on the blue side of the line width [45]. The 2D anisotropy has also been calculated with MD simulations for the OH stretch of HOD in D_2O [74]. The study found that the anisotropy of molecules that are initially in broken or strained hydrogen bonds (NHB) drops from 0.4 to 0.25 within 300 fs, whereas there is little change in anisotropy for molecules initially in stable hydrogen bonds (HB) within that time scale. Also, the drop in anisotropy in the off-diagonal region of the 2D surface is similar to the diagonal region for NHB indicating that molecules reorient in order to switch from NHB to HB and vice versa [74].

Bakker et al. measured the pump-probe anisotropy of the OD stretch of HOD in H_2O pumping at the center and blue wing of the line width [119]. They find that when pumping at the center of the line width the anisotropy decay is independent of frequency. However, when pumping on the blue wing, the anisotropy of the molecules on the red side of the line width drops to 0.2 by the initial time point, 200 fs. This observation suggests that molecules initially excited on the blue wing must reorient to return to the red side of the line width [119]. Moilenan et al. measured the pump-

probe anisotropy of the OD stretch of HOD in H₂O at three temperatures: 1, 25, and 65°C [121]. Although spectral information is obscured within the first 200 fs due to non-resonant effects, the authors extrapolate to 100 fs and find, at room temperature, there is a greater initial drop in anisotropy on the blue side of the line width (~ 0.36 at 2500 cm^{-1} compared to ~ 0.32 at 2625 cm^{-1}) and after 200 fs, the anisotropy decay is frequency independent. At 65°C the difference across the line width at 100 fs is exaggerated compared to room temperature and at 1°C they observe little difference across the line width [121]. Finally, Skinner et al. calculated the temperature dependence of the pump-probe anisotropy with MD simulations and found that although there is a larger initial drop in anisotropy at higher temperature, the frequency dependence, in which the anisotropy drops to a lower value on the blue side of the line width upon inertial reorientation, is independent of temperature [179].

In this section we will present the room temperature pump-probe and waiting time dependent 2D anisotropy of the OD stretch of HOD in H₂O. We find a larger initial drop in anisotropy on the blue side of the line width for both measurements. We will also show the effect of non-resonant effects on the pump-probe anisotropy, which must be treated with care when extracting information on the inertial decay.

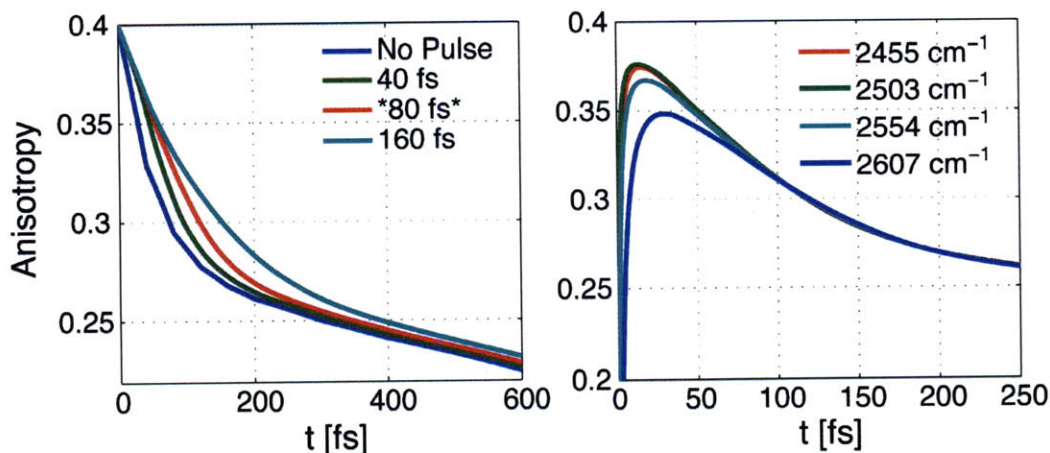


Figure -23: The calculated anisotropy at room temperature from our spectral model with the effect of pulse convolution (left). The frequency-dependence of the calculated anisotropy at room temperature from our spectral model including the effect of pulse convolution and cross phase modulation (right).

First we will show the effect of the pulse and non-resonant effects, explicitly cross phase modulation, on pump-probe anisotropy. In the model calculation, we begin with the S_{zzzz} and S_{zzyy} pump-probes calculated with our spectral model at room temperature and convolve a Gaussian pulse with different pulse lengths with both polarization geometries before determining the anisotropy. We show the result in Figure S-23 for 40, 80 and 160 fs pulses. The anisotropy still begins at 0.4 but the inertial decay, 50 fs without pulse convolution, appears slower when the pulse is included. In the current study the pulse width is ~ 80 fs (shown in red), which will obscure the anisotropy until ~ 200 fs. Next we include cross phase modulation from a fit to the experimentally measured cross phase modulation (XPM) assuming the pulse is not chirped (see Chapter 2). The result is shown in Figure S-23(right). There is no frequency-dependence included in the model, however, XPM introduces an apparent difference across the frequency range until ~ 80 fs. Additionally, the anisotropy does not begin at 0.4. The XPM has the smallest effect near the peak frequency of the pulse and becomes more important with detuning between the peak of the pulse and probe frequency. In other words, if one were to take a slice at 50 fs the value of the anisotropy would appear progressively smaller as the probe frequency is detuned from the peak of the pulse.

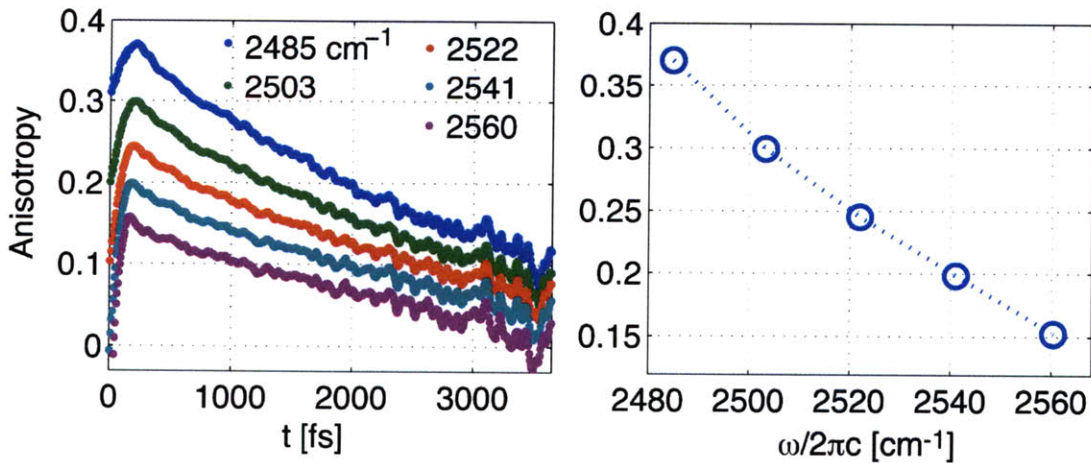


Figure -24: Slices in frequency (left) and $t = 200$ fs (right) of the dispersed pump-probe anisotropy acquired at room temperature.

In Figure S-24 we show the experimental dispersed pump-probe anisotropy of the OD stretch of HOD in H₂O acquired at room temperature. Similar to what we observe in the model calculation when the XPM is included, the anisotropy does not begin at 0.4. Nonetheless, if we take a slice at $t = 200$ fs, where pulse effects should no longer be important, we find that the anisotropy has dropped to a considerably lower value on the blue side of the line width. This observation agrees with the molecular jump mechanism for reorientation [1, 32] and previous MD simulations of the frequency dependence of the anisotropy [45]. Also, although the frequency dependence of the initial drop is more severe compared to the previous measurement [121], we notice the measurements agree in that the long time decay is identical over the frequency range.

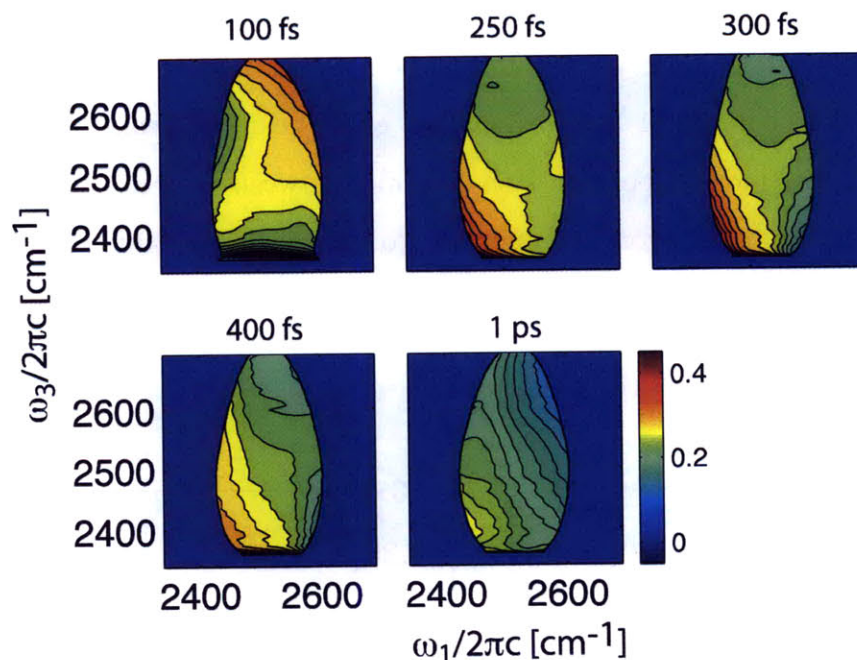


Figure S-25: Absolute value 2D anisotropy of dilute HOD in H₂O acquired at $\tau_2 = 100, 250, 300, 400, 1000$ fs.

In Figure S-25 we show the absolute value 2D anisotropy of HOD in H₂O at the waiting times, $\tau_2 = 100, 250, 300, 400,$ and 1000 fs. The absolute value 2D anisotropy, which is calculated from absolute value 2D surfaces acquired in the parallel and

perpendicular geometry, is used to avoid divergence in the anisotropy determined from the absorptive surfaces due to the node between the $\nu=1\leftarrow 0$ and $\nu=2\leftarrow 1$ peaks. At the earliest waiting time, $\tau_2 = 100$ fs, the anisotropy is higher at $\omega_1 = \omega_3 = \text{blue}$, which disagrees with the trend observed for the following waiting times. However, at 100 fs pulse effects are most likely still important. Past 100 fs the anisotropy is higher on the red side of the diagonal relative to both the blue side of the diagonal and the off-diagonal regions. This observation is in reasonable agreement with what has been calculated with MD simulations [74] and what is suggested by the molecular jump mechanism for reorientation [1]. In Figure S-26 we show slices in the absolute value anisotropy at $\omega_1 = 2475$ (left) and 2550 cm^{-1} (right). On the red side of the line width the anisotropy is slightly lower at $\omega_3 = \text{blue}$ and remains largely unchanged for the first four waiting times. At 1 ps the anisotropy drops to ~ 0.22 . On the blue side of the line width the anisotropy is again slightly lower on the $\omega_3 = \text{blue}$ side and drops faster than the red side. The results of the 2D anisotropy measurements need to be confirmed experimentally and analyzed in more detail to extract quantitative information on the correlation between frequency shifts and reorientation.

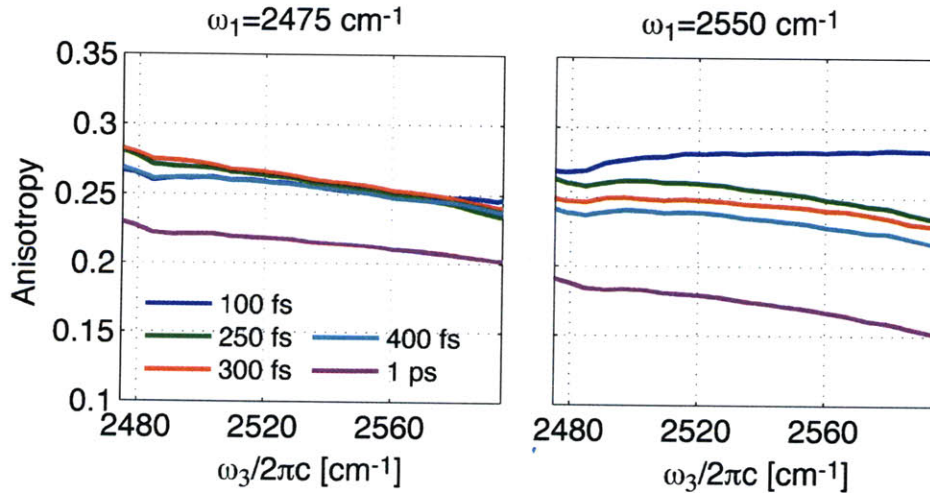


Figure -26: Slices in the 2D absolute value anisotropy with waiting time at $\omega_1 = 2475 \text{ cm}^{-1}$ (left) and $\omega_1 = 2550 \text{ cm}^{-1}$ (right)

Appendix A

Pump-Probes and 2D IR of Pure D₂O

In this thesis we presented linear and non-linear measurements of dilute HOT and HOD in H₂O. An isotopically dilute system provides a probe of local structural dynamics as resonant intermolecular transfer is turned off and non-resonant intermolecular transfer will occur on a longer time scale than spectral diffusion. Dynamics of the isotopically dilute system imitates neat water for any process largely dominated by electrostatics. However, studying pure water and the effects of delocalization is an interesting problem in of itself. We have, therefore, performed preliminary experiments on pure D₂O. In the gas phase, the symmetric (ν_1) and antisymmetric (ν_3) stretch of D₂O absorb at 2669.40 and 2787.92 cm⁻¹, respectively [199]. In the condensed phase the degeneracy between the local modes is largely broken, given the different local environments, although there is opportunity for coupling to nearby oscillators. Band center shifts to 2500 cm⁻¹ and the FWHM is 325 cm⁻¹, which is ~ 2.7 x broader than the frequency splitting in the gas phase. Delocalization has been shown to affect both linear and non-linear measurements of pure water [200, 56]. For instance, Auer and Skinner recently calculated the IR and Raman spectra of H₂O with a mixed quantum classical theoretical method and found the peak at 3250 cm⁻¹ in the VV Raman spectrum arises from collective interactions [56]. The calculation of the line shapes included both intramolecular coupling and intermolecular coupling

estimated by transition dipole coupling. They found the instantaneous distribution of local mode frequencies of HOD in D₂O and pure H₂O was very similar and, when the coupling was turned off, the relatively broad IR line shape calculated for H₂O resembled the line shape for the isotopically dilute system. In Figure A-1 we show the normalized linear absorption spectrum of pure H₂O (blue), pure D₂O (green), and the OD stretch of HOD in H₂O (red) scaled in frequency by their respective gas phase frequencies (2723.68 cm⁻¹ for the OD stretch of HOD [159]). For H₂O and D₂O the average of the symmetric and antisymmetric gas phase frequencies was used (for H₂O $\nu_1 = 3657.05$ cm⁻¹ and $\nu_3 = 3755.93$ cm⁻¹ [199]). Indeed the line shape for H₂O and D₂O is broader than the isotopically dilute system. It is interesting to note that the line shape of D₂O is broader than H₂O. This is the opposite trend than what is expected for motional narrowing and what has been observed for the isotopically dilute system [174].

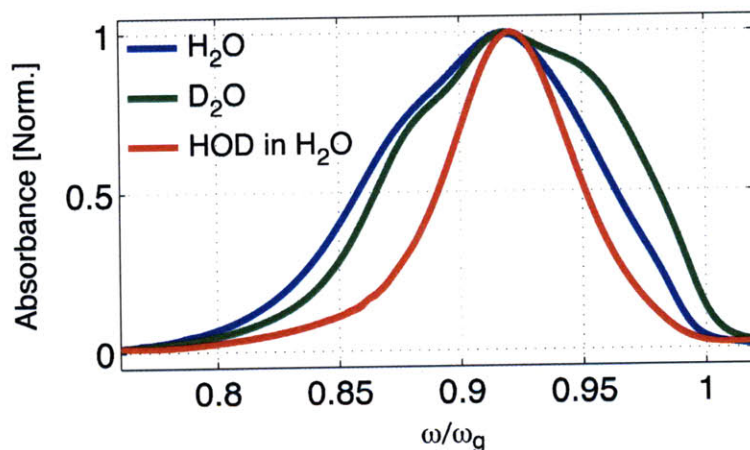


Figure A-1: Normalized linear absorption spectrum of H₂O (blue), D₂O (green), and the OD stretch of HOD in H₂O (red) scaled in frequency by their respective gas phase frequencies.

Miller and co-workers measured the room temperature and temperature dependent 2D IR and pump-probes of pure H₂O [200, 107]. At room temperature they found spectral diffusion occurred within 50-100 fs, which lead to the suggestion that spectral diffusion was dominated by librational motion. They found that as temper-

ature was decreased to 274 K frequency correlations persisted beyond ~ 200 fs. The relatively fast ~ 80 fs anisotropy decay, which was attributed to resonant intermolecular energy transfer, was unaffected by temperature. Finally, it was found that the lifetime increased from 180 fs at 274 K to 300 fs at 340 K. Paarman et al. used a fully anharmonic nonadiabatic simulation procedure, which explicitly treated intermolecular coupling as well as fluctuations and anharmonicities of transition frequencies and dipole moments, to calculate the pure H_2O 2D IR and anisotropy measurements [201]. They found the fast dephasing observed in the 2D IR measurements was mainly a result of intramolecular mixing between states in the two-dimensional anharmonic OH stretch potential. Intermolecular coupling was necessary match the fast anisotropy decay, but they found 12 cm^{-1} coupling sufficient [201]. For pure D_2O , only pump probes have been reported to this point, which show a 400 fs lifetime [113]. Here we present 2D IR measurements and pump-probes (S_{zzzz}) for pure D_2O . Indeed we observe that the dynamics are very fast and, given the broad absorption line shape of D_2O , our pulse width limits the spectral information.

In Figure A-2a we show the dispersed pump-probe of pure D_2O acquired in the $zzzz$ polarization geometry. We held D_2O between two CaF_2 windows without a spacer. The optical density was ~ 1 . We acquired dispersed pump-probes by fast scanning the delay between the pump and probe, then averaging the scans. Slices in frequency are shown in Figure A-2c. Based on the previous measurement of the lifetime of the OD stretch of D_2O the decay observed within the first ~ 500 fs corresponds to decay from the excited state. The positive (negative) amplitude to the red (blue) of $\sim 2600 \text{ cm}^{-1}$ that grows in with delay between the pump and probe is most likely due to the TSGS, which appears to have a much larger effect in pure D_2O compared to isotopically dilute water. In Figure A-2b and Figure A-2d we show slices in time. Also, in Figure A-2b we show the absorption spectrum of D_2O as the dashed gray line. Since our pulse width ($\sim 230 \text{ cm}^{-1}$) is narrower than the absorption band the transient absorption signal is narrowed. The delay times in Figure A-2b correspond to the waiting times of the 2D surfaces we will show shortly. In Figure A-2d the delay times are 0 (blue), 100 fs (green), 200 fs (red), 400 fs (cyan), 800 fs (magenta), 1.6 ps

(gold), and 3.2 ps (dark gray). It is surprising to see the signal at long time surpasses the signal at $t = 0$ fs. If we fit a mono-exponential the frequency slice that corresponds to the zero crossing between the positive and negative amplitude of the TSGS, the magenta line shown Figure A-2a, we find a decay time of 355 fs. This time scale is faster than the reported T_1 , which is expected since molecular rotations contribute to the decay given that the measurement is in the $zzzz$ polarization geometry.

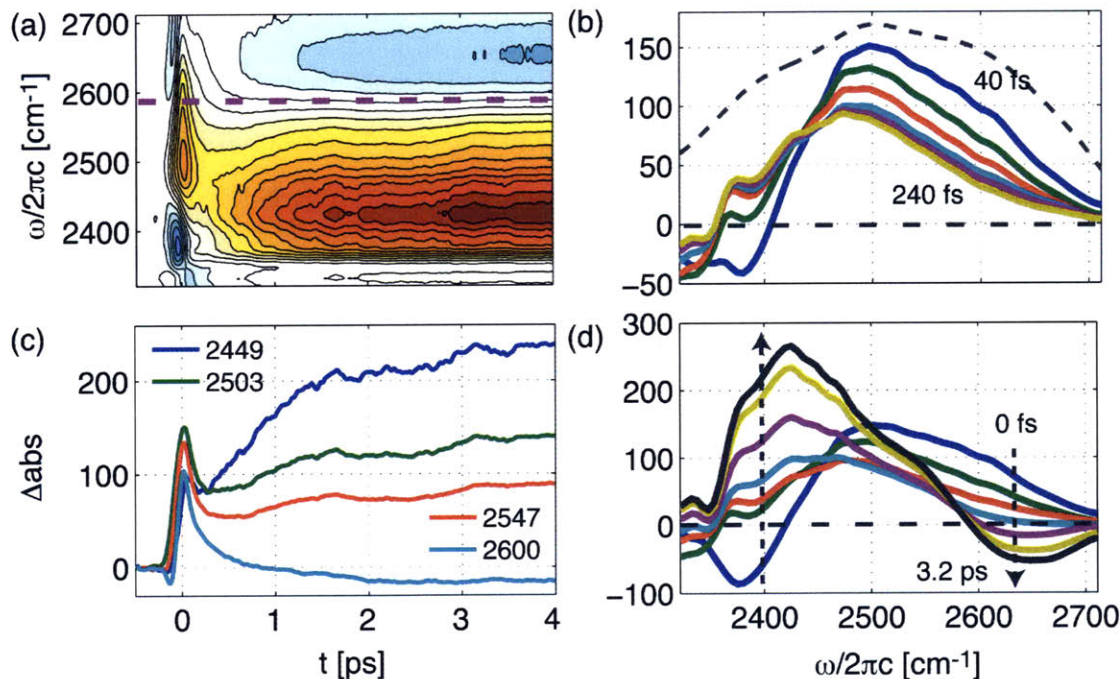


Figure A-2: (a) DPP of pure D₂O in the $zzzz$ polarization, (b) Slices in frequency of the DPP, (c) Slices in time of the DPP with the D₂O spectrum shown in dashed gray, and (d) Slices in time to longer delay times.

In Figure A-3 we show 2D IR surfaces for pure D₂O taken in the $zzzz$ polarization geometry in the pump-probe geometry by step-scanning the τ_1 axis in 2 fs steps to 600 fs. The sample conditions were the same as the PP experiments. Again, the response is spectrally narrowed by our pulse spectrum. The $\nu=1\leftarrow 0$ peak is very broad, and although it is singly peaked, the line shape is not symmetric. At the two earliest waiting times there appears to be off-diagonal broadening that disappears by ~ 120 -160 fs. This is most likely due to non-resonant response. From $T = 120$ - 200 fs the spectra look very similar, although the $\nu=2\leftarrow 1$ peak is decaying. At $T = 240$

fs the $\nu=1\leftarrow 0$ peak appears to have broadened along ω_1 . Since the dynamics in pure water are relatively very fast it would be best to repeat the experiments with shorter pulses in time and, therefore, a broader spectral range.

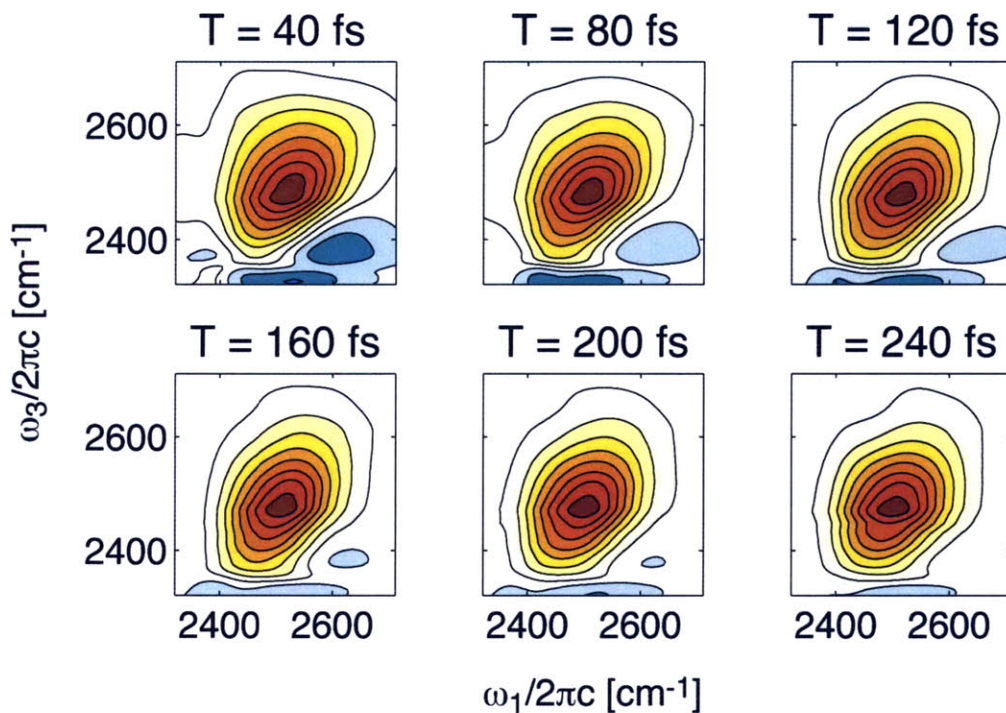


Figure A-3: 2D IR of pure D₂O at six waiting times, $T = 40, 80, 120, 160, 200,$ and 240 fs.

Appendix B

Linear Absorption of Isotopically Dilute Ice Ih

The vibrational frequency of the proton stretch in water is sensitive to its environment. This link stems from the studies of Novak [42], who found a strong correlation between the interatomic oxygen-oxygen distance of hydrogen bonded partners, R_{OO} , and ω_{OH} in hydrogen bonded solids, which was corroborated with molecular dynamics (MD) simulations [68, 46]. Tokmakoff and co-workers used two dimensional infrared spectroscopy (2D IR), a technique capable of distinguishing dynamics of spectrally distinct environments while maintaining fast time resolution, to study dynamics across the line width of the OH stretch of HOD in D_2O [71, 73]. They found an asymmetric line shape that indicated water molecules originally absorbing at non-hydrogen bonded (NHB) frequencies, which include both broken and strained hydrogen bonds, return to hydrogen bonded (HB) frequencies within the fastest intermolecular time scales in water [71, 73]. How would the line shape appear in an experiment where the NHB species are largely removed? This experiment can be realized with 2D IR of ice.

All crystalline phases of ice follow the ice rules set forth Bernal and Fowler in 1933 [23], which are: (1) water molecules in ice are intact, i.e. two hydrogens are covalently bonded to each oxygen, neglecting the small fraction of ionized molecules (this rule has the exception ice X), (2) each water molecule is orientated such that two

intramolecular OH bonds are directed approximately toward two of the four nearest neighboring oxygen atoms, and (3) only one hydrogen atom lies approximately along the line joining adjacent oxygen atoms. Weaknesses, or Bjerrum defects, in the ice crystal occur when the ice rules are disobeyed. A L ("leere") defect occurs when two adjacent oxygen atoms have no intervening proton (O...O), and a D ("doppel") defect occurs when there are two hydrogen atoms between adjacent oxygens (O-H...H-O). Other defects may be caused by the presence of H_3O^+ and OH^- ions. Hexagonal ice (ice Ih) is the form of all natural snow and ice on Earth, as evidenced in the six-fold symmetry in ice crystals grown from water vapor, or snow flakes. The average structure belongs to the P63/mmc centrosymmetric space group. The structure is shown in Figure B-1. It consists of puckered layers perpendicular to the c-crystal axis containing water molecules in a chair form hexagonal ring. There are also boat form hexagonal rings formed by three molecules in one layer and three in an adjacent layer. The O...O distance for H_2O is approximately 2.75 Å [202], compared to 2.98 Å for the gas phase dimer [203]. As Pauling noticed in 1935 [204], even under the ice rules there are six possible orientations for every water, or put another way, the hydrogens are disordered. This is true for ice Ih and this give rise to a zero point energy of 3.41 J mol⁻¹ K⁻¹ [205].

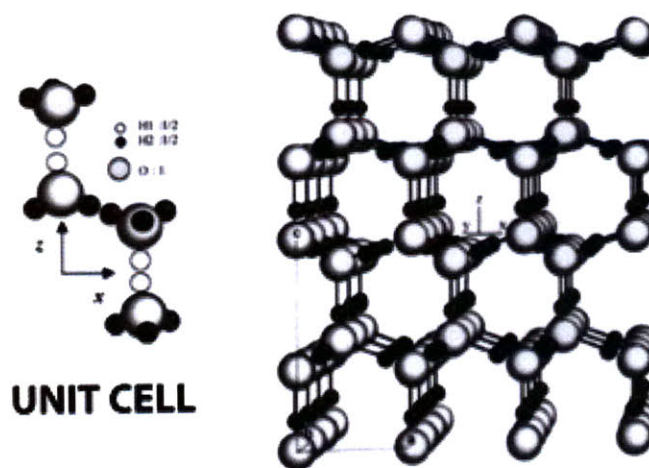


Figure B-1: Structure of Ice Ih [206]

We show the linear absorption of H₂O and dilute HOD in H₂O in Figure B-2. The sample is held in a brass sample cell between CaF₂ windows with a 6 μm spacer and the temperature is controlled by water/glycerol circulation. The temperature is monitored with a thermocouple taped to the top of the brass sample cell. The red trace was taken near room temperature (25°C) and the dark blue trace is ice (which forms at $\sim -4^\circ\text{C}$, according to the thermocouple). The peak wavelength, line width (FWHM), and peak absorption of the OD stretch, with the background H₂O subtracted, are shown in Figure B-3. Starting at room temperature, the OD stretch red-shifts from 2509 cm^{-1} to 2444 cm^{-1} , the peak absorbance increases by $\sim 4.7\times$ (0.24 to 1.15), and the FWHM decreases by $\sim 4.1\times$ (165 to 40 cm^{-1}) upon freezing. The red-shift in frequency is expected given that R_{OO} in ice Ih is $\sim 2.75 \text{ \AA}$ (H₂O) compared to $\sim 2.85 \text{ \AA}$ (HOD in D₂O) [207] on average at room temperature. In crystalline ice the oxygen atoms are ordered, therefore, one would expect a large decrease in the static distribution of frequencies and correspondingly a decrease in the line width. In the liquid phase the line shape is mainly inhomogeneously broadened [155]. For instance, a simple calculation shows that the lifetime of ω_{OD} in water contributes $\sim 3.5 \text{ cm}^{-1}$ to the 165 cm^{-1} line width. The lifetime of ω_{OD} in ice has yet to be measured, however, the lifetime of ω_{OH} in isotopically dilute ice is 380 fs [97]. The FWHM of ω_{OH} in the ice form is $\sim 50 \text{ cm}^{-1}$ compared to $\sim 265 \text{ cm}^{-1}$ in the liquid phase (not shown). Therefore the lifetime contributes $\sim 25\%$ to the line width in ice compared to $\sim 3\%$ in the liquid phase (given a 700 fs lifetime [93]). Li and Skinner calculated the Raman and IR spectrum for isotopically dilute HOD in H₂O and D₂O [208]. They found the spectra could be understood as a convolution of Gaussian inhomogeneous broadening due to proton disorder and Lorentzian homogeneous broadening due to motional narrowing from thermal fluctuations [208].

Given that the oxygens in ice are ordered, a lack of inhomogeneous broadening, or even very fast dephasing compared to the width of the static distribution of frequencies, will produce a small, if any, photon echo. If this is the case, the 2D IR line shape of ice will be symmetric in ω_1 and ω_3 at all waiting times. However, disorder of the protons will most likely introduce inhomogeneity, as seen in the calculations of

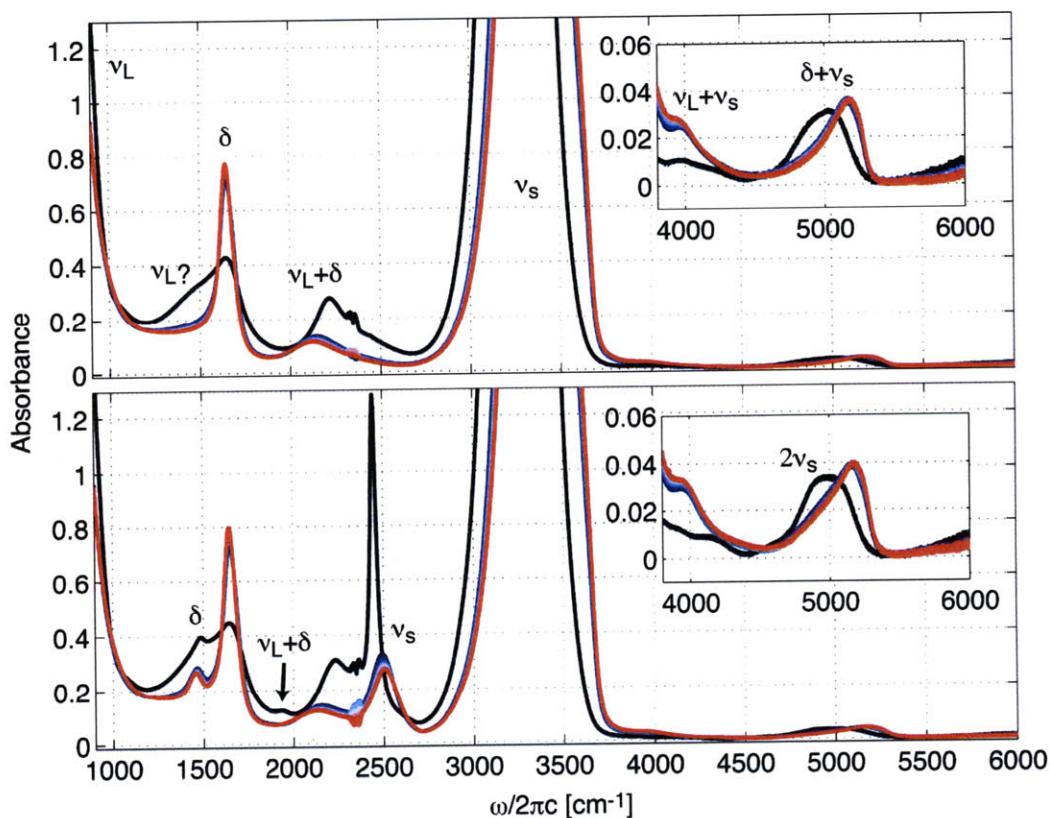


Figure B-2: Linear absorption of H₂O (upper) and dilute HOD in H₂O (lower) in the liquid and ice phase. The peaks labeled in the upper (lower) spectra correspond to H₂O (HOD) transitions.

the linear absorption [208]. With the constraints of the lattice, spectral diffusion may very well be slower for ice than water. If this is the case, there will be elongation along the diagonal that may persist past ~ 1 ps. Li and Skinner calculated the frequency correlation function for HOD in D₂O at 245 K [208] and found an initial decay faster than water to negative correlation, a recurrence at 145 fs from the hydrogen bond stretch, and several subsequent beats. This correlation function indicates that within 145 fs the peak will appear homogeneously broadened.

We attempted to acquire a 2D IR measurement of ice in the same manner as the linear absorption measurements were acquired but scatter from the ice dominated the signal. Sample preparation will need to be carefully considered before this experiment is realized.

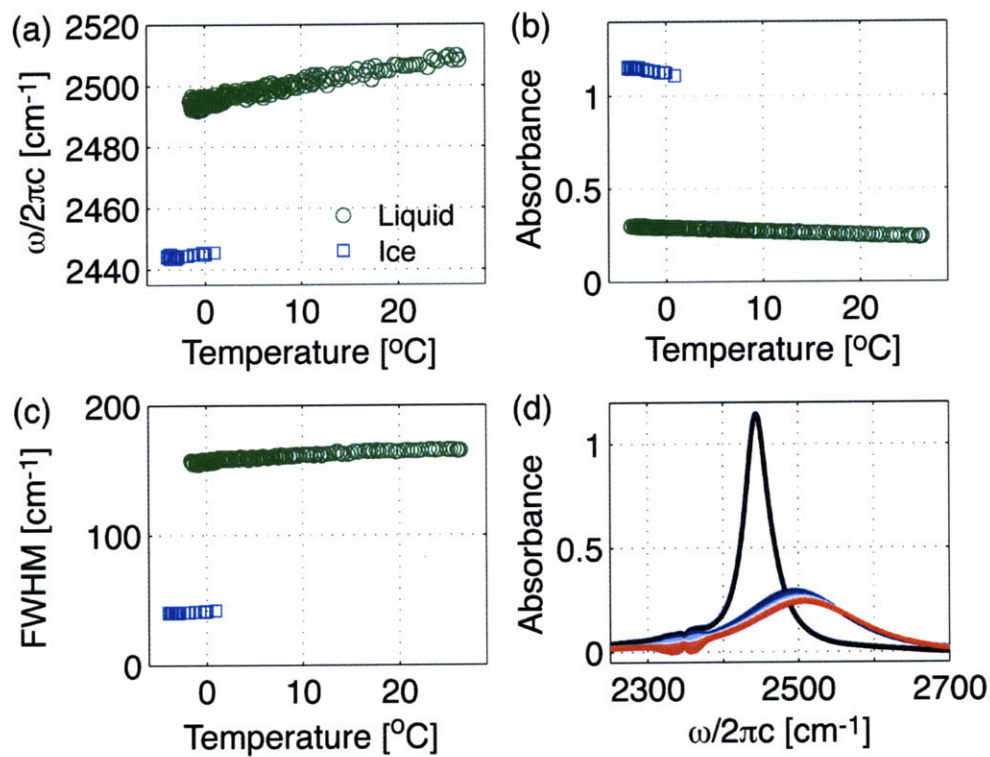


Figure B-3: (a) Peak wavelength, (b) peak absorbance, (c) line width (FWHM), and (d) linear absorption of ω_{OD} of HOD in H₂O with the background H₂O subtracted.

Appendix C

Urea

Osmolytes are small organic molecules that affect the stability of proteins. Stabilizing osmolytes include trimethylamine N-oxide (TMAO), glycerol, and sugars. Urea is a known denaturant of proteins but the mechanism of denaturation is unknown. Urea may disrupt the hydrogen bond network of water surrounding the protein allowing for the solvation of hydrophobic groups. In this case, urea is considered a structure-breaker of water and a chaotropic solute under the Hofmeister series nomenclature. Alternatively, it may interact directly with the side chains and/or protein backbone through electrostatic and/or van der Waals forces. The indirect and direct interaction mechanisms are not mutually exclusive and the dominant mechanism may shift as the protein undergoes conformational changes.

In this appendix we present linear absorption and 2D IR measurements of urea in water and urea and *N*-methylacetamide (NMA) in water as part of a study of the mechanism of denaturation. Urea association has been studied through infrared spectroscopy by means of principle component analysis (PCA) and 2D correlation spectroscopy [209]. The authors found that the maximum efficiency of urea dimerization occurs at ~ 2 M, after which urea forms higher aggregates [209]. Ultrafast pump-probe experiments probing water directly upon addition of urea have shown that urea has a negligible effect on the hydrogen bond dynamics of water [210]. There has not been an ultrafast nonlinear infrared experiment performed that directly probes the vibrations of urea. Cross peaks in a 2D measurement arise from coupling, whether

through space or through bond, between spectrally distinct species. Therefore, polarization selective 2D IR measurements of different isotopic species of urea are capable of directly probing if urea forms dimers in water and, if so, the geometry of the dimer. Likewise, 2D IR measurements of urea and spectrally distinct peptides and proteins are capable of providing information on the direct mechanism of denaturation.

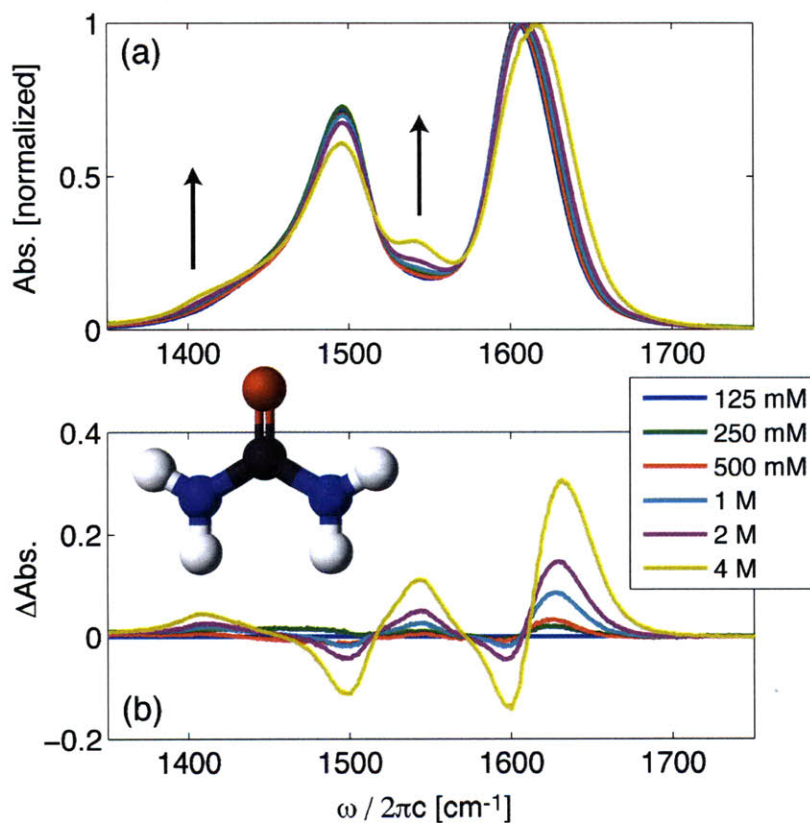


Figure C-1: (a) Linear absorption of deuterated ¹²C-urea in D₂O as a function of concentration normalized to the carbonyl stretch. The background D₂O is subtracted. (b) Difference spectrum between each concentration and the 125 mM solution and a ball and stick representation of a urea molecule [oxygen (red), carbon (black), nitrogen (blue), and deuterium (white)].

The concentration dependent linear absorption spectrum of deuterated ¹²C-urea in D₂O is shown in Figure C-1a and a ball and stick representation of a urea molecule is shown in Figure C-1b. The peak at ~ 1600 cm⁻¹ is primarily composed of carbonyl stretch and the peak at ~ 1500 cm⁻¹ is primarily composed of C-N stretch. As the concentration is increased, additional peaks appear to the red and blue of

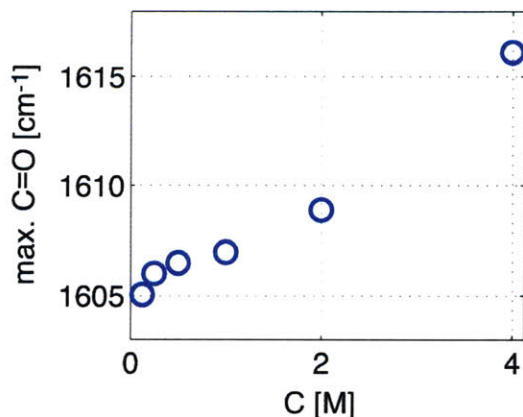


Figure C-2: Shift in peak of carbonyl stretch of urea with concentration.

the C-N stretch at $\sim 1405\text{ cm}^{-1}$ and $\sim 1545\text{ cm}^{-1}$, respectively. The carbonyl stretch blue-shifts with increasing concentration. The frequency of the peak maximum with concentration, which shows a cubic behavior, is shown in Figure C-2. In Figure C-1b we show the difference spectrum between each concentration and the $C = 125\text{ mM}$ solution. The blue-shift of the carbonyl stretch is seen along with the decrease in intensity of the C-N stretch at $\sim 1500\text{ cm}^{-1}$ and increase at $\sim 1405\text{ cm}^{-1}$ and $\sim 1545\text{ cm}^{-1}$. It appears as the additional peaks that grow in with concentration are a result of coupling between associated urea molecules.

In Figure C-3 we show waiting time dependent 2D IR surfaces of $1\text{ M }^{12}\text{C}$ -urea in D_2O acquired in the ZZYY polarization geometry. The surfaces were acquired in the pump-probe geometry with the mid-infrared pulse centered at $\sim 1575\text{ cm}^{-1}$ with $\sim 450\text{ cm}^{-1}$ of band width (FWHM). There are peaks along the diagonal from the carbonyl and C-N stretch and the intermediate peak at $\sim 1545\text{ cm}^{-1}$. The cross peaks between the carbonyl and C-N stretch are present at the earliest waiting time, $\tau_2 = 75\text{ fs}$, and grow in with increasing waiting time. Also, the C-N stretch becomes more intense with increasing waiting time relative to the carbonyl stretch due to the downhill flow of vibrational energy. The cross peaks are more intense relative to the diagonal peaks in the ZZYY polarization geometry compared to the ZZZZ polarization geometry (not shown) indicating that the transition dipoles are closer to 90° than 0° . In agreement with the concentration dependent linear absorption measurements, there is not an

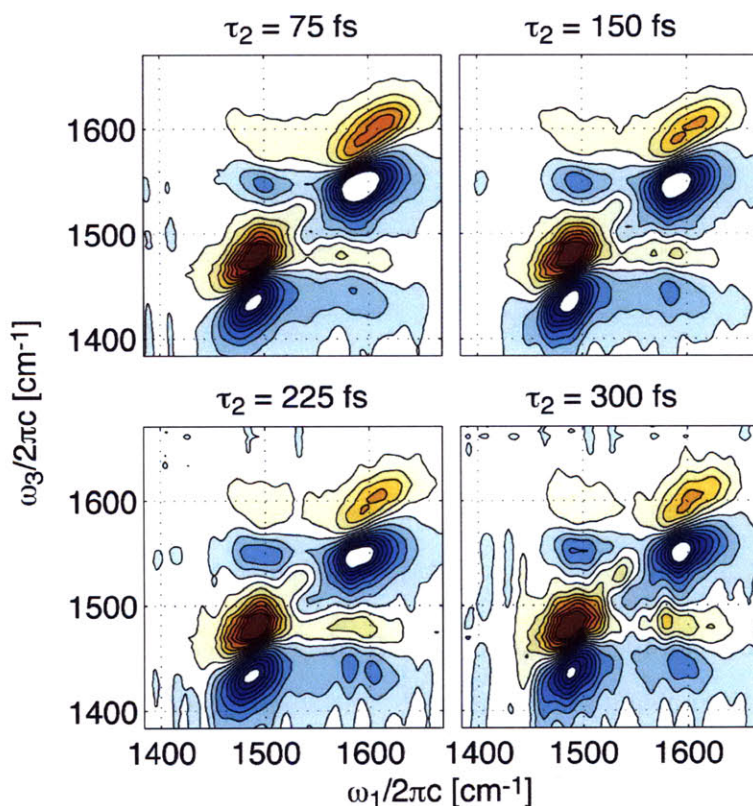


Figure C-3: Waiting time dependent 2D IR surfaces of 1 M ^{12}C -urea in D_2O acquired in the ZZYY polarization geometry.

intermediate peak observed between the carbonyl and main C-N stretching modes in a waiting time dependent series of 2D IR surfaces of 100 mM ^{12}C -urea in D_2O acquired in the ZZYY polarization geometry (not shown).

We can directly confirm the association of urea in water by identifying cross peaks in a 2D IR measurement between isotopically distinct species, namely ^{12}C -urea and ^{13}C -urea. In Figure C-4 we show the linear absorption of 2.5 M ^{12}C -urea and ^{13}C -urea in D_2O . The carbonyl and C-N stretches of ^{13}C -urea are red-shifted from the stretches of ^{12}C -urea by approximately 45 and 35 cm^{-1} , respectively (determined at 250 mM). In Figure C-5 we show concentration dependent 2D IR surfaces of ^{12}C -urea and ^{13}C -urea in D_2O acquired at $\tau_2 = 100$ fs in the ZZYY polarization geometry. The cross peaks between the intramolecular carbonyl and C-N stretch of each species is clearly seen. On the blue side of the cross peak between the ^{12}C -urea carbonyl and C-

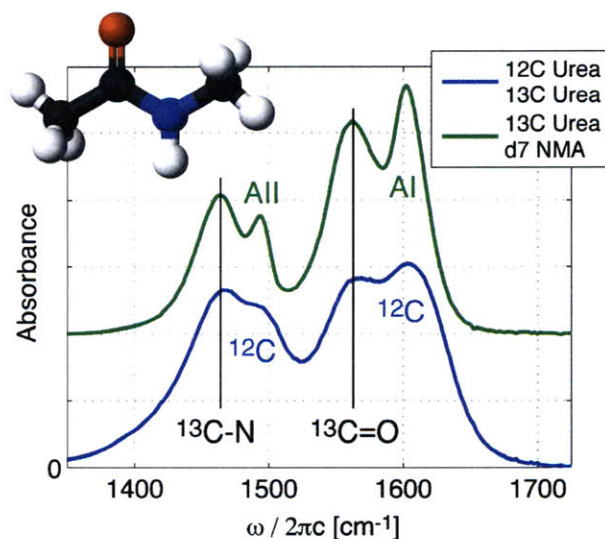


Figure C-4: Linear absorption of 2.5 M ^{12}C -urea and ^{13}C -urea in D_2O (blue). Linear absorption of ^{13}C -urea and d7-NMA in D_2O (green). The amide I and II modes of NMA are indicated. The molecule is a ball and stick representation of NMA [oxygen (red), carbon (black), nitrogen (blue), and deuterium (white)].

N stretch there is additional amplitude that appears with increasing concentration. This additional amplitude may arise from association between isotopically distinct species. However, it may also arise from coupling to the additional intermediate peak that grows in with increasing concentration for each species. In either case, it appears to arise from association between urea molecules.

We additionally acquired a waiting time series of 2D IR surfaces of 2.5 M ^{12}C -urea and ^{13}C -urea in D_2O in the ZZYY and ZZZZ polarization geometries. The surfaces are shown in Figure C-6 for five waiting times in the ZZYY polarization geometry and at $\tau_2 = 300$ fs for the ZZZZ polarization geometry. With increasing waiting time a ridge grows in between the C-N stretches of ^{12}C -urea and ^{13}C -urea. This may be direct evidence for association between isotopically distinct species. The surface acquired in the ZZZZ polarization geometry suggests that if association is occurring, the transition dipoles between molecules are less likely to be aligned parallel to one another.

NMA is a small molecule representation of a single unit of the protein backbone that is ideal to study how urea may interact with a protein, if it indeed denatures by

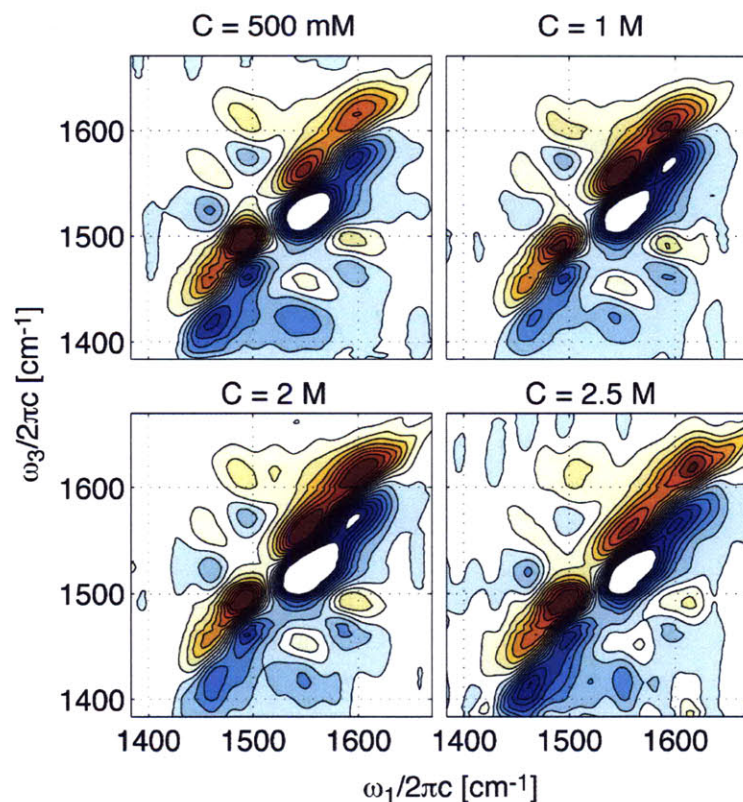


Figure C-5: Concentration dependent 2D IR surfaces of ^{12}C -urea and ^{13}C -urea in D_2O acquired at $\tau_2 = 100$ fs in the ZZYY polarization geometry.

direct interaction. In Figure C-4 we show the linear absorption spectrum of ^{13}C -urea and d7-NMA in D_2O and in Figure C-7 we show 2D IR surfaces of ^{13}C -urea and d7-NMA in D_2O in the ZZYY and ZZZZ polarization geometries at two waiting times. The peaks along the diagonal from red to blue frequency correspond to the C-N stretch of ^{13}C -urea, the amide II mode of d7-NMA (C-N stretch and N-D bend), the carbonyl stretch of ^{13}C -urea, and the amide I mode of d7-NMA (primarily carbonyl stretch). The cross peaks between intramolecular modes are clearly seen in the ZZYY polarization geometry, but there is no indication of intermolecular coupling, even at low contours. The surfaces acquired in the ZZZZ polarization geometry indicate that the intramolecular transition dipoles are aligned closer to 90° than 0° .

In conclusion, linear absorption measurements of a single isotope of urea appear to indicate association of urea molecules in water. Calculations of frequency shifts upon dimerization, or upon oligomer formation, would be helpful in confirming this

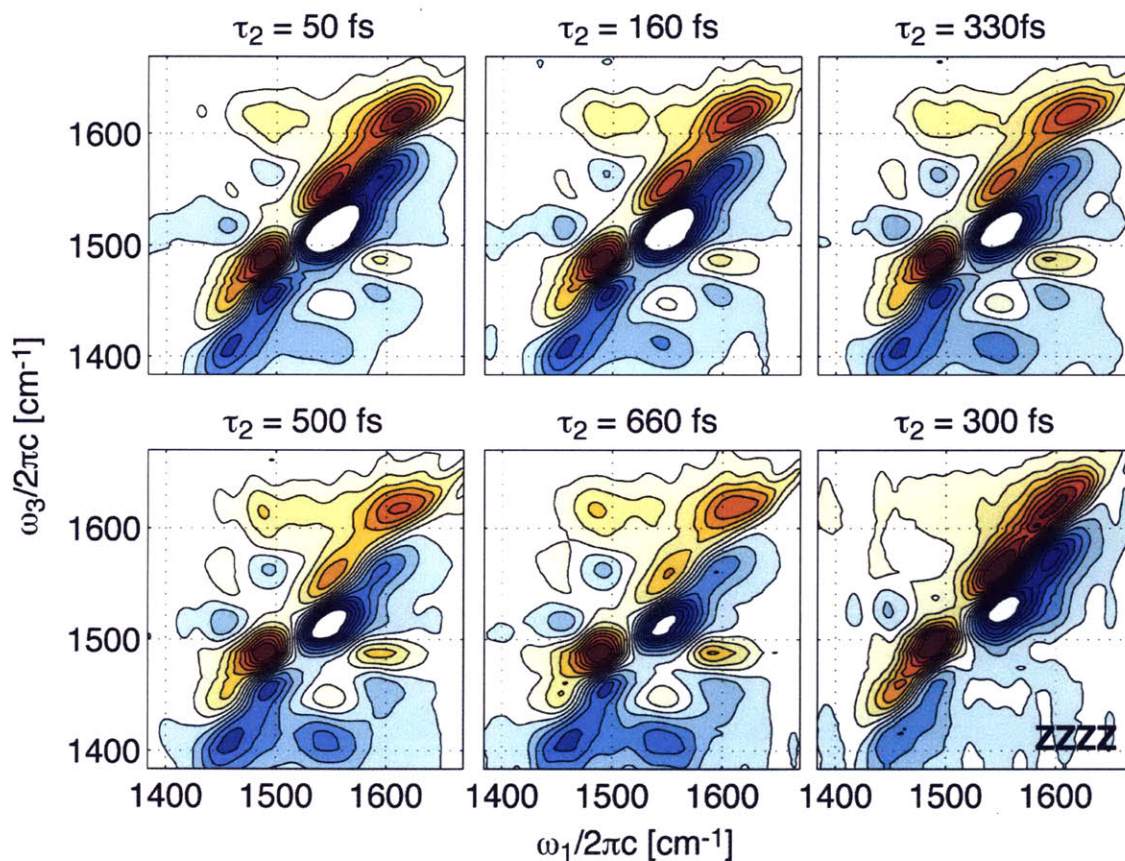


Figure C-6: 2D IR surfaces of 2.5 M ^{12}C -urea and ^{13}C -urea in D_2O acquired at five waiting times in the ZZYY polarization geometry and $\tau_2 = 300$ fs in the ZZZZ polarization geometry.

hypothesis. Additionally, the increasing intensity of a ridge between the C-N stretches of ^{12}C -urea and ^{13}C -urea with increasing waiting time observed in 2D IR measurements acquired in the ZZYY polarization geometry is an initial direct confirmation of the association of urea molecules. Linear absorption and 2D IR measurements of urea in an apolar solvent and/or film would help in the characterization of associated urea molecules. 2D IR surfaces of ^{13}C -urea and d7-NMA in D_2O initially indicate that the molecules do not associate in water. Further tests of how urea may interact directly with a protein can include measurements of urea and polyglycine (model of protein backbone), urea and polytryptophan, polyalanine, or polyisoleucine (models of a hydrophobic side chain), and urea and polyasparagine (model of a hydrophilic side chain). Finally, linear and nonlinear measurements of urea and a protein would

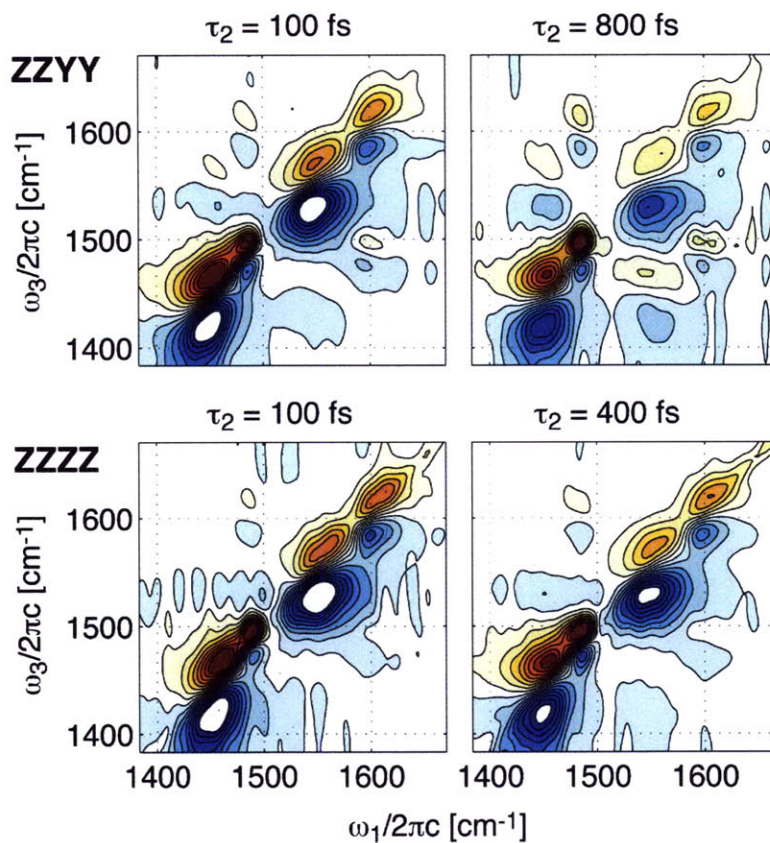


Figure C-7: 2D IR surfaces of ^{13}C -urea and d7-NMA in D_2O in the ZZYY and ZZZZ polarization geometries at two waiting times.

be most interesting.

C.1 Acknowledgments

We would like to thank Benjamin Dietzek for his help acquiring the linear and non-linear measurements of urea.

Bibliography

- [1] D. Laage and J. T. Hynes. A molecular jump mechanism of water reorientations. *Science*, 311(5762):832–835, Jan 2006.
- [2] J. J. Max and C. Chapados. Isotope effects in liquid water by infrared spectroscopy. III. H₂O and D₂O spectra from 6000 to 0 cm⁻¹. *J. Chem. Phys.*, 131:184505, 2009.
- [3] K. Winkler, J. Lindner, H. Bursing, and P. Vohringer. Ultrafast Raman-induced Kerr-effect of water: Single molecule versus collective motions. *J. Chem. Phys.*, 113(11):4674–4682, Jan 2000.
- [4] R. Ludwig, F. Weinhold, and T. C. Farrar. Experimental and theoretical determination of the temperature-dependence of deuteron and oxygen quadrupole coupling-constants of liquid water. *J. Chem. Phys.*, 103(16):6941–6950, Jan 1995.
- [5] C. Ronne, L. Thrane, P. O. Astrand, A. Wallqvist, K. V. Mikkelsen, and S. R. Keiding. Investigation of the temperature dependence of dielectric relaxation in liquid water by THz reflection spectroscopy and molecular dynamics simulations. *J. Chem. Phys.*, 107(14):5319–5331, Jan 1997.
- [6] R. Buchner, J. Barthel, and J. Stauber. The dielectric relaxation of water between 0 degrees C and 35 degrees C. *Chem. Phys. Lett.*, 306(1-2):57–63, Jan 1999.
- [7] S. Ragot, J.-M. Gillet, and P. J. Becker. Interpreting Compton anisotropy of ice I_h: A cluster partitioning method. *Phys. Rev. B*, 65:235115, 2002.
- [8] J. R. Schmidt, S. A. Corcelli, and J. L. Skinner. Pronounced non-Condon effects in the ultrafast infrared spectroscopy of water. *J. Chem. Phys.*, 123:044513, 2005.
- [9] A. Werner. Beitrag zur chemie des phenanthrens. *Justus Liebigs annalen der Chemie*, 322:147, 1902.
- [10] G. W. Stewart. X-ray diffraction in water: The nature of molecular association. *Phys. Rev.*, 37:9–16, 1931.

- [11] S. Katzoff. X-ray studies of the molecular arrangement in liquids. *J. Chem. Phys.*, 2:841, 1934.
- [12] G. E. Hilbert, O. R. Wulf, S. B. Hendricks, and U. Liddel. The hydrogen bond between oxygen atoms in some organic compounds. *J. Am. Chem. Soc.*, 58:548–555, Jan 1936.
- [13] George C. Pimental and Aubrey L. McClellan. *The Hydrogen Bond*. W. H. Freeman and Company, 1960.
- [14] A. Luzar and D. Chandler. Effect of environment on hydrogen bond dynamics in liquid water. *Phys. Rev. Lett.*, 76(6):928–931, Jan 1996.
- [15] T. H. Maiman. Stimulated optical radiation in ruby. *Nature*, 187:493–494, 1960.
- [16] A. Javan, W. R. Bennett Jr., and D. R. Herriot. Population inversion and continuous optical maser oscillation in a gas discharge containing a He-Ne mixtures. *Phys. Rev. Lett.*, 6:106–110, 1961.
- [17] D. Eisenberg and W. Kauzmann. *The Structure and Properties of Water*. Clarendon Press, 1969.
- [18] W. C. Roentgen. *Annals of Physics*, 45:91, 1892.
- [19] Henry S. Frank and Wen-Yang Wen. Ion-solvent interaction. Structural aspects of ion-solvent interaction in aqueous solutions: A suggested picture of water structures. *Discuss. Faraday Soc.*, 24:133, 1957.
- [20] George Nemethy and Harold A. Scheraga. Structure of water and hydrophobic bonding in proteins. I. A model for the thermodynamic properties of liquid water. *J. Phys. Chem.*, 36:3382, 1962.
- [21] O. Ya. Samoilov. *Structure of aqueous electrolyte solutions and the hydration of ions*. Consultants Bureau, New York, 1965.
- [22] G. Walrafen. *Water a Comprehensive Treatise*, volume 1. Plenum Press, 1972.
- [23] J. A. Pople. Molecular association in liquids. II. A theory of the structure of water. *Proc. R. Soc. Lond. A*, 205:163–178, 1951.
- [24] J. D. Bernal and R. H. Fowler. A theory of water and ionic solution, with particular reference to hydrogen and hydroxyl ions. *J. Chem. Phys.*, 1:515–548, 1933.
- [25] P. Wernet, D. Nordlund, U. Bergmann, M. Cavalleri, M. Odellius, H. Ogasawara, L. A. Naslund, T. K. Hirsch, L. Ojamae, P. Glatzel, L. G. M. Pettersson, and A. Nilsson. The structure of the first coordination shell in liquid water. *Science*, 304(5673):995–999, Jan 2004.

- [26] Gary N. I. Clark, Greg L Hura, Jose Teixeira, Alan K. Soper, and Teresa Head-Gordon. Small-angle scattering and the structure of ambient liquid water. *P. Natl. Acad. Sci. USA*, 107(32):14003–14007, Jan 2010.
- [27] M. G. Sceats, M. Stavola, and S. A. Rice. Zeroth order random network model of liquid water. *J. Chem. Phys.*, 70(8):3927–3938, Jan 1979.
- [28] H. E. Stanley and J. Teixeira. Interpretation of the unusual behavior of H₂O and D₂O at low-temperatures - Tests of a percolation model. *J. Chem. Phys.*, 73(7):3404–3422, Jan 1980.
- [29] F. H. Stillinger and T. A. Weber. Inherent structure in water. *J. Phys. Chem.*, 87(15):2833–2840, Jan 1983.
- [30] I. Ohmine, H. Tanaka, and P. G. Wolynes. Large local energy fluctuations in water. II. Cooperative motions and fluctuations. *J. Chem. Phys.*, 89:5852, 1988.
- [31] F. Sciortino, A. Geiger, and H. E. Stanley. Effect of defects on molecular mobility in liquid water. *Nature*, 354(6350):218–221, Jan 1991.
- [32] H. J. C. Berendsen, J. R. Grigera, and T. P. Straatsma. The missing term in effective pair potentials. *J. Phys. Chem.*, 91:6269–6271, 1987.
- [33] Damien Laage and James T. Hynes. On the molecular mechanism of water reorientation. *J. Phys. Chem. B*, 112(45):14230–14242, Jan 2008.
- [34] Francesco Paesani. Temperature-dependent infrared spectroscopy of water from a first-principles approach. *J. Phys. Chem. A*, 2011. Submitted.
- [35] M. Parrinello and A. Rahman. Study of an F center in molten KCl. *J. Chem. Phys.*, 80:860, 1984.
- [36] G. A. Voth. *Path-Integral Centroid Methods in Quantum Statistical Mechanics and Dynamics, in Advances in Chemical Physics: New Methods in Computational Quantum Mechanics*, volume 93. John Wiley & Sons, Inc., Hoboken, NJ, USA, 2007.
- [37] G. S. Fanourgakis and S. S. Xantheas. Development of transferable interaction potentials for water. V. Extension of the flexible, polarizable, Thole-type model potential (TTM3-F, v. 3.0) to describe the vibrational spectra of water clusters and liquid water. *J. Chem. Phys.*, 128:074506, 2008.
- [38] Joseph W. Ellis. The near infra-red absorption spectra of some aldehydes, ketones, esters and ethers. *J. Am. Chem. Soc.*, 51:1384–1394, 1929.
- [39] C. E. H. Bawn. The infrared spectra and structure of tautomeric compounds. *J. Chem. Soc.*, pages 1189–1198, 1932.
- [40] R. Freymann. *Compt. rend.*, 195:39, 1932.

- [41] W. S. Benedict, N. Gailar, and E. K. Plyler. Rotation-vibration spectra of deuterated water vapor. *J. Chem. Phys.*, 24:1139, 1956.
- [42] R. E. Rundle and Matthew Parasol. O-H stretching frequencies in very short and possibly symmetrical hydrogen bonds. *J. Chem. Phys.*, 20(9):1487–1488, 1952.
- [43] A. Novak. *Structure and Bonding*. Springer-Verlag, 1974.
- [44] Richard M. Badger. A relation between internuclear distances and bond force constants. *J. Chem. Phys.*, 2:128, 1934.
- [45] T. T. Wall and D. F. Hornig. Raman intensities of HDO and structure in liquid water. *J. Chem. Phys.*, 43(6):2079, Jan 1965.
- [46] C. P. Lawrence and J. L. Skinner. Vibrational spectroscopy of HOD in liquid D₂O. III. Spectral diffusion, and hydrogen-bonding and rotational dynamics. *J. Chem. Phys.*, 118(1):264–272, Jan 2003.
- [47] J. D. Eaves, A. Tokmakoff, and P. L. Geissler. Electric field fluctuations drive vibrational dephasing in water. *J. Phys. Chem. A*, 109(42):9424–9436, 2005.
- [48] R. Rey, K. B. Moller, and J. T. Hynes. Hydrogen bond dynamics in water and ultrafast infrared spectroscopy. *J. Phys. Chem. A*, 106(50):11993–11996, Jan 2002.
- [49] K. B. Moller, R. Rey, and J. T. Hynes. Hydrogen bond dynamics in water and ultrafast infrared spectroscopy: A theoretical study. *J. Phys. Chem. A*, 108(7):1275–1289, Jan 2004.
- [50] Kersti Hermansson. *Ab Initio* calculations of the fundamental OH frequency of bound OH⁻ ions. *J. Chem. Phys.*, 95:3578, 1991.
- [51] K. Hermansson. From cluster to crystal - *ab initio* calculations of the OH⁻ frequency in lithium hydroxide monohydrate. *Chem. Phys.*, 159(1):67–73, 1992.
- [52] K. Hermansson. Electric-field effects on the OH vibrational frequency and infrared-absorption intensity for water. *J. Chem. Phys.*, 99(2):861–868, Jan 1993.
- [53] K. Hermansson, J. Lindgren, and M. M. Probst. Nonadditivity of OH frequency-shifts in ion water-systems. *Chem. Phys. Lett.*, 233(4):371–375, Jan 1995.
- [54] U. Buck, I. Ettischer, M. Melzer, V. Buch, and J. Sadlej. Structure and spectra of three-dimensional (H₂O)_n clusters, n = 8, 9, 10. *Phys. Rev. Lett.*, 80(12):2578–2581, Jan 1998.
- [55] S. A. Corcelli, C. P. Lawrence, and J. L. Skinner. Combined electronic structure/molecular dynamics approach for ultrafast infrared spectroscopy of dilute HOD in liquid H₂O and D₂O. *J. Chem. Phys.*, 120(17):8107–8117, Jan 2004.

- [56] B. Auer, R. Kumar, J. R. Schmidt, and J. L. Skinner. Hydrogen bonding and Raman, IR, and 2D-IR spectroscopy of dilute HOD in liquid D₂O. *P. Natl. Acad. Sci. USA*, 104(36):14215–14220, Jan 2007.
- [57] B. M. Auer and J. L. Skinner. IR and Raman spectra of liquid water: Theory and interpretation. *J. Chem. Phys.*, 128(22):224511, Jan 2008.
- [58] H. Graener, G. Seifert, and A. Laubereau. New spectroscopy of water using tunable picosecond pulses in the infrared. *Phys. Rev. Lett.*, 66(16):2092–2095, Jan 1991.
- [59] R. Laenen, C. Rauscher, and A. Laubereau. Dynamics of local substructures in water observed by ultrafast infrared hole burning. *Phys. Rev. Lett.*, 80(12):2622–2625, 1998.
- [60] G. M. Gale, G. Gallot, F. Hache, N. Lascoux, S. Bratos, and J. C. Leicknam. Femtosecond dynamics of hydrogen bonds in liquid water: A real time study. *Phys. Rev. Lett.*, 82(5):1068–1071, Jan 1999.
- [61] S. Woutersen and H. J. Bakker. Hydrogen bond in liquid water as a Brownian oscillators. *Phys. Rev. Lett.*, 83(10):2077–2080, Jan 1999.
- [62] H. J. Bakker, H. K. Nienhuys, G. Gallot, N. Lascoux, G. M. Gale, J. C. Leicknam, and S. Bratos. Transient absorption of vibrationally excited water. *J. Chem. Phys.*, 116:2592, 2002.
- [63] J. Stenger, D. Madsen, P. Hamm, E. T. J. Nibbering, and T. Elsaesser. Ultrafast vibrational dephasing of liquid water. *Phys. Rev. Lett.*, 87(2):027401, Jan 2001.
- [64] G. E. Walrafen, M. R. Fisher, M. S. Hokmabadi, and W. H. Yang. Temperature dependence of the low- and high-frequency Raman scattering from liquid water. *J. Chem. Phys.*, 85:6970, 1986.
- [65] J. D. Smith, C. D. Cappa, K. R. Wilson, R. C. Cohen, P. L. Geissler, and R. J. Saykally. Unified description of temperature-dependent hydrogen-bond rearrangements in liquid water. *P. Natl. Acad. Sci. USA*, 102(40):14171–14174, Jan 2005.
- [66] S. Yeremenko, M. S. Pshenichnikov, and D. A. Wiersma. Hydrogen-bond dynamics in water explored by heterodyne-detected photon echo. *Chem. Phys. Lett.*, 369(1-2):107–113, 2003.
- [67] J. Stenger, D. Madsen, P. Hamm, E. T. J. Nibbering, and T. Elsaesser. A photon echo peak shift study of liquid water. *J. Phys. Chem. A*, 106(10):2341–2350, Jan 2002.
- [68] Sergey Yeremenko, Maxim Pshenichnikov, and Douwe Wiersma. Interference effects in IR photon echo spectroscopy of liquid water. *Phys. Rev. A*, 73(2):021804, Feb 2006.

- [69] C. J. Fecko, J. D. Eaves, J. J. Loparo, A. Tokmakoff, and P. L. Geissler. Ultrafast hydrogen-bond dynamics in the infrared spectroscopy of water. *Science*, 301(5640):1698, 2003.
- [70] C. J. Fecko, J. J. Loparo, S. T. Roberts, and A. Tokmakoff. Local hydrogen bonding dynamics and collective reorganization in water: Ultrafast infrared spectroscopy of HOD/D₂O. *J. Chem. Phys.*, 122(5):054506, Jan 2005.
- [71] S. Mukamel. *Principles of Nonlinear Optical Spectroscopy*. Oxford University Press, 1995.
- [72] J. D. Eaves, J. J. Loparo, C. J. Fecko, S. T. Roberts, A. Tokmakoff, and P. L. Geissler. Hydrogen bonds in liquid water are broken only fleetingly. *P. Natl. Acad. Sci. USA*, 102(37):13019, 2005.
- [73] Joseph J. Loparo, Sean T. Roberts, and Andrei Tokmakoff. Multidimensional infrared spectroscopy of water. I. Vibrational dynamics in 2D lineshapes. *J. Chem. Phys.*, 125:194521, 2006.
- [74] Joseph J. Loparo, Sean T. Roberts, and Andrei Tokmakoff. Multidimensional infrared spectroscopy of water. II. Hydrogen bond switching dynamics. *J. Chem. Phys.*, 125(19):194522, Jan 2006.
- [75] Sean T. Roberts, Krupa Ramasesha, and Andrei Tokmakoff. Structural rearrangements in water viewed through two-dimensional infrared spectroscopy. *Acc. Chem. Res.*, 42(9):1239–1249, Jan 2009.
- [76] M. F. Kropman, H. K. Nienhuys, S. Woutersen, and H. J. Bakker. Vibrational relaxation and hydrogen-bond dynamics of HDO:D₂O. *J. Phys. Chem. A*, 105(19):4622–4626, Jan 2001.
- [77] R. Laenen, K. Simeonidis, and A. Laubereau. Subpicosecond spectroscopy of liquid water in the infrared: Effect of deuteration on the structural and vibrational dynamics. *J. Phys. Chem. B*, 106(2):408–417, Jan 2002.
- [78] J. B. Asbury, T. Steinell, K. Kwak, S. A. Corcelli, C. P. Lawrence, J. L. Skinner, and M. D. Fayer. Dynamics of water probed with vibrational echo correlation spectroscopy. *J. Chem. Phys.*, 121(24):12431–12446, Jan 2004.
- [79] S. A. Corcelli and J. L. Skinner. Infrared and Raman line shapes of dilute HOD in liquid H₂O and D₂O from 10 to 90 °C. *J. Phys. Chem. A*, 109(28):6154–6165, 2005.
- [80] Jesko Bruderemann, Mario Melzer, Udo Buck, Jan K. Kazimirski, Joanna Sadlej, and Victoria Buch. The asymmetric cage structure of (H₂O)₇ from a combined spectroscopic and computational study. *J. Chem. Phys.*, 110:10649, 1999.

- [81] Joanna Sadlej, Victoria Buch, and J. K. Kazimirski. Theoretical study of structure and spectra of cage clusters $(\text{H}_2\text{O})_n$, $n=7-10$. *J. Phys. Chem. A*, 103(25):4933–4947, 1999.
- [82] Minhaeng Cho. Correlation between electronic and molecular structure distortions and vibrational properties. I. Adiabatic approximations. *J. Chem. Phys.*, 118:3480, 2003.
- [83] Sihyun Ham, Joo-Hee Kim, Hochan Lee, and Minhaeng Cho. Correlation between electronic and molecular structure distortions and vibrational properties. II. Amide I modes of NMA- $n\text{D}_2\text{O}$ complexes. *J. Chem. Phys.*, 118:3491, 2003.
- [84] Kijeong Kwac and Minhaeng Cho. Molecular dynamics simulation study of N-methylacetamide in water. I. Amide I mode frequency fluctuations. *J. Chem. Phys.*, 119:2247, 2003.
- [85] Kijeong Kwac and Minhaeng Cho. Molecular dynamics simulation study of N-methylacetamide in water. II. Two-dimensional infrared pump-probe spectra. *J. Chem. Phys.*, 119:2256, 2003.
- [86] S. A. Corcelli, C. P. Lawrence, J. B. Asbury, T. Steinell, M. D. Fayer, and J. L. Skinner. Spectral diffusion in a fluctuating charge model of water. *J. Chem. Phys.*, 121(18):8897–8900, Jan 2004.
- [87] J. R. Schmidt, S. T. Roberts, J. J. Loparo, A. Tokmakoff, M. D. Fayer, and J. L. Skinner. Are water simulation models consistent with steady-state and ultrafast vibrational spectroscopy experiments? *Chem. Phys.*, 341(1-3):143–157, 2007.
- [88] W. L. Jorgensen, J. Chandrasekhar, J. D. Madura, R. W. Impey, and M. L. Klein. Comparison of simple potential functions for simulating liquid water. *J. Chem. Phys.*, 79(2):926–935, Jan 1983.
- [89] S. W. Rick, S. J. Stuart, and B. J. Berne. Dynamical fluctuating charge force-fields - application to liquid water. *J. Chem. Phys.*, 101(7):6141–6156, Jan 1994.
- [90] S. W. Rick. A reoptimization of the five-site water potential (TIP5P) for use with Ewald sums. *J. Chem. Phys.*, 120:6085, 2004.
- [91] L. X. Dang and T. M. Chang. Molecular dynamics study of water clusters, liquid, and liquid–vapor interface of water with many-body potentials. *J. Chem. Phys.*, 106:8149, 1997.
- [92] G. M. Gale, G. Gallot, and N. Lascoux. Frequency-dependent vibrational population relaxation time of the OH stretching mode in liquid water. *Chem. Phys. Lett.*, 311(3-4):123–125, Jan 1999.

- [93] J. C. Deak, S. T. Rhea, L. K. Iwaki, and D. D. Dlott. Vibrational energy relaxation and spectral diffusion in water and deuterated water. *J. Phys. Chem. A*, 104(21):4866–4875, Jan 2000.
- [94] J. J. Loparo, C. J. Fecko, J. D. Eaves, S. T. Roberts, and A. Tokmakoff. Reorientational and configurational fluctuations in water observed on molecular length scales. *Phys. Rev. B*, 70(18):180201, 2004.
- [95] T. Steinel, J. B. Asbury, J. R. Zheng, and M. D. Fayer. Watching hydrogen bonds break: A transient absorption study of water. *J. Phys. Chem. A*, 108(50):10957–10964, Jan 2004.
- [96] I. R. Piletic, D. E. Moilanen, D. B. Spry, N. E. Levinger, and M. D. Fayer. Testing the core/shell model of nanoconfined water in reverse micelles using linear and nonlinear IR spectroscopy. *J. Phys. Chem. A*, 110(15):4985–4999, Jan 2006.
- [97] P. Bodis, O. F. A. Larsen, and S. Woutersen. Vibrational relaxation of the bending mode of HDO in liquid D₂O. *J. Phys. Chem. A*, 109(24):5303–5306, Jan 2005.
- [98] S. Woutersen, U. Emmerichs, H. K. Nienhuys, and H. J. Bakker. Anomalous temperature dependence of vibrational lifetimes in water and ice. *Phys. Rev. Lett.*, 81(5):1106–1109, 1998.
- [99] H. K. Nienhuys, S. Woutersen, R. A. van Santen, and H. J. Bakker. Mechanism for vibrational relaxation in water investigated by femtosecond infrared spectroscopy. *J. Chem. Phys.*, 111(4):1494–1500, Jan 1999.
- [100] D. Schwarzer, J. Lindner, and P. Vöhringer. OH-stretch vibrational relaxation of HOD in liquid to supercritical D₂O. *J. Phys. Chem. A*, 110(9):2858–2867, Jan 2006.
- [101] K. J. Tielrooij, C. Petersen, Y. L. A. Rezus, and H. J. Bakker. Reorientation of HDO in liquid H₂O at different temperatures: Comparison of first and second order correlation functions. *Chem. Phys. Lett.*, 471(1-3):71–74, Jan 2009.
- [102] T. Schäfer, J. Lindner, P. Vöhringer, and D. Schwarzer. OD stretch vibrational relaxation of HOD in liquid to supercritical H₂O. *J. Chem. Phys.*, 130:224502, 2009.
- [103] Fivos Perakis and Peter Hamm. Two-dimensional infrared spectroscopy of supercooled water. *J. Phys. Chem. B*, 2010.
- [104] R. Rey and J. T. Hynes. Vibrational energy relaxation of HOD in liquid D₂O. *J. Chem. Phys.*, 104(6):2356–2368, Jan 1996.

- [105] C. P. Lawrence and J. L. Skinner. Vibrational spectroscopy of HOD in liquid D₂O. I. Vibrational energy relaxation. *J. Chem. Phys.*, 117(12):5827–5838, Jan 2002.
- [106] C. P. Lawrence and J. L. Skinner. Vibrational spectroscopy of HOD in liquid D₂O. VII. Temperature and frequency dependence of the OH stretch lifetime. *J. Chem. Phys.*, 119(7):3840–3848, Jan 2003.
- [107] G. Tian. Molecular dynamics study on the vibrational energy relaxation of OD stretch of HOD in liquid H₂O. *Chem. Phys.*, 328(1-3):216–220, 2006.
- [108] D. Kraemer, M. L. Cowan, A. Paarmann, N. Huse, E. T. J. Nibbering, T. Elsaesser, and R. J. Dwayne Miller. Temperature dependence of the two-dimensional infrared spectrum of liquid H₂O. *P. Natl. Acad. Sci. USA*, 105(2):437–442, Jan 2008.
- [109] A. J. Lock and H. J. Bakker. Temperature dependence of vibrational relaxation in liquid H₂O. *J. Chem. Phys.*, 117(4):1708–1713, Jan 2002.
- [110] J. Lindner, P. Vöhringer, M. S. Pshenichnikov, D. Cringus, D. A. Wiersma, and M. Mostovoy. Vibrational relaxation of pure liquid water. *Chem. Phys. Lett.*, 421(4-6):329–333, 2006.
- [111] S. Ashihara, N. Huse, A. Espagne, E. T. J. Nibbering, and T. Elsaesser. Vibrational couplings and ultrafast relaxation of the O-H bending mode in liquid H₂O. *Chem. Phys. Lett.*, 424(1-3):66–70, 2006.
- [112] N. Huse, S. Ashihara, E. T. J. Nibbering, and T. Elsaesser. Ultrafast vibrational relaxation of O-H bending and librational excitations in liquid H₂O. *Chem. Phys. Lett.*, 404(4-6):389–393, Jan 2005.
- [113] L. Chieffo, J. Shattuck, J. J. Amsden, S. Erramilli, and L. D. Ziegler. Ultrafast vibrational relaxation of liquid H₂O following librational combination band excitation. *Chem. Phys.*, 341(1-3):71–80, Jan 2007.
- [114] L. Piatkowski, K. B. Eisenthal, and H. J. Bakker. Ultrafast intermolecular energy transfer in heavy water. *Phys. Chem. Chem. Phys.*, 11(40):9033, Jan 2009.
- [115] E. W. Lang, D. Girlich, H. D. Ludemann, L. Piculell, and D. Muller. Proton spin-lattice relaxation rate in supercooled H₂O and H₂¹⁷O under high-pressure. *J. Chem. Phys.*, 93(7):4796–4803, Jan 1990.
- [116] J. Teixeira, A. Luzar, and S. Longeville. Dynamics of hydrogen bonds: How to probe their role in the unusual properties of liquid water. *J. Phys.: Condens. Matt.*, 18:S2353–S2362, 2006.

- [117] H. K. Nienhuys, R. A. van Santen, and H. J. Bakker. Orientational relaxation of liquid water molecules as an activated process. *J. Chem. Phys.*, 112(19):8487–8494, Jan 2000.
- [118] G. Gallot, S. Bratos, S. Pommeret, N. Lascoux, J. C. Leicknam, M. Koziński, W. Amir, and G. M. Gale. Coupling between molecular rotations and OH...O motions in liquid water: Theory and experiments. *J. Chem. Phys.*, 117:11301, 2002.
- [119] Y. L. A. Rezus and H. J. Bakker. Orientational dynamics of isotopically diluted H₂O and D₂O. *J. Chem. Phys.*, 125(14):144512, Jan 2006.
- [120] H. J. Bakker, Y. L. A. Rezus, and R. L. A. Timmer. Molecular reorientation of liquid water studied with femtosecond midinfrared spectroscopy. *J. Phys. Chem. A*, 112(46):11523–11534, 2008.
- [121] Y. L. A. Rezus and H. J. Bakker. On the orientational relaxation of HDO in liquid water. *J. Chem. Phys.*, 123(11):114502, Jan 2005.
- [122] David E. Moilanen, Emily E. Fenn, Yu-Shan Lin, J. L. Skinner, B. Bagchi, and Michael D. Fayer. Water inertial reorientation: Hydrogen bond strength and the angular potential. *P. Natl. Acad. Sci. USA*, 105(14):5295–5300, Jan 2008.
- [123] D. F. Underwood and D. A. Blank. Ultrafast solvation dynamics: A view from the solvent’s perspective using a novel resonant-pump, nonresonant-probe technique. *J. Phys. Chem. A*, 107(7):956–961, 2003.
- [124] Patrick O’Shea, Mark Kimmel, Xun Gu, and Rick Trebino. Highly simplified device for ultrashort-pulse measurement. *Opt. Lett.*, 26:932–934, 2001.
- [125] V. V. Yakovlev, B. Kohler, and K. R. Wilson. Broadly tunable 30-fs pulses produced by optical parametric amplification. *Opt. Lett.*, 19(23):2000–2002, 1994.
- [126] V. Petrov, F. Rotermund, and F. Noack. Generation of high-power femtosecond light pulses at 1 kHz in the mid-infrared spectral range between 3 and 12 microns by second-order nonlinear processes in optical crystals. *J. Opt. A: Pure and Applied Optics*, 3(3):R1–R19, 2001.
- [127] K. Kato. Second-harmonic generation to 2048 Angstroms in β -Ba₂O₄. *IEEE Journal of Quantum Electronics*, 22(7):1013–1014, 1986.
- [128] F. Seifert, V. Petrov, and M. Woerner. Solid-state laser system for the generation of midinfrared femtosecond pulses tunable from 3.3 to 10 microns. *Opt. Lett.*, 19(23):2009–2011, 1994.
- [129] B. Golubovic and M. K. Reed. All-solid-state generation of 100-kHz tunable mid-infrared 50-fs pulses in type I and type II AgGaS₂. *Opt. Lett.*, 23(22):1760–1762, 1998.

- [130] Peter Hamm, Robert A. Kaindl, and Jens Stenger. Noise suppression in femtosecond mid-infrared light sources. *Opt. Lett.*, 25(24):1798–1800, 2000.
- [131] N. Demirdoven, M. Khalil, O. Golonzka, and A. Tokmakoff. Dispersion compensation with optical materials for compression of intense sub-100-fs mid-infrared pulses. *Opt. Lett.*, 27(6):433–435, Jan 2002.
- [132] P. Kupecek, C. Schwartz, and D. Chemla. Silver thiogallate (AgGaS_2) - Part 1: Nonlinear optical properties. *IEEE Journal of Quantum Electronics*, 10(7):540–545, 1974.
- [133] Lauren P. DeFlores, Rebecca A. Nicodemus, and Andrei Tokmakoff. Two dimensional Fourier transform spectroscopy in the pump-probe geometry. *Opt. Lett.*, 32(20):2966–2968, Jan 2007.
- [134] T. Brixner, I. V. Stiopkin, and G. R. Fleming. Tunable two-dimensional femtosecond spectroscopy. *Opt. Lett.*, 29(8):884–886, Jan 2004.
- [135] Ellen H. G. Backus, Sean Garrett-Roe, and Peter Hamm. Phasing problem of heterodyne-detected two-dimensional infrared spectroscopy. *Opt. Lett.*, 33(22):2665–2667, Jan 2008.
- [136] Jeffrey A. Myers, Kristin L. M. Lewis, Patrick F. Tekavec, and Jennifer P. Ogilvie. Two-color two-dimensional Fourier transform electronic spectroscopy with a pulse-shaper. *Opt. Express*, 16(22):17420–17428, Jan 2008.
- [137] S. Backus, C. G. Durfee, M. M. Murnane, and H. C. Kapteyn. High power ultrafast lasers. *Rev. Sci. Instrum.*, 69(3):1207–1223, Jan 1998.
- [138] W. J. Tropf, M. E. Thomas, and T. J. Harris. *Handbook of Optics*, volume 2. McGraw-Hill, New York, 2nd edition, 1995.
- [139] J. Y. Sung and R. J. Silbey. Four wave mixing spectroscopy for a multilevel system. *J. Chem. Phys.*, 115(20):9266–9287, Jan 2001.
- [140] M. Khalil, N. Demirdoven, and A. Tokmakoff. Obtaining absorptive line shapes in two-dimensional infrared vibrational correlation spectra. *Phys. Rev. Lett.*, 90(4):047401, Jan 2003.
- [141] S. M. G. Faeder and D. M. Jonas. Two-dimensional electronic correlation and relaxation spectra: Theory and model calculations. *J. Phys. Chem. A*, 103(49):10489–10505, 1999.
- [142] Sean T. Roberts, Joseph J. Loparo, and Andrei Tokmakoff. Characterization of spectral diffusion from two-dimensional line shapes. *J. Chem. Phys.*, 125(8):084502, Jan 2006.
- [143] S. A. Kovalenko, A. L. Dobryakov, J. Ruthmann, and N. P. Ernsting. Femtosecond spectroscopy of condensed phases with chirped supercontinuum probing. *Phys. Rev. A*, 59(3):2369–2384, Jan 1999.

- [144] K. Ekvall, P. van der Meulen, C. Dhollande, L. E. Berg, S. Pommeret, R. Naskrecki, and J. C. Mialocq. Cross phase modulation artifact in liquid phase transient absorption spectroscopy. *J. Appl. Phys.*, 87(5):2340–2352, Jan 2000.
- [145] G. E. Walrafen and L. A. Blatz. Raman spectral studies of HTO in H₂O. *J. Chem. Phys.*, 56:4216, 1972.
- [146] L. L. Lucas and M. P. Unterweger. Comprehensive review and critical evaluation of the half-life of tritium. *J. Res. Natl. Inst. Stan.*, 105(4):541–549, Jan 2000.
- [147] J. C. Duplan, L. Mahi, and J. L. Brunet. NMR determination of the equilibrium constant for the liquid H₂O-D₂O mixtures. *Chem. Phys. Lett.*, 413(4-6):400–403, Jan 2005.
- [148] Robert Zwanzig. *Nonequilibrium statistical mechanics*. Oxford University Press, Oxford, Jan 2001.
- [149] K. Hermansson, S. Knuts, and J. Lindgren. The OH vibrational-spectrum of liquid water from combined *ab initio* and monte-carlo calculations. *J. Chem. Phys.*, 95(10):7486–7496, Jan 1991.
- [150] C. Haas and D. F. Hornig. Intermolecular and intramolecular potentials and the spectrum of ice. *J. Chem. Phys.*, 32(6):1763–1769, Jan 1960.
- [151] J. Bournay and Y. Marechal. Anomalous isotope-effect in H bonds of acetic-acid dimers. *J. Chem. Phys.*, 59(9):5077–5087, Jan 1973.
- [152] J. Bournay and Y. Marechal. Possible origin of an anomalous isotope-effect encountered in H-bonds. *Chem. Phys. Lett.*, 27(2):180–182, Jan 1974.
- [153] P. Schuster, G. Zundel, and C. Sandorfy. *The hydrogen bond: Recent developments in theory and experiments.*, volume 1. Jan 1976.
- [154] Kubo. A stochastic theory of line shape. *Adv. Chem. Phys.*, 15:101–127, 1969.
- [155] D. ter Haar. *Fluctuation, relaxation, and resonance in magnetic systems*. Jan 1962.
- [156] C. P. Lawrence and J. L. Skinner. Vibrational spectroscopy of HOD in liquid D₂O. II. Infrared line shapes and vibrational Stokes shifts. *J. Chem. Phys.*, 117:8847, 2002.
- [157] J. J. Loparo, S. T. Roberts, R. A. Nicodemus, and A. Tokmakoff. Variation of the transition dipole moment across the OH stretching band of water. *Chem. Phys.*, 341(1-3):218–229, 2007.
- [158] T. Steinel, J. B. Asbury, S. A. Corcelli, C. P. Lawrence, J. L. Skinner, and M. D. Fayer. Water dynamics: dependence on local structure probed with vibrational echo correlation spectroscopy. *Chem. Phys. Lett.*, 386(4-6):295–300, 2004.

- [159] J. B. Asbury, T. Steinel, C. Stromberg, S. A. Corcelli, C. P. Lawrence, J. L. Skinner, and M. D. Fayer. Water dynamics: Vibrational echo correlation spectroscopy and comparison to molecular dynamics simulations. *J. Phys. Chem. A*, 108(7):1107–1119, Jan 2004.
- [160] B. Rowland, M. Fisher, and J. P. Devlin. Probing icy surfaces with the dangling-OH-mode absorption - large ice clusters and microporous amorphous ice. *J. Chem. Phys.*, 95(2):1378–1384, Jan 1991.
- [161] J. Devlin. Preferential deuterium bonding at the ice surface: A probe of surface water molecule mobility. *J. Chem. Phys.*, 112:5527, Jan 2000.
- [162] A. Engdahl and B. Nelander. On the relative stabilities of H- and D-bonded water dimers. *J. Chem. Phys.*, 86:1819, Jan 1987.
- [163] E. Diken, J. Shin, E. Price, and M. Johnson. Isotopic fractionation and zero-point effects in anionic H-bonded complexes: a comparison of the $\text{I}^- \cdot \text{HDO}$ and $\text{F}^- \cdot \text{HDO}$ ion-molecule clusters. *Chem. Phys. Lett.*, 387:17, Jan 2004.
- [164] M. Khalil, N. Demirdoven, and A. Tokmakoff. Coherent 2D IR spectroscopy: Molecular structure and dynamics in solution. *J. Phys. Chem. A*, 107(27):5258–5279, Jan 2003.
- [165] M. F. DeCamp, L. DeFlores, J. M. McCracken, A. Tokmakoff, K. Kwac, and M. Cho. Amide I vibrational dynamics of N-methylacetamide in polar solvents: the role of electrostatic interactions. *J. Phys. Chem. B*, 109(21):11016–11026, 2005.
- [166] L. P. DeFlores, Z. Ganim, S. F. Ackley, H. S. Chung, and A. Tokmakoff. The anharmonic vibrational potential and relaxation pathways of the amide I and II modes of N-methylacetamide. *J. Phys. Chem. B*, 110(38):18973–18980, 2006.
- [167] R. Kumar, J. R. Schmidt, and J. L. Skinner. Hydrogen bonding definitions and dynamics in liquid water. *J. Chem. Phys.*, 126:204107, 2007.
- [168] J. R. Schmidt, S. A. Corcelli, and J. L. Skinner. Ultrafast vibrational spectroscopy of water and aqueous N-methylacetamide: Comparison of different electronic structure/molecular dynamics approaches. *J. Chem. Phys.*, 121:8887, 2004.
- [169] A. K. Soper and M. G. Phillips. A new determination of the structure of water at 25°C. *Chem. Phys.*, 107(1):47–60, Jan 1986.
- [170] J. Teixeira and M. Bellissent-Funel. Dynamics of water studied by neutron scattering. *J. Phys.: Condens. Matt.*, 2, 1990.
- [171] J. C. Owrutsky, D. Raftery, and R. M. Hochstrasser. Vibrational relaxation dynamics in solutions. *Annu. Rev. Phys. Chem.*, 45(1):519–555, 1994.

- [172] G. A. Voth and R. M. Hochstrasser. Transition state dynamics and relaxation processes in solutions: a frontier of physical chemistry. *J. Phys. Chem.*, 100(31):13034–13049, 1996.
- [173] A. Staib and J. T. Hynes. Vibrational predissociation in hydrogen-bonded OH...O complexes via OH stretch-OO stretch energy-transfer. *Chem. Phys. Lett.*, 204(1-2):197–205, Jan 1993.
- [174] Poul B. Petersen and Andrei Tokmakoff. Source for ultrafast continuum infrared and terahertz radiation. *Opt. Lett.*, 35(12):1962–1964, Jan 2010.
- [175] R. A. Nicodemus and A. Tokmakoff. Infrared spectroscopy of tritiated water. *Chem. Phys. Lett.*, 449(1-3):130–134, 2007.
- [176] A. J. Lock, S. Woutersen, and H. J. Bakker. Ultrafast energy equilibration in hydrogen-bonded liquids. *J. Phys. Chem. A*, 105(8):1238–1243, 2001.
- [177] A. Rahman and F. H. Stillinger. Molecular dynamics study of liquid water. *J. Chem. Phys.*, 55(7):3336–&, Jan 1971.
- [178] I. Ohmine and H. Tanaka. Fluctuation, relaxations, and hydration in liquid water - hydrogen-bond rearrangement dynamics. *Chem. Rev.*, 93(7):2545–2566, Jan 1993.
- [179] H. J. Bakker and J. L. Skinner. Vibrational spectroscopy as a probe of structure and dynamics in liquid water. *Chem. Rev.*, 110(3):1498–1517, Jan 2010.
- [180] James L. Skinner, Benjamin M. Auer, and Yu-Shan Lin. *Vibrational Line Shapes, Spectral Diffusion, and Hydrogen Bonding in Liquid Water*, volume 142. John Wiley & Sons, Inc., 2009.
- [181] N. Demirdoven, M. Khalil, and A. Tokmakoff. Correlated vibrational dynamics revealed by two-dimensional infrared spectroscopy. *Phys. Rev. Lett.*, 89(23):237401, Jan 2002.
- [182] Kyungwon Kwak, Sungnam Park, Ilya J. Finkelstein, and M. D. Fayer. Frequency-frequency correlation functions and apodization in two-dimensional infrared vibrational echo spectroscopy: A new approach. *J. Chem. Phys.*, 127(12):124503, Jan 2007.
- [183] Rebecca A. Nicodemus, Krupa Ramasesha, Sean T. Roberts, and Andrei Tokmakoff. Hydrogen bond rearrangements in water probed with temperature-dependent 2D IR. *J. Phys. Chem. Lett.*, Mar 2010.
- [184] J. G. Saven and J. L. Skinner. A molecular theory of the line-shape - inhomogeneous and homogeneous electronic-spectra of dilute chromophores in nonpolar fluids. *J. Chem. Phys.*, 99(6):4391–4402, Jan 1993.

- [185] Y. S. Lin, P. A. Pieniazek, Mino Yang, and J. L. Skinner. On the calculation of rotational anisotropy decay, as measured by ultrafast polarization-resolved vibrational pump-probe experiments. *J. Chem. Phys.*, 132(17):174505, Jan 2010.
- [186] C. P. Lawrence and J. L. Skinner. Quantum corrections in vibrational and electronic condensed phase spectroscopy: Line shapes and echoes. *P. Natl. Acad. Sci. USA*, 102(19):6720, 2005.
- [187] A. Tokmakoff. Orientational correlation functions and polarization selectivity for nonlinear spectroscopy of isotropic media. I. Third order. *J. Chem. Phys.*, 105(1):1–12, Jan 1996.
- [188] Sergey Yeremenko. *Water dynamics explored by femtosecond infrared spectroscopy*. PhD thesis, University of Groningen, 2004.
- [189] C. Petersen, K.-J. Tielrooij, and H. J. Bakker. Strong temperature dependence of water reorientation in hydrophobic hydration shells. *J. Chem. Phys.*, 130(21):214511, Jan 2009.
- [190] Damien Laage. Reinterpretation of the liquid water quasi-elastic neutron scattering spectra based on a nondiffusive jump reorientation mechanism. *J. Phys. Chem. B*, 113(9):2684–2687, Jan 2009.
- [191] C. H. Cho, J. Urquidi, S. Singh, and G. W. Robinson. Thermal offset viscosities of liquid H₂O, D₂O, and T₂O. *J. Phys. Chem. B*, 103(11):1991–1994, Jan 1999.
- [192] R. J. Speedy and C. A. Angell. Isothermal compressibility of supercooled water and evidence for a thermodynamic singularity at 45°C. *J. Chem. Phys.*, 65:851, 1976.
- [193] C.A. Angell. *Water-A Comprehensive Treatise*, volume 7. Plenum, 1980.
- [194] K. Ito, C. T. Moynihan, and C. A. Angell. Thermodynamic determination of fragility in liquids and a fragile-to-strong liquid transition in water. *Nature*, 398(6727):492–495, Jan 1999.
- [195] Sow-Hsin Chen, Francesco Mallamace, Chung-Yuan Mou, Matteo Broccio, Carmelo Corsaro, Antonio Faraone, and Li Liu. The violation of the Stokes-Einstein relation in supercooled water. *P. Natl. Acad. Sci. USA*, 103(35):12974–12978, Jan 2006.
- [196] D. J. Adams and G. S. Dubey. Taming the Ewald sum in the computer-simulation of charged systems. *J. Computational Phys.*, 72:156–176, 1987.
- [197] J. Ropp, C. Lawrence, T. C. Farrar, and J. L. Skinner. Rotational motion in liquid water is anisotropic: A nuclear magnetic resonance and molecular dynamics simulation study. *J. Am. Chem. Soc.*, 123(33):8047–8052, Jan 2001.

- [198] M. Kozinski, S. Garrett-Roe, and P. Hamm. 2D-IR spectroscopy of the sulfhydryl band of cysteines in the hydrophobic core of proteins. *J. Phys. Chem. B*, 112(25):7645–7650, 2008.
- [199] Sean T. Roberts, Krupa Ramasesha, Poul B. Petersen, Aritra Mandal, and Andrei Tokmakoff. Proton transfer in concentrated aqueous hydroxide visualized using ultrafast infrared spectroscopy. Accepted.
- [200] R. Lemus. Vibrational excitations in H₂O in the framework of a local model. *J. Mol. Spectrosc.*, 225(1):73–92, Jan 2004.
- [201] M. L. Cowan, B. D. Bruner, N. Huse, J. R. Dwyer, B. Chugh, E. T. J. Nibbering, T. Elsaesser, and R. J. D. Miller. Ultrafast memory loss and energy redistribution in the hydrogen bond network of liquid H₂O. *Nature*, 434(7030):199–202, 2005.
- [202] A. Paarmann, T. Hayashi, S. Mukamel, and R. J. D. Miller. Probing intermolecular couplings in liquid water with two-dimensional infrared photon echo spectroscopy. *J. Chem. Phys.*, 128(19):191103, Jan 2008.
- [203] W. F. Kuhs and M. S. Lehmann. *Water Sci. Rev.*, 2, 1986.
- [204] A. Halkier, W. Klopper, T. Helgaker, P. Jorgensen, and P. R. Taylor. Basis set convergence of the interaction energy of hydrogen-bonded complexes. *J. Chem. Phys.*, 111:9157, 1999.
- [205] Linus Pauling. The structure and entropy of ice and other crystals with some randomness of atomic arrangement. *J. Am. Chem. Soc.*, 57:2680–2684, 1935.
- [206] V. F. Petrenko and R. W. Whitworth. *Physics of Ice*. Oxford University Press, 1999.
- [207] S. Bratos, J.-Cl. Leicknam, G. Gallot, and H. Ratajczak. *Ultrafast Hydrogen Bonding Dynamics and Proton Transfer Processes in the Condensed Phase*, chapter 2, pages 5–28. Kluwer Academic, 2002.
- [208] F. Li and J. L. Skinner. Infrared and Raman line shapes for ice Ih. I. Dilute HOD in H₂O and D₂O. *J. Chem. Phys.*, 132(20):204505, Jan 2010.
- [209] Y. M. Jung, B. Czarnik-Matuszewicz, and S. Bin Kim. Characterization of concentration-dependent infrared spectral variations of urea aqueous solutions by principal component analysis and two-dimensional correlation spectroscopy. *J. Phys. Chem. B*, 108(34):13008–13014, Jan 2004.
- [210] Y. L. A. Rezus and H. J. Bakker. Effect of urea on the structural dynamics of water. *Proc. Natl. Acad. Sci. USA*, 103(49):18417, 2006.